UNIVERSITY OF BELGRADE

SCHOOL OF ELECTRICAL ENGINEERING

Jelena Lj. Dinkić

NONUNIFORM HELICAL ANTENNAS

Doctoral Dissertation

Belgrade, 2021.

УНИВЕРЗИТЕТ У БЕОГРАДУ

ЕЛЕКТРОТЕХНИЧКИ ФАКУЛТЕТ

Јелена Љ. Динкић

НЕУНИФОРМНЕ ХЕЛИКОИДАЛНЕ АНТЕНЕ

докторска дисертација

Београд, 2021.

Supervisors/ментори:
Dr. Antonije Đorđević, retired professor
University of Belgrade – School of Electrical Engineering

Dr. Dragan Olćan, associate professor
University of Belgrade – School of Electrical Engineering

Jury members/чланови комисије:
Dr. Marija Stevanović, associate professor
University of Belgrade – School of Electrical Engineering

Dr. Vesna Javor, associate professor
University of Niš – Faculty of Electronic Engineering

Dr. Dejan Gvozdić, full professor
University of Belgrade – School of Electrical Engineering

Defense date/датум одбране: _____

Acknowledgment

Nonuniform helical antennas

Abstract

The objective of this thesis is to systematically analyze and optimize nonuniformly-wound helical antennas, along with classical (uniform) helical antennas. The optimization of the nonuniform helical antennas has many degrees of freedom. Hence, the optimization space is large and the optimization task is challenging. It is shown that, in most practical cases, the optimal nonuniform helical antennas outperform the uniform helical antennas presented in the literature. It is also shown that the nonuniform helical antennas are the preferable choice when the losses are low or medium, whereas for high losses, the uniform helical antennas should be used.

A large database is assembled from the optimization results, wherefrom a complete design procedure is developed for the nonuniform helical antennas. This procedure comprises all necessary equations and graphs for evaluating the optimal antenna parameters and estimating the antenna characteristics. The design procedure is verified experimentally, by measurements of a fabricated prototype.

Quad (2×2) arrays of nonuniform helical antennas are also investigated. Their design procedure includes the optimization of single antennas along with their positions in the array. The solution of a real engineering problem is presented: a quad array that meets predefined specifications is designed and a prototype is fabricated and measured.

Key words: antenna design, helical antennas, optimization, quad arrays of helical antennas

Scientific field: Electrical and Computer Engineering

Scientific subfield: Electromagnetics, Antennas, and Microwaves

Неуниформне хеликоидалне антене

Сажетак

Циљ ове тезе је систематична анализа и оптимизација неуниформно мотаних хеликоидалних антена, као и класичних (униформних) хеликоидалних антена. Оптимизација неуниформних хеликоидалних антена има много степени слободе. Стога је оптимизациони простор велики, а оптимизација изазован задатак. Показано је да, у највећем броју практичних случајева, оптималне неуниформне хеликоидалне антене надмашују по перформансама униформне хеликоидалне антене представљене у литератури. Осим тога, показано је да су неуниформне хеликоидалне антене бољи избор када су губици мали или средњи, док би у случају великих губитака требало користити униформне хеликоидалне антене.

Резултати оптимизације чине велику базу података, на основу које је развијен поступак пројектовања неуниформних хеликоидалних антена. Овај поступак обухвата све потребне једначине и графике за одређивање оптималних параметара антена и процену карактеристика антена. Поступак дизајна је потврђен експериментално, мерењем карактеристика реализованог прототипа.

Такође су испитивани низови од 2 x 2 неуниформне хеликоидалне антене. Процедура за њихов дизајн садржи оптимизацију засебних антена, као и оптимизацију положаја антена у низу. Представљено је и решење реалног инжењерског проблема: дизајниран је низ од 2 x 2 антене који испуњава унапред дефинисане спецификације, а прототип је направљен и измерен.

Кључне речи: дизајн антена, хеликоидалне антене, оптимизација, низови хеликоидалних антена

Научна област: Електротехника и рачунарство

Ужа научна област: Електромагнетика, антене и микроталаси

Table of Contents

1. Introduction

Helical antennas were first reported by Kraus in [1] and explained in more details in [2]. The classical helical antenna consists of a conductor uniformly wound in the form of a helix and positioned above a ground plane or another convenient counterbalance. The sketch of a typical helical antenna is shown in Fig. 1.1a. The main parameters that define the geometry of the helical antenna are:

- the axial antenna length, L, or the number of turns, N,
- the turn radius, r, and
- the pitch angle, φ, or the pitch, p.

The relation between the pitch angle, turn radius, and pitch is defined by $\varphi = \arctan\left(p/(2\pi r)\right)$. We assume the ground plane to be horizontal, so that the axis of the helix is vertical (the z axis in Fig. 1.1a). In the case of uniform helical antennas, the turn radius and pitch angle are constant, whereas the turn radius and pitch angle of nonuniform helical antennas vary along the antenna axis (the z axis in Fig. 1.1a). The feeding port is between the counterbalance and the helix. The helical conductor (usually, a wire of a circular cross-section and radius r_w, uniform along the conductor) can be located above a ground conductor of various shapes and sizes. The simplest theoretical case is an infinite perfectly conducting (perfect electric conductor, PEC) ground plane. Such a ground conductor is suitable for investigation of the antenna characteristics, since the influence of the currents on the ground plane can be replaced by the image theorem. However, for practically feasible realizations, the ground conductor of finite dimensions is required. The ground conductors of finite dimensions can be flat (most often of a circular or a square shape, Fig. 1.1a), or in a shape of a circular cup (Fig. 1.1b) or a truncated cone (Fig. 1.1c).
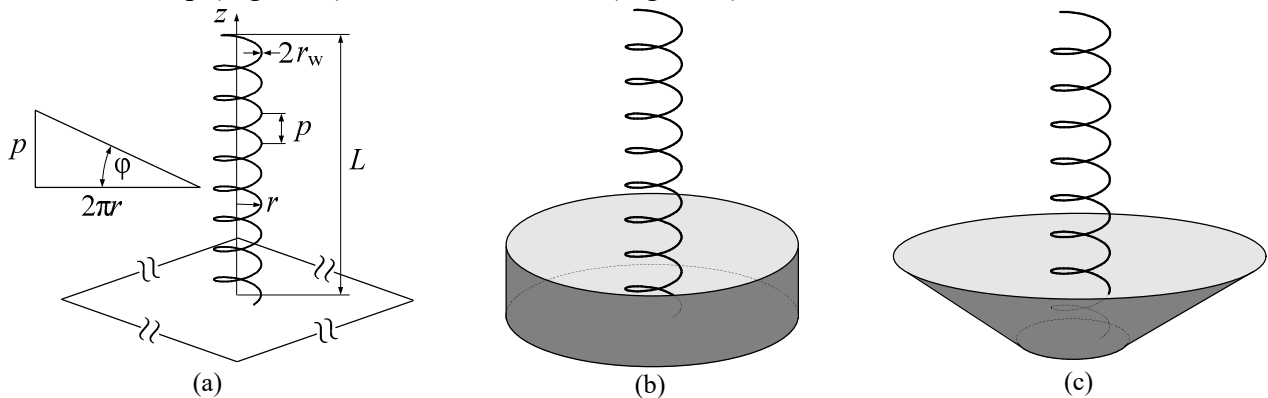
Figure 1.1. Sketch of the uniform helical antenna above (a) flat ground plane, (b) circular cup, and (c) truncated cone.

Helical antennas can radiate in two different radiation modes, i.e., the normal mode and the axial (or beam) mode. For the operation in the normal mode, the helix must be short ($L \ll \lambda$) and the circumference of the helix turns and pitch must be small compared to the wavelength (smaller than 0.5λ), where λ is the free-space wavelength at the antenna operating frequency [2]. In the normal mode, the antenna radiates almost equally in all directions perpendicular to the helix axis; hence, the radiation pattern is omnidirectional in the equatorial plane. In the general case, the radiated field is elliptically polarized. However, for certain dimensions, the polarization can be circular or linear. Namely, if the pitch angle is equal to 0, the helical antenna collapses into a loop. The radiation is

perpendicular to the helix axis (i.e., in the equatorial plane), but the polarization is linear and horizontal. With the increase in the pitch angle, the polarization becomes elliptical. The polarization is circular when the pitch angle achieves the value such that the turn circumference is equal to $\sqrt{2p\lambda}$, where p is the corresponding pitch [2]. With further increase in the pitch angle, the polarization becomes elliptical again. Finally, when the pitch angle is $90°$, the helical antenna becomes a straight conductor. Hence, the polarization is linear and vertical.

Helical antennas working in the normal mode are employed in WLAN applications [3]–[5], mobile communications [6]–[9], and medical applications [10]–[14]. However, note that they are narrowband and their directivity is low.

The axial mode occurs when the circumference of the turns is around one wavelength at the antenna operating frequency. In the axial mode, the maximum of the radiation is along the helix axis, the field is circularly or elliptically polarized in that direction, and the main beam is well defined. Hence, in [2] it is also referred to this mode as the beam mode, so that helical antennas radiating in the axial mode can be referred to as axial or beam helical antennas [2].

Since an almost accidental invention of helical antennas working in the axial mode by Kraus, they have been widely used because of their good mechanical and electrical properties: a simple and robust structure, almost circular polarization, inherently broad bandwidth, etc. These good performances promote helical antennas as a good choice for various applications. First applications were primarily in the space communications [2], [15]. During the last two decades, besides space applications [16]–[22], helical antennas have also been used in medical applications [23]–[26], wireless communications [27]–[35], unmanned aerial vehicle (UAV) applications [36], [37], radio-frequency identification (RFID) systems [38]–[40], radar systems [41], [42], cyber security [43], and hybrid free-space optics/radio-frequency (FSO/RF) systems [44].

The focus of this thesis are helical antennas working in the axial mode. Various designs of helical antennas are widely investigated: designs devoted to the specific application [15]–[44], designs according to the defined specifications, or designs which improve specific antenna characteristics [45]–[84]. However, general and reliable guidelines for the design of the helical antennas are rarely found (especially for nonuniformly-wound helical antennas). To generate such guidelines, extensive numerical computations (simulations) are necessary. Modern computers have recently reached performances that allow running the necessary amount of simulations in reasonable and acceptable time. Therefore, the main motivation of this thesis is to build a large database of the optimal helical antennas by extensive numerical computations and, based on it, define general guidelines for the design of helical antennas. Within this work, several million simulations have been performed. The obtained data have been used for the formulation of a complete, standalone, and rapid procedure for designing the axial-mode nonuniform helical antennas. The antennas designed using this procedure have been investigated in detail, compared in terms of their characteristics with different types of helical antennas (i.e., uniform helical antennas and helical antennas with exponential and piecewise-linear variation of geometrical parameters) and with helical antennas whose design is presented in the literature. The results of the presented design procedure have been verified experimentally. In addition, this procedure has been expanded to the design of arrays of helical antennas.

1.1. Design of helical antennas

Some practical design guidelines (design equations and diagrams) are available in the open literature for designing uniform helical antennas, with constant turn radius and pitch angle along the antenna [1], [2], and [45]–[50].

Firstly, Kraus presented guidelines for the design of uniform helical antennas [1], [2]. For the antennas with more than $N = 3$ turns, it is suggested that the circumference, C, and pitch angle of each turn should be in the ranges $0.8\lambda < C < 1.15\lambda$ and $12° < \varphi < 14°$, respectively [2]. The

corresponding antenna gain in the main radiating direction (along the antenna axis), assuming no losses, can be calculated as

$$g\,[\mathrm{dBi}] = 10\log_{10}\left(12\left(\frac{C}{\lambda}\right)^2 \frac{L}{\lambda}\right),$$ (1.1)

where λ is the free-space wavelength at the antenna operating frequency (f) and L is the axial antenna length. The antenna terminal resistance depends on the way antenna is fed. In case of the axial feed (i.e., the feed is on the axis of the helix, and a conductor is used to connect the feed and the helix wire), the resistance is $R = 140\,(C/\lambda)\,\Omega$, whereas for the peripheral feed (i.e., the feed is located directly at the onset of the helix wire, as in Fig. 1.1a), the resistance is $R = 150/\sqrt{C/\lambda}\ \Omega$. The axial ratio (the ratio of the major to the minor axis of the polarization ellipse of the electric-field intensity) is $AR = (2N+1)/(2N)$. However, in Kraus's early work, the shape and size of the ground plane is not clearly defined. This can lead to ambiguities when other, later results presented in the literature are compared with the Kraus's results since the size and shape of the ground plane can strongly affect the antenna gain.

The experimental results presented in [45] and [46] show that the results given by (1.1) overestimate the gain. For the helical antennas of a fixed length, containing 8.6 to 10 turns whose circumference is in the interval $0.8\lambda < C < 1.2\lambda$, instead of the coefficient 12 in (1.1), the numerical factor should be between 4.2 and 7.7, whereas in [47] it is suggested that 6.2 is suitable for this numerical factor. These results claim that the actual gain is for 1.9–4.6 dB smaller than given by (1.1), which is a significant reduction.

Also, in [45] a new equation is derived to fit the measured gain of the fixed-length antenna of around 10 turns: $g\,[\mathrm{dBi}] = 10\log_{10}\!\left(8.3\,(\pi r/(2\lambda))^{\sqrt{N+2}-1}(L/\lambda)^{0.8}(\tan 12.5°/\tan\alpha)^{\sqrt{N}/2}\right)$. The gain calculated from this equation is within ±0.1 dB of the measured data. It should be noted that experimental results utilized in this research are obtained for antennas located above a circular cup instead above a flat ground, whereas in [47] the type of the ground plane is not specified.

Later, by extensive numerical modeling, Emerson [48] has found that the maximal possible gain of uniform helical antennas is up to 5 dB lower than the gain calculated from (1.1). More precisely, the antenna gain increases more slowly with increasing the antenna length than Kraus's equation predicts. Further, in [48] a new equation for the antenna gain is presented, $g\,[\mathrm{dBi}] = 10.25 + 1.22\,L/\lambda - 0.0726\,(L/\lambda)^2$, along with an equation for the optimal turn radius, $r/\lambda = 0.2025 - 0.0079\,L/\lambda + 0.000515\,(L/\lambda)^2$. These design equations are valid for the axial antenna lengths in the range $2\lambda < L < 7\lambda$ and the constant pitch $p = 0.24\lambda$. The gain is almost independent of the wire radius and conductivity (losses in the antenna conductor). Furthermore, in terms of the gain, a square ground plane of a $\lambda/2$ side is nearly as good as an infinite ground plane [48].

Obviously, there exist significant differences among the results presented in the literature. In [49], these differences are pointed out and summarized. Further, a systematic investigation is performed of uniform helical antennas placed above an infinite ground plane in order to present a reliable procedure for designing such antennas. The optimal parameters for the narrowband (NB) design and three types of wideband (WB) designs are presented. These parameters depend on the axial antenna length, the wire radius, and the operating frequency. The gain of the optimal antennas is compared with the results available in the literature. The NB design achieves higher gain than almost all other designs, except the gain calculated from Kraus's equation, which is known to significantly overestimate the gain. The smallest discrepancy is between the gain of the NB design and the design from [50]. (The on-line reference [50] has been last accessed in 2006, but it is not available any more.) It should be noticed that the optimal pitch angles in [49] are in the range $3° < \alpha < 16°$ and they strongly depend on the wire radius. This range of pitch angles is much wider than the

classical range declared in [1], [2], and [45]–[47]. In [49] is indicated that the pitch angles from [50] are in good agreement with the optimal pitch angles for the NB design from [49].

In order to investigate causes of the discrepancies among the results presented in the literature, in [51] different shapes and sizes of the ground conductors are considered. Firstly, it is confirmed that the gain of the antenna located above an infinite ground plane is practically the same as reported in [48]. Further, it is shown that the optimal square ground plane is of a side 1.5 λ, although [52] recommends a circular or a square ground plane of a diameter or a side between 0.5 λ and 0.75 λ. In [51] antennas placed above a cylindrical cup (Fig. 1.1b) and a truncated cone (Fig. 1.1c) are also investigated. A cylindrical cup whose diameter is 1 λ and the height is 0.25 λ increases the gain for 1.4 dB in comparison with the antenna located above an infinite ground plane. However, the increase in the gain depends on the antenna length, i.e., for shorter antennas and pitch angles considered in [51] the enhancement of the gain is negligibly small, but it increases with increasing the antenna length. A truncated cone significantly increases the gain. The optimal dimensions of the truncated-cone reflector are presented in [53]. In [53] by simultaneous optimization of the antenna geometry and the dimensions of the truncated-cone reflector, the gain enhancement is obtained to be up to 5 dB in comparison with helical antennas located above a square ground plane. The axial lengths of the helical antennas considered in [53] are 1 λ, 2 λ, and 5 λ, while the wire radius is 0.0015 λ. The optimal pitch angles are several times larger than with a flat reflector, and the optimal lower and upper cone radii are $R_{\text{lower}} \approx 0.5\lambda$ and $R_{\text{upper}} \approx 0.5H + \lambda$, respectively, where H is the height of the cone reflector.

The explanation of the cup and cone functionality and various factors that improve the radiation pattern and gain are investigated in [54]. By analyzing the current distribution along different parts of the antenna conductor, it is confirmed that the traveling wave (along the upper part of the antenna) produces a relatively well-shaped radiation pattern, whereas the sidelobes are created by the current of the lowest turns. The current along the lowest turns does not resemble a traveling wave and it radiates almost omnidirectionally in horizontal directions. The field radiated by the lowest turns can easily be reflected into more favorable directions by the rim of the cup or the cone. Also, the field produced by the lowest turns can be suppressed by decreasing the pitch angles near the feed of the antenna. Additionally, it is explained that an infinite ground plane can make some helical antennas more broadband by reflecting waves that are launched from the antenna downwards, which justifies the WB design from [49].

Further, it is shown in [54] that for tall cones the length of the helical antenna practically has no influence on the antenna gain. This result confirms that the cone is the main radiation source: it acts like a horn antenna exited by the helical antenna, as it was previously indicated in [55].

Square-shaped corrugated reflectors are investigated [56]. It is shown that the rear surface of the reflector changes the currents on the reflector, which reduces the backward radiation.

In order to increase the gain or improve antenna characteristics, adding different parasitic elements is suggested in [33], [57]–[63]. Adding a circular plate on top of helical antenna is used for widening the axial-ratio bandwidth [57] and increasing the gain [58], [59]. A parasitic cylindrical ring is mounted on the top of antenna [60] or parasitic rings are mounted inside the helical antenna [61], both with the same purpose to increase the gain. To reduce the overall dimensions of the helical antenna, loading stubs are periodically placed around the turn circumference [62]. In order to keep the advantage (i.e., the size reduction) of the stub-loaded helical antennas from [62], but also to achieve a purely real input impedance, a new design is proposed in [33]. With the same aim to minimize the antenna overall dimensions (without sacrificing the gain), a lossy ferrite core with a dielectric shell is placed inside the helical antenna [63].

As it is mentioned, the antenna conductor is usually a wire of a circular cross-section, uniform along the conductor (Fig. 1.1a). However, in some applications, the antenna conductor can be a strip, a wire of a nonuniform circular cross-section, or the conductor can be realized as a printed conducting trace [5], [24], [38], [39], [57], [64], and [65]–[68]. The influence of different conductor types on the antenna characteristics is investigated in [64]. For a uniformly-wound helical antenna,

where the optimal design parameters are adopted as for the NB design from [49], various shapes and sizes of the antenna conductor are investigated. Three different sets of models are utilized that correspond to different manufacturing technologies: thin-wire models, wire-cage models, and plate models. In [64] it is shown that the thin-wire model is appropriate as long as the antenna conductor is thin (its radius is smaller than about 0.01 λ) and the gap between the turns is wide (larger than the wire radius). When the antenna conductor becomes thicker and the turns are closer, the proximity effect becomes pronounced, so that the thin-wire model is not appropriate any more [64].

Recently it was suggested that the metallic conductor of a conventional helical antenna can be replaced with a plastic tube of a circular cross-section filled with pure water [69]. This allows reconfigurability of polarization over a wide frequency range. Reconfigurability of polarization is also achieved using liquid metal as the antenna conductor [70]. Further, switchable sense of polarization is also obtained using origami helical antennas [65]. The origami helical antennas are used to obtain reconfigurability in terms of frequency [66], [67] or both mode and frequency [68]. Finally, reconfiguration of the radiation pattern can be obtained by using shape-memory alloy spring actuator [71].

In [1] Kraus claims that near the operating frequency, the real part of the input impedance is between $100\,\Omega$ and $500\,\Omega$, whereas the imaginary part is $\pm j300\,\Omega$. However, in [72] it is indicated that an axial-fed helical antenna has a terminal impedance of $140\,\Omega$. Further, it is suggested that the impedance can be matched to $50\,\Omega$ simply by increasing the conductor size close to the fed point. This way of impedance transformation is used for antenna matching in [43]. A similar idea for impedance matching is used in [73], where it is shown that increasing the pitch of the first turn increases the input resistance and decreases the input reactance, whereas increasing the feed height increases the input resistance and negligibly influences the input reactance. A detailed investigation of an impedance matching network that consists of a single wire (which enables fast analysis) is presented in [74], [75]. Another method for impedance matching is proposed in [76], where controlling the dimension of the top layer of a double-layer metal structure (bottom layer acts like a ground plane) enables tuning of the input impedance.

As an upgrade of the classical, uniform helical antennas, nonuniform helical antennas are also investigated in the literature. Various types of nonuniformities are used to improve antenna characteristics. In [77], it is shown that tapered radii at the feeding end and at the termination of the antenna suppress unwanted current waves that travel along the helix, which improves the axial ratio. Further, by varying the angle of the truncated-cone reflector of the tapered antenna, the input impedance can be adjusted to an arbitrary value [77].

Continuously tapered (or conical) helices and quasi-tapered helices are considered in [78]. Such helices enable shaping the gain versus frequency and also improve the axial ratio and radiation pattern. A quasi-tapered helical antenna is proposed in [73] with an aim to broaden the bandwidth. This antenna consists of two segments. The bottom segment is conical and it is responsible for increasing the bandwidth towards lower frequencies. The top segment is uniform and it is used to increase the gain at higher frequencies. Further, quasi-tapered helical antennas are investigated with the same aim (to achieve a wide bandwidth) in [79]. Here, the quasi-tapered antenna consists of two uniform segments (of different turn radii) that are connected by a short intermediate segment. In [79] is stated that, in order to maximize the gain bandwidth, the ratio of lower-to-upper diameter should be around 1.41, and the axial lengths of two uniform segments should be equal.

Logarithmic, linear, and exponential variations of the turn radius along the antenna are investigated and compared in [80], [81]. However, the gain of the antennas with the exponential variation of the turn radii, proposed as the best solution in [80], [81], is around 6.5 dB lower than the gain of uniform helical antenna of the same axial length [49], and around 7 dB lower than the gain of the nonuniform antenna of the same length from [82]. Hence, the data presented in [80], [81] do not seem to define optimal nonuniform helical antennas.

Nonuniform pitch angles are also reported in the literature [82]–[85]. In [82], nonuniform helical antennas are considered that have a wire pigtail instead of a ground conductor. In order to maximize the gain, both the radii and pitches are optimized. The resulting gain is very close to the gain of the

optimal uniformly-wound helical antennas with a large ground plane [49], while the obtained nonuniform antennas are smaller and handier. In [83] and [84], nonlinear pitch profiles are considered with a constant or exponentially varying turn radius aimed at maximizing the gain and minimizing the axial ratio. In [85], an exponential pitch is considered and it is used for widening the bandwidth compared to uniform helical antennas. This improvement is explained by analyzing the current distribution along the antenna.

Data presented in the literature strongly indicate that nonuniform helical antennas may outperform uniform helical antennas. Hence, for engineering purposes, it is desirable to have reliable guidelines how to achieve optimal properties of these antennas. However, in contrast to uniform helical antennas, where systematic investigation and practical design guidelines already exist in [1], [2], and [45]–[50], such design guidelines do not exist for nonuniform helical antennas. This fact has motivated us to perform a detailed study of nonuniform helical antennas, which would result in clear engineering design guidelines and procedures. This task is challenging because nonuniform helical antennas have many degrees of freedom, which significantly aggravates the search for the optimal solutions.

1.2. Arrays of helical antennas

In order to further increase the achieved gain, several helical antennas (uniform or nonuniform) can be arranged so to form an array. This concept is introduced by Kraus in [86], and investigated in more detail in [2]. Antenna arrays (instead of a single helix) can obtain the same gain, but allow using shorter antennas. Namely, to achieve the same gain, with an increase of the antenna number, the required antenna length is decreased. Similarly, using an antenna array instead of a single helical antenna of the same axial length (as the antennas that make up the array), increases the achieved gain. According to the theory of antenna arrays, the level of increase depends on the number of antennas used in the array (under condition that antennas are properly spaced) [2], [87]. For example, an array of four helical antennas achieves around 5 dB higher gain than a single helical antenna (of the same axial antenna length as the antennas used in the array) [88]. Arrays of helical antennas that contain various numbers of elements (arranged in different ways) are investigated in the literature: linear arrays in [89]–[92], planar square arrays in [88], [93]–[102], and circular arrays in [103]–[107].

The main parameters that define the geometry of the helical antenna array are the geometrical parameters of a single helix (i.e., the axial antenna length, turn radius, and pitch or pitch angle), the shape and size of the ground conductor, and number and spacing between the array elements. The influence on the antenna characteristics of the geometrical parameters of a single helix and shape and size of the ground conductor are similar as for a single helical antenna. Increase in the number of array elements increases the gain. The optimal spacing between the elements and the influence of the element spacing on the antenna characteristics are widely investigated in the literature [92], [94]–[98], [105], [106], [108]. The curves presented in [96] give a first-order approximation for two design questions. Firstly, in the case of a specified array aperture, the minimal number of elements is given that is required for the maximal directivity. Secondly, in the case of a specified number of elements, the optimal spacing for the maximal directivity is given. In [108] an equation that defines the minimal distance between the array elements is introduced. It is stated that the array-element spacing should be at least $\sqrt{G_{\mathrm{h}}/(4\pi)}\lambda$, where G_{h} is the (numerical) gain of the single helical antenna. In [98] adjustment of the spacing between the array elements is utilized to tilt the radiated beam at the certain angle. Finally, by controlling the amplitude distribution, beams of complicated shapes can be generated [92].

The range of applications that employ arrays of helical antennas is similar as for single helical antennas: mobile communications [90], [95], [97], [109], satellite communications [107], and broadcasting satellite TV programs [105], [106]. In addition, arrays of helical antennas are used in radar applications [92] and high-power microwave applications [101], [104].

The feeding of the antenna array requires an appropriate network. An antenna array can be matched to $50\,\Omega$ using a properly designed feeding network. The design of feeding networks is presented in [90], [91], [98], [101], [104]–[106], and [109]. Feeding networks are usually realized in the printed-circuit technology [90], [98], [109] or using waveguides [91], [104]–[106]. For the high-power applications, special attention is paid to the design of the feeding network [101].

In this thesis, arrays of helical antennas will be considered in the form of a planar, square array of four (2×2) nonuniform helical antennas, referred to as a quad array. Firstly, a complete design procedure for an antenna array (the optimal geometry of helical antennas utilized in the array, positions of the antennas, and the feeding network) is presented. The designed antenna array meets pre-set specifications. Hence, this part of the thesis presents a good solution of a real-world engineering problem. Further, general guidelines for the design of quad arrays are presented and a procedure for designing these arrays is formulated. The design procedure yields all necessary data; hence, it allows fast designing of quad arrays without additional calculations.

1.3. Thesis outline

This thesis contains eight chapters and two appendixes.

The current chapter (Chapter 1) gives the basic information about helical antennas and arrays of helical antennas, their geometry, design guidelines, and applications, through the literature overview. It also outlines the main motivation and contributions of the thesis.

In Chapter 2, the geometry of the considered (uniform and nonuniform) helical antennas is presented in more details. Nowadays, the simulations are widely used in the engineering world (as well as in this thesis). Details about the models of helical antennas utilized for the simulations within this thesis are brought out in Chapter 2.

Finding the optimal design and formulation of a fast and reliable design procedure for nonuniform helical antennas is one of the main contributions of the thesis. Hence, optimizations are an important part of this investigation. Details about the optimization setup, choosing the most appropriate optimization algorithms, and processing of the optimization results with the mentioned purposes are presented in Chapter 3. The steps that precede the formulation of the set of equations for the designing of nonuniform helical antennas with linearly varying geometrical parameters are also given in Chapter 3. The formulated set of equations contains:

- equations for calculating the geometrical parameters of helical antennas,
- equation for gain estimation, and
- equations for evaluating the validity of the design.

Characteristics of the antennas designed utilizing the set of equations formulated in Chapter 3 are investigated in Chapter 4. Further, a flat square or circular ground plate of finite dimensions are used to replace an infinite ground plane. The influence of this replacement on the antenna characteristics is investigated and results are reported. Finally, the designed helical antennas with linearly varying geometrical parameters are compared with other types of helical antennas (uniform, exponential, piecewise-linear, etc.) and antennas whose design is presented in the literature.

Chapter 5 summarizes the proposed fast procedure for designing helical antennas utilizing the formulated set of design equations. The validity of the design procedure is confirmed by measurements of a fabricated prototype of a helical antenna that is designed following this procedure. Details about the design, fabrication, and measurements of the prototype are presented.

Chapter 6 presents steps for detailed design and fabrication of an array of nonuniform helical antennas. This chapter describes the design of the geometry of helical antennas that make up the array, design of the feeding network, fabrication, and measurements of the designed array. Chapter 6 details solution of a real engineering problem, which results in a designed and fabricated array that meets the required project specifications.

In Chapter 7, the investigation of the quad arrays is generalized and the procedure for their design is presented. This procedure represents an extension of the design procedure formulated in Chapter 5 since it utilizes design equations for nonuniform helical antennas.

Finally, Chapter 8 summarizes the results presented within the thesis and outlines the main conclusions, contributions of the thesis, and guidelines for the future research.

Appendix A explains antenna terms, definitions of the units, and definitions of some quantities which are frequently used within this thesis.

Appendix B introduces the theorem of electromagnetic similitude, which is utilized within the thesis.

1.4. Key references

The results presented in this thesis are based on the following publications:

[64] **J. Lj. Dinkić**, M. S. Tasić, and A. R. Đorđević, "Influence of conductor shape and size on properties of helical antennas," *Proceedings of 5th International Conference on Electrical, Electronic and Computing Engineering iETRAN 2018*, Palić, Serbia, June, 2018.

[88] **J. Lj. Dinkić**, D. I. Olćan, A. R. Djordjević, and A. G. Zajić, "High-gain quad array of nonuniform helical antennas," *International Journal of Antennas and Propagation*, *Hindawi*, vol. 2019, 12 pages, 2019, doi: 10.1155/2019/8421809.

[110] **J. Dinkić**, D. Olćan, and A. Đorđević, "Comparison of various geometries of nonuniform helical antennas", *Proceedings of 6th International Conference on Electrical, Electronic and Computing Engineering icETRAN 2019*, Srebrno jezero, Serbia, June 3-6, 2019.

[113] **J. Dinkić**, D. Olćan, A. Djordjević, and A. Zajić, "Design and optimization of nonuniform helical antennas with linearly varying geometrical parameters," *IEEE Access*, vol. 7, pp. 136855-136866, 2019, doi: 10.1109/ACCESS.2019.2942363.

[114] **J. Dinkić**, D. Olćan, A. Djordjević, and A. Zajić, "Comparison of optimization approaches for designing nonuniform helical antennas," *Proceedings of 2018 IEEE International Symposium on Antennas and Propagation & USNC/URSI National Radio Science Meeting*, Boston, MA, 2018, pp. 1581-1582, doi: 10.1109/APUSNCURSINRSM.2018.8608928.

[120] **J. Dinkić**, D. Olćan, A. Djordjević and A. Zajić, "Comparison of the optimal uniform and nonuniform lossy helical antennas," *Proceedings of 2020 IEEE International Symposium on Antennas and Propagation and North American Radio Science Meeting*, Montreal, QC, Canada, 2020, pp. 423-424, doi: 10.1109/IEEECONF35879.2020.9330063.

2. Geometry and models of nonuniform helical antennas

2.1. Geometry of nonuniform helical antennas

As it is indicated in Chapter 1, the geometry of the helical antenna is defined by the axial antenna length, L, the turn radius, r, and the pitch angle, φ, or the pitch, p (Fig. 1.1a). In the case of nonuniform helical antennas, the turn radius and pitch angle can vary along the antenna in various ways. The design of this type of helical antennas has many degrees of freedom, which can result in ill-posed solutions with a very high gain, but also very narrow bandwidth. This is impractical for the applications where small deviations due to manufacturing tolerances can cause a shift of the operating frequency. Therefore, it is often adopted that the variations of the turn radius and pitch angle along the antenna have fewer degrees of freedom. Hence, these variations are taken to be linear, exponential, piecewise-linear (with a small number of linear segments) or based on other simple functions of the axial coordinate (the z coordinate in Fig. 2.1). In this thesis, linear, exponential, and piecewise-linear variations of geometrical parameters will be considered, and these types of geometries are discussed in more details in this chapter.

The investigation within this thesis utilizes wire conductors of a circular cross-section, which is uniform along the conductor. Considered wire radii will be within the range where the thin-wire approximation is appropriate, with an aim to cover most commercially available wires. The helical conductor will be located above infinite PEC ground plane, but also ground planes of finite dimensions (square and circular) will be considered.

2.1.1. Linear variation of geometrical parameters

In the case of nonuniform helical antennas with linear variation of geometrical parameters, the radius and pitch angle of each turn are linear functions of the axial coordinate z (Fig. 2.1). These geometrical parameters are defined by:

$$r = (r_2 - r_1)\frac{z}{L} + r_1, \tag{2.1}$$

$$\varphi = (\varphi_2 - \varphi_1)\frac{z}{L} + \varphi_1, \tag{2.2}$$

where r_1 is the radius of the lowest (bottom) turn (for $z = 0$), r_2 is the radius of the highest (top) turn (for $z = L$), and, similarly, φ_1 and φ_2 are the pitch angles at the bottom and top of the helix, respectively.

Note that uniform helical antennas can be considered as the special case of nonuniform helical antennas with linear variation of geometrical parameters where $r_1 = r_2$ and $\varphi_1 = \varphi_2$.
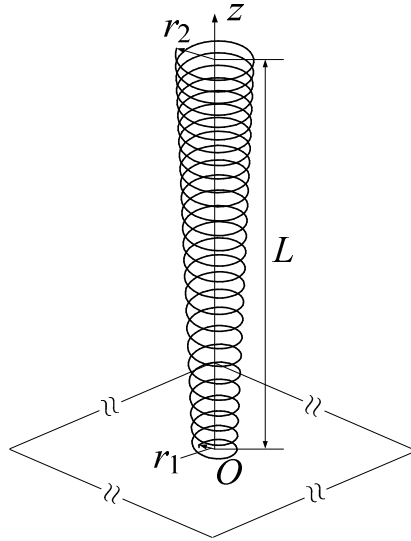
Figure 2.1. Sketch of the nonuniform helical antenna with linearly varying geometrical parameters.

For simplification, if not stated otherwise, we shall refer to the nonuniform helical antennas with linearly varying geometrical parameters simply as nonuniform helical antennas. However, in the parts of the thesis where other types of nonuniformities are investigated, it will be clearly indicated what type of variation is considered. In those parts we shall refer to the antenna governed by (2.1) and (2.2) as the linear helical antenna.

2.1.2. Exponential and piecewise-linear variations of geometrical parameters

In the case of nonuniform helical antennas with exponentially varying geometrical parameters (which we refer to as exponential helical antennas), shown Fig. 2.2a, the turn radius and pitch angle are defined by:

$$r = A_{\mathrm{r}} + B_{\mathrm{r}} \mathrm{e}^{C_{\mathrm{r}} z} , \tag{2.3}$$

$$\varphi = A_{\varphi} + B_{\varphi} \mathrm{e}^{C_{\varphi} z} , \tag{2.4}$$

where $A_{\mathrm{r}} = r_1 - B_r$, $B_{\mathrm{r}} = (r_2 - r_1)/(e^{C_{\mathrm{r}}L} - 1)$, $A_{\varphi} = \varphi_1 - B_{\varphi}$, $B_{\varphi} = (\varphi_2 - \varphi_1)/(e^{C_{\varphi}L} - 1)$, r_1, r_2, φ_1, φ_2 are the same as in the previous subsection, and C_{r} and C_{φ} are arbitrary coefficients.

Further, nonuniform helical antennas with piecewise-linear variations of the geometrical parameters (along concatenated segments) will be considered (Fig. 2.2b). These antennas will be referred to as piecewise-linear helical antennas. The full range ($0 \le z \le L$) along the antenna axis is divided into segments. Along each segment, the geometrical parameters are defined in a similar way as for the linear helical antenna:

$$r = (r_{k+1} - r_k)\frac{z_k}{L_k} + r_k , \ k = 1, 2, \ldots, N , \tag{2.5}$$

$$\varphi = (\varphi_{k+1} - \varphi_k)\frac{z_k}{L_k} + \varphi_k , \ k = 1, 2, \ldots, N , \tag{2.6}$$

where r_k, r_{k+1}, φ_k and φ_{k+1} are radii and pitch angles of the first turn and the last turn of the k-th segment, respectively, z_k is the local coordinate along each segment ($0 \le z_k \le L_k$), L_k is the axial length of each segment, and N is the total number of segments.
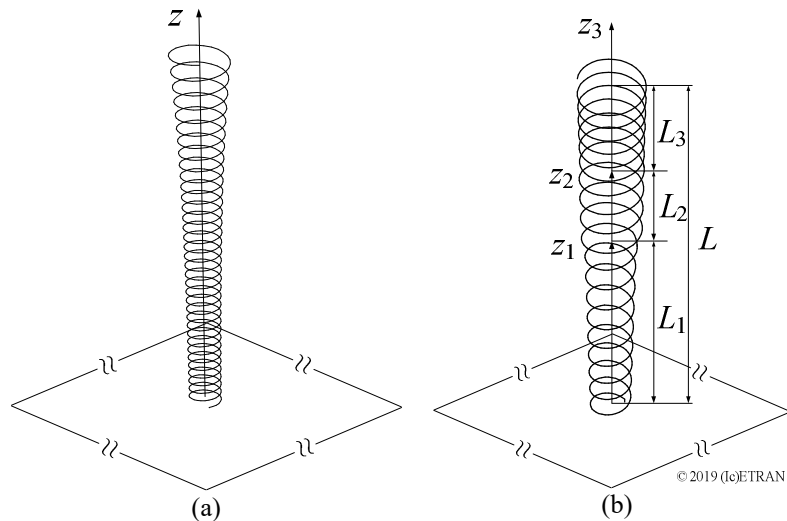
Figure 2.2. Sketch of the nonuniform helical antenna with (a) exponential and (b) piecewise-linear variations of geometrical parameters (three linear segments) [110].

In this thesis, linear, exponential, and piecewise-linear variations of the geometrical parameters are investigated and the characteristics of the best found (optimal) antennas are compared. The antennas with exponential and piecewise-linear variations of geometrical parameters can achieve slightly higher gain than linear antennas of the same axial length [110]. However, the bandwidth can be much narrower, which can cause problems in the fabrication and applications. If the antenna geometries are optimized in a given frequency range, the gain and bandwidth of all antennas is almost the same [110]. Further, the geometry of antennas with exponential and, especially, piecewise-linear variations is defined by more parameters; hence, the optimization requires more iterations and lasts significantly longer.

For these reasons, in the first part of this investigation, nonuniform helical antennas with linear variation of geometrical parameters will be considered. In Subsection 4.4.4, a detailed comparison among various types of geometry will be presented.

2.2. Models of helical antennas

In the modern engineering, a huge part of the design process and research relies on various types of computer simulations. Hence, reliable models and simulators are required. For this investigation, simulations are performed in software WIPL-D [111] and AWAS [112]. These simulators perform a full-wave 3D electromagnetic analysis, based on the method of moments (MoM). As an example, the WIPL-D model of a helical antenna is shown in Fig. 2.3a. The antenna is fed by a voltage delta-gap (point) generator located at the bottom of a short vertical wire segment, between the ground plane and the beginning of the first turn.
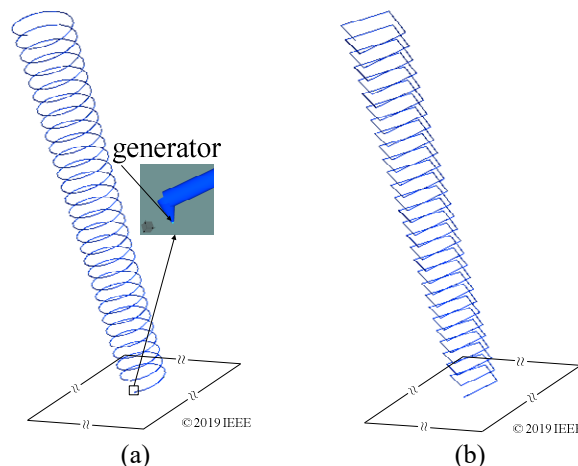

Figure 2.3. WIPL-D model of nonuniform helical antenna (a) with polygonal turns (16 sides) [113] and (b) with square turns [113].

11

WIPL-D and AWAS can analyze only straight-line wire segments. For this reason, a perfectly circular turn of the radius r has to be approximated by a regular polygonal line of n sides, having an appropriate side length.

A heuristic choice of the polygon side is as follows. A circle, whose radius is r, is approximated by a polygon constructed in such a way that this circle is positioned midway between the circle that is inscribed into the polygon (whose radius is r_{in}) and the circle that is circumscribed around the polygon (whose radius is r_{out}), i.e., $r = (r_{out} + r_{in})/2$ (Fig. 2.4). Hence, the polygon is inscribed into a circle whose radius is

$$r_{out} = \frac{2r}{1 + \cos\left(\dfrac{\Delta\gamma}{2}\right)},$$

(2.7)

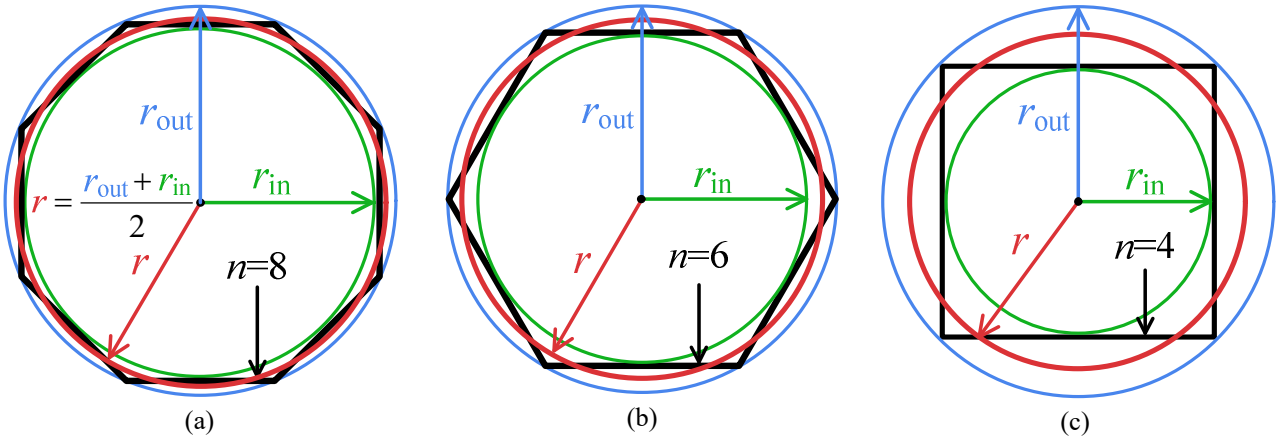where $\Delta\gamma = 2\pi / n$ is the central angle of the polygon.

Figure 2.4. Approximation of a circle by a polygonal line of (a) 8 sides, (b) 6 sides, and (c) 4 sides.

If the number of polygon sides is large, the duration of the simulation increases. However, if n is small, it can be expected that the error made due to the approximation can increase. In order to confirm the validity of the utilized approximation and to find the optimal n, we have performed the following numerical experiments.

Various axial antenna lengths (L) and wire radii (r_w) are considered. For each axial antenna length and wire radius, models with various numbers of polygon sides (n) are simulated and the gain is inspected. The gains of these antennas as the function of utilized number of polygon sides (n) are presented in Fig. 2.5. Each graph corresponds to one considered wire radius, whereas traces in the graphs correspond to the considered axial antenna length.

These results show that for $n \geq 12$ the gain practically does not depend on the number of polygon sides, i.e., for $n \geq 12$ the gain deviates less than 0.1 dB compared to a very large n. Nonetheless, the same low discrepancy can be noted for $n = 4$. Hence, in the majority of models considered in this dissertation, perfectly circular turns are approximated by square turns ($n = 4$), when $r_{out} = 2r / \left(1 + \sqrt{2}/2\right)$. An example of the corresponding model is shown in Fig. 2.3b.

The approximation with four straight segments per turn speeds-up the computations. Further, it enables manufacturing of a simple dielectric support for the antenna that has an almost negligible influence on the antenna characteristics. More details about the fabrication of such antenna prototypes will be provided in Subsection 5.3.
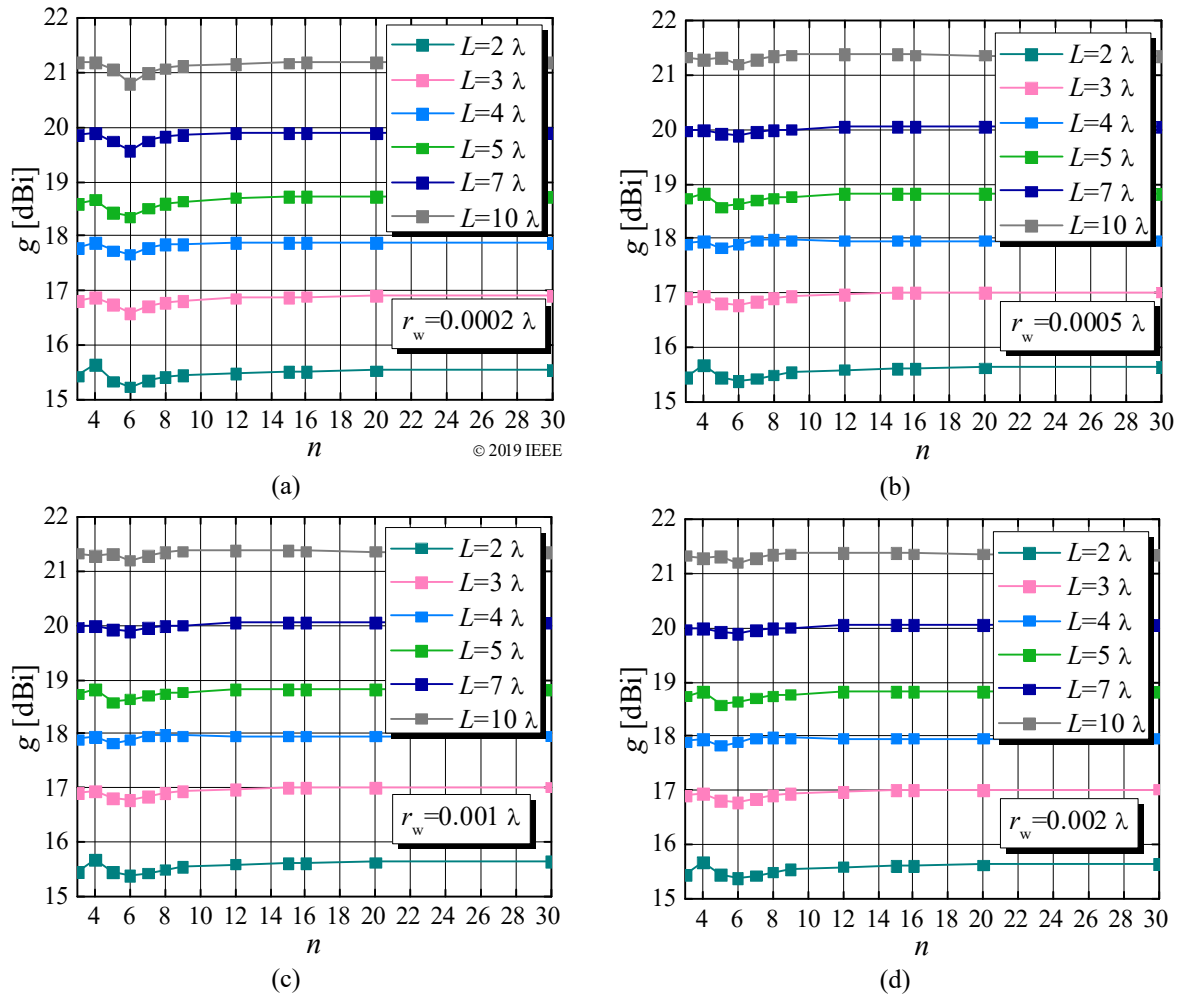
Figure 2.5. Gain of the antennas for various numbers of sides of the approximating polygon (n) for various axial lengths (L) and wire radius (a) $r_w = 0.0002\lambda$ [113], (b) $r_w = 0.0005\lambda$, (c) $r_w = 0.001\lambda$, and (d) $r_w = 0.002\lambda$.

As it is already said in Chapter 1, the counterbalance of the helical antenna can be an infinite PEC ground plane or a ground plane of finite dimensions (e.g., a circular or square flat plate, a circular cup, or a truncated cone). If the antenna is located above an infinite PEC ground plane, the influence of the currents in the ground plane can be taken into account by utilizing the antenna image (image theorem).

Flat square and circular ground planes will also be considered in this thesis. In WIPL-D models, square or circular ground planes are divided into smaller metallic plates. The current distributions over these plates are approximated by two-dimensional polynomials (basis functions). The simulator also allows considering losses in the ground plane. All helical antenna parameters of interest, e.g., the gain, input impedance, axial ratio, etc., are calculated in WIPL-D by post-processing of those (numerically calculated) current distributions.

3. Optimization

In this chapter, we explain in detail the optimization procedures utilized for finding the optimal design of the nonuniform helical antennas with linearly varying geometrical parameters and present results of these optimizations. The optimization results consist of the geometrical parameters of the found antennas (radii and pitch angles of the first and the last turn). The optimal geometrical parameters and the gain of the optimal antennas are analyzed and used with the aim to define a set of equations for the rapid calculation of these quantities. This set of equations represents the base of the design (synthesis) procedure (presented in Subsection 5.1) that allows fast and reliable design of nonuniform helical antennas.

3.1. Optimization setup

The main criteria for the optimization of helical antennas are
1. to maximize the antenna gain and
2. to obtain circular polarization (axial ratio in dB as close to 0 as possible),

which requires multicriteria optimization. However, the second criterion can be met (relatively) more easily than the first one. Therefore, we combined those two criteria into one. This simplifies the optimization and allows formulation of the unique optimization (cost) function.

To that aim, we set the optimization goal to maximize the partial gain for the circular polarization in the main radiating direction (see Appendix A.1). By maximizing the partial gain, instead of the gain or the absolute gain (see Appendix A.1), the effects of imperfect circular polarization are also taken into account. Hence, thereby not only the gain is maximized (the first task), but also the axial ratio in dB is kept as low as possible (the second task), i.e., both tasks are included into the cost function.

The partial gain is defined by

$$g\,[\text{dBi}] = g_{\text{absolute}}\,[\text{dBi}] + c\,, \tag{3.1}$$

where c is the gain reduction due to the imperfect circular polarization (see Appendix A.1). In the case of the right-hand circular polarization (RHCP)

$$c = 20\log_{10}\!\left(\frac{E_{\text{RHCP}}}{E_{\text{tot}}}\right)\text{dB}\,, \quad E_{\text{RHCP}} = \sqrt{2}\left|\frac{\underline{E}_\theta + \mathrm{j}\,\underline{E}_\varphi}{2}\right|, \tag{3.2}$$

where E_{RHCP} is the rms value of $\mathbf{E}_{\text{RHCP}}(t)$, $\underline{E}_\theta$ and $\underline{E}_\varphi$ are the θ and φ components of the complex electric far field as defined in Appendix A.3, and $E_{\text{tot}} = \sqrt{\left|\underline{E}_\theta\right|^2 + \left|\underline{E}_\varphi\right|^2}$. For the left-hand circular polarization (LHCP)

$$c = 20\log_{10}\!\left(\frac{E_{\text{LHCP}}}{E_{\text{tot}}}\right)\text{dB}\,, \quad E_{\text{LHCP}} = \sqrt{2}\left|\frac{\underline{E}_\theta - \mathrm{j}\,\underline{E}_\varphi}{2}\right|, \tag{3.3}$$

where E_{LHCP} is the rms value of $\mathbf{E}_{\text{LHCP}}(t)$, as defined in Appendix A.3.

Further, as it is defined in Appendix A.3, the axial ratio is

$$ar[\text{dB}] = 20\log_{10}\left\|\frac{\left\||\underline{E}_{\text{RHCP}}| + |\underline{E}_{\text{LHCP}}|\right\|}{\left\||\underline{E}_{\text{RHCP}}| - |\underline{E}_{\text{LHCP}}|\right\|}\right\|. \tag{3.4}$$

Finally, we will formulate the optimization in terms of finding the minimum of the cost function. Hence, the cost function is defined as

$$f_{\text{cost}} = 100 - g[\text{dBi}], \tag{3.5}$$

where the constant 100 is well above the maximal partial gain for all considered helical antennas in this thesis. The cost function (3.5) is always positive. The ultimate goal of the optimization is to find the global minimum of (3.5), taking into account the predefined ranges of the parameters of the antenna geometry, i.e., optimization variables.

The optimization variables are the radii and pitch angles of the first turn and the last turn (r_1, r_2, φ_1, and φ_2, respectively). We consider the optimization variables within the following limits:

- $0.02\lambda \le r_1, r_2 \le 0.5\lambda$ and

- $0.5° \le \varphi_1, \varphi_2 \le 15°$,

where λ is the free-space wavelength at the operating frequency. Some combinations of the optimization variables correspond to infeasible geometries, i.e., geometries that cannot be practically realized (for example, if the desired spacing between adjacent turns is smaller than the conductor diameter, or this spacing is very small so in the real situation these turns can touch). These geometries are automatically identified and rejected during the optimization, by setting the cost function to 150, which is larger than the largest f_{cost} for all feasible geometries. The radii and pitch angles of other turns are calculated using (2.1) and (2.2), respectively. During the optimization, the antenna is located above an infinite perfectly conducting ground plane. The antenna conductor is assumed to be lossy, but PEC conductors are also considered as a special case. The optimizations are performed for various axial antenna lengths, wire radii, and wire conductivities.

The cost function defined by (3.5) is an instance of a constrained NLP (nonlinear programming) optimization problem. Various combinations of the optimization algorithms for the optimization of the helical antenna geometry are investigated in [114]. The random search, Nelder-Mead simplex [115], gradient method, and particle swarm optimization (PSO) [116], [117] are tested. The random search and randomly initialized PSO are stochastic algorithms that usually yield a different solution in each independent run. Hence, the random search or PSO are used in the first stage of the optimization, whereas in the second stage the Nelder-Mead simplex or gradient method are utilized in order to speed up the convergence to the (local) optimum. The second stage of the optimization is launched from the best-found solution within the first stage. Results from [114] show that the random search or PSO (in the first stage) followed by the Nelder-Mead simplex (in the second stage) have the highest probability of finding the best solution.

Here, we will additionally investigate different combinations of the optimization algorithms, different numbers of iterations, and algorithm setups, with an ultimate goal to choose the combination that finds the best solution with the minimal number of iterations, i.e., electromagnetic-solver calls.

In order to compare different combinations of the stochastic optimization algorithms, we perform investigation similar to the investigation performed in [114]. Each combination of the optimization algorithms is independently restarted 100 times. For each independent run, the best-found solution and the corresponding cost function are saved. The solutions are classified into 200 bins in terms of the gain. Thereby, k-th bin corresponds to the gain in the range $g_k \in 0.1[k-1, k)\,\text{dBi}, \quad k = 1, 2, \ldots, 200$. The probability of finding a solution within the bin g_k is estimated as $p_k = N/N_{\text{tot}}$, where N is the total number of found solutions within the considered bin and N_{tot} is the total number of independent runs ($N_{\text{tot}} = 100$).

Fig. 3.1 shows the (estimated) probabilities, p_k, for the axial antenna lengths 2λ, 5λ, and 10λ, and various combinations of the optimization algorithms. The helix conductor is considered to have a circular cross-section of radius 0.0002λ and to be lossy, of conductivity 58 MS/m. The simulations are performed at the operating frequency 300 MHz, where the free-space wavelength is $\lambda \approx 1\text{m}$.

With an aim to select the algorithm for the first stage of the optimization, i.e., the random search or PSO, the results in Figs. 3.1b, c, e, and f can be compared. Namely, the same number of iterations is utilized in Figs. 3.1b and e, as well as in Figs. 3.1c and f. These results undoubtedly confirm that the PSO is better than the random search for the first stage of the optimization. Further, the results in Figs. 3.1c and d show that for the second stage of optimization the Nelder-Mead simplex is better than the gradient method. Hence, the chosen combination of optimization algorithms is the PSO followed by the Nelder-Mead simplex. (This agrees with the conclusion made in [114].) Finally, the results in Figs. 3.1e and f can be used for choosing the number of iterations. For shorter antennas (2λ and 5λ), it can be noticed that 2000 PSO iterations (swarm size 20) followed by (maximum of) 200 Nelder-Mead simplex iterations have a notably higher probability to achieve the maximal gain (around 20 % higher) than 500 PSO iterations (swarm size 20) followed by (maximum of) 200 Nelder-Mead simplex iterations. For 10λ antennas the probability difference is smaller, i.e., it is around 5 %. Therefore, for the optimization of the geometry of the nonuniform helical antennas with linear variation of turn radius and pitch angle 2000 iterations of PSO (swarm size 20) followed by (maximum of) 200 Nelder-Mead simplex iterations, launched from the best found PSO solution, are utilized.
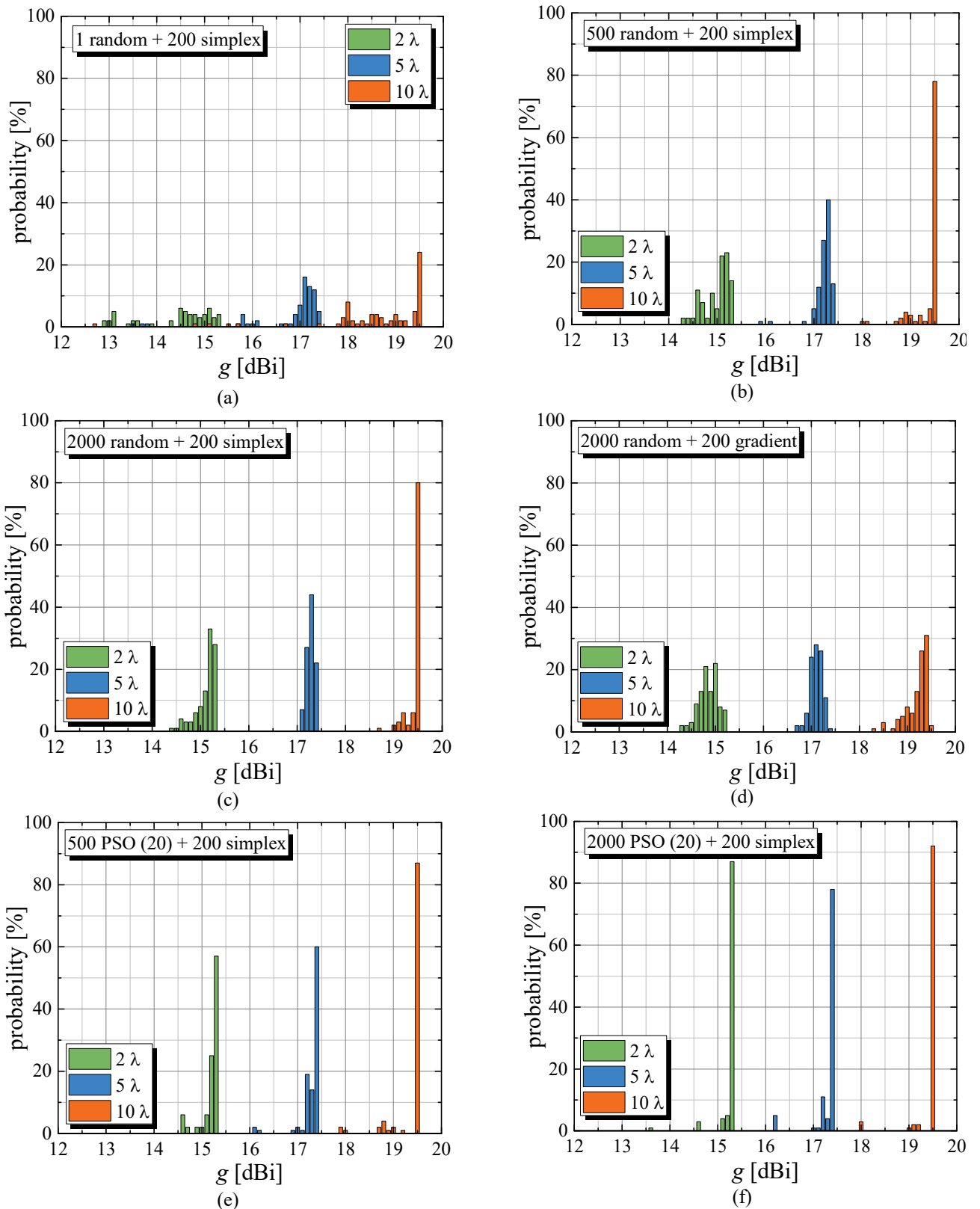
Figure 3.1. Probabilities, p_k, for the axial antenna lengths 2 λ, 5 λ, and 10 λ for (a) 1 random and 200 simplex iterations, (b) 500 random and 200 simplex iterations, (c) 2000 random and 200 simplex iterations, (d) 2000 random and 200 gradient iterations, (e) 500 PSO (swarm size 20) and 200 simplex iterations, and (f) 2000 PSO (swarm size 20) and 200 simplex iterations.

3.2. Optimization results

The optimization, utilizing the combination of the optimization algorithms chosen in Subsection 3.1, is performed for finding the optimal nonuniform helical antennas of various axial

antenna lengths, wire radii, and conductivities, including PEC. During the optimization, the helix is located above an infinite PEC ground plane. The optimal geometrical parameters, obtained from the optimization, are further analyzed and used to make conclusions presented in the following subsections.

3.2.1. Lossless conductors (PEC)

The chosen optimization setup is utilized for the optimization of lossless nonuniform helical antennas. The optimization is performed for different axial antenna lengths and wire radii. The gain and the geometrical parameters of the optimal antennas are shown in Figs. 3.2 and 3.3, respectively. The results in Fig. 3.2 show that, for lossless conductors, the gain practically does not depend on the conductor radius. Further, the gain dependence on the antenna axial length can be easily described by a logarithmic function, i.e., $g[\text{dBi}] = A\log(L/\lambda) + B$. The values of the coefficients A and B are approximated so that this equation always underestimates the gain, but also keeping as low as possible the discrepancy between the gain of the optimal antennas and the calculated gain. As the result, the equation that estimates the gain of the optimal nonuniform helical antennas with lossless conductors is

$$g[\text{dBi}] = 8.31\log_{10}\left(\frac{L}{\lambda}\right) + 13.86 . \tag{3.6}$$

From the results shown in Fig. 3.2 it can be noticed that (3.6) successfully predicts the gain of antennas whose axial length is an integer multiple of a half wavelength, $L = k\lambda/2, k \geq 4$. The discrepancy between the simulated gain and the gain calculated from (3.6) is less than 0.25 dB. However, in other cases ($L \neq k\lambda/2, k \geq 4$), the gain of the optimal antennas is lower than predicted by (3.6), but also, in some cases, it is almost equal (or just negligibly higher) than the gain of the shorter antennas for which the condition $L = k\lambda/2, k \geq 4$ is fulfilled. For example, in the case of the conductor radius $r_w = 0.0002\lambda$, the gain of the antenna whose axial length is 2λ is 16.47 dBi, whereas the gain of the antenna whose axial length is 2.25λ is 16.46 dBi. Hence, there is no justification for using the longer antenna (2.25λ).
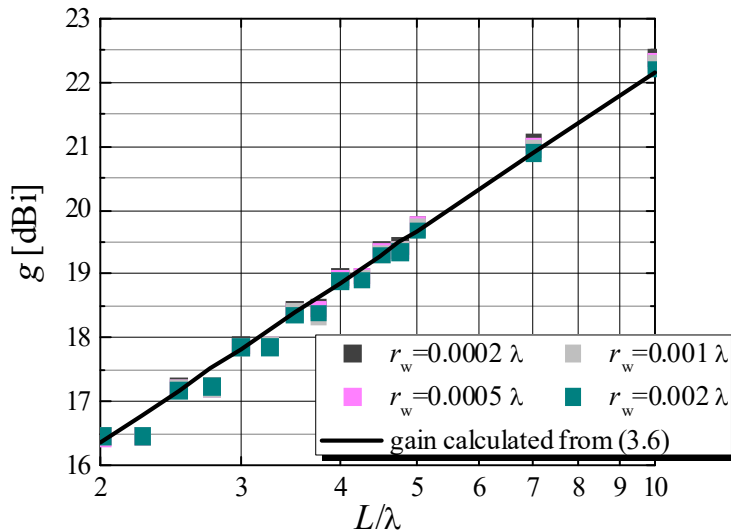

Figure 3.2. Gain of the optimal lossless nonuniform helical antennas.

Fig. 3.3 shows the geometrical parameters (radii and pitch angles of the first and the last turn) of the optimal nonuniform helical antennas with lossless conductor for characteristic axial antenna lengths and conductor radii. (The considered axial antenna lengths and conductor radii are chosen within the ranges defined in Subsection 3.2.2.) These geometrical parameters show high regularity. This feature allows fitting of the data with the ultimate goal of defining a fast design procedure which contains design equations for calculating geometrical parameters of the optimal antennas.
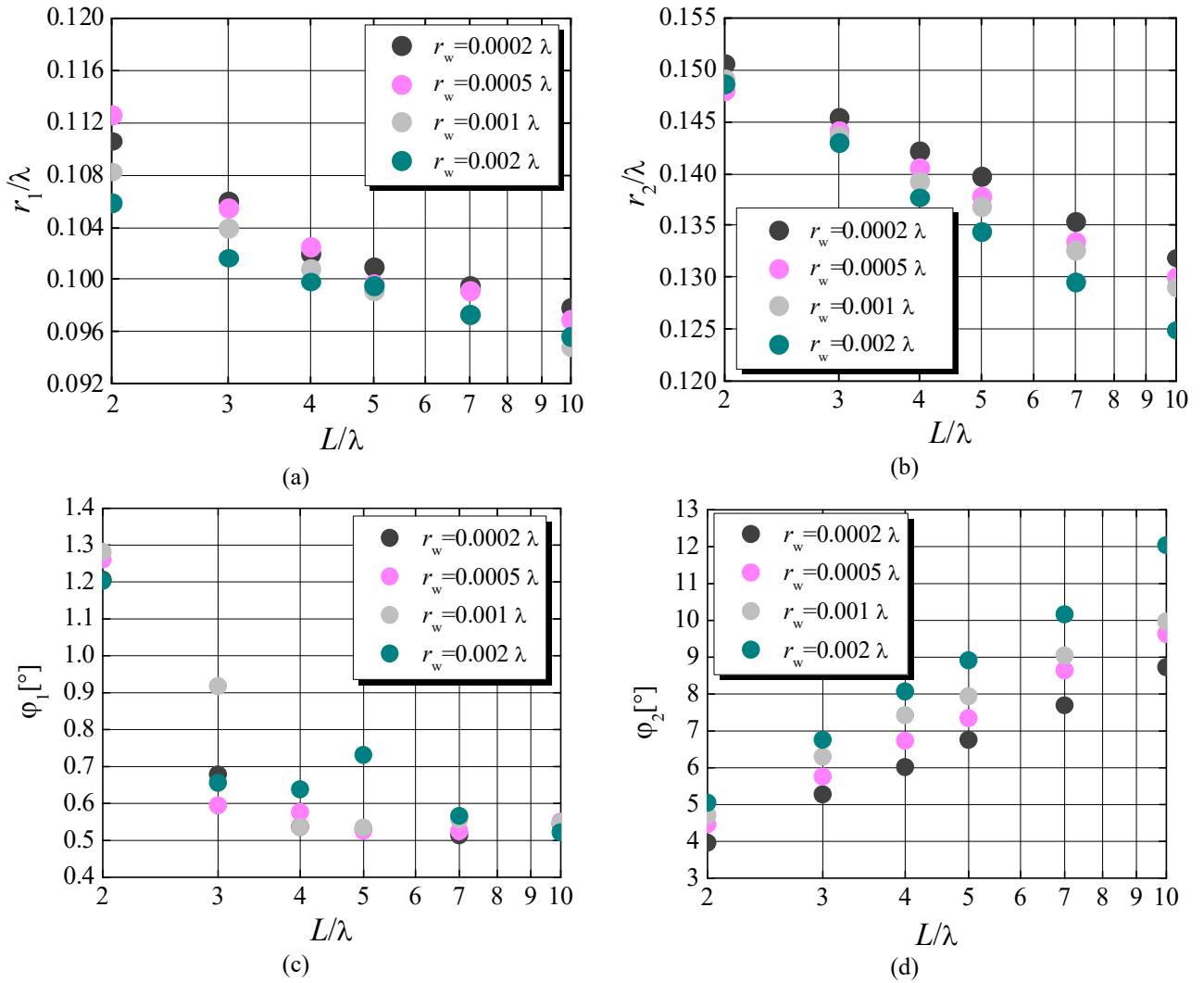
Figure 3.3. Geometrical parameters of the optimal lossless nonuniform helical antennas: (a) radius of the first turn, (b) radius of the last turn, (c) pitch angle of the first turn, and (d) pitch angle of the last turn.

3.2.2. Lossy conductors

As a preparation for the optimization, the limits for the considered axial antenna lengths, antenna conductors, and antenna operation have to be adopted. These limits are defined by having practical applications in mind.

The operating frequency and the antenna overall dimensions are inversely proportional, i.e., the antenna overall dimensions are linearly proportional to the wavelength at the operating frequency.

Since very large and very small low-loss helices are hard to be fabricated, helical antennas are commonly used from the VHF range up to lower microwave frequencies. Hence, in this work we will consider operating frequencies from 30 MHz up to 6 GHz.

The conductivities of the most commonly used conductors (copper, silver, gold, aluminum, brass, steel) range from 10 MS/m to several tens of MS/m. Hence, for the considered wire conductivities we adopt the range from 10 MS/m to 100 MS/m.

The range of the axial antenna lengths is confined by the applications and the fabrication limitations (from the upper side) and by the nature of the helical antennas (from the lower side), i.e., for short antennas some features of the helical antennas can be undeveloped. Hence, considered range for the axial antenna lengths is from 2λ to 10λ, where λ is the wavelength at the operating frequency.

The considered radii of the conductors are from 0.0002λ to 0.002λ, which mostly covers commercially available wires, for the considered frequency range.

19

Finally, the following limits are considered for the optimization of nonuniform helical antennas with lossy conductors:

- operating frequencies from 30 MHz to 6 GHz,
- wire conductivities from 10 MS/m to 100 MS/m,
- axial antenna lengths from 2 λ to 10 λ, and
- wire radii from 0.0002 λ to 0.002 λ.

These limits define a design hyper rectangle.

When considering the operating frequency, it is convenient to perform all optimizations at a single frequency, e.g., 300 MHz, where the wavelength is (around) 1 m, and thereafter scale the obtained solution (the antenna dimensions) and conductivity to the actual operating frequency. This procedure significantly reduces the optimization load that is necessary to obtain optimal antennas for all points within the design hyper rectangle. Inherently, significant data compression is thereby achieved.

This procedure is based on the theorem of electromagnetic similitude [118]. According to the theorem, if the operating frequency is increased s times, all linear geometrical dimensions of the antenna should be decreased s times and the wire conductivity should be increased s times in order to obtain the electromagnetic similarity (see Appendix B). Note that the original antenna and the scaled antenna have the same gain and the same input impedance. Hence, the wire conductivities in the scaled model are taken to be in the range from 0.5 MS/m to 1000 MS/m, which corresponds to the targeted wire conductivities within the considered frequency range.

Solid lines in Fig. 3.4 show the gain of the optimal antennas in the range of the targeted wire conductivities, for various axial lengths and wire radii. (Dark blue solid lines correspond to the gain of the antennas with lossless conductors calculated from (3.6).) All geometrical dimensions are expressed in terms of the wavelength at the operating frequency (λ). Note that the gain is plotted as a function of the conductivity multiplied by the wavelength at the operating frequency. (We refer to this product as the normalized conductivity.) Hence, in addition to the geometrical dimensions, the conductivity is also expressed in terms of the wavelength at the operating frequency. This way of expressing the geometrical dimensions and conductivity allows fast scaling of the model to an arbitrary operating frequency (within the design hyper rectangle, i.e., the limits defined at the beginning of this subsection). Therefore, the data shown in Fig. 3.4 are not valid only for the frequency utilized during the optimizations (300 MHz), but also are applicable to any other frequency (within the defined range).

Further, in all graphs shown in Fig. 3.4, i.e, for all axial antenna lengths and wire radii, it can be noticed that by moving from the highest normalized conductivities towards the lowest normalized conductivities (from the right to the left part of the graphs) the traces have steep slopes. This behavior shows that the wire losses strongly affect the gain of the nonuniform helical antennas.

The shape of the optimal nonuniform helical antennas depends on the wire conductivity, i.e., on the losses. When the losses are high (the conductivity is low), the radii and pitch angles of the turns near the feeding point are larger than the radii and pitch angles at the helix top. In addition, the turns at the helix top almost touch each other. A typical geometry of the antenna in this case is shown in Fig. 3.5a. As the losses decrease (the conductivity increases), the geometry smoothly changes to the geometry shown in Fig. 3.5b. In this case, the radii and pitch angles increase from the helix bottom towards the top. For simplicity, these losses are referred to as the medium losses. With a further diminish of the losses (increase in the conductivity, including PEC wires, Subsection 3.2.1), the typical antenna geometry looks like the one shown in Fig. 3.5c. The turns at the helix bottom become dense. Hence, the required conductor length becomes longer, which may be impractical.

The main objective of this part of the work is to provide a fast and simple, but sufficiently accurate, design procedure valid for as large as possible subspace within the design hyper rectangle, defined at the beginning of Subsection 3.2.2. For that purpose, the geometry that corresponds to the medium losses (shown in Fig. 3.5b) is utilized, since it is considered to be the most interesting one from the practical point of view for two reasons.

Firstly, the gain of those antennas (indicated by dots in Fig. 3.4) is sufficiently high, i.e., the decrease in the gain of those antennas in comparison with the gain of the antennas from Fig. 3.5c (indicated by dark blue solid line in Fig 3.4) is between 0.8 dB and 0.9 dB. Namely, the ordinate values of the dots in Fig. 3.4 are between 0.8 dB and 0.9 dB below the level indicated by dark blue line. This discrepancy in gain is indicated as the margin in Fig. 3.4.

Secondly, the turns are not overcrowded; hence, the total conductor length is shorter.

The dots shown in Fig. 3.4 correspond to the designs with medium losses, i.e., the dots indicate antennas that are chosen for the reference design. (In the case of the longest antennas, whose axial lengths are 7 λ and 10 λ, with the thinnest wire, the normalized conductivity which corresponds to the medium losses is larger than 1000 MS. Hence, the dots for these two examples are not plotted in Fig. 3.4.)
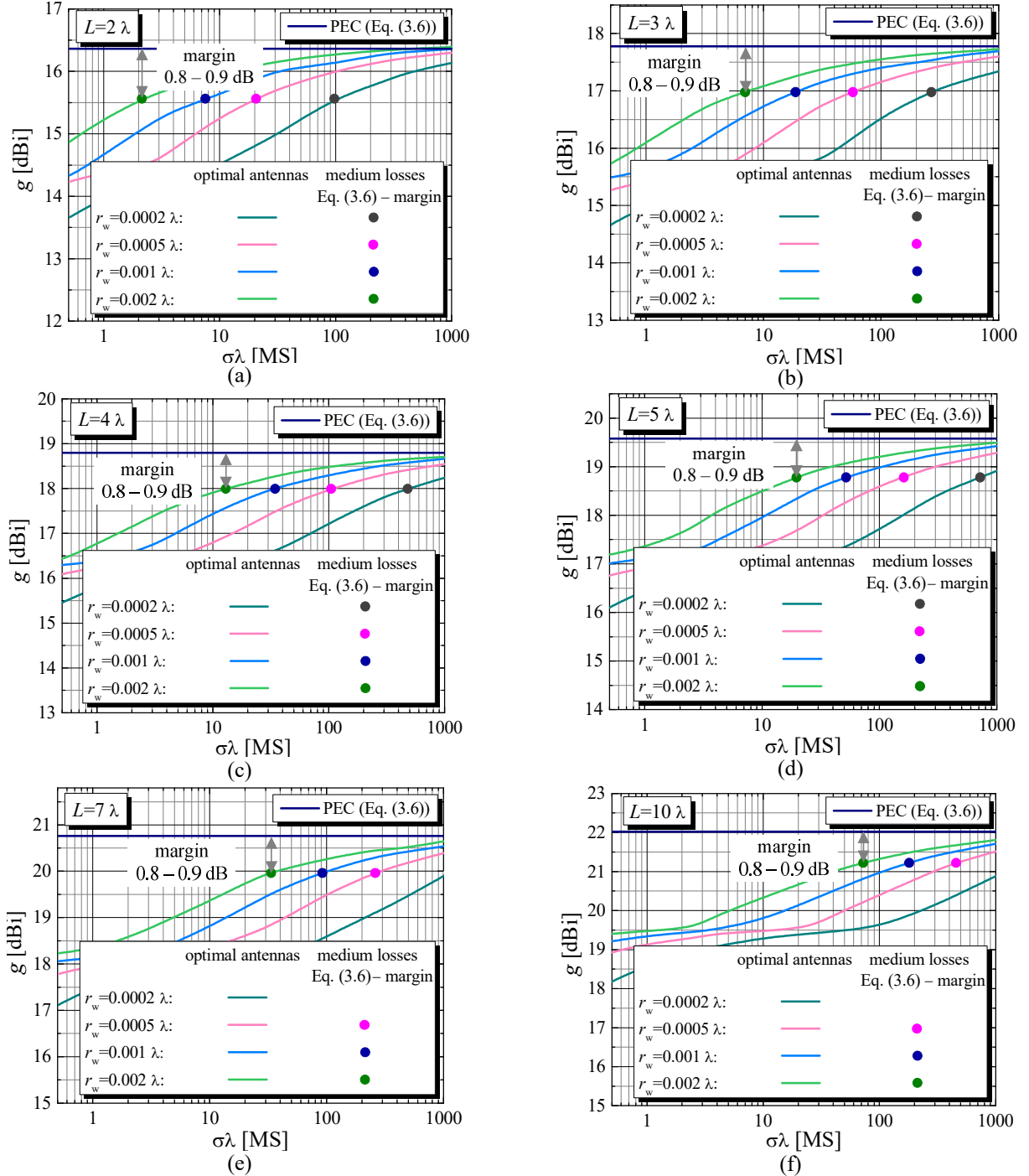

Figure 3.4. Gain of the optimal nonuniform helical antennas within considered conductivity range for various wire radii and (a) $L=2\,\lambda$, (b) $L=3\,\lambda$, (c) $L=4\,\lambda$, (d) $L=5\,\lambda$, (e) $L=7\,\lambda$, and (f) $L=10\,\lambda$, solid lines. Gain of the nonuniform helical antennas with PEC wire calculated from (3.6), solid dark blue line. Dots indicate antennas that are chosen for the reference design.
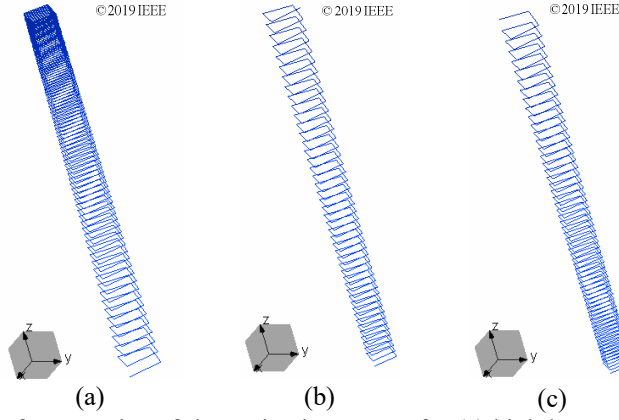
Figure 3.5. Typical examples of geometries of the optimal antennas for (a) high losses [113], (b) medium losses [113], and (c) low losses [113].

Through a detailed investigation of the antennas that correspond to the medium losses, it is found that these designs can also be valid for a wider range of conductivities. Hence, we refer to these designs as reference designs, and the corresponding conductivity as the reference conductivity, σ_{ref}. Dots in Fig. 3.6a indicate the normalized conductivities that correspond to the medium losses (abscissas of the dots shown in Fig. 3.4). By heuristic investigation of logarithmic and linear dependencies, and by fine-tuning of each term, σ_{ref} is approximated by

$$\sigma_{\text{ref}}\lambda = 10^{\left(0.5154\log_{10}\left(\frac{r_{\text{w}}}{\lambda}\right)+3.601\right)\log_{10}\left(\frac{L}{\lambda}\right)-1.750\log_{10}\left(\frac{r_{\text{w}}}{\lambda}\right)-4.850}, \tag{3.7}$$

where L, r_{w}, and λ are in meters, and σ_{ref} is in MS/m. The validity of the approximation given by (3.7) is confirmed in Fig. 3.6a, where the normalized reference conductivities are compared with σ_{ref} calculated from (3.7).

Further, the normalized reference conductivity is plotted in Fig. 3.6b as a function of the normalized axial length and normalized wire radius. The normalization is with respect to the wavelength at the operating frequency.
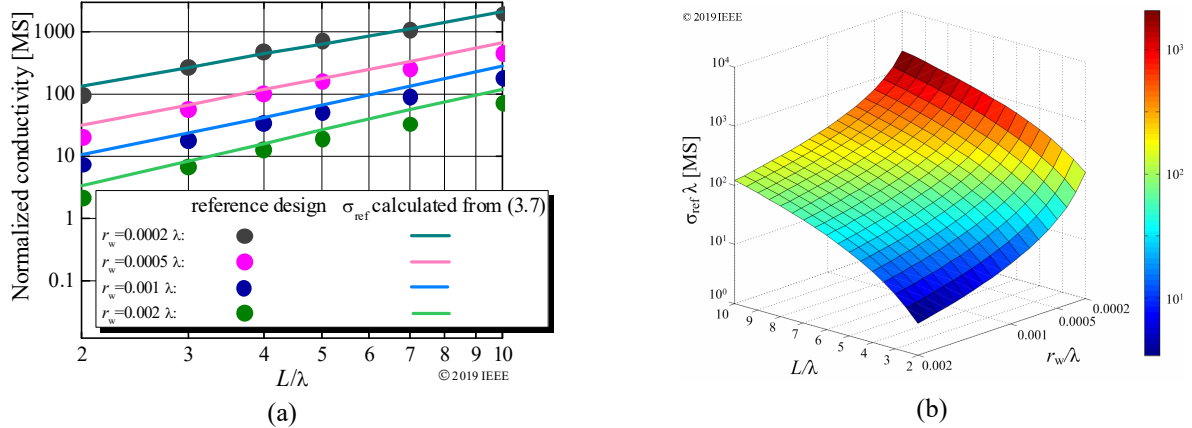

(a)

(b)

Figure 3.6. (a) Normalized conductivities that correspond to the reference design and normalized reference conductivities calculated from (3.7) [113], and (b) normalized reference conductivity, calculated from (3.7), as a function of the normalized axial antenna length (L/λ) and normalized wire radius (r_{w}/λ) [113].

Normalized optimal geometrical parameters for the reference design (r_1, r_2, φ_1, and φ_2), for various axial antenna lengths and wire radii, are shown in Fig. 3.7. As for the antennas with lossless conductors, the optimal geometrical parameters for the reference design show high regularity, which allows this data to be fitted successfully. Normalized optimal radii of the first turn (Fig. 3.7a) and the last turn (Fig. 3.7b), and the optimal pitch angles of the last turn (Fig. 3.7d) are in the same ranges as for the antennas with lossless conductors (see Fig. 3.3). However, the optimal pitch angles of the first turn are around five times larger in the reference design. This was expected since the

turns at the antenna bottom in the case of lossless antennas are denser (Fig. 3.5c) than in the reference design (Fig. 3.5b).
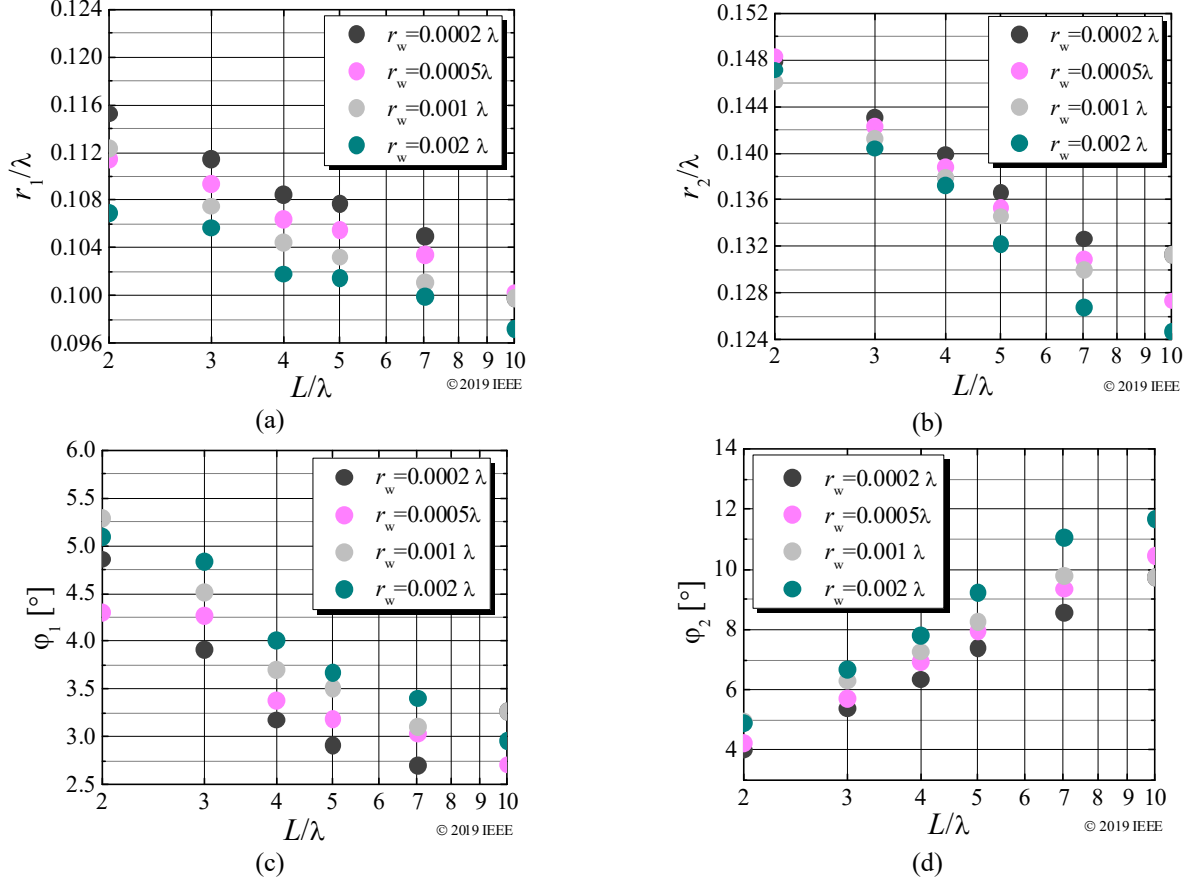

(a)

(b)

(c)

(d)

Figure 3.7. Optimal geometrical parameters of the reference design: (a) normalized radius of the first turn [113], (b) normalized radius of the last turn [113], (c) pitch angle of the first turn [113], and (d) pitch angle of the last turn [113].

The gain of the antennas whose geometrical parameters are shown in Fig. 3.7 is compared in Fig. 3.8 with the gain of the antennas whose geometries are optimized at the corresponding normalized conductivities. The dots shown in Fig. 3.8 indicate the designs with the medium losses (as in Fig. 3.4). Hence, the abscissas and the ordinates of these dots correspond to the normalized reference conductivity and the gain calculated from (3.6) reduced by the margin (defined in Fig. 3.4), respectively. As it is explained for Fig. 3.4, for the longest antennas (axial antenna lengths 7λ and 10λ), with the thinnest wire (0.0002λ), the normalized conductivity which corresponds to the medium losses is larger than 1000 MS, so the dots for these two examples are not plotted in Fig. 3.8.

In the range of the normalized conductivities $\sigma_{ref}\lambda < \sigma\lambda < 1000\,\mathrm{MS}$, the gain of the antennas obtained using the reference design is only up to 0.25 dB lower than the gain of the corresponding optimal antennas (Fig. 3.8). This confirms the assumption that the reference design can be used as the optimal design in a wider range of conductivities, i.e., in the range of the normalized conductivities $\sigma_{ref}\lambda < \sigma\lambda < 1000\,\mathrm{MS}$.

Further, the discrepancy between the corresponding traces in Fig. 3.8 is negligible even for the conductivities smaller than the reference conductivity. We adopt that the reference design can be used as the optimal design as long as the discrepancy between the corresponding traces in Fig. 3.8 is lower than around 0.5 dB. This condition is fulfilled for the normalized conductivities within the range $\sigma_{min}\lambda < \sigma\lambda < 1000\,\mathrm{MS}$, where the normalized minimal conductivity ($\sigma_{min}\lambda$) is indicated by square markers in Fig. 3.8. The normalized minimal conductivity can be calculated from

$$\sigma_{min}\lambda = \left(0.5954 - 0.4830\log_{10}\left(\frac{L}{\lambda}\right)\right)\sigma_{ref}\lambda. \tag{3.8}$$

23

The coefficients in (3.8) are heuristically obtained by considering linear and logarithmic dependencies (for which our analysis determines that they are the most suitable), and by fine-tuning. The main goal is to meet the previously defined condition, i.e., the maximal discrepancy between the gain of the antennas obtained using the reference design and the gain of the corresponding optimal antennas should be 0.5 dB.
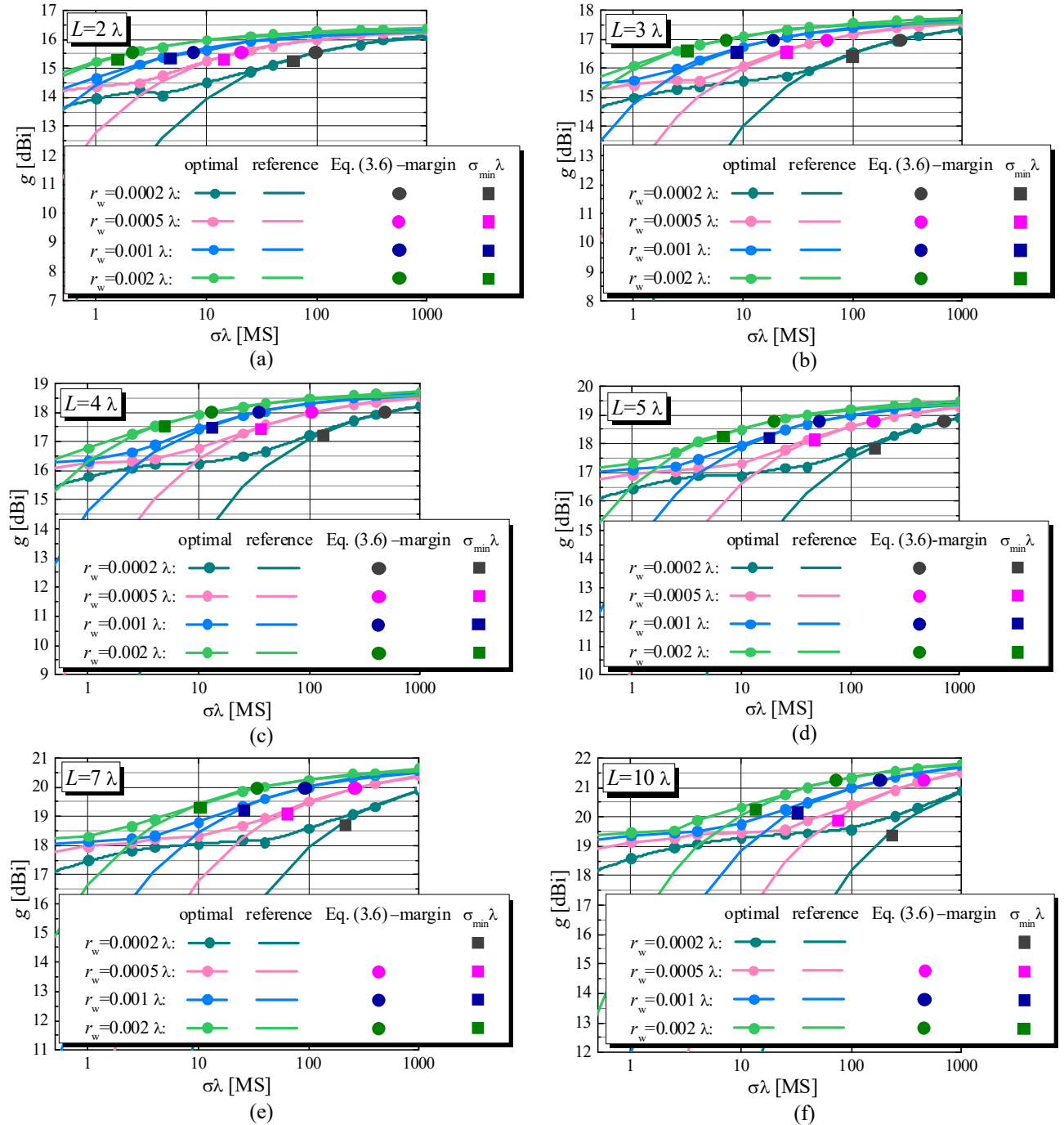

Figure 3.8. Gain of the optimal nonuniform helical antennas and the reference design within considered conductivity range for various wire radii and (a) $L=2\ \lambda$, (b) $L=3\ \lambda$, (c) $L=4\ \lambda$, (d) $L=5\ \lambda$, (e) $L=7\ \lambda$, and (f) $L=10\ \lambda$. Abscissas of the circle and square markers correspond to the normalized reference conductivity and $\sigma_{min}\lambda$, respectively.

Although the normalized conductivities that are higher than 1000 MS do not correspond to any design within the design hyper rectangle, defined in Subsection 3.2.2, it can be illustrative to compare the gain of the reference design (with a PEC wire) with the gain of the optimal lossless antennas. If the reference design is used with a PEC wire, the resulting gain is up to 0.4 dB lower than the gain of the antennas optimized immediately assuming a PEC wire (Subsection 3.2.1). This confirms that the considered condition for defining the lower border of the normalized-conductivities range (the discrepancy between the corresponding traces in Fig. 3.8 is

24

lower than around 0.5 dB) is also fulfilled for the conductivities higher than 1000 MS, all the way up to PEC wires.

For reference, in Fig. 3.9 the conductivities of the frequently used metals, i.e., copper (58 MS/m), gold (41 MS/m), silver (63 MS/m), and aluminum (37.7 MS/m), are compared with σ_{min} for various axial lengths and wire radii, in the considered frequency range (from 30 MHz to 6 GHz). Each graph in Fig. 3.9 corresponds to a different wire radius. Horizontal lines indicate the conductivities of frequently used wire materials. These lines intersect with the traces that correspond to σ_{min} for various axial antenna lengths. These intersections denote the points where σ_{min} of the observed axial antenna length and wire radius is equal to the conductivity of the considered metal (copper, gold, silver, or aluminum). Hence, at the operating frequencies lower than the frequency that corresponds to the intersection point, the reference design can be used as the optimal one with the considered metal as the wire material. For example, if we consider the axial antenna length 2λ, the wire radius 0.0002λ, and copper as the wire material, the operating frequency has to be below 300 MHz. In addition, if we consider the same axial antenna length and wire material, but we assume the wire radius to be 0.002λ, the operating frequency can be anywhere within the considered frequency range (from 30 MHz to 6 GHz).

Further, if a certain metal (as the wire material) and operating frequency are considered, the intersection points in Fig. 3.9 indicate for which axial antenna lengths the reference design can be used as the optimal one. For example, if we consider a copper wire of the radius 0.001λ and the operating frequency is 1 GHz, the reference design can be used as the optimal design for the axial antenna lengths up to 5λ. However, if the same wire material and the operating frequency are considered, but the wire radius is 0.002λ, the reference design is valid as the optimal design for all axial antenna lengths within the defined range (from 2λ to 10λ).
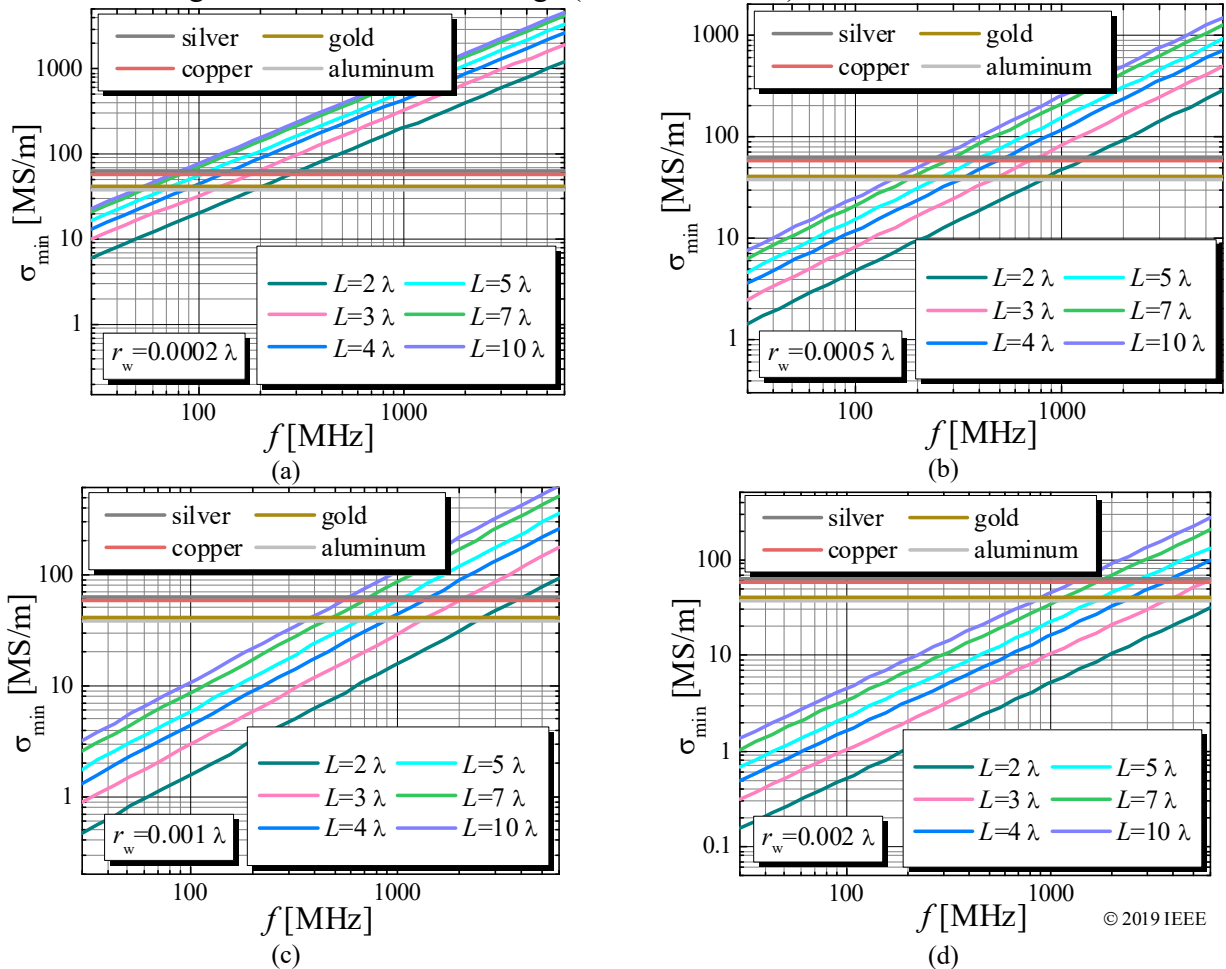

Figure 3.9. σ_{min} for various axial lengths and (a) r_w=0.0002 λ, (b) r_w=0.0005 λ, (c) r_w=0.001 λ, and (d) r_w=0.002 λ [113], in the considered operating frequency range. For reference, horizontal lines show conductivities of copper, gold, silver, and aluminum.

3.2.3. Approximating equations – geometrical parameters

The results obtained in the previous subsection confirm that the gain of the reference design is very close to the gain of the optimal antennas in the wide range of conductivities (for the normalized conductivities $\sigma_{\min}\lambda < \sigma\lambda < 1000\,\mathrm{MS}$). Further, the results from Fig. 3.7 indicate that the dependence of the optimal geometrical parameters, for the reference design, on the axial antenna length and wire radius can be described by analytical equations. These analytical equations will enable a rapid and reliable procedure for designing the optimal nonuniform helical antennas in just a few steps.

In Fig. 3.7 the abscissas of all graphs are in logarithmic scale. Hence, the dependence of the geometrical parameters on the axial antenna length can be approximated by the equation of the following form: $GP = A\log(L/\lambda) + B$, where GP are geometrical parameters r_1/λ, r_2/λ, φ_1, or φ_2, and A and B are unknown coefficients, different for each geometrical parameter. By further inspection of the optimal geometrical parameters, it can be noticed that the values of the coefficients A and B depend on the radius of the conductor. Hence, $A = A(r_w/\lambda)$ and $B = B(r_w/\lambda)$.

For each geometrical parameter, a detailed investigation is performed in order to describe dependences of the geometrical parameters on the axial antenna length and wire radius. The main task for finding the equations that approximate the optimal geometrical parameters is to maintain as low as possible the differences between the gain of the optimal antennas and the antennas designed using the proposed design equations. Hence, the antennas designed using the proposed equations achieve nearly the same gain as the optimal antennas. For that purpose, instead of fitting the optimal coefficients A and B using a standard method for data fitting, equations that approximate the values of the coefficients are found by heuristic investigation of various dependencies on linear and logarithmic scale, and by fine-tuning of each term in these equations. During this process, the gain differences are carefully monitored.

In Fig. 3.10 square markers correspond to the optimal values of the coefficients A and B for different wire radii, and these optimal values are fitted by solid lines. Fig. 3.11 compares the optimal geometrical parameters with the geometrical parameters calculated from the equations where the optimal coefficients A and B (shown by square markers in Fig. 3.10) are utilized. The gain of the optimal antennas and the gain of antennas whose geometrical parameters are calculated from the equations with the optimal coefficients A and B are compared in Fig. 3.12. In the worst case, the discrepancy between the gains of those antennas is less than 0.5 dB, for the normalized conductivities higher than $\sigma_{\min}\lambda$. Note that the largest discrepancy between the gain of the optimal antennas and the reference design, in the same range of the normalized conductivities, is also less than 0.5 dB (Fig. 3.8). Hence, antennas designed using the calculated geometrical parameters (where the coefficients A and B are optimal) achieve almost the same gain as antennas whose geometrical parameters are optimal for the reference design.
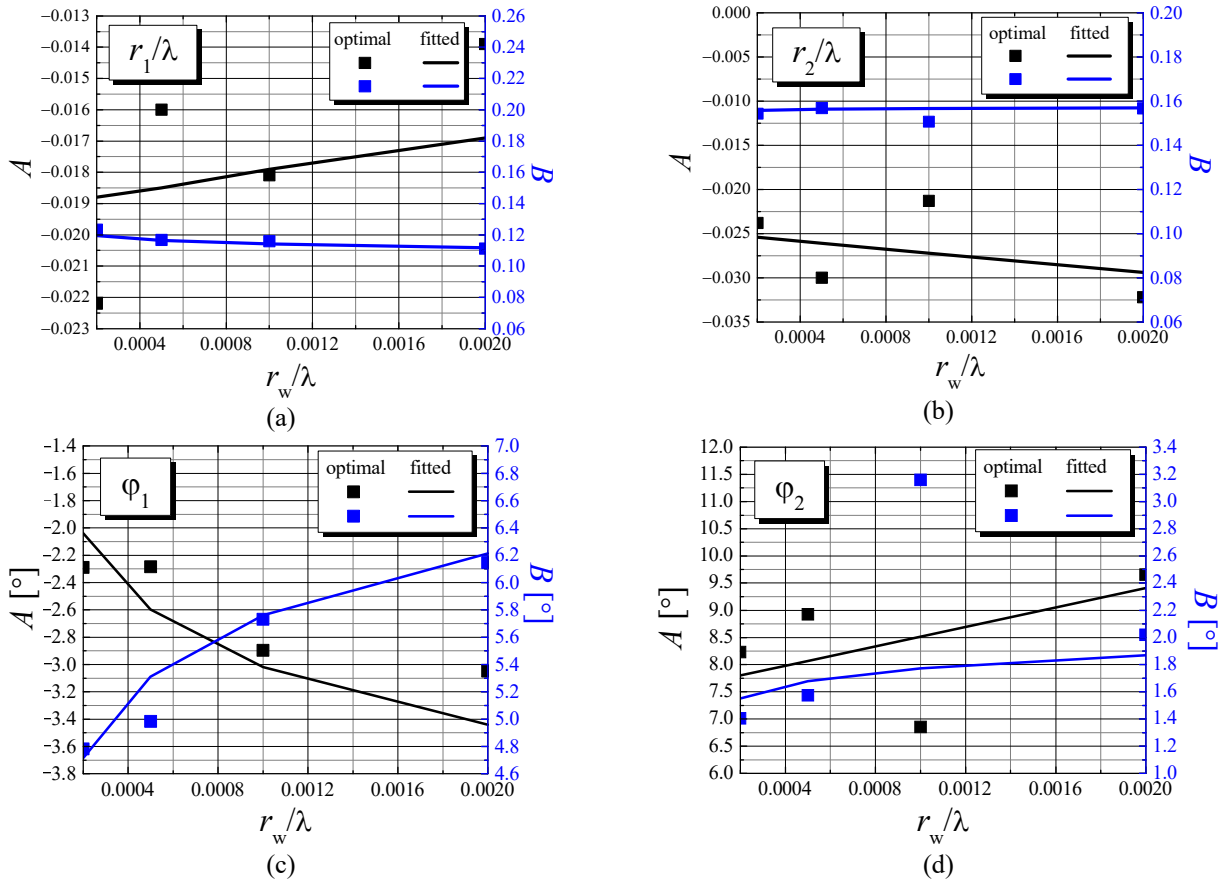
Figure 3.10. Coefficients *A* and *B* for approximating the optimal geometrical parameters: (a) normalized radius of the first turn, (b) normalized radius of the last turn, (c) pitch angle of the first turn, and (d) pitch angle of the last turn.
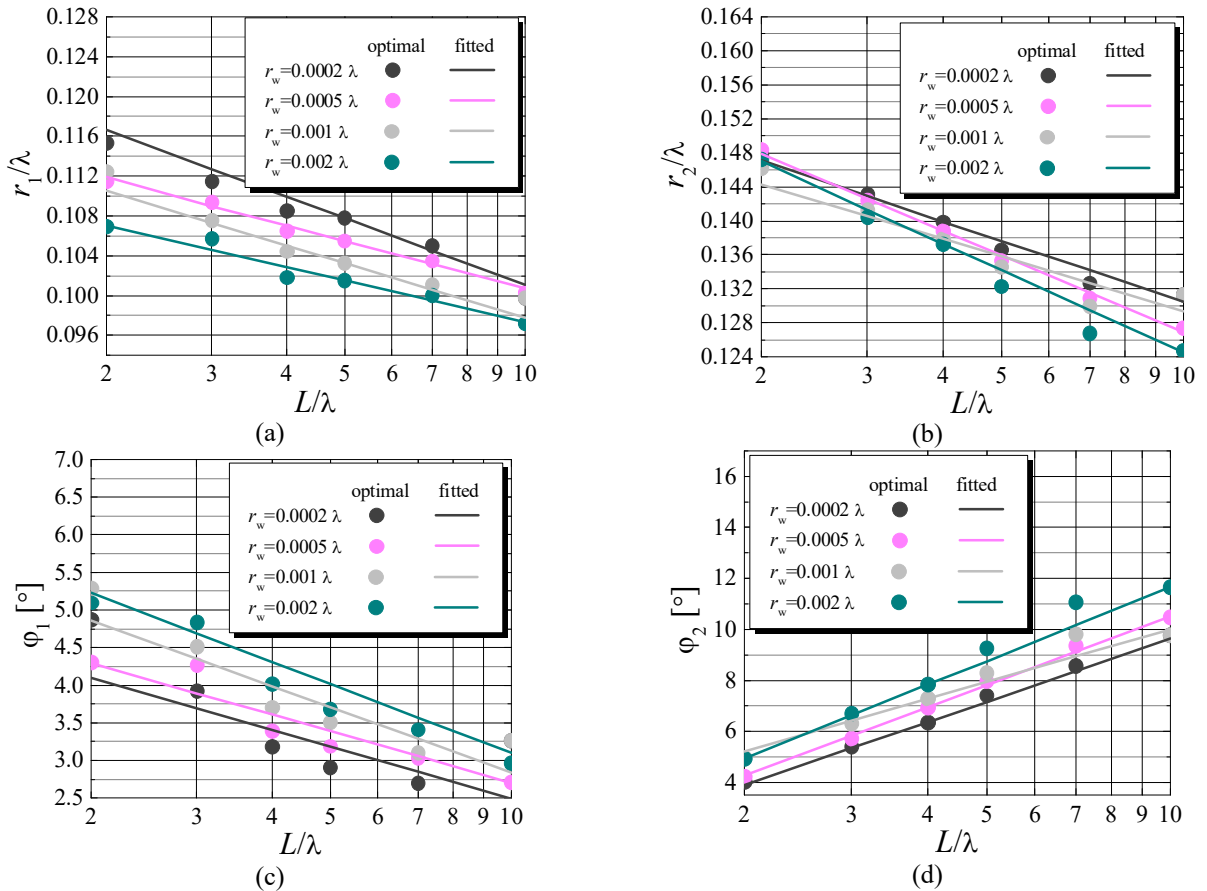

Figure 3.11. Optimal geometrical parameters of the reference design and geometrical parameters calculated from equations where the optimal coefficients *A* and *B* are utilized: (a) normalized radius of the first turn, (b) normalized radius of the last turn, (c) pitch angle of the first turn, and (d) pitch angle of the last turn.
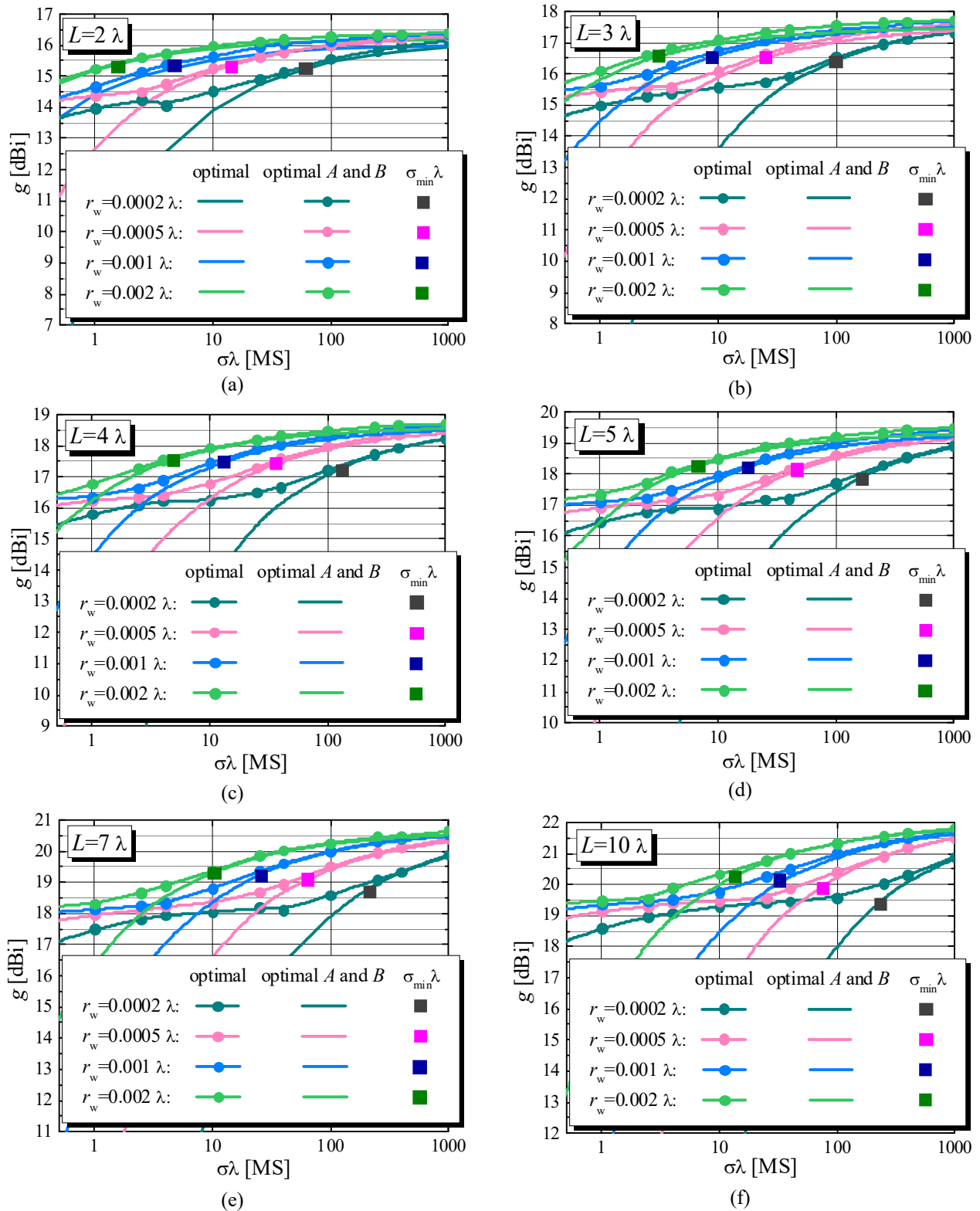
Figure 3.12. Gain of the optimal nonuniform helical antennas and antennas whose geometrical parameters are calculated from the equations with the optimal coefficients A and B, within considered conductivity range for various wire radii and (a) $L=2\,\lambda$, (b) $L=3\,\lambda$, (c) $L=4\,\lambda$, (d) $L=5\,\lambda$, (e) $L=7\,\lambda$, and (f) $L=10\,\lambda$. Square markers correspond to the normalized conductivity $\sigma_{min}\lambda$.

For the radii of the first and the last turn, the dependence of the optimal coefficient A on the wire radius is nearly linear (Figs. 3.10a and b). Hence, the optimal values of these coefficients are approximated in the following way:

$$A_{r_1} = 1.0681\frac{r_{\mathrm{w}}}{\lambda} - 0.0190,$$

(3.9)

$$A_{r_2} = -2.2001 \frac{r_w}{\lambda} - 0.0250. \tag{3.10}$$

The optimal coefficients B for the first and the last turn are approximated by the logarithmic functions

$$B_{r_1} = -0.00770 \log_{10}\left(\frac{r_w}{\lambda}\right) + 0.0910, \tag{3.11}$$

$$B_{r_2} = 0.00113 \log_{10}\left(\frac{r_w}{\lambda}\right) + 0.160. \tag{3.12}$$

Finally, the optimal normalized radii of the first and the last turn are approximated by

$$\frac{r_1}{\lambda} = \left(1.0681\frac{r_w}{\lambda} - 0.0190\right)\log_{10}\left(\frac{L}{\lambda}\right) + \left(-0.00770\log_{10}\left(\frac{r_w}{\lambda}\right) + 0.0910\right), \tag{3.13}$$

$$\frac{r_2}{\lambda} = \left(-2.2001\frac{r_w}{\lambda} - 0.0250\right)\log_{10}\left(\frac{L}{\lambda}\right) + \left(0.00113\log_{10}\left(\frac{r_w}{\lambda}\right) + 0.160\right). \tag{3.14}$$

From Fig. 3.10c it can be noticed that, for the pitch angle of the first turn, the dependencies of the coefficients A and B on the wire radius are logarithmic. The coefficient A in the equation for the pitch angle of the last turn linearly depends on the wire radius, whereas the dependence of the coefficient B is logarithmic. Hence, these coefficients are defined by the following equations

$$A_{\varphi_1} = -\left(1.4010 \log_{10}\left(\frac{r_w}{\lambda}\right) + 7.2219\right), \tag{3.15}$$

$$A_{\varphi_2} = 891.19\frac{r_w}{\lambda} + 7.6254, \tag{3.16}$$

$$B_{\varphi_1} = 1.4980 \log_{10}\left(\frac{r_w}{\lambda}\right) + 10.256, \tag{3.17}$$

$$B_{\varphi_2} = 0.31695 \log_{10}\left(\frac{r_w}{\lambda}\right) + 2.7238. \tag{3.18}$$

Finally, the optimal pitch angles of the first turn and the last turn (φ_1 and φ_2) are approximated by

$$\varphi_1[^\circ] = -\left(1.4010 \log_{10}\left(\frac{r_w}{\lambda}\right) + 7.2219\right)\log_{10}\left(\frac{L}{\lambda}\right) + \left(1.4980\log_{10}\left(\frac{r_w}{\lambda}\right) + 10.256\right), \tag{3.19}$$

$$\varphi_2[^\circ] = \left(891.19\frac{r_w}{\lambda} + 7.6254\right)\log_{10}\left(\frac{L}{\lambda}\right) + \left(0.31695\log_{10}\left(\frac{r_w}{\lambda}\right) + 2.7238\right). \tag{3.20}$$

In the following text, we refer to the set of equations (3.13), (3.14), (3.19), and (3.20) as the **design equations**, including equation (3.8) that is used to determine if this design is valid.

In Fig. 3.13 the radii and pitch angles of the first turn and the last turn of the reference design (obtained from the optimization), referred to as "optimal", are compared with the radii and pitch angles calculated from the design equations, referred to as "calculated". The discrepancy between the "optimal" and "calculated" geometrical parameters is noticeable (the discrepancy in this case is much bigger than in Fig. 3.11, where the coefficients A and B are the optimal). However, this discrepancy does not mean that the design equations poorly fit the optimal geometrical parameters. The main parameter for the evaluation of the design equations is the antenna gain. Hence, the main goal during the fine-tuning of the coefficients in the design equations is to maintain as low as

possible the discrepancy between the gain of the optimal reference design and the gain of the antennas whose geometrical parameters are calculated from the design equations.

Therefore, the gain of the optimal antennas and the antennas whose geometrical parameters are calculated from the design equations are compared in Fig. 3.14. From these results it can be noticed that the largest discrepancy of the gain is around 0.5 dB for the conductivities higher than $\sigma_{min}\lambda$. This leads to the conclusion that the design equations enable a rapid design procedure of the nonuniform helical antennas without significantly deteriorating the antenna performance in comparison with the optimal nonuniform helical antennas.
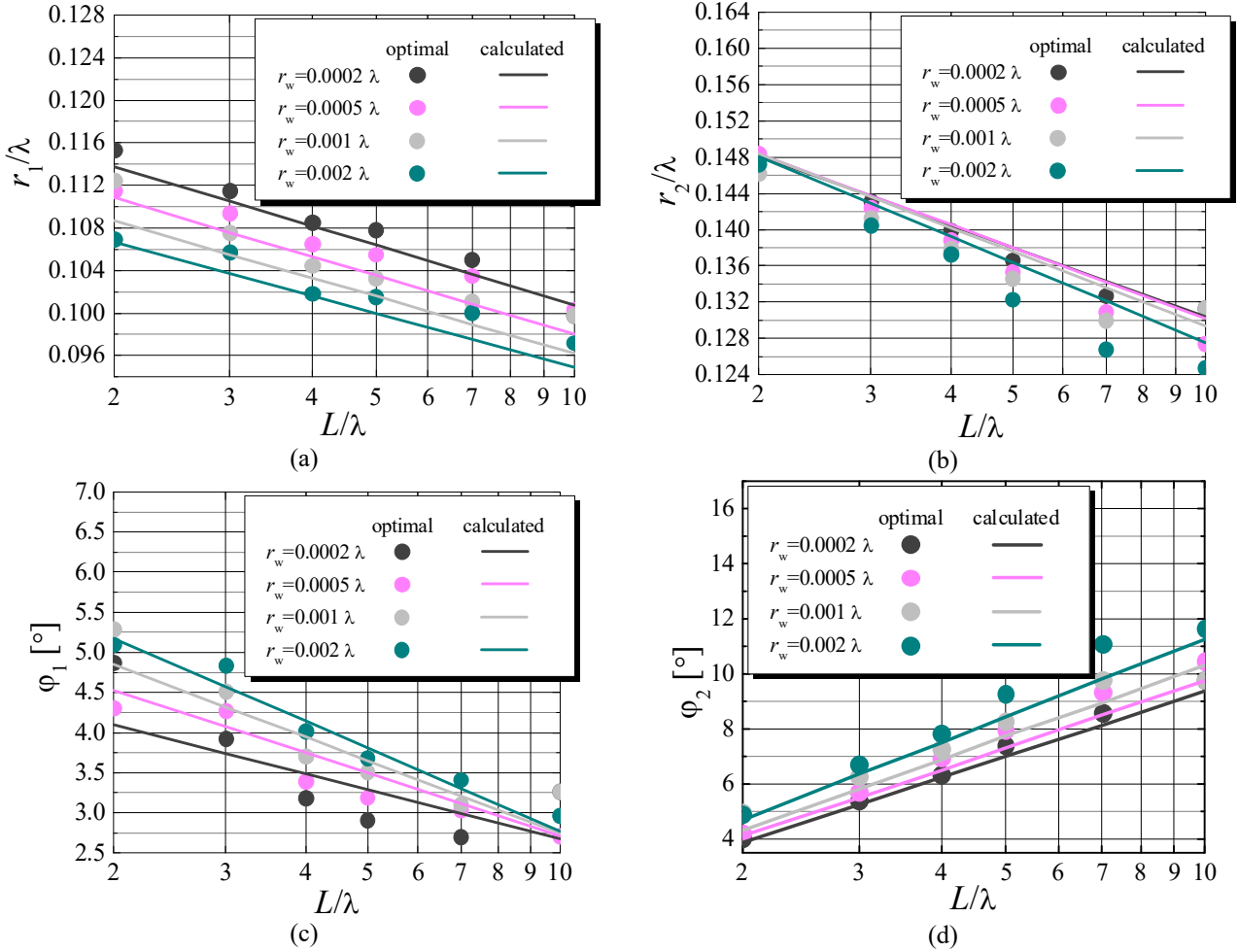

Figure 3.13. Optimal geometrical parameters of the reference design and the geometrical parameters calculated from (3.13), (3.14), (3.19), and (3.20): (a) normalized radius of the first turn, (b) normalized radius of the last turn, (c) pitch angle of the first turn, and (d) pitch angle of the last turn.
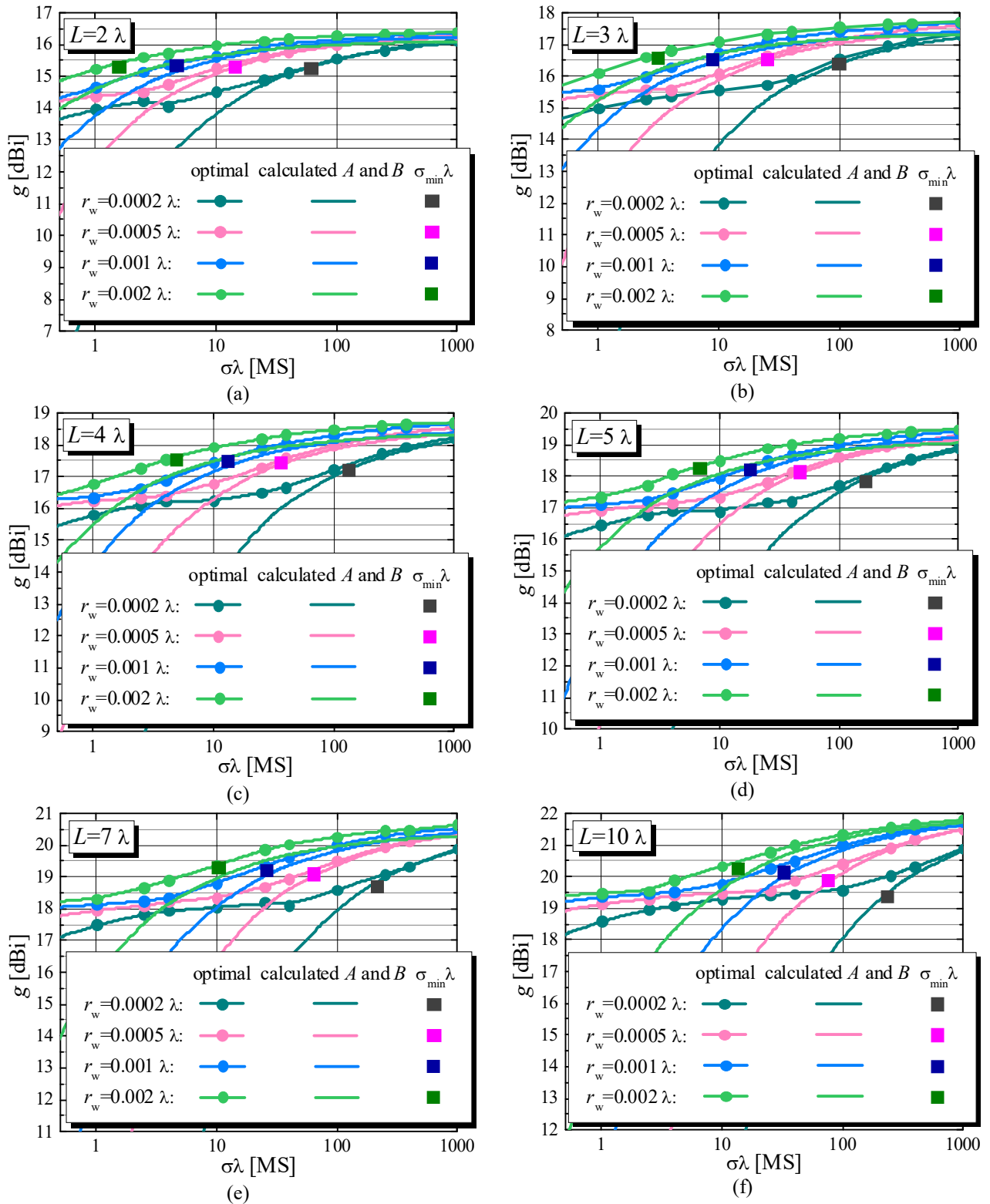
Figure 3.14. Gain of the optimal nonuniform helical antennas and antennas whose geometrical parameters are calculated from equations (3.13), (3.14), (3.19), and (3.20), within considered conductivity range for various wire radii and (a) $L=2\,\lambda$, (b) $L=3\,\lambda$, (c) $L=4\,\lambda$, (d) $L=5\,\lambda$, (e) $L=7\,\lambda$, and (f) $L=10\,\lambda$. Square markers correspond to the normalized conductivity $\sigma_{min}\lambda$.

Finally, by using the design equations for the design of the nonuniform helical antennas, the optimization of the antenna geometrical parameters (by the designer or user) can be avoided. Hence, computer resources (software and hardware for EM simulations) are not needed, and the design procedure is very short and fast. This can be very useful and preferable for practical applications.

3.2.4. Approximating equation – antenna gain

The gain in the main radiating direction is one of the most important parameters that characterize an antenna. Therefore, the gain of the antennas designed using the presented design equations ((3.13), (3.14), (3.19), and (3.20)) will also be approximated by an equation.

Solid lines in Fig. 3.14 show the gain of antennas whose geometrical parameters are calculated from the design equations. It can be noticed that the gain dependences on the normalized conductivity are very similar regardless of the axial length and wire radius. For a more detailed investigation of these dependences, the antenna gain is simulated in a wider range of the normalized conductivities, $\sigma_{min}\lambda \le \sigma\lambda \le 10^6\,\text{MS}$ (Fig. 3.15a) and the same conclusion is being drawn. This is also confirmed by the results shown in Fig. 3.15b, where all traces are translated and overlapped. The first step is the vertical translation, which is made so that the maximum of all traces is 0. In the second step the traces are horizontally translated so that all traces have a common point $(1\,\text{MS}, -0.5\,\text{dB})$. Thereafter, the behavior shown in Fig. 3.15b can roughly be approximated by the equation

$$g_{\text{normalized}} = \frac{-0.5}{\sqrt{\sigma_{\text{overlapped}}\,\lambda}}, \tag{3.21}$$

where $\sigma_{\text{overlapped}}\lambda$ is the normalized conductivity that corresponds to the x axis in Fig. 3.15b, whereas we refer to the values on the ordinate after the translation as the normalized gain ($g_{\text{normalized}}$).
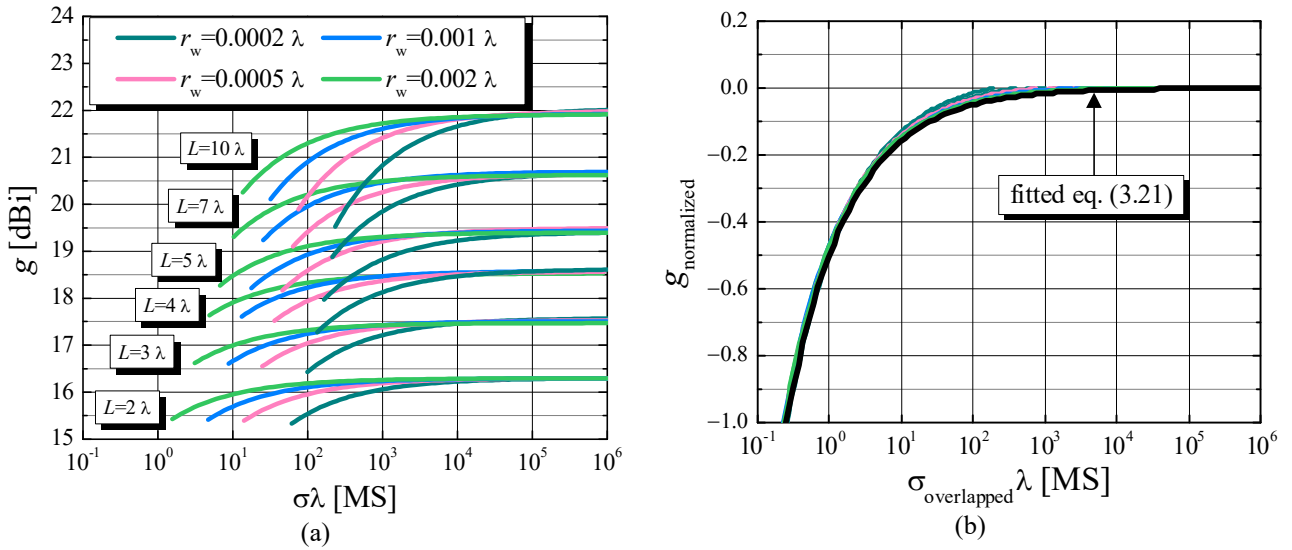

Figure 3.15. (a) Gain of antennas whose geometrical parameters are calculated from the design equations in a wider range of normalized conductivities and (b) overlapped gain traces.

The maximal gain strongly depends on the antenna axial length, whereas the wire radius only slightly affects the maximal gain. Circular markers in Fig. 3.16 correspond to the maximal gain for each axial length. Since the abscissa scale is logarithmic, the maximal gain can be fitted by the equation $g_{\text{max}} = A_{g\,\text{max}} \log_{10}(L/\lambda) + B_{g\,\text{max}}$, where $A_{g\,\text{max}} = 8.385$ and $B_{g\,\text{max}} = 13.48$ (solid line in Fig. 3.16a). The fitting by this equation is satisfactory for longer antennas. However, this fitting is not good for shorter antennas, especially for $L=2\,\lambda$. Hence, we added an additional term, which improves the fitting for the shortest antennas, $g_{\text{max}} = A_{g\,\text{max}} \log_{10}(L/\lambda) + B_{g\,\text{max}} + C_{g\,\text{max}}/(L/\lambda)^{D_{g\,\text{max}}}$, where the values of $A_{g\,\text{max}}$ and $B_{g\,\text{max}}$ are the same as previously defined, whereas $C_{g\,\text{max}} = 26.89$ and $D_{g\,\text{max}} = 6.763$, Fig. 3.16b.
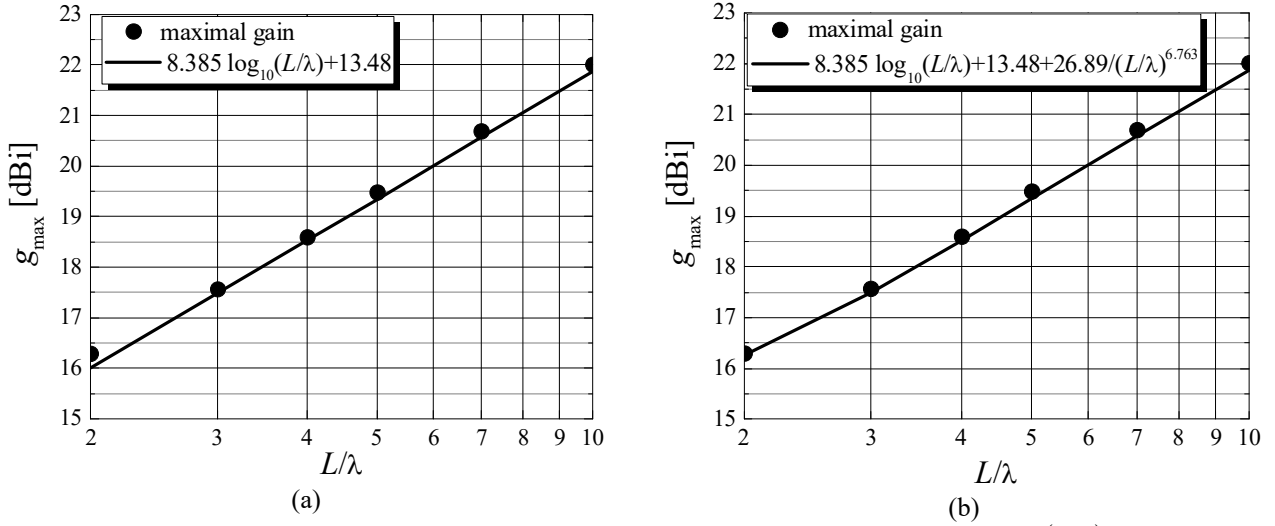
Figure 3.16. Fitting the maximal antenna gain by (a) $8.385\log_{10}(L/\lambda)+13.48$ and (b) $8.385\log_{10}(L/\lambda)+13.48+26.89/(L/\lambda)^{6.763}$.

Thereafter, the dependence on the wire radius should also be fitted. For that purpose, the overlapped traces in Fig. 3.15b have to be separated in order to obtain the dependence of the gain on the wire radius for the normalized conductivities higher than $\sigma_{min}\lambda$ (Fig. 3.15a). Hence, the term $\dfrac{-0.5}{\sqrt{\sigma_{\text{overlapped}}\,\lambda}}$, which fits the overlapped traces in Fig. 3.15b, needs to be expanded. Various dependencies are investigated and satisfactory fitting is achieved utilizing the term $\dfrac{-0.5\left(A_g\,L/\lambda\right)}{\left(r_w/\lambda\right)^{B_g}\sqrt{\sigma_{\text{overlapped}}\,\lambda}}$, where the coefficients are $A_g=0.005966$ and $B_g=0.8411$. Note that in order to achieve satisfactory fitting, it is necessary to introduce the dependence on the axial antenna length. This dependence cannot be easily noticed from the data shown in Fig. 3.15a, but it significantly improves the fitting. The fitted and actual traces are compared in Fig. 3.17 for various axial antenna lengths, demonstrating good agreement.

Finally, in Fig. 3.18 the gain of the antennas whose geometrical parameters are calculated from the design equations in a wide range of the normalized conductivities is compared with the gain fitted by the equation

$$g\,[\text{dBi}]=8.385\log_{10}\left(\frac{L}{\lambda}\right)+13.48-\frac{0.002983\,\dfrac{L}{\lambda}}{\left(\dfrac{r_w}{\lambda}\right)^{0.8411}\sqrt{\lambda\sigma}}+\frac{26.89}{\left(\dfrac{L}{\lambda}\right)^{6.763}}\,. \tag{3.22}$$

However, in the case of the axial antenna lengths 7λ and 10λ, the thickest wire, and the normalized conductivities close to $\sigma_{min}\lambda$, equation (3.22) overestimates the gain. Hence, equation (3.22) needs to be further modified in order to ensure that the equation for the gain estimation always underestimates the gain. The additional (the last) term is included and the final equation is

$$g\,[\text{dBi}]=8.385\log_{10}\left(\frac{L}{\lambda}\right)+13.48-\frac{0.002983\,\dfrac{L}{\lambda}}{\left(\dfrac{r_w}{\lambda}\right)^{0.8411}\sqrt{\lambda\sigma}}+\frac{26.89}{\left(\dfrac{L}{\lambda}\right)^{6.763}}-68.71\frac{r_w}{\lambda}\,. \tag{3.23}$$
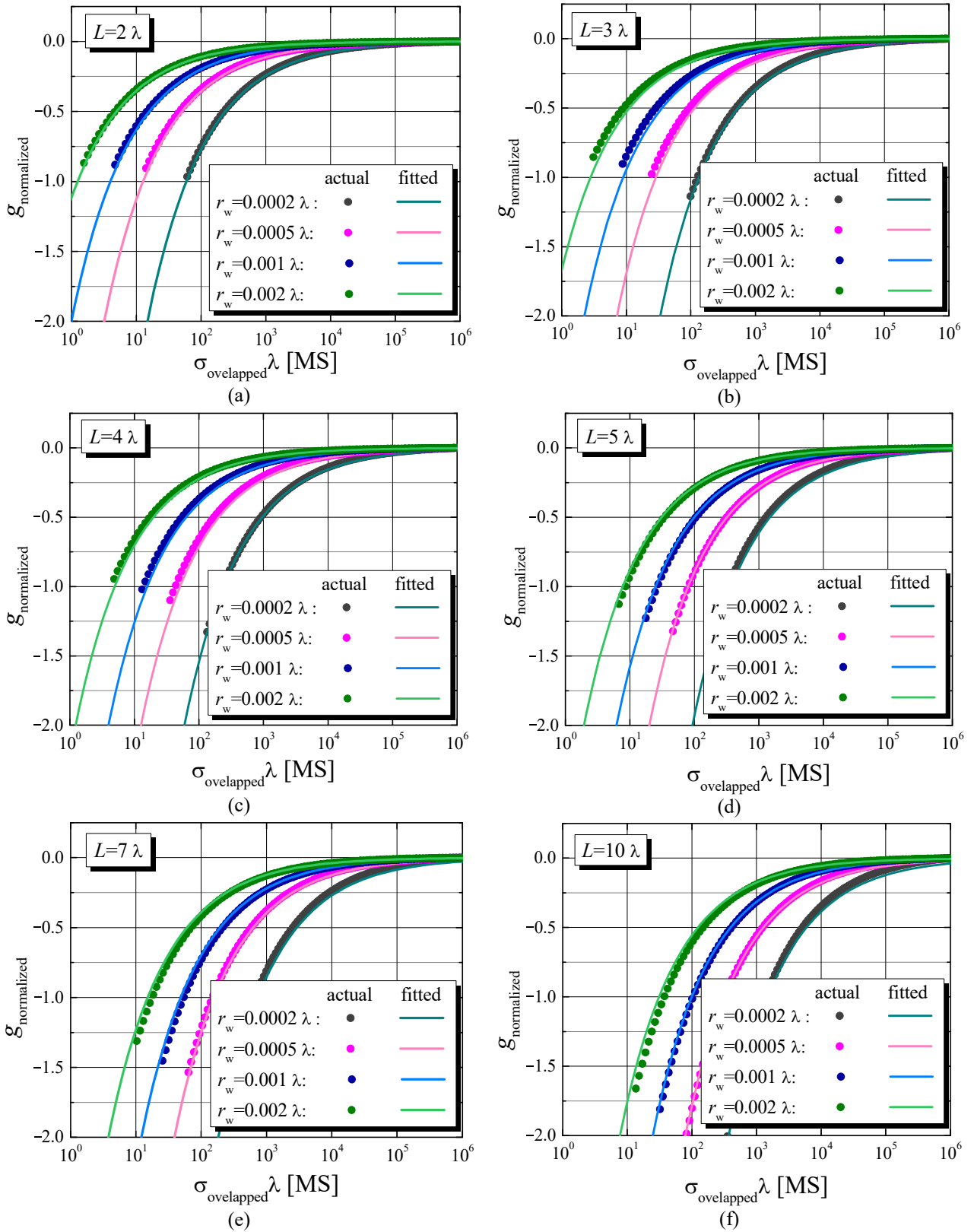
Figure 3.17. Fitting the gain dependence on the wire radius for (a) $L=2\,\lambda$, (b) $L=3\,\lambda$, (c) $L=4\,\lambda$, (d) $L=5\,\lambda$, (e) $L=7\,\lambda$, and (f) $L=10\,\lambda$.
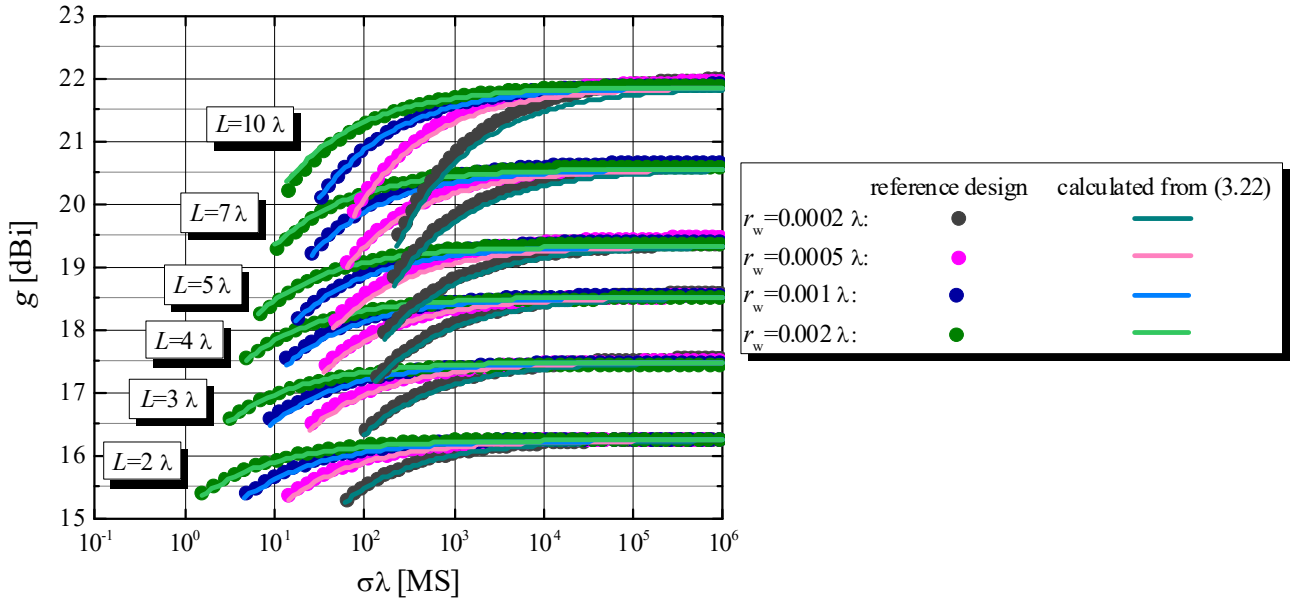
Figure 3.18. Gain of the antennas whose geometrical parameters are calculated from the design equations in a wide range of the normalized conductivities and the gain calculated from (3.22).

The gain calculated from (3.23) and the gain of the antennas whose geometrical parameters are calculated using the design equations are compared in Fig. 3.19.
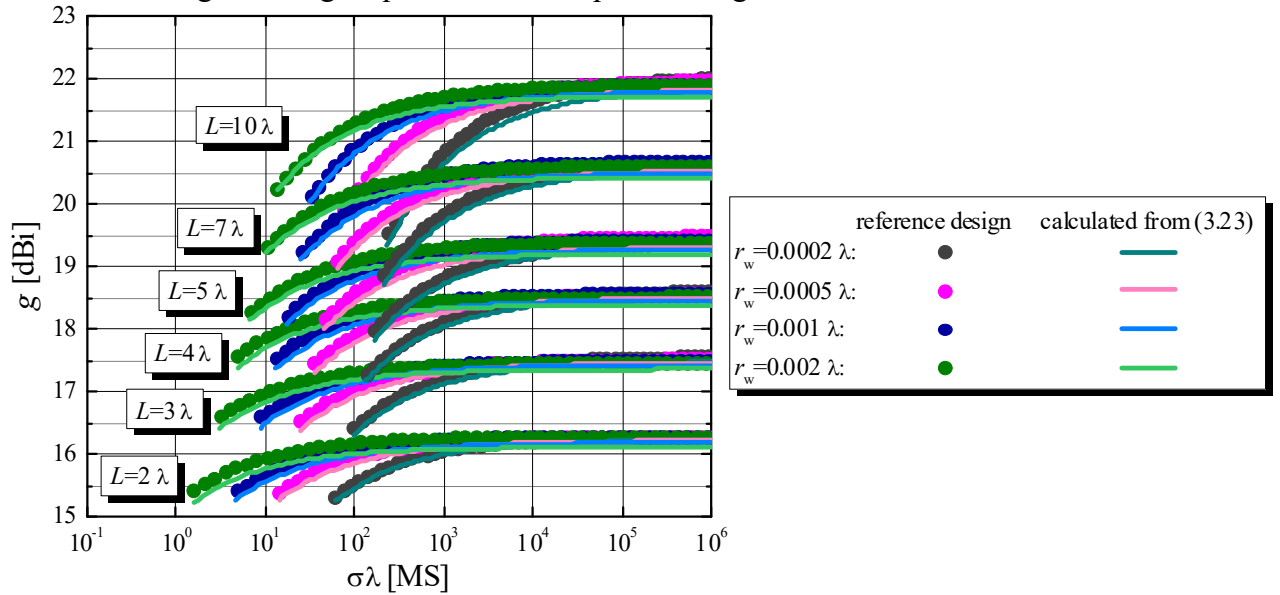

Figure 3.19. Gain of the antennas whose geometrical parameters are calculated from the design equations in a wide range of the normalized conductivities and the gain calculated from (3.23).

Results compared in Fig. 3.19 confirm that (3.23) estimates well the gain of the designed antennas, but also underestimates the gain in the range of the normalized conductivities $\sigma_{min}\lambda \leq \sigma\lambda \leq 1000\,\mathrm{MS}$, in which the design equations are valid. Moreover, (3.23) underestimates the gain in an even wider conductivity range, considered in Fig. 3.19, $\sigma_{min}\lambda \leq \sigma\lambda \leq 10^6\,\mathrm{MS}$. The property that (3.23) underestimates the gain is important from the practical point of view since it ensures that designed antennas achieve at least the gain calculated from (3.23), but in most cases even a (slightly) higher gain. This secures that by using the design equations and the design procedure (which will be presented in Chapter 5), the designer will be able to meet the desired specification, i.e., the targeted gain.

The maximal discrepancy between the gain of the designed antennas and the gain calculated from (3.23) is less than 0.3 dB (in the range of the normalized conductivities $\sigma_{min}\lambda \leq \sigma\lambda \leq 10^6\,\mathrm{MS}$).

4. Characteristics of designed antennas

During the optimization only the gain and the axial ratio are explicitly taken into account (through the cost function). However, some other antenna characteristics (e.g., bandwidth and input impedance) are also important for the applications. These characteristics are investigated in this chapter for the antennas designed using the design equations presented in Subsection 3.2.3.

Further, the influence of the ground plane of finite dimensions on the gain, axial ratio, and other antenna characteristics is explored in this chapter.

Finally, antennas, whose geometrical parameters are calculated from the design equations, are compared (in terms of the gain, axial ratio, and other characteristics) with other types of helical antennas (uniform and nonuniform) presented in the literature and obtained from additional optimizations.

4.1. Bandwidth, axial ratio, and input impedance

In this subsection, the relative bandwidths, axial ratios, and input impedances of the designed antennas are investigated in detail.

The relative bandwidth is defined here as $BW[\%] = 100(f_{max} - f_{min})/f$, where f_{max} and f_{min} stand for frequencies where the gain is for 1 dB (termed as BW_1), 2 dB (BW_2), or 3 dB (BW_3) lower than the maximal gain (Fig. 4.1), and f is the operating frequency.
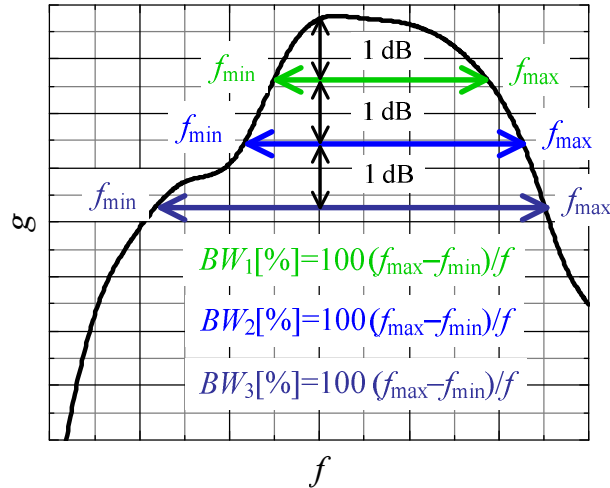

Figure 4.1. Definitions of the relative bandwidths.

The relative bandwidths of the designed antennas for various wire radii and two different wire conductivities (σ_{ref} and PEC) as a function of the axial antenna length are shown in Fig. 4.2. Note that the wire conductivity slightly influences the relative bandwidths (less than 8 %) for all considered wire radii (within the design hyper rectangle defined in Subsection 3.2.2, i.e., from $0.0002\,\lambda$ to $0.002\,\lambda$) and axial antenna lengths (from $2\,\lambda$ to $10\,\lambda$, also defined by the design hyper rectangle). The discrepancies of BW_2 caused by the different conductivities are negligibly small. However, for BW_1 and BW_3, these discrepancies are more pronounced. Namely, in all considered cases, BW_1 is larger for the reference conductivity than for the PEC wire, whereas for BW_3 the

situation is reversed, i.e., the PEC wire provides larger BW_3. Further, as the wire radius increases, all the relative bandwidths increase.
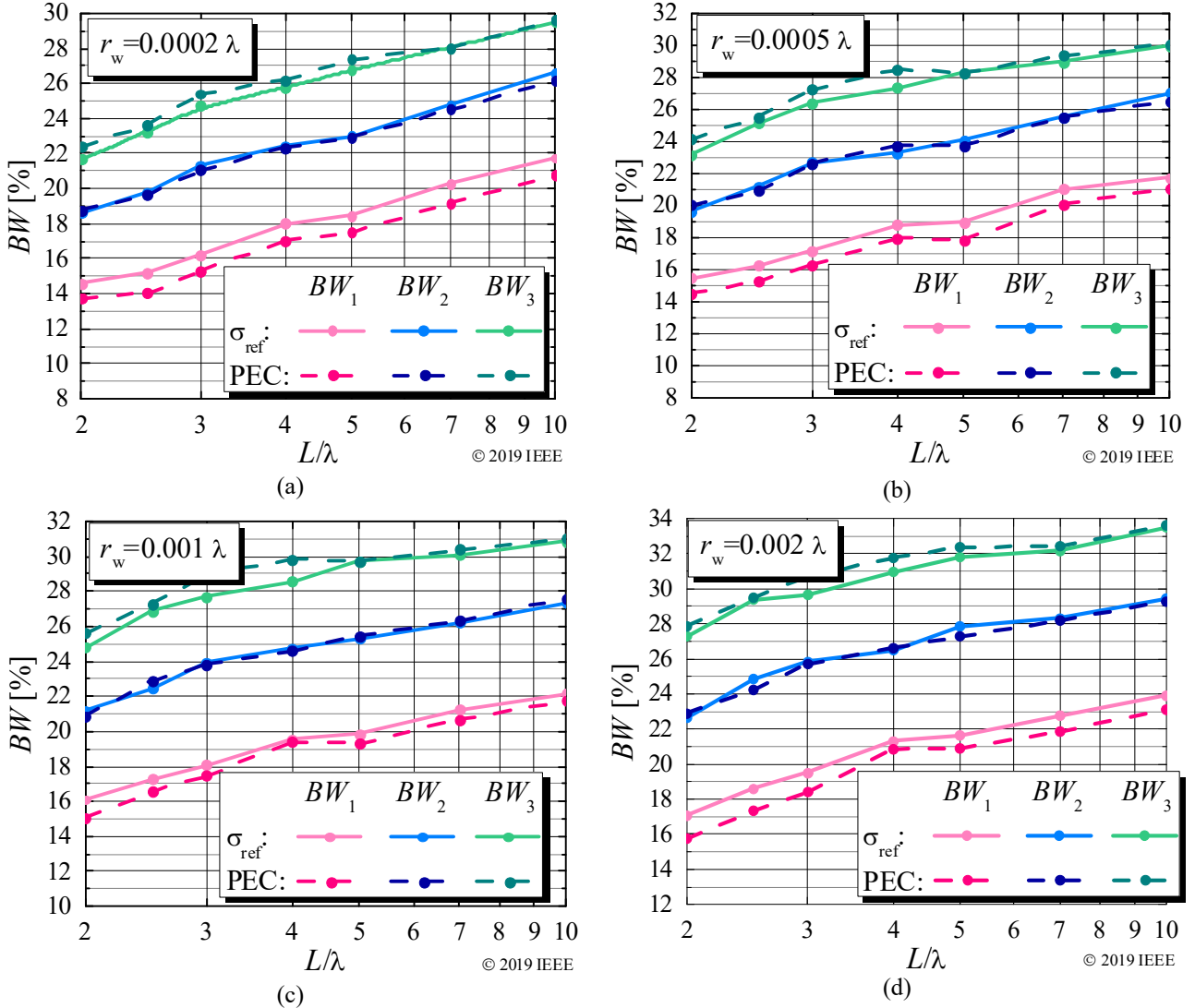

Figure 4.2. Relative bandwidths for various axial lengths and wire radii (a) r_w=0.0002 λ [113], (b) r_w=0.0005 λ [113], (c) r_w=0.001 λ [113], and (d) r_w=0.002 λ [113].

The axial ratio (ar, defined by (3.4)) of the designed antennas for various antenna lengths, wire radii, and wire conductivities σ_{ref} and PEC is shown in Fig. 4.3a. The axial ratio practically does not depend on the wire conductivity (for the conductivities within the range where the design is valid). For all considered axial antenna lengths and wire radii, the axial ratio is maintained below 0.7 dB (i.e., 1.17). Further, the increase in the axial antenna length is followed by the decrease in the axial ratio, except for the shortest antennas (2 λ and 2.5 λ) with the thickest wire (0.002 λ). Finally, the axial ratio gets smaller as the conductor becomes thinner.

Fig. 4.3b shows the (complex) input impedance ($\underline{Z} = R + \mathrm{j}X$) of the designed antennas. The same axial antenna lengths, wire radii, and wire conductivities are considered as for the relative bandwidths and the axial ratio. The input impedance is not influenced by the wire conductivity (for the normalized conductivities higher than $\sigma_{ref}\lambda$), whereas the axial antenna length slightly influences the input impedance. However, the wire radius affects the input impedance. Namely, when the wire radius is increased, the absolute values of the real and imaginary part of the input impedance are decreased.
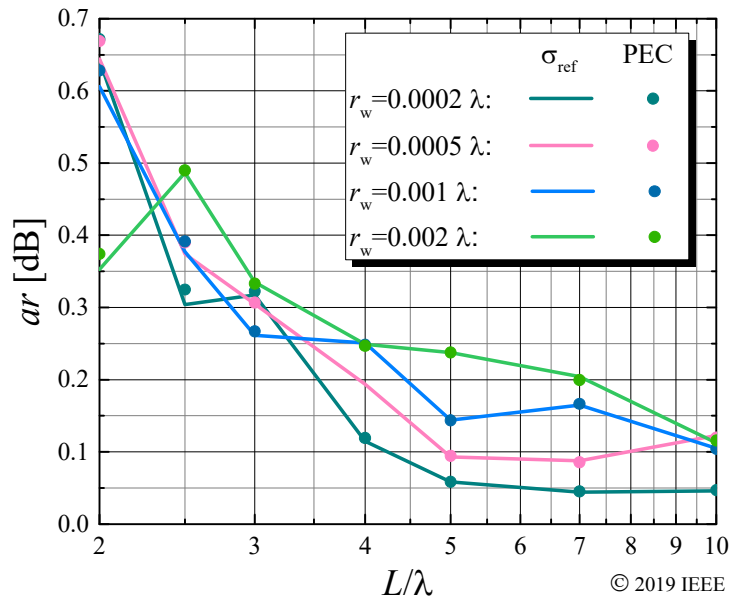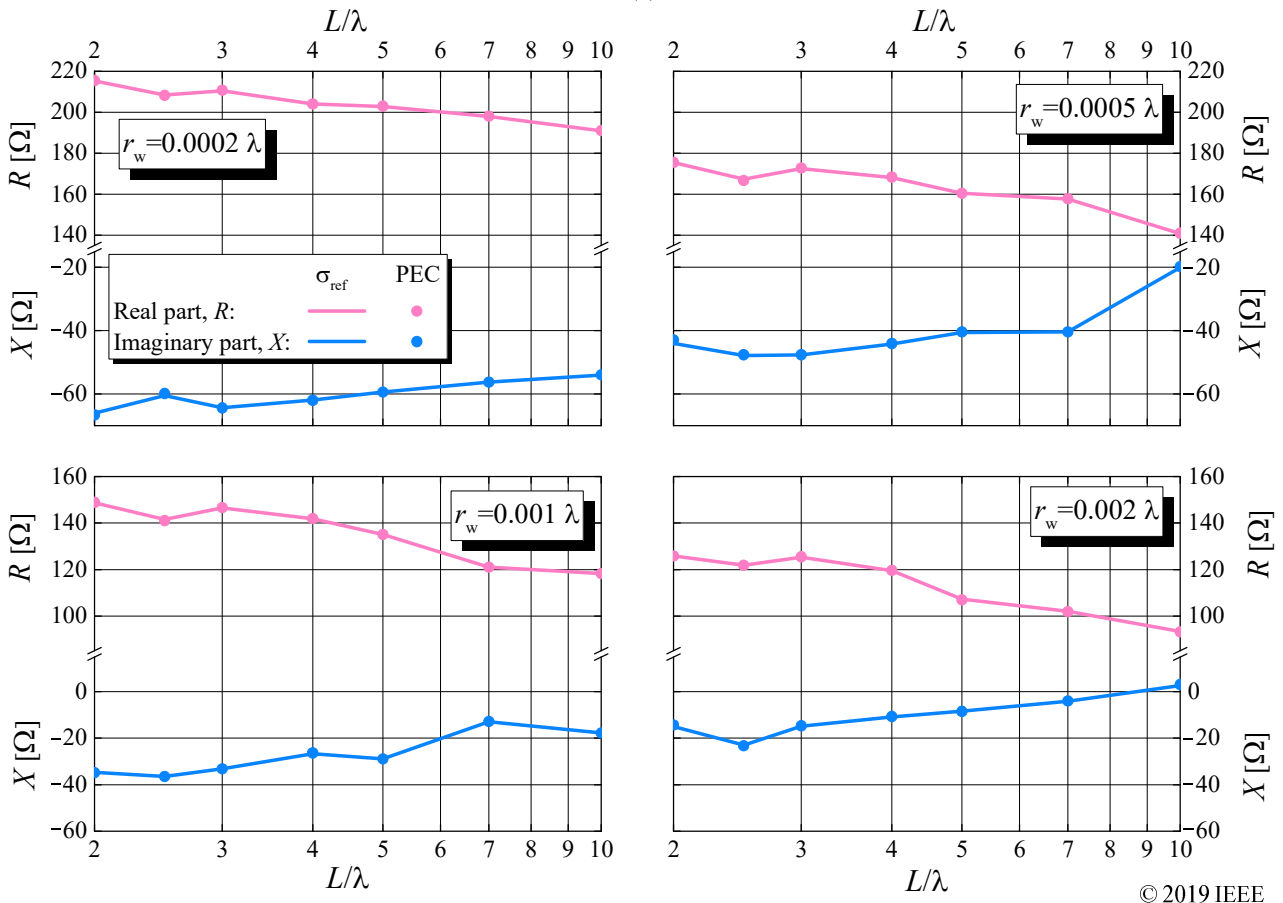
Figure 4.3. (a) Axial ratio [113] and (b) input impedance for various axial lengths and wire radii [113].

4.2. Note on antenna axial length

In the case of the antennas with lossless conductors (Subsection 3.2.1), the axial antenna lengths which are non-integer multiples of the half wavelength are also investigated. It is shown that these antennas achieve lower gain than the gain predicted by (3.6), i.e., (3.6) successfully predicts the gain of antennas whose axial lengths are integer multiples of the half wavelength.

Here, we want to investigate the gain of the designed antennas (with lossy conductors) of various axial lengths (integer and non-integer). We utilize different wire radii (within the considered range defined in Subsection 3.2.2) and the normalized conductivity $\sigma\lambda = \sigma_{ref}\lambda$. The gain of these antennas is shown in Fig. 4.4 by discrete points. These antennas show similar behavior as the antennas with lossless conductors (see Fig. 3.2).
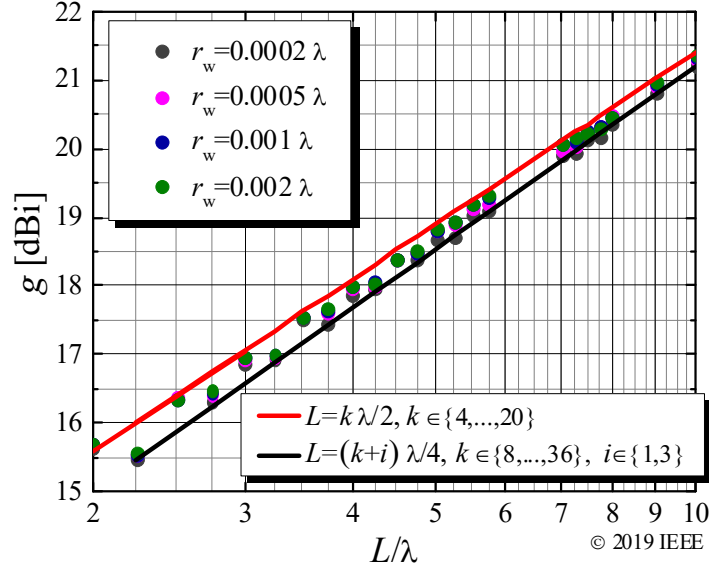

Figure 4.4. Gain for various axial antenna lengths for $\sigma\lambda = \sigma_{ref}\lambda$ [113].

It can be concluded that (3.23) accurately predicts the gain of antennas whose axial length is an integer multiple of the half wavelength, i.e.,

$$L = k\frac{\lambda}{2}, k \in \{4,...,20\}. \tag{4.1}$$

However, the gain is lower for the optimal antennas for which this condition is not fulfilled. Therefore, in order to achieve the maximal gain, the axial antenna lengths defined by (4.1) are recommended. Particularly, the worst results are observed for the axial antenna lengths

$$L = \frac{(k+i)}{4}\lambda, k \in \{8,...,36\}, i \in \{1,3\}, \tag{4.2}$$

when, for shorter antennas, the gain is around 0.4 dB lower than the gain calculated from (3.23). For longer antennas, the discrepancies decrease. The red solid line in Fig. 4.4 fits the gain of the antennas whose axial lengths are defined by (4.1), whereas the black solid line fits the gain of the antennas whose axial lengths are calculated from (4.2).

4.3. Antennas above finite ground plane

All the previously given results are obtained assuming the helix to be located above an (infinite) perfectly conducting ground plane. According to the image theory, the influence of an infinite perfectly conducting ground plane can be emulated by the antenna image (when both the antenna and the image are placed in free space). This significantly reduces the computation time, which justifies using an infinite ground plane in the simulations.

However, in practice such a plane can only be approximated. Therefore, in this subsection the influence of finite-size ground planes on the antenna gain and other characteristics will be considered. Since the scope of this work is primarily oriented towards the design of the antenna conductor (i.e., the helix), not the design of the ground plane, here we consider only flat ground planes of a square or circular shape. Other shapes of the ground plane (circular cup, truncated cone, etc.) can significantly change the gain, as it is shown in [51]–[54], [56]. However, analyzing their

influence on the gain of the designed antennas and their characteristics is beyond the scope of this work.

Fig. 4.5a shows a helical antenna with a square ground plane, and Fig. 4.5b shows an antenna with a circular ground plane. We denote the length of a side of the square plane by a and the surface areas of the square and circular planes by S. The ground plane of finite dimensions influences the gain of the designed antennas, i.e., the antenna gain can be different from the gain calculated from (3.23). Fig. 4.6 shows the gain differences, Δg, between the gain of antennas above the square or the circular ground plane and the antennas above an infinite ground plane (calculated from (3.23)), for various dimensions of the ground plane, various axial antenna lengths, and wire conductivity σ_{ref}. The considered ground planes are supposed to be made of a PEC. Additional numerical experiments show that the influence of the ground-plane conductivity on Δg is negligible, i.e., for the ground-plane conductivity σ_{ref}, Δg is almost the same as in Fig. 4.6.

The results in Fig. 4.6 demonstrate that the circular and the square ground plane are equivalent if their surface areas are equal. Therefore the abscissas in Fig. 4.6 correspond to $\sqrt{S}/\lambda$. As it is expected, when the ground-plane dimensions are increased, i.e., when the finite-size ground plane approaches the infinite ground plane, the gain differences tend to zero. Further, note that for some dimensions of the ground plane Δg is larger than 0. This indicates that, with a ground plane of proper dimensions, even higher gain can be achieved than in the case of the infinite ground plane (the gain calculated from (3.23)), which is of significant practical importance. This increase can be up to 0.5 dB. We denote the smallest dimension of the ground plane that corresponds to $\Delta g = 0$ (i.e., the antenna achieves the same gain as with the infinite ground plane) by $\sqrt{S_0}/\lambda$, whereas the dimension of the ground plane for which Δg is maximal is denoted by $\sqrt{S_{\mathrm{max}}}/\lambda$. These dimensions are shown in Fig. 4.7 for various axial antenna lengths and wire radii.

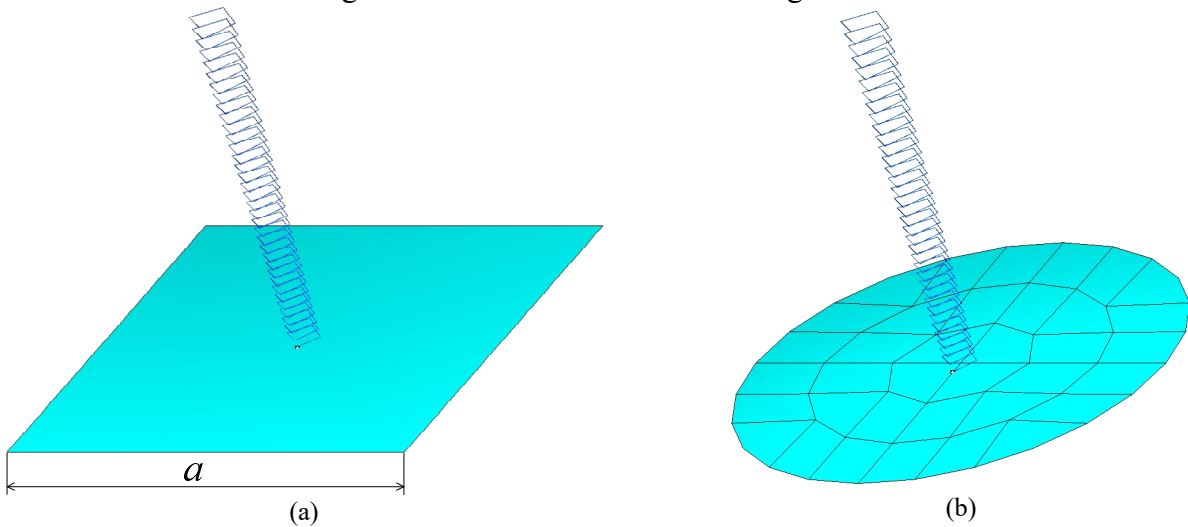(a)   (b)

Figure 4.5. Helix located above (a) a square ground plane and (b) a circular ground plane.
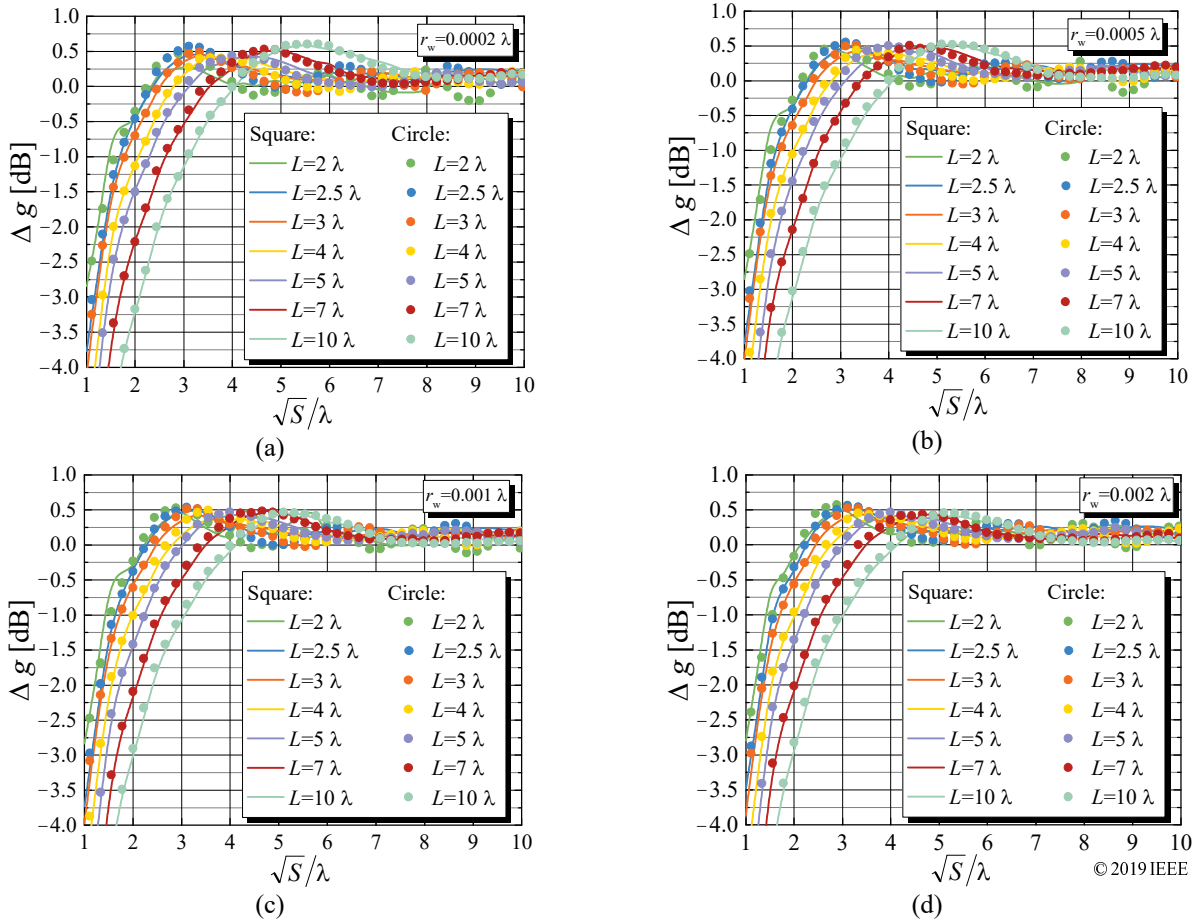
Figure 4.6. Δg for square or circular ground plane, various axial antenna lengths, and wire radii (a) r_w=0.0002 λ, (b) r_w=0.0005 λ, (c) r_w=0.001 λ, and (d) r_w=0.002 λ [113]. Wire conductivity is σ_{ref}.
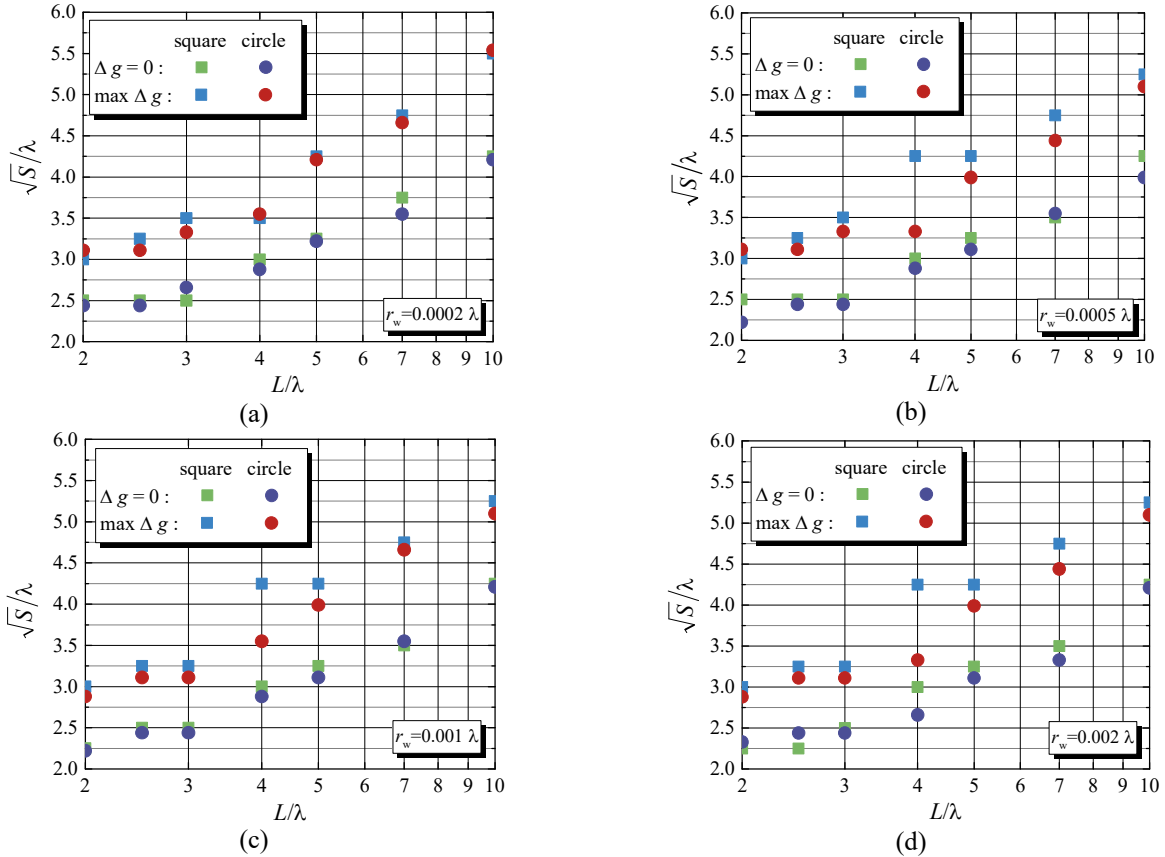

Figure 4.7. $\sqrt{S_0}/\lambda$ ($\Delta g = 0$) and $\sqrt{S_{max}}/\lambda$ (max Δg) for various axial antenna lengths and wire radii (a) r_w=0.0002 λ, (b) r_w=0.0005 λ, (c) r_w=0.001 λ, and (d) r_w=0.002 λ. Wire conductivity is σ_{ref}.

41

The need for a relatively large ground plane can quantitatively be explained in the following way. The actual antenna consists of the helix and the ground plane. The electric field created by this structure, at any point in the space (including the far-field region), due to the superposition principle, is given as the sum of the field due to the current in the helix ($\underline{\mathbf{E}}_h$) and the field due to the current in the ground plane ($\underline{\mathbf{E}}_{gp}$), i.e., $\underline{\mathbf{E}} = \underline{\mathbf{E}}_h + \underline{\mathbf{E}}_{gp}$.

We consider a representative example – a helical antenna whose axial length is $L = 2\lambda$ at the operating frequency $300\,\text{MHz}$, the wire radius is 0.002λ, and the wire conductivity is σ_{ref}. Assuming an infinite ground plane, we use program AWAS [112] and evaluate the radiated electric field of this antenna. The gain of the actual system, as the function of the zenith angle θ, is shown in Fig. 4.8, labeled "actual". Since the ground plane is infinite, $\underline{\mathbf{E}}_{gp}$ cancels $\underline{\mathbf{E}}_h$ at all points under the ground plane, so that there is no radiated field in the lower half-space. In the upper half-space, $\underline{\mathbf{E}}_{gp}$ can be, mathematically, replaced by the electric field due to the (negative) image of the helix current, i.e., $\underline{\mathbf{E}}_{gp} = \underline{\mathbf{E}}_{hi}$. Hence, in the upper half-space, the actual electric field can be represented as $\underline{\mathbf{E}} = \underline{\mathbf{E}}_h + \underline{\mathbf{E}}_{hi}$.

Using a customized version of program AWAS, we now compute $\underline{\mathbf{E}}_h$ in the whole space. The corresponding gain pattern is shown in Fig. 4.8, labeled "original full space". The current of the helix radiates both upwards and downwards, i.e., we clearly see an upward-radiated field and a downward-radiated field. (The field radiated downwards is even stronger than the field radiated upwards.) In the actual system, we can consider that the downward-radiated field is totally reflected by the ground plane and redirected upwards. This reflected field is $\underline{\mathbf{E}}_{hi}$ and in Fig. 4.8 the corresponding gain pattern is labeled "image".

If the helix is wound according to the right-hand rule, then $\underline{\mathbf{E}}_h$ is RHC polarized in the upward directions (within the main beam), but it is LHC polarized in the downward directions. The downward-radiated wave, reflected from the ground plane, changes its polarization and becomes RHC polarized. Hence, in the upper half-space, $\underline{\mathbf{E}}_h$ and $\underline{\mathbf{E}}_{hi}$ interfere constructively in the zenith direction ($\theta=0$). The intensity of $\underline{\mathbf{E}} = \underline{\mathbf{E}}_h + \underline{\mathbf{E}}_{hi}$ is stronger than the intensities of both $\underline{\mathbf{E}}_h$ and $\underline{\mathbf{E}}_{hi}$. Thus, the gain of the actual antenna is larger than the gain that is attributed individually to $\underline{\mathbf{E}}_h$ and $\underline{\mathbf{E}}_{hi}$.

If we consider a finite ground plane, the size of this plane must be large enough to properly reflect $\underline{\mathbf{E}}_h$ (which, after reflection, becomes $\underline{\mathbf{E}}_{hi}$). In other words, the ground plane must be large enough to encompass the major part of the currents that exist in an infinite ground plane.

Note that the effect of the reflection of the downward-radiated wave from the ground plane is utilized in [49] to enhance the operating bandwidth of the helical antenna, in particular, for the WB3 design, but at the cost of reducing the peak gain compared to the narrowband (NB) design. On the other hand, the nonuniform helical antenna from [82] is optimized so to minimize the downward radiation from the helix current. Hence, this antenna does not need a ground plane, except for a small counterbalance required to feed the helix.

We can also qualitatively explain the high gain of our nonuniform helical antenna in the following way. Generally, a helical antenna can be considered as a linear array of individual turns [2]. The axis of the array is the axis of the helix. In the classical design, this array radiates predominantly upwards. In our design, however, this array radiates both upwards and downwards. The downward radiation is reflected by the ground plane, which is equivalent to augmenting the original array by its image. The resulting array is two times longer than the original array. Hence, theoretically, the resulting numerical gain may be expected to be up to two times larger [119], i.e., the gain may be larger for up to 3 dB.
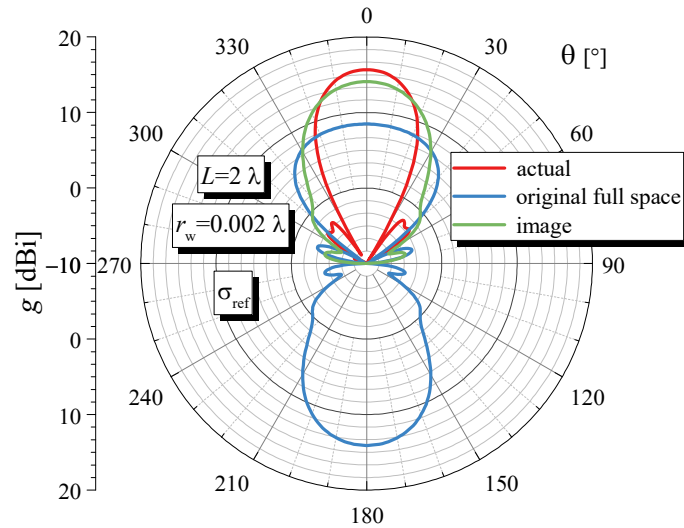
Figure 4.8. Actual radiation pattern, radiation pattern due to the original in the whole space, and radiation pattern due to the image.

From the practical point of view, sometimes it is also important to take care of the antenna overall dimensions, instead of separately observing the axial antenna length and the dimensions of the ground plane. Fig. 4.9 shows the dependences of the gain of the designed antennas, located above a ground plane of finite dimensions, on the volume of the box or cylinder in which the antenna (together with the ground plane) fits. Therefore, the abscissas in Fig. 4.9 correspond to LS/λ^3, which is the normalized volume of that box or cylinder. As it is previously mentioned, the influence of the losses in the ground plane on the antenna gain is negligible. Hence, here we consider ground planes to be lossless, whereas the wire conductivity is σ_{ref}.
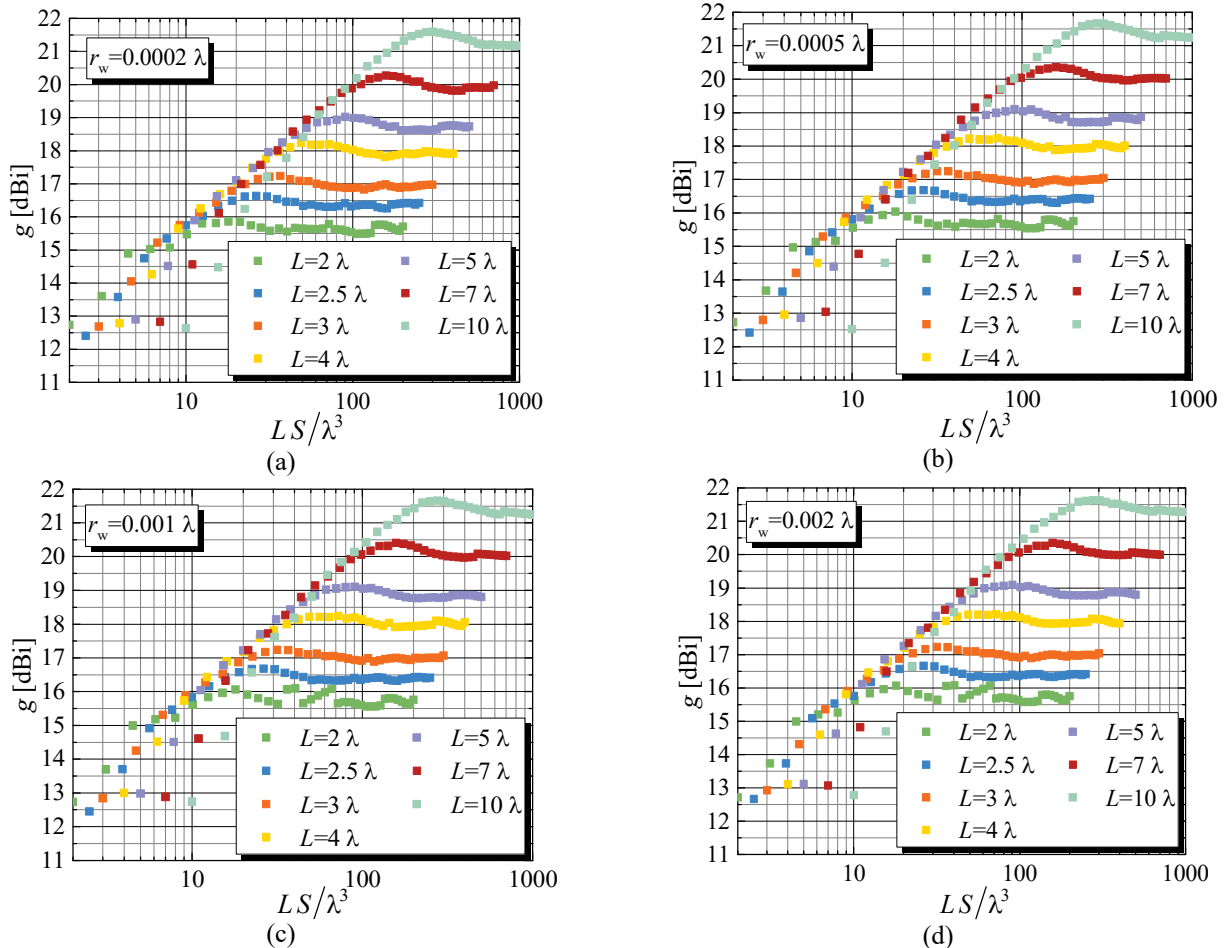

Figure 4.9. Dependences of the gain of the designed antennas on the antenna overall dimensions for (a) r_w=0.0002 λ, (b) r_w=0.0005 λ, (c) r_w=0.001 λ, and (d) r_w=0.002 λ. Wire conductivity is σ_{ref} and the ground plane is lossless.

For example, if we consider the wire radius 0.0005 λ, the targeted gain of 18 dBi can be achieved with different axial antenna lengths and corresponding ground planes (Fig. 4.9). For the axial antenna length 4 λ, a square ground plane of a side 3.25 λ is required. Also, the same gain can be achieved with antennas of the axial lengths 5 λ, 7 λ, or 10 λ located above square ground planes of sides 2.5 λ, 2.25 λ, or 2 λ, respectively. Depending on the application and desired antenna overall dimensions, the final decision can be made by the designer.

The ground plane of finite dimensions also influences other antenna characteristics, i.e., the bandwidth, axial ratio, and input impedance.

The differences between the relative bandwidths when the antennas are located above a PEC ground plane of a finite dimensions and above an infinite PEC ground plane are ΔBW_1, ΔBW_2, and ΔBW_3. For various axial antenna lengths, wire radii, and two different wire conductivities (PEC and σ_{ref}) ΔBW_1, ΔBW_2, and ΔBW_3 are shown in Figs. 4.10–4.12 (for square ground planes) and Figs. 4.13–4.15 (for circular ground planes).

These results confirm that the relative bandwidths are negligibly influenced by conductor losses as well as by the shape (square or circular) of the ground plane (when their surface areas are equal). The ground plane of a finite size can increase the gain. However, its influence on the relative bandwidths is very small. Moreover, when the ground-plane dimension is larger than $\sqrt{S_0}/\lambda$, the relative bandwidths are almost the same as with the infinite ground plane. This conclusion is important from a practical point of view since it is expected that ground planes of dimensions smaller than $\sqrt{S_0}/\lambda$ will not be used often. Hence, the finite-size ground plane, used instead of the infinite ground plane, does not degrade the relative bandwidths.
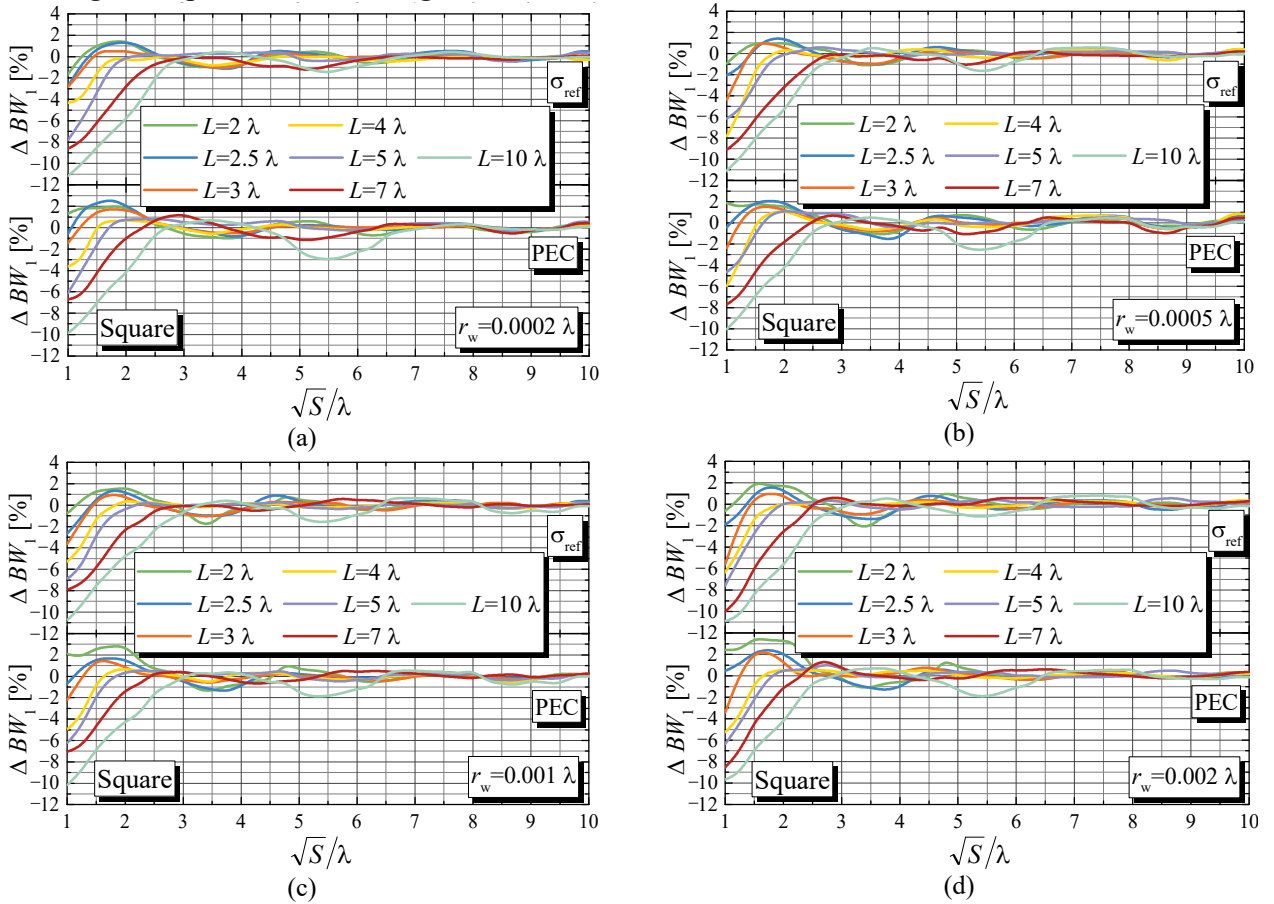

Figure 4.10. ΔBW_1 for square ground plane, various axial antenna lengths, wire conductivities σ_{ref} and PEC, and wire radii (a) r_w=0.0002 λ, (b) r_w=0.0005 λ, (c) r_w=0.001 λ, and (d) r_w=0.002 λ.
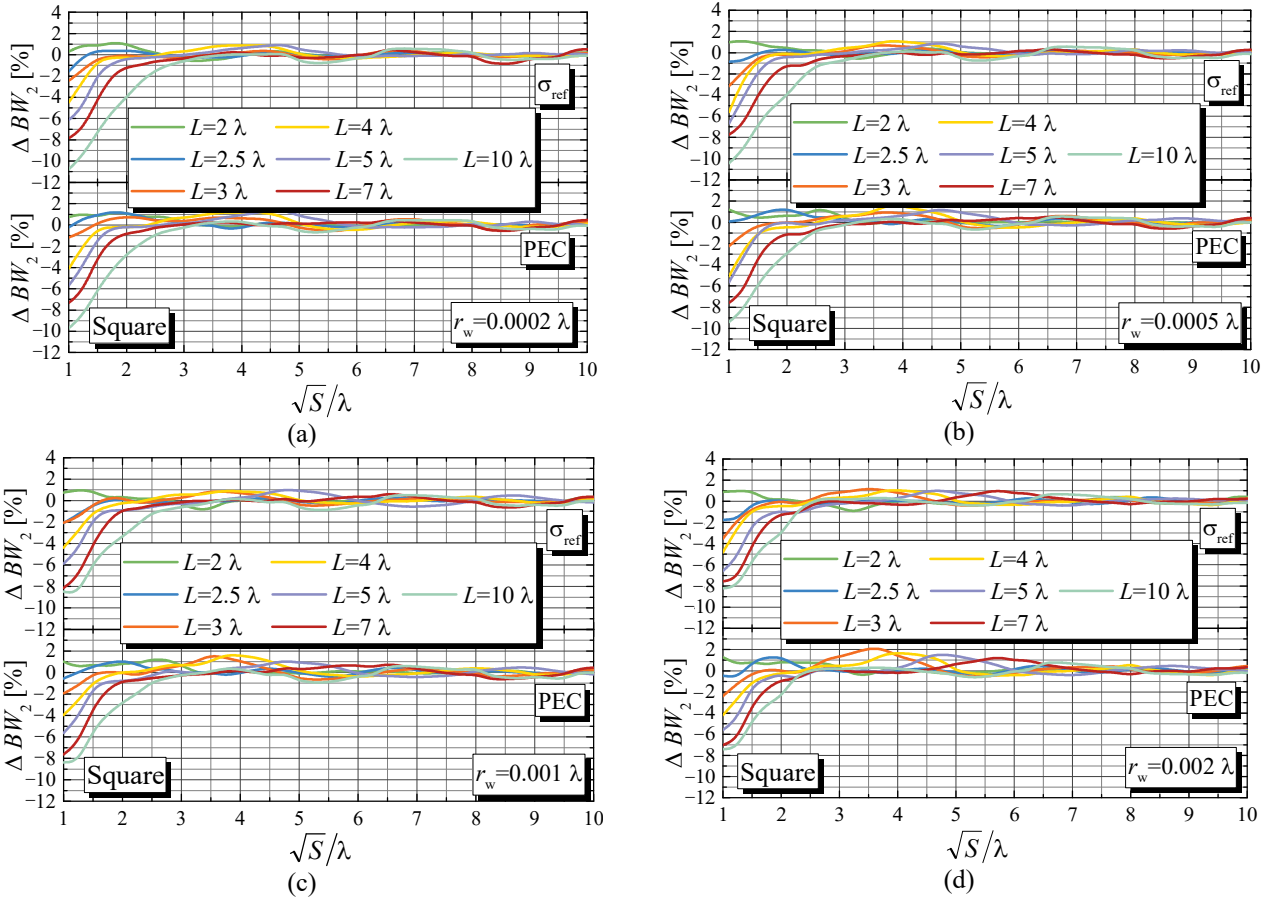
Figure 4.11. ΔBW_2 for square ground plane, various axial antenna lengths, wire conductivities σ_{ref} and PEC, and wire radii (a) r_w=0.0002 λ, (b) r_w=0.0005 λ, (c) r_w=0.001 λ, and (d) r_w=0.002 λ.
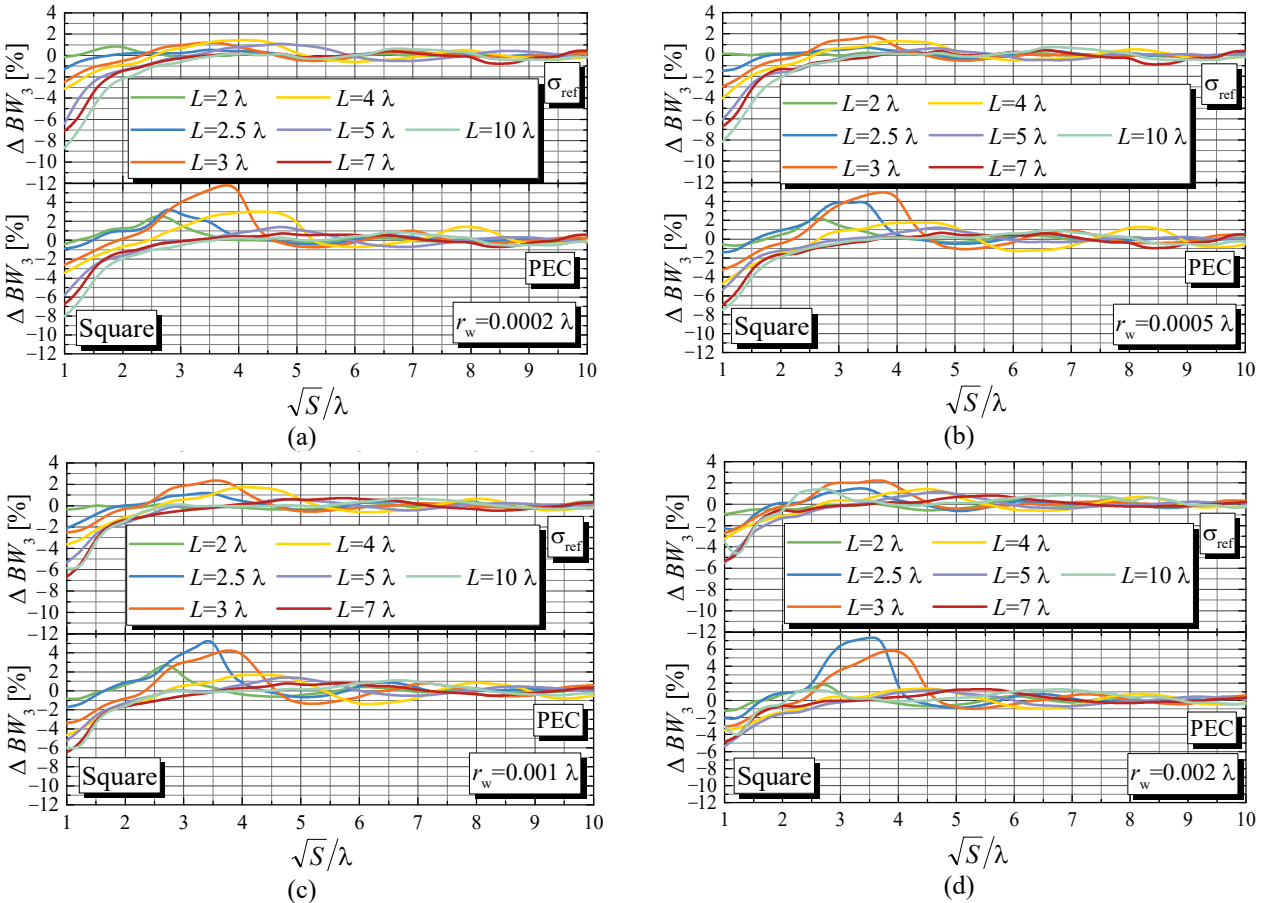

Figure 4.12. ΔBW_3 for square ground plane, various axial antenna lengths, wire conductivities σ_{ref} and PEC, and wire radii (a) r_w=0.0002 λ, (b) r_w=0.0005 λ, (c) r_w=0.001 λ, and (d) r_w=0.002 λ.

45

Figure 4.13. ΔBW_1 for circular ground plane, various axial antenna lengths, wire conductivities σ_{ref} and PEC, and wire radii (a) r_w=0.0002 λ, (b) r_w=0.0005 λ, (c) r_w=0.001 λ, and (d) r_w=0.002 λ.
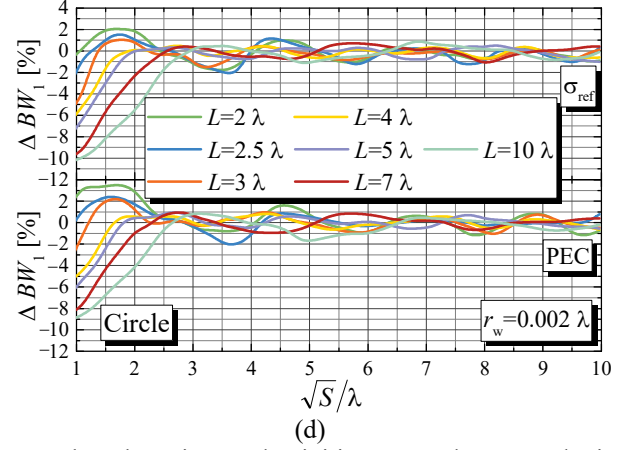

Figure 4.14. ΔBW_2 for circular ground plane, various axial antenna lengths, wire conductivities σ_{ref} and PEC, and wire radii (a) r_w=0.0002 λ, (b) r_w=0.0005 λ, (c) r_w=0.001 λ, and (d) r_w=0.002 λ.
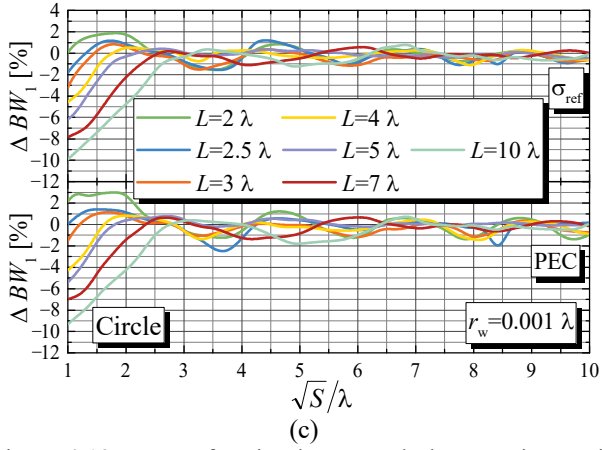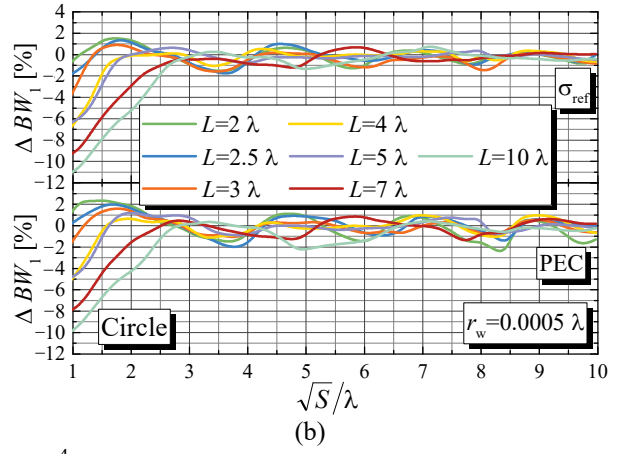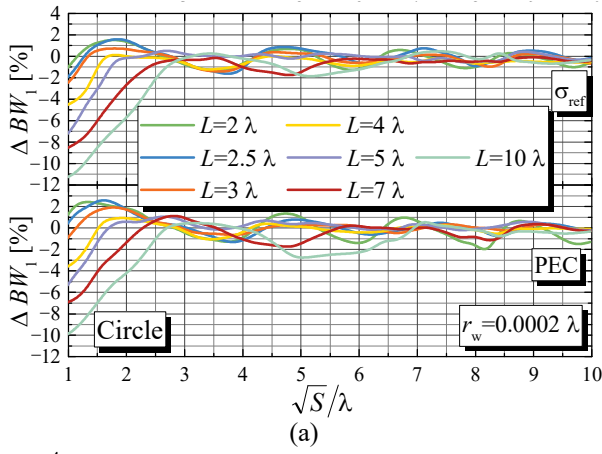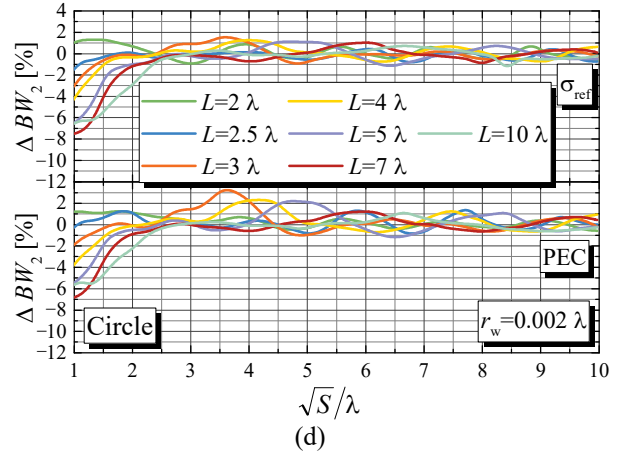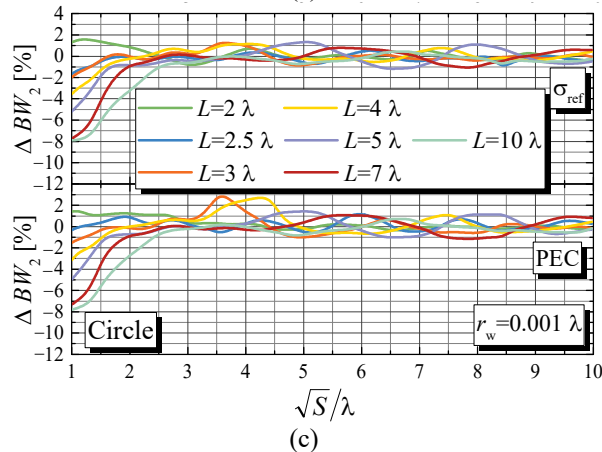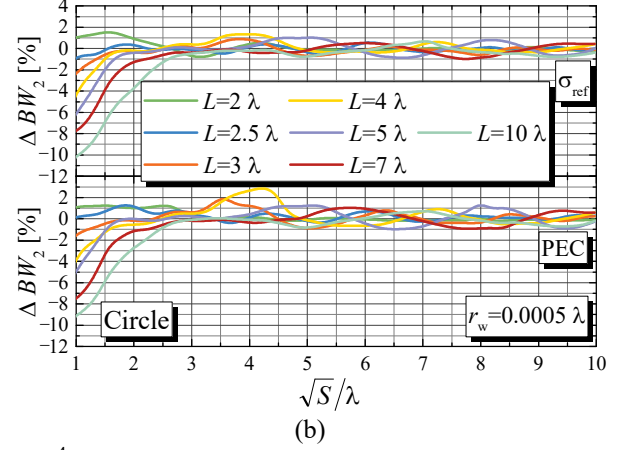
Figure 4.15. ΔBW_3 for circular ground plane, various axial antenna lengths, wire conductivities σ_{ref} and PEC, and wire radii (a) r_w=0.0002 λ, (b) r_w=0.0005 λ, (c) r_w=0.001 λ, and (d) r_w=0.002 λ.

The differences between the axial ratio (Δar) and the input impedances ($\Delta \underline{Z} = \Delta R + j\Delta X$) when the antennas are located above a PEC square ground plane of a surface area S (square side $a = \sqrt{S}$) and above an infinite PEC ground plane for various axial antenna lengths, wire radii, and two different wire conductivities (PEC and σ_{ref}) are shown in Figs. 4.16 and 4.18, respectively. These differences when the antennas are located above a PEC circular ground plane (instead of a square ground plane) are shown in Figs. 4.17 and 4.19, respectively.

Figs. 4.16–4.19 confirm that conductor losses do not influence the axial ratio and the input impedance. The shape of the ground plane (if the surface areas of the square and circle are equal) negligibly influences the axial ratio, in particular for the ground planes whose dimensions are larger than $\sqrt{S_0}/\lambda$. In these cases, the considered differences of the axial ratio vary closely around zero (the variation is less than $\pm 0.25\,\mathrm{dB}$). However, the influence of the ground plane shape on the input impedance is noticeable. From the practical point of view, the most preferable are the dimensions around $\sqrt{S_0}/\lambda$. Hence, the most preferable part of the graphs in Figs. 4.18 and 4.19 are the middle regions. Within these regions, for the square ground plane, ΔR and ΔX vary around $10\,\Omega$ and $-15\,\Omega$, respectively. For the circular ground plane, ΔX varies around 0. However, ΔR changes depending on the wire radius, i.e., with the increase of the wire radius, ΔR decreases.

Figure 4.16. Δar for square ground plane, various axial antenna lengths, wire conductivities σ_{ref} and PEC, and wire radii (a) r_w=0.0002 λ, (b) r_w=0.0005 λ, (c) r_w=0.001 λ, and (d) r_w=0.002 λ.
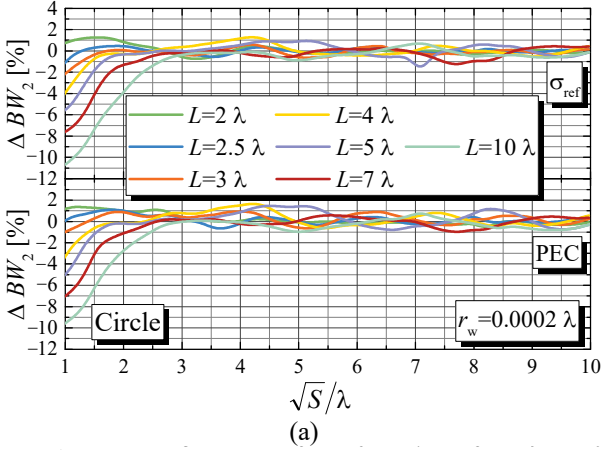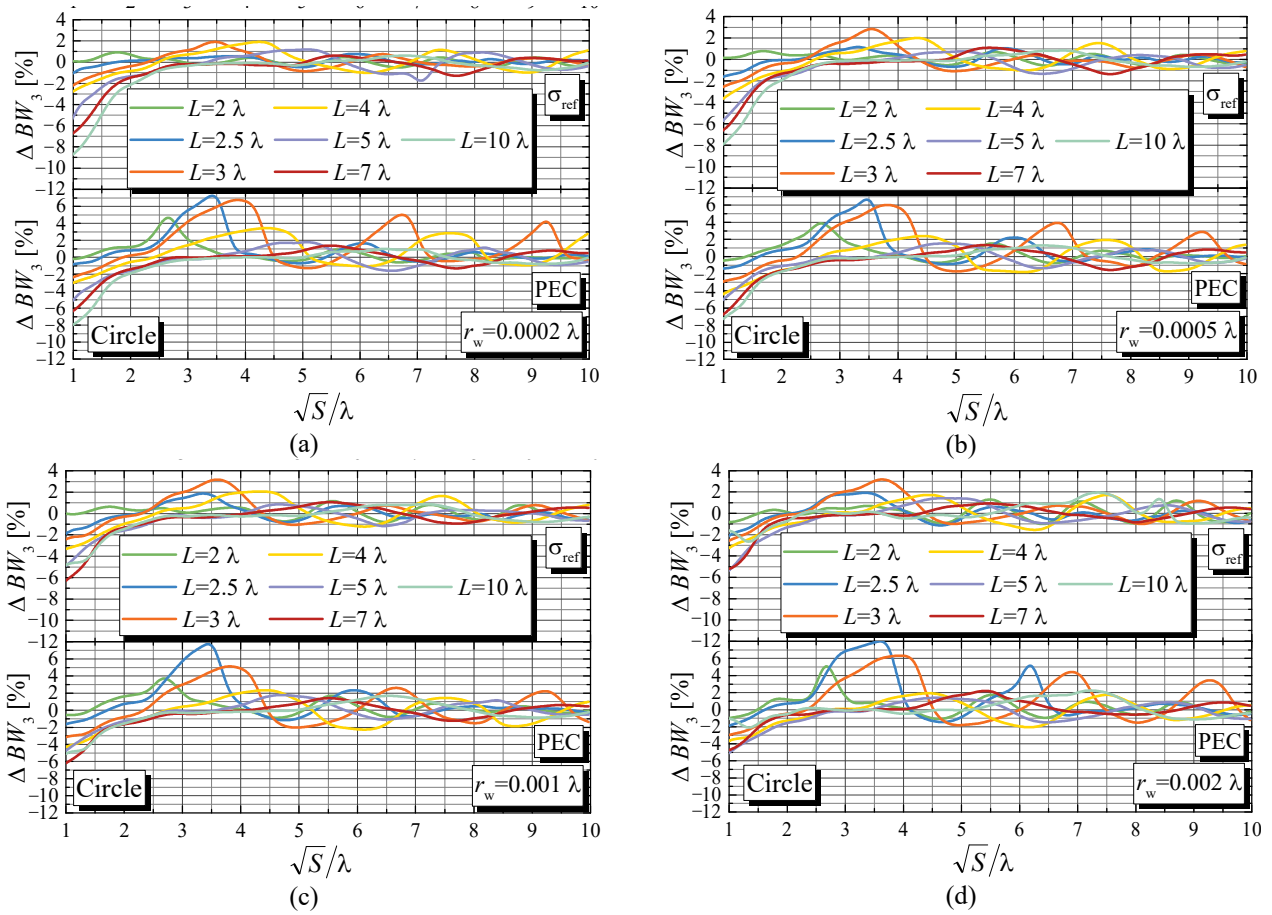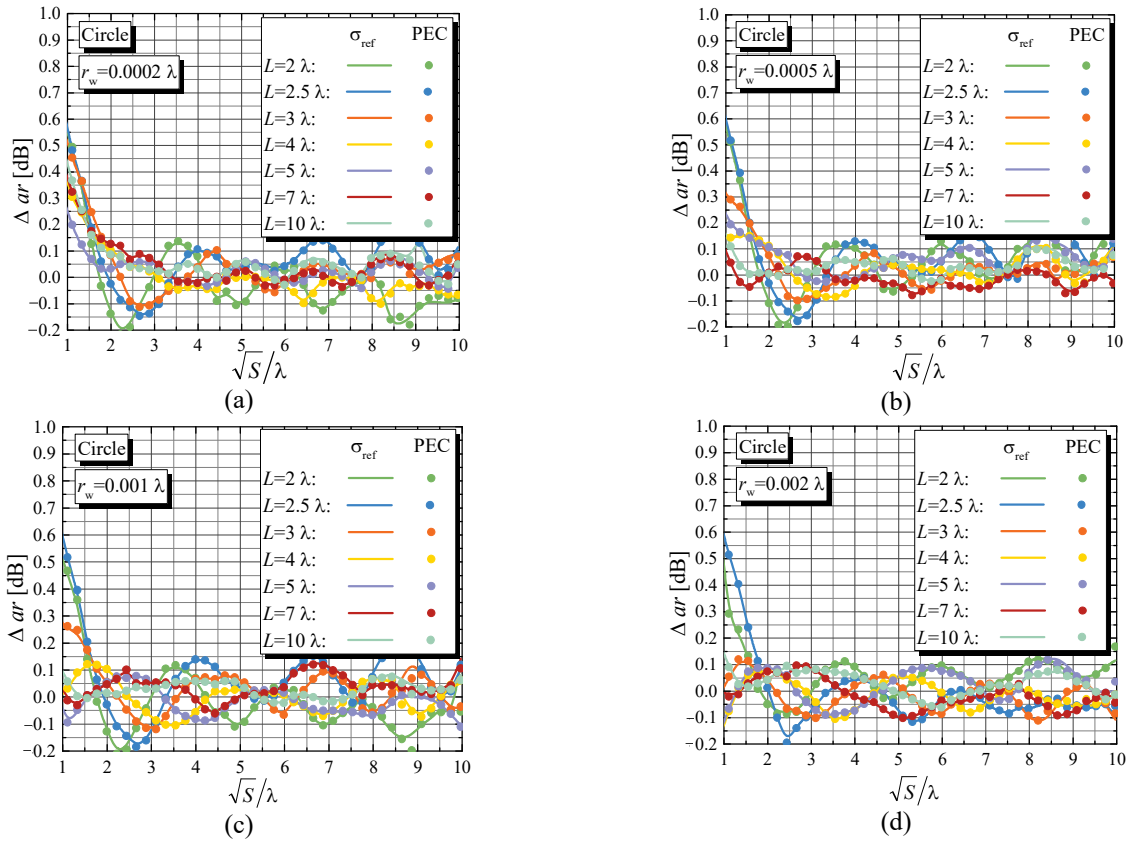

Figure 4.17. Δar for circular ground plane, various axial antenna lengths, wire conductivities σ_{ref} and PEC, and wire radii (a) r_w=0.0002 λ, (b) r_w=0.0005 λ, (c) r_w=0.001 λ, and (d) r_w=0.002 λ.

Figure 4.18. $\Delta \underline{Z}$ for square ground plane, various axial antenna lengths, wire conductivities σ_{ref} and PEC, and wire radii (a) r_w=0.0002 λ, (b) r_w=0.0005 λ, (c) r_w=0.001 λ, and (d) r_w=0.002 λ.
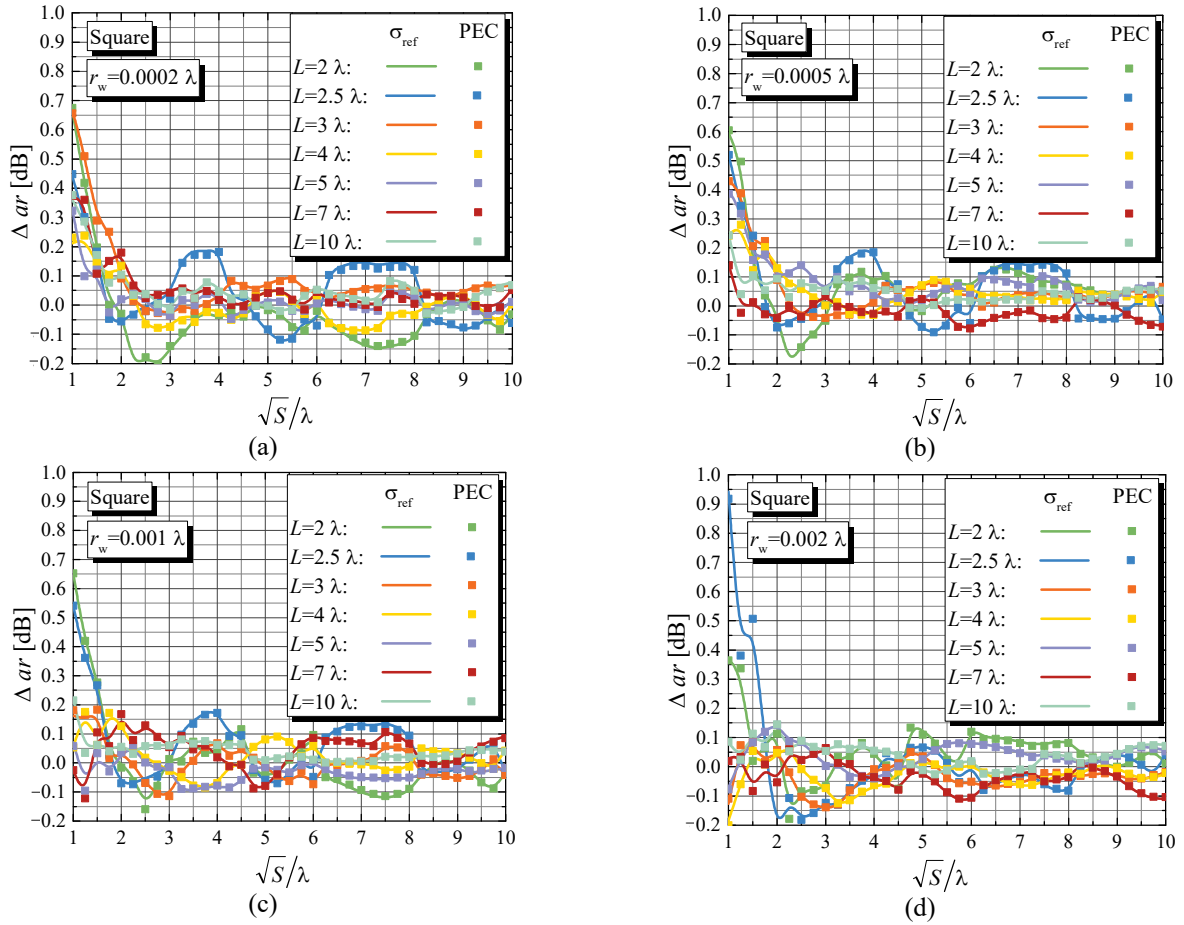

Figure 4.19. $\Delta \underline{Z}$ for circular ground plane, various axial antenna lengths, wire conductivities σ_{ref} and PEC, and wire radii (a) r_w=0.0002 λ, (b) r_w=0.0005 λ, (c) r_w=0.001 λ, and (d) r_w=0.002 λ.
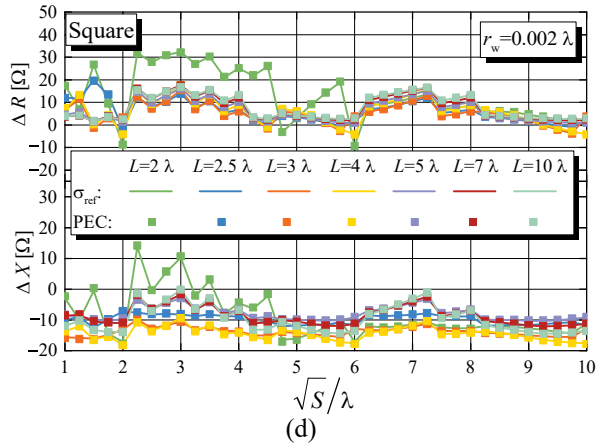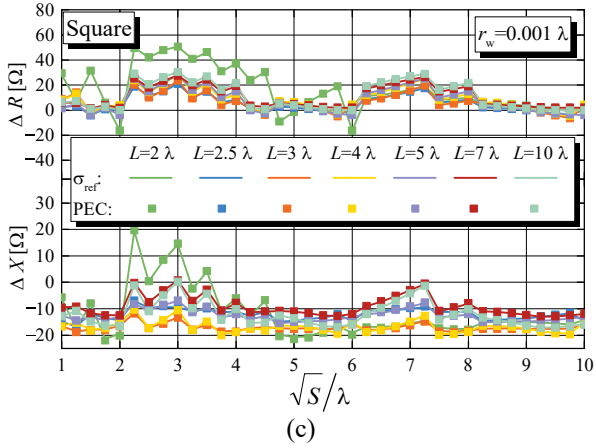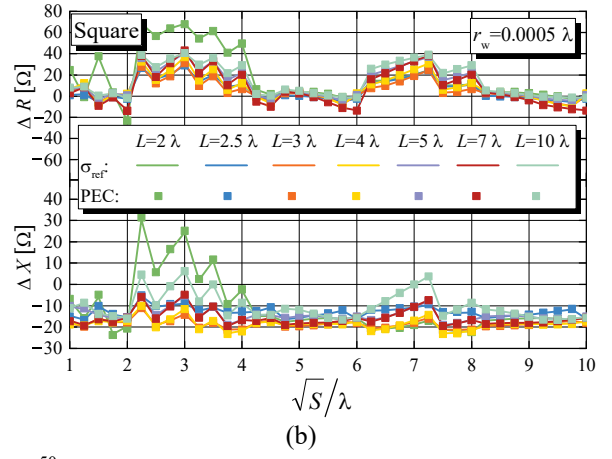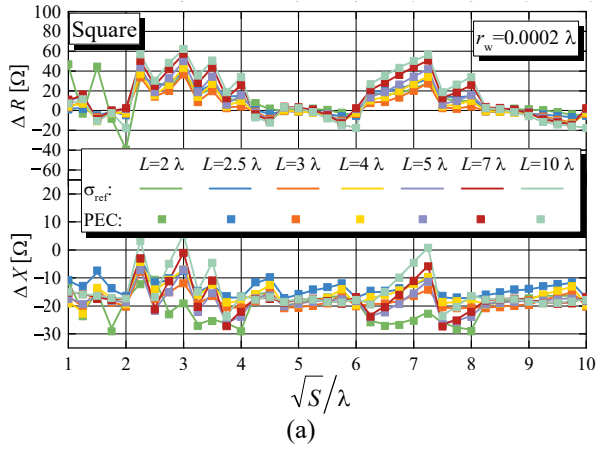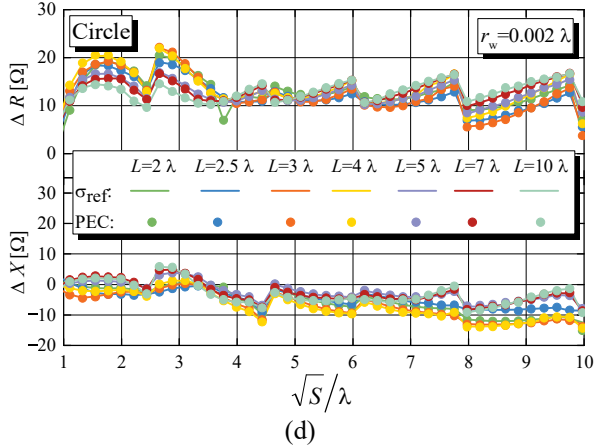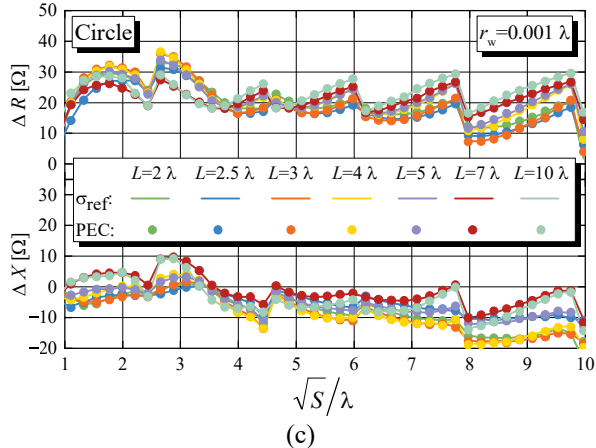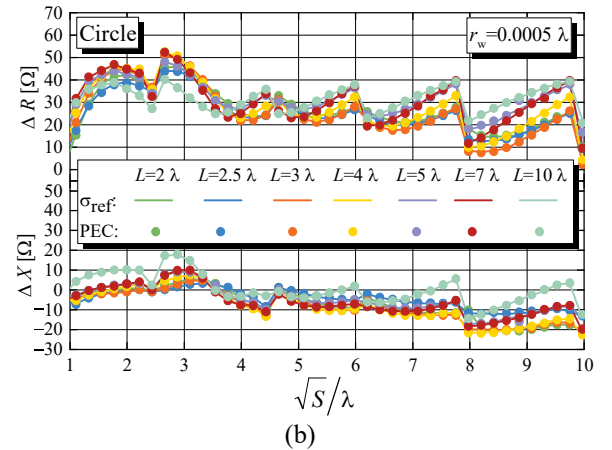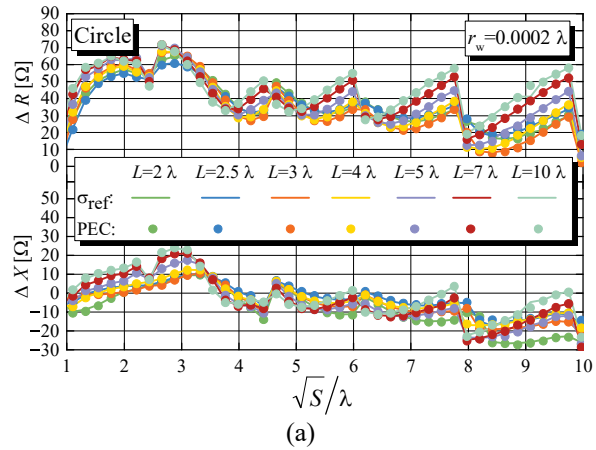
4.4. Comparison of designed nonuniform helical antennas with other helical antennas

In this subsection the designed nonuniform helical antennas are compared with the uniform helical antennas and other types of nonuniform helical antennas (designed within this work), and with different types of helical antennas presented in the literature.

4.4.1. Comparison of designed nonuniform helical antennas with the optimal uniform helical antennas

The basic helical antennas are the uniform helical antennas, where the turn radius and the pitch angle are constant along the antenna axis. Hence, the uniform helical antennas can be observed as the special case of the nonuniform helical antennas with linearly varying geometrical parameters when $r_1 = r_2$ and $\varphi_1 = \varphi_2$ in (2.1) and (2.2), respectively. For the sake of comparison, using the same combination of the optimization algorithms as for the optimization of the nonuniform helical antennas (defined in Subsection 3.1), the optimization of the uniform helical antennas is performed for various axial lengths and wire radii within the ranges considered in the case of nonuniform antennas. The gain of these antennas is compared in Fig. 4.20 with the gain of the corresponding nonuniform helical antennas, designed using the presented design equations (3.13), (3.14), (3.19), and (3.20). The presented design of nonuniform antennas is valid for the normalized conductivities higher than the minimal normalized conductivity, $\sigma_{min} \lambda$, defined for each axial antenna length and wire radius by (3.8). These minimal normalized conductivities are indicated by diamond markers in Fig. 4.20. For the normalized conductivities higher than the minimal normalized conductivity, the designed nonuniform helical antennas achieve higher gain than the optimal uniform helical antennas. However, note that even for the normalized conductivities lower than $\sigma_{min} \lambda$ the designed nonuniform helical antennas still achieve higher gain than the optimal uniform antennas, although this advantage reduces with increasing losses.

From the practical point of view, as long as the gain of the designed nonuniform antennas is more than 0.5 dB higher than the maximal gain achieved with the optimal uniform antennas of the same axial length and wire radius (red dashed line in Fig. 4.20), the designed nonuniform antennas can be considered as the preferable choice. However, for lower normalized conductivities it is suggested to use the uniform helical antennas due to their easier design (fewer degrees of freedom) and fabrication (since the turn radius is constant along the antenna; hence, the supporting structure for the antenna conductor can be constructed easier than in the case of nonuniform turn radius). For each axial antenna length and wire radius, the normalized conductivity that defines the proposed border can be calculated from

$$\sigma_b \lambda = \left(10^{-1.62 \log_{10}\left(\frac{r_w}{\lambda}\right) - 3.89} \right) \log_{10}\left(\frac{L}{\lambda}\right) + 1.08 \log_{10}\left(\frac{r_w}{\lambda}\right) + 2.82 , \tag{4.3}$$

where σ_b is in MS/m, and λ, L, and r_w are in m. The coefficients in (4.3) are obtained by fitting the normalized border conductivities indicated in Fig. 4.20 by cross markers.
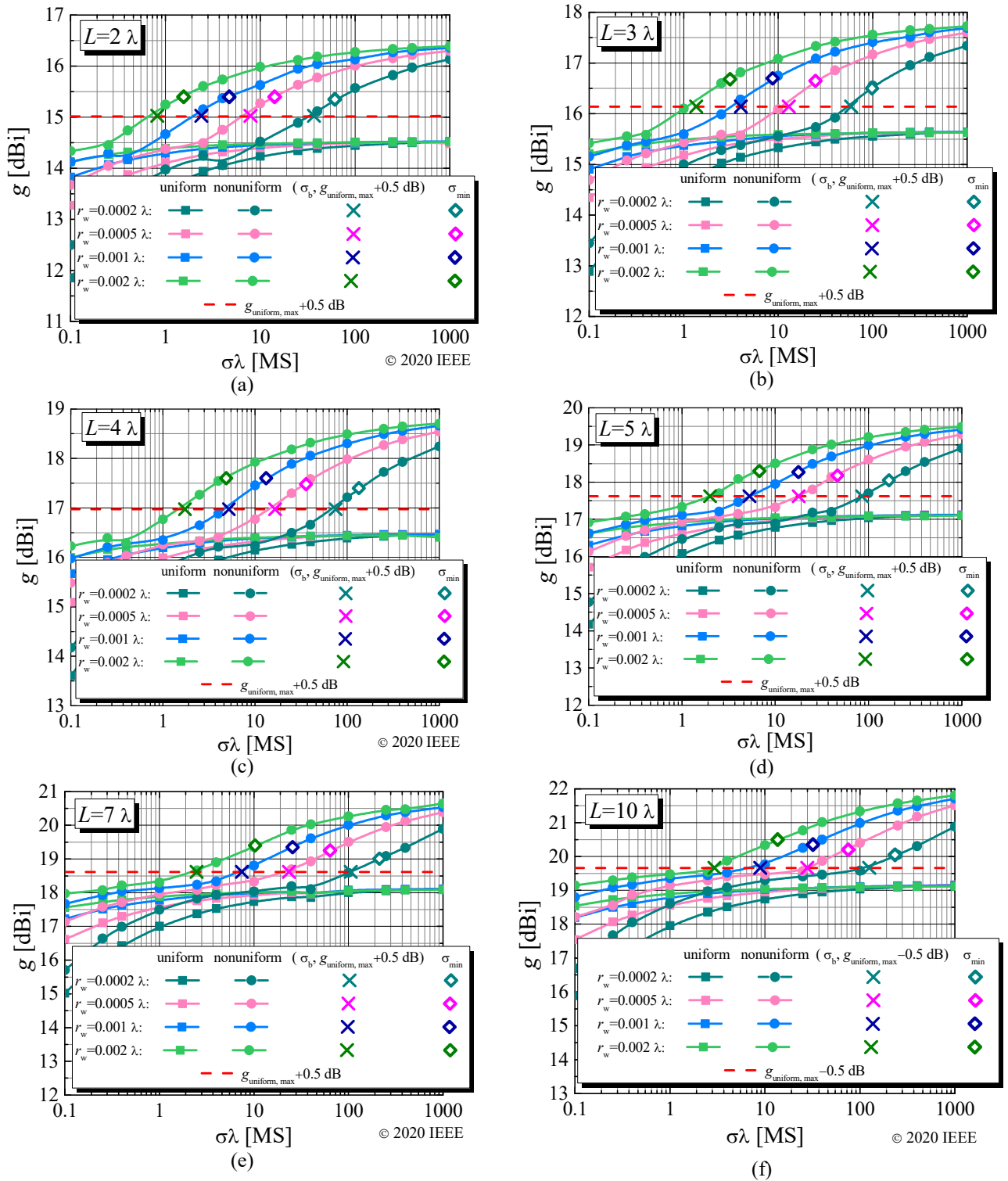
Figure 4.20. Compared gain of the designed nonuniform and the optimal uniform helical antennas, (a) $L=2 \lambda$ [120], (b) $L=3 \lambda$, (c) $L=4 \lambda$ [120], (d) $L=5 \lambda$, (e) $L=7 \lambda$ [120], and (f) $L=10 \lambda$ [120]. Diamond markers indicate the minimal normalized conductivities for which the design of the nonuniform helical antennas is valid ($\sigma_{min}\lambda$ from (3.8)). Cross markers indicate normalized border conductivities ($\sigma_b\lambda$). Red dashed lines indicate gains for 0.5 dB higher than the maximal gains of the uniform helical antennas for the corresponding axial length and wire radius.

Further, the gain of the optimal uniform helical antennas (optimized at the corresponding normalized conductivity) is compared with the gain of the uniform antennas whose design is the optimal one for the normalized border conductivity. This comparison is made in the range of the normalized conductivities from 0.1 MS to 1000 MS in Fig. 4.21. It can be noticed that the optimal uniform antennas for the normalized border conductivity achieve almost the same gain as the optimal uniform antennas. This conclusion allows us to define the optimal design for the normalized border conductivity as the optimal design of the uniform helical antennas valid in the

range of the normalized conductivities where the uniform helical antennas are the preferable choice (from 0.1 MS to $\sigma_b\lambda$). Hence, the optimal geometrical parameters of the uniform helical antennas (turn radius and pitch angle) do not depend on the wire conductivity (same as the optimal geometrical parameters of the nonuniform helical antennas).
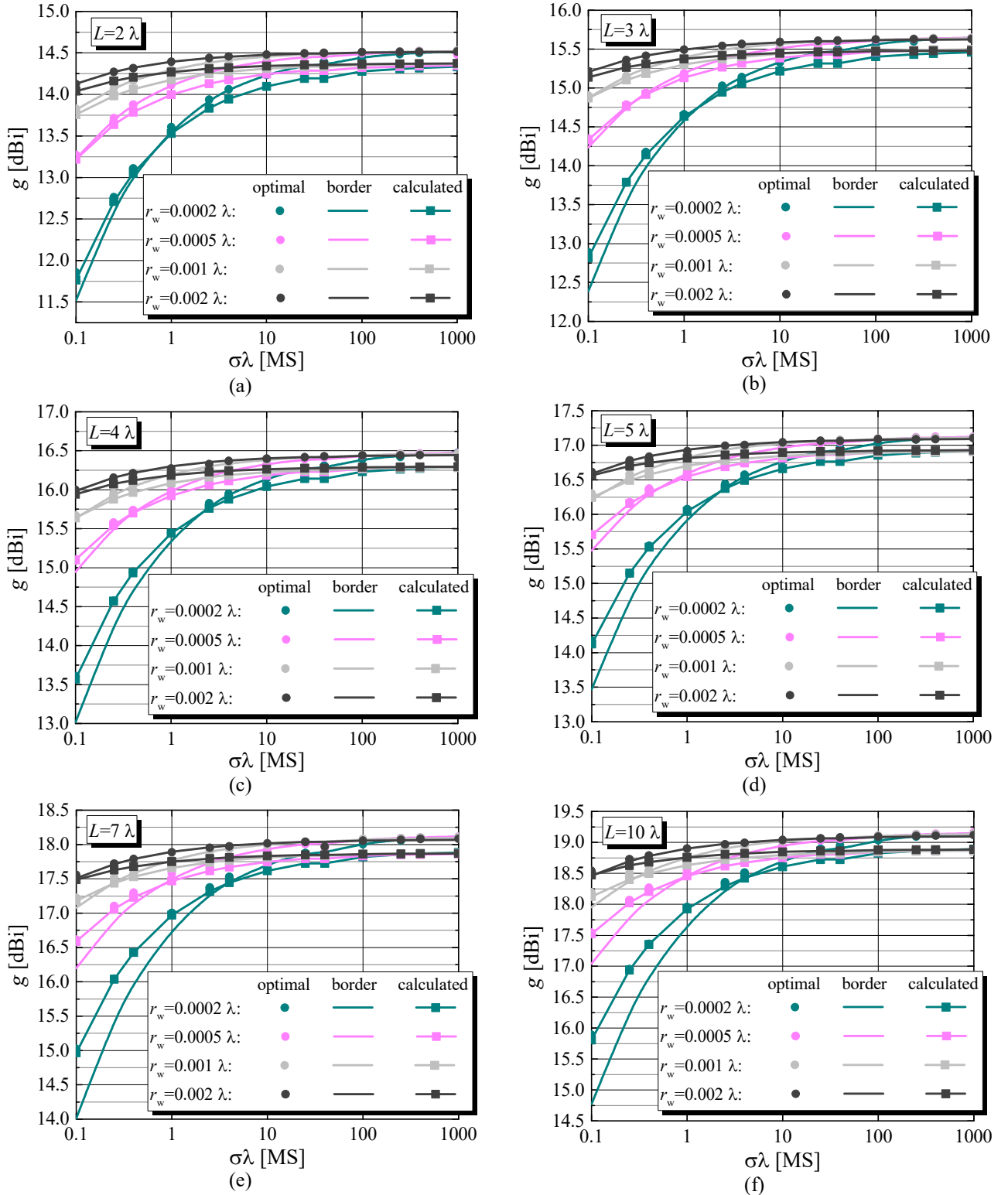
Figure 4.21. Compared gain of the optimal uniform helical antennas ("optimal"), the optimal uniform helical antennas for the normalized border conductivity ("border"), and the antennas whose geometrical parameters are calculated from (4.4) and (4.5) ("calculated") for (a) $L=2\,\lambda$, (b) $L=3\,\lambda$, (c) $L=4\,\lambda$, (d) $L=5\,\lambda$, (e) $L=7\,\lambda$, and (f) $L=10\,\lambda$.

The geometrical parameters of the optimal uniform helical antennas for the normalized conductivity $\sigma_b\lambda$ are shown in Fig. 4.22 (by circular markers). Following a similar procedure as

described for the fitting of the geometrical parameters of the nonuniform helical antennas (Subsection 3.2.3), the geometrical parameters of the optimal uniform helical antennas can be approximated by

$$\frac{r}{\lambda} = 10^{-3}\left(\left(-3.22\log_{10}\left(\frac{r_w}{\lambda}\right) - 28.1\right)\log_{10}\left(\frac{L}{\lambda}\right) + \left(0.0687\log_{10}\left(\frac{r_w}{\lambda}\right) + 154\right)\right), \quad (4.4)$$

$$\varphi[°] = \left(0.620\log_{10}\left(\frac{r_w}{\lambda}\right) + 4.77\right)\log_{10}\left(\frac{L}{\lambda}\right) + \left(0.499\log_{10}\left(\frac{r_w}{\lambda}\right) + 5.55\right). \quad (4.5)$$

The coefficients in (4.4) and (4.5) are found so that the discrepancy between the gain of the antennas whose geometrical parameters are calculated (from (4.4) and (4.5)) and the gain of the optimal uniform helical antennas is maintained as low as possible, instead of simply fitting the optimal geometrical parameters. Therefore, the discrepancies between the optimal (circular markers) and fitted (solid lines) turn radii and pitch angles are noticeable in Fig. 4.22.

Note that the optimal radius of a turn of the uniform helical antennas is larger than the average turn radius (the arithmetic mean of the turn radius of the first and the last turn) of the optimal nonuniform helical antennas. The optimal pitch angle of the uniform helical antennas increases with the increase of axial antenna length. The same behavior shows the optimal pitch angle of the last turn of the nonuniform helical antennas, whereas the optimal pitch angle of the first turn decreases with the increase of the axial antenna length.

Further, in Fig 4.21 the gain of the uniform helical antennas whose geometrical parameters are calculated from (4.4) and (4.5) is compared with the gain of the optimal antennas and the optimal antennas for the normalized border conductivity. The maximal discrepancy between the gain of the optimal uniform antennas and the gain of the antennas whose geometrical parameters are calculated is less than 0.3 dB, for the considered axial antenna lengths and wire radii.
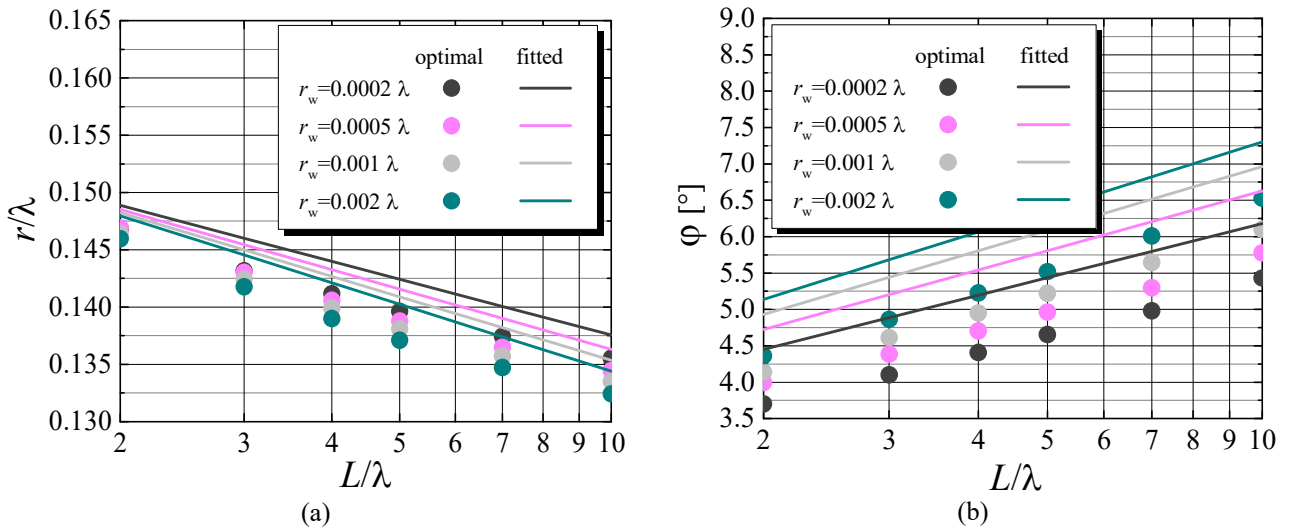
Figure 4.22. Optimal geometrical parameters of the uniform helical antennas for the normalized conductivity $\sigma_b\lambda$ and calculated geometrical parameters from (4.4) and (4.5): (a) normalized turn radius and (b) pitch angle.

4.4.1.1. Comparison of the optimal uniform helical antennas and uniform helical antennas from the literature

In Subsection 4.4.1 the results of the optimization of the uniform helical antennas are presented, the designed nonuniform helical antennas are compared with the optimal uniform helical antennas and the geometrical parameters of the optimal uniform helical antennas are approximated by (4.4) and (4.5). Here, we want to compare the optimal uniform helical antennas (obtained utilizing the same optimization procedure as described in the previous subsection) with other uniform helical

antennas presented in the literature and to point out and clarify some misunderstandings and discrepancies.

The results of the detailed and comprehensive investigation of the uniform helical antennas are presented in [49]. As it is shown there, the narrow-band (NB) design achieves the highest gain compared to the other designs presented in the literature, except the gain calculated using the equation from [2], which is considered to overestimate the gain. For these reasons, we believe that the most important comparison of the optimal uniform antennas (designed here) is with the NB design from [49]. In [49] the considered conductors are lossy, and the conductor losses are as for the copper at 300 MHz. However, it is stated that the effect of losses is negligible even for the thinnest considered wire. (Losses in the thinnest wire reduce the gain by 0.1–0.2 dB.) In order to check this conclusion, we performed the optimization of the antenna geometry for various axial antenna lengths, wire radii (considered in [49]), and normalized wire conductivities ($\sigma\lambda$) from 0.1 MS to 1000 MS. We consider the same axial antenna lengths and wire radii as in [49], summarized in Table 4.1. The gains of the optimal uniform antennas are shown by circular markers in Fig. 4.23. Further, the gains of the antennas whose geometrical parameters are presented as the optimal ones in [49] are shown in Fig. 4.23 by solid lines. In [49] the expected gains of the designed antennas are specified, for axial antenna lengths between λ and 7λ. Hence, we also indicated these values in Fig. 4.23 by pink solid lines.

Table 4.1.
Considered axial antenna lengths and corresponding wire radii [49].

L/λ	r_{w1}/λ	r_{w2}/λ	r_{w3}/λ
0.7175	0.00015375	0.0015375	0.015375
1.0175	0.00015255	0.0015255	0.015255
1.98	0.00014850	0.0014850	0.014850
4.5	0.00013500	0.0013500	0.013500
8.5	0.00012750	0.0012750	0.012750
16.6	0.00012450	0.0012450	0.012450

Results in Fig. 4.23 definitely show that the gain of the uniform helical antennas does depend on the conductor losses, especially for the thinnest wire, when, for the normalized conductivities lower than 58 MS (copper at 300 MHz), the gain can be decreased for a few decibels due to the increase in losses. Further, antennas whose geometrical parameters are obtained from our optimization achieve slightly higher gain in almost all cases, especially for the longest antenna and the thickest wire, where this discrepancy is almost 1 dB. For the medium-length antennas, this discrepancy is around 0.5 dB, whereas for the shortest antennas this discrepancy becomes negligible. However, the gain of the optimal uniform antennas predicted in [49] is overestimated in most cases, especially for the lower normalized conductivities.
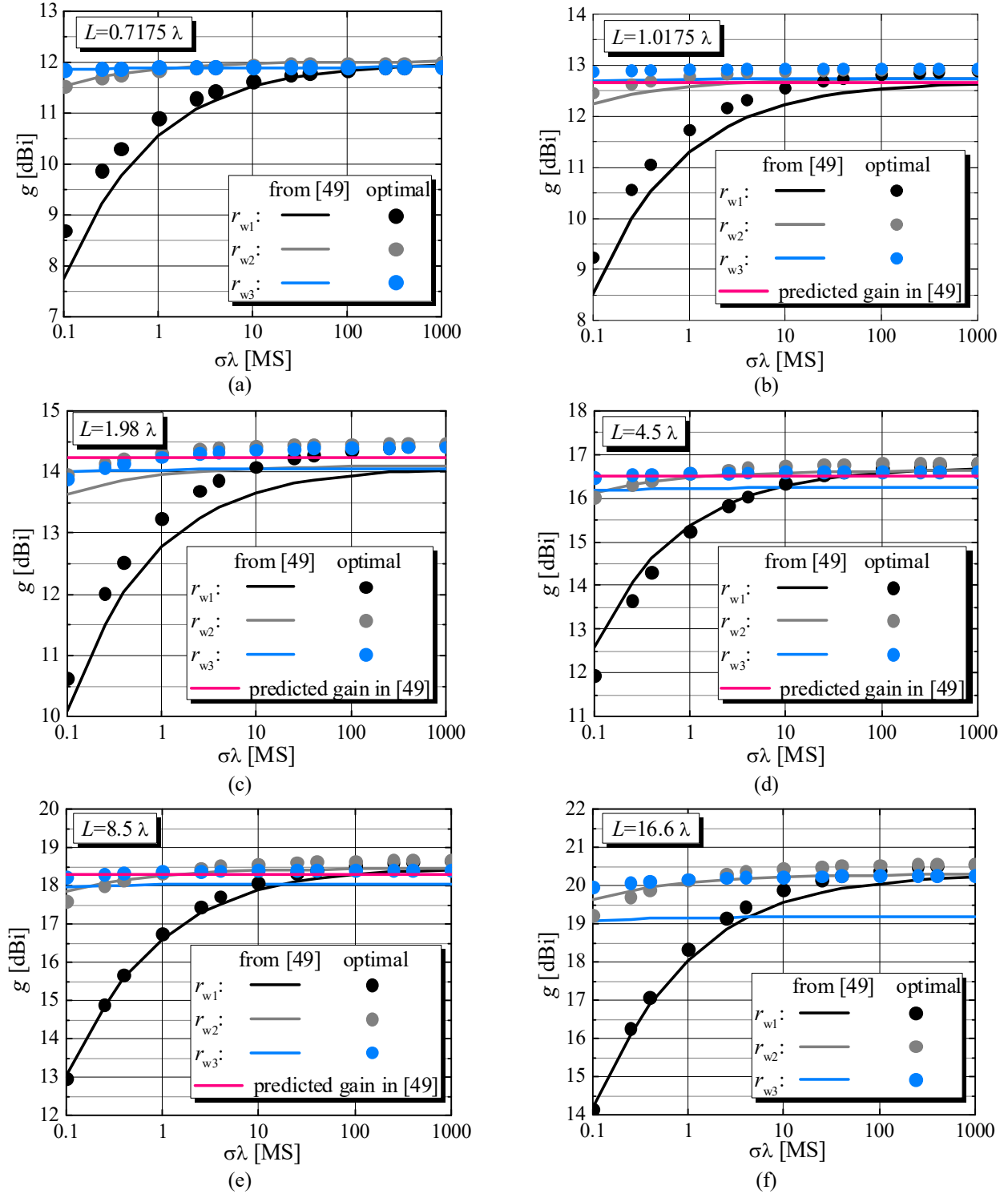
Figure 4.23. Gain of uniform antennas of the geometrical parameters from [49] and the optimal uniform antennas for axial lengths (a) L=0.7175 λ, (b) L=1.017 λ, (c) L=1.98 λ, (d) L=4.5 λ, (e) L=8.5 λ, and (f) L=16.6 λ.

4.4.2. Comparison of designed nonuniform helical antennas and uniform helical antennas from the literature

In this subsection we present comparison of the characteristics of the nonuniform helical antennas designed using design equations with the narrow-band (NB) design for uniform helical antennas from [49] (the compared characteristics are gain, bandwidths, and axial ratio). These comparisons are made for the antennas at the operating frequency 300 MHz, wire radius is r_w=0.0015 λ, whereas two different wire conductivities (σ_{ref} and 1000 MS/m) are considered. The results of the comparison are presented in Tables 4.2–4.4. When the losses are low, the nonuniform helical

antennas achieve about 2 dB higher gain than the NB design. The gain of nonuniform antennas is more affected by the increase of losses than the gain of the NB design. However, even for higher losses, nonuniform antennas still achieve a higher gain than NB antennas. The bandwidths of uniform antennas are wider for shorter antennas, whereas for longer antennas the situation is reversed. For all considered cases, the axial ratio of nonuniform helical antennas is better than of NB antennas.

Table 4.2.
Comparison of the uniform antennas from [49] and the designed nonuniform helical antennas for $L=2\lambda$ [113].

		$L=2\lambda$				
		g [dBi]	BW_1 [%]	BW_2 [%]	BW_3 [%]	ar [dB]
NB from [49]	σ_{ref}	14.12	20.61	28.46	30.23	1.71
	1000 MS/m	14.18	21.45	29.42	31.73	1.72
designed nonuniform helical antennas	σ_{ref}	15.71	16.61	21.73	26.18	0.53
	1000 MS/m	16.26	15.5	21.98	26.74	0.54

Table 4.3.
Comparison of the uniform antennas from [49] and the designed nonuniform helical antennas for $L=4.5\lambda$ [113].

		$L=4.5\lambda$				
		g [dBi]	BW_1 [%]	BW_2 [%]	BW_3 [%]	ar [dB]
NB from [49]	σ_{ref}	16.61	14.33	17.95	22.22	1.26
	1000 MS/m	16.63	14.67	18.73	25.27	1.26
designed nonuniform helical antennas	σ_{ref}	18.38	20.47	26.10	30.40	0.13
	1000 MS/m	18.84	20.30	25.90	30.86	0.13

Table 4.4.
Comparison of the uniform antennas from [49] and the designed nonuniform helical antennas for $L=8.6\lambda$ [113].

		$L=8.6\lambda$				
		g [dBi]	BW_1 [%]	BW_2 [%]	BW_3 [%]	ar [dB]
NB from [49]	σ_{ref}	18.48	11.31	13.46	15.04	1.19
	1000 MS/m	18.49	11.35	13.55	15.18	1.19
designed nonuniform helical antennas	σ_{ref}	20.71	23.02	28.05	31.74	0.51
	1000 MS/m	21.09	22.68	27.99	31.85	0.50

4.4.3. Comparison of designed nonuniform helical antennas with other types of helical antennas from the literature

The designed nonuniform helical antennas are compared here with other (different) types of helical antennas presented in the literature.

Different types of tapered helical antennas are investigated in [78] (including the uniform helix). Since in [78] the radius and the conductivity of the considered conductor are not indicated, for our design (which is used for comparison) we adopt r_w=0.002 λ and σ=58 MS/m. Further, we utilize an infinite perfectly conducting ground plane, instead of a cavity used in [78]. Note that the influence of cavity is investigated in [51], where it is shown that the cavity can increase the gain for about 1.5 dB compared to the gain with the infinite ground plane.

The results are presented in Table 4.5. For all considered cases, the nonuniform antennas, designed using design equations achieve more than 2 dB higher gain than the antennas presented in [78]. However, the target in [78] is to use the nonuniform helical antennas in order to broaden the bandwidth in comparison with the uniform helical antennas. Hence, the nonuniform helical antennas from [78] (continuously tapered and quasi-tapered) have wider bandwidth than the nonuniform antennas designed using the design equations, although the gain of our design is significantly higher. Finally, all considered antennas have comparable axial ratios.

Table 4.5.
Comparison of the antennas from [78] and the designed nonuniform helical antennas [113].

	g [dBi]		BW_2 [%]		ar [dB]	
	[78]	designed nonuniform helical antennas	[78]	designed nonuniform helical antennas	[78]	designed nonuniform helical antennas
Uniform 4.46 λ at 900 MHz	16.2	18.4	23	27.5	1	0.3
Tapered-end 4.46 λ at 900 MHz	15.7	18.4	23.8	27.5	0.2	0.3
Continuously tapered 4.8 λ at 1000 MHz	15.8	18.5	31.2	27.3	0.5	1.1
Quasi-tapered 3.84 λ at 800 MHz	14.8	17.8	43.1	24.4	0.5	1.4

A very compact design of nonuniform helical antennas with a wire pigtail counterbalance is reported in [82]. We compare our design with the design presented in [82] in Table 4.6. The comparison is made for the axial lengths and wire radii for which our design is applicable. For our design, the wire conductivity is 58 MS/m and antennas are located above an infinite perfectly conducting ground plane.

Although our design achieves significantly higher gain, the antennas designed in [82] do not require a ground plane (a small ground plane is only used to enable easier practical realization of the antenna feeding). Hence, these antennas are very handy and can be the preferable choice for some applications.

Table 4.6.
Comparison of the antennas from [82] and the designed nonuniform helical antennas [113].

L/λ	g [dBi] r_w=0.001 λ	
	[82]	designed nonuniform helical antennas
2.0	14.03	16.04
2.5	14.68	16.65
3.0	15.55	17.16
3.5	16.10	17.71
4.0	16.44	18.09
4.5	16.83	18.39
5	17.26	18.76

In [83] and [84] helical antennas with a pitch profile modeled using Catmull-Rom spline are optimized using PSO. In [83] the turn radius is constant, whereas in [84] an exponential variation of the turn radius is utilized. Moreover, these designs are compared (in terms of gain) with the classical design suggested by Kraus. In Table 4.7, the designs presented in [83] and [84] and the

classical Kraus's design are compared with the nonuniform helical antennas designed using the design equations from the work presented in this thesis. The axial antenna lengths of the analyzed Kraus's designs are calculated based on the known number of turns. In our design of nonuniform helical antennas, the corresponding axial lengths are the same as for the Kraus's design, but rounded to the nearest integer multiple of the half-wavelength, as suggested in Subsection 4.2. Rounding is done towards smaller integers to ensure that our design is not favored. In our design of nonuniform helical antennas, infinite ground planes are utilized, the conductor radius is $0.002\,\lambda$, and the conductivity is 58 MS/m.

The results in Table 4.7 show that our nonuniform helical antennas achieve higher gain in all cases except for the design from [84]. However, this discrepancy is small. Moreover, utilizing other conductor properties (radius or conductivity) or a ground plane of an appropriate (finite) dimension, this discrepancy can be reversed.

Table 4.7.
Comparison of the antennas from [83], [84], and Kraus's design with our design of nonuniform helical antennas.

number of turns	g [dBi]				
	[83]	[84]	Kraus's design	designed nonuniform helical antennas	
10	14.6	16.02	11.79	L=2 λ	15.89
15	15.5	✘	13.17	L=3.5 λ	17.39
20	16.6	✘	14.04	L=4.5 λ	18

Exponentially varying spacing between turns is considered in [85], and the comparison with uniform helical antennas is made. In Table 4.8 we compare our design (of wire radius $0.002\,\lambda$) with the designs from [85]. The compared antennas are of the same axial length, wire conductivity, ground plane shape, and dimension. It can be noticed that the gain of the antennas designed using our design equations is more than 4.5 dB higher than the gain of the antennas from [85].

Table 4.8.
Comparison of the antennas from [85] and our design of nonuniform helical antennas [113].

Operating frequency, axial length	Type of design	g [dBi]
f=2.9 GHz, L=2.48 λ	exponential [85]	11.2
	designed nonuniform helical antennas	16.4
f=2.5 GHz, L=2.13 λ	uniform [85]	10.8
	designed nonuniform helical antennas	15.5
f=2.8 GHz, L=3.56 λ	exponential [85]	12.3
	designed nonuniform helical antennas	16.8
f=2.5 GHz, L=3.17 λ	uniform [85]	11.8
	designed nonuniform helical antennas	16.1

4.4.4. Comparison of designed nonuniform helical antennas and helical antennas with exponential and piecewise-linear variation of geometrical parameters

The geometrical parameters of the nonuniform helical antennas with exponential (here referred to as exponential or EG antennas) and piecewise-linear (here referred to as piecewise-linear or PWLG antennas) variation of geometrical parameters are defined in Subsection 2.1.2 by (2.3)–(2.6). The models of these antennas are made following the same procedure as for the nonuniform helical antennas with linearly varying geometrical parameters. (In this subsection we refer to these antennas as linear or LG antennas.) Hence, the perfectly circular turns are approximated by square turns and the antennas are located above an infinite perfectly conducting ground plane. WIPL-D models of EG and PWLG antennas are shown in Fig. 4.24b–c.

Similarly to LG antennas, the geometrical parameters of EG and PWLG antennas are firstly optimized at a single (operating) frequency in order to maximize the partial gain for the circular polarization. Additionally, for the sake of a more detailed comparison, the optimization of the geometrical parameters of LG, EG, and PWLG antennas is also performed in a frequency range.

The optimization of the geometrical parameters of the EG antennas utilizes the same optimization setup as for the LG antennas (defined in Subsection 3.1), i.e., 2000 PSO iterations (swarm size 20), followed by (maximum of) 200 Nelder-Mead simplex iterations launched form the best-found PSO solution. In this case, the optimization variables are r_1, r_2, φ_1, φ_2 (the same variables as defined for LG antennas), with the additional variables C_r and C_φ from (2.3) and (2.4).

Since the geometry of PWLG antennas implies more degrees of freedom (also depending on the considered number of linear segments along the antenna axis), for the optimization of this antenna type, 5000 PSO iterations (swarm size 20) are followed by (maximum of) 200 Nelder-Mead simplex iterations. Within this work we consider only PWLG helical antennas with three linear segments, i.e., $k \in \{1,2,3\}$ in (2.5) and (2.6). Hence, the optimization variables are r_j and φ_j, $j \in \{1,2,3,4\}$, from (2.5) and (2.6). Additionally, the axial lengths of the two lower linear segments are also optimized, whereas the length of the third segment is $L_3 = L - L_1 - L_2$, where L_1, L_2, and L_3 are the axial lengths of the three segments (Fig. 2.2b).

The optimization in a frequency range utilizes the same combinations of the optimization algorithms, but each combination is independently repeated five times in order to increase the possibility to find the best solution. The optimal solution is the best-found solution within those five independent optimizations.

Firstly, the single-frequency optimization is performed at 300 MHz. The considered axial antenna length is $L = 3\lambda$, the wire radius $r_w = 0.002\lambda$, and the wire conductivity $\sigma = 58\,\mathrm{MS/m}$ (copper). The models of the optimal LG, EG, and PWLG antennas are shown in Fig. 4.24a–c. In addition, the LG antenna is designed following the presented design procedure, i.e., the geometrical parameters are calculated from (3.13), (3.14), (3.19), and (3.20). We refer to this antenna as LG (designed), and the model is shown in Fig. 4.24d.

(a)   (b)   (c)   (d)
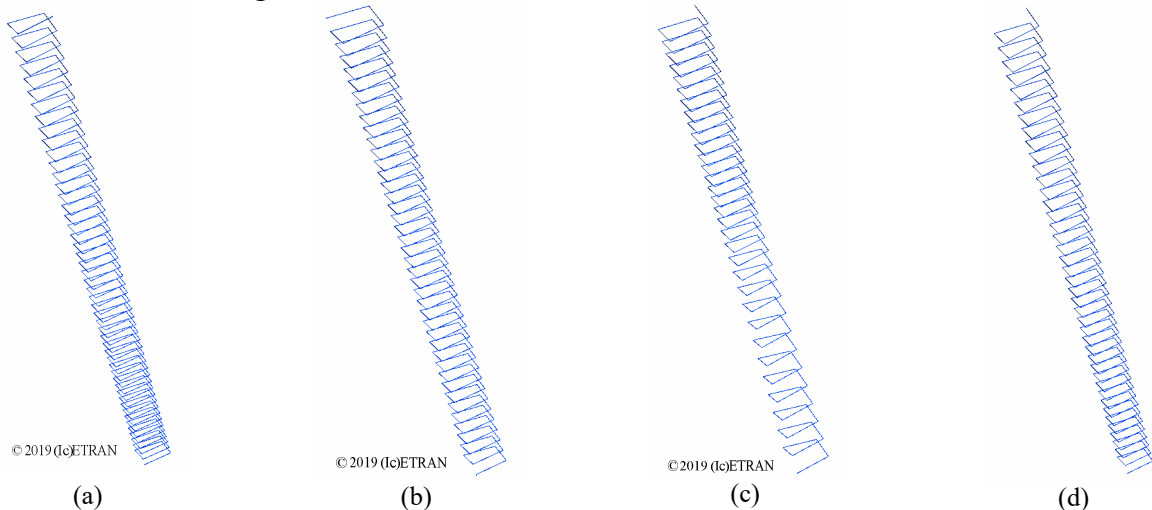
Figure 4.24. WIPL-D models of the optimal (single-frequency optimization): (a) LG [110], (b) EG [110], (c) PWLG [110], and (d) LG antenna designed following the presented design procedure.

Although the optimization is performed at the single frequency (300 MHz), the gain of the helical antennas is compared in a wider frequency range in Fig. 4.25a.

At 300 MHz the PWLG antenna achieves more than 0.5 dB higher gain than LG and EG antennas. However, this advantage is accompanied with a very narrow bandwidth of the PWLG antenna (the gain has a sharp peak around 300 MHz). From the practical point of view, this can be critical, since the manufacturing tolerances can cause the frequency response to shift.

Further, for the practical purposes, the overall length of the conductor is also an important parameter. According to this criterion, the PWLG antenna can be considered as the preferable choice, since it requires the shortest conductor (27.63 λ). The required conductor lengths for the LG, LG (designed), and EG antennas are 39.02 λ, 33.44 λ, and 33.50 λ, respectively. In Fig. 4.24 it can be noticed that the optimal LG antenna has significantly more turns at the lower part compared with the other optimal antennas, which explains the request for the long conductor.

To make a fair comparison, we additionally perform the optimization in a frequency range. The goal is to achieve as high as possible gain, but in a reasonably wide frequency range. During the optimization, we consider the frequency range slightly shifted towards higher frequencies, from 280 MHz to 340 MHz, instead the frequency range symmetrically positioned around the operating frequency. The reason for this is that the discrepancies of the gain in Fig. 4.25a are bigger (up to 3 dB) at the higher frequencies. We consider seven equidistantly spaced frequencies within the defined range. We calculate the (partial) cost function for each frequency (in the same way as for the optimization at a single frequency), whereas the (total) cost function is the arithmetic mean of the (partial) cost functions. For this optimization the same axial antenna length, wire radius, and conductivity are utilized.

The gains of the optimal LG, EG, and PWLG helical antennas are compared in Fig. 4.25b, whereas the models of those antennas are shown in Fig. 4.26. Visually, small differences between the geometries of the antennas shown in Fig. 4.24 and Fig. 4.26 can be noticed. Further, antennas in Fig. 4.26 have more densely spaced turns at the bottom of the antenna than at the top. Finally, the conductor lengths of LG, EG, and PWLG antennas optimized in the frequency range are 34.88 λ, 31.79 λ, and 32.97 λ, respectively.
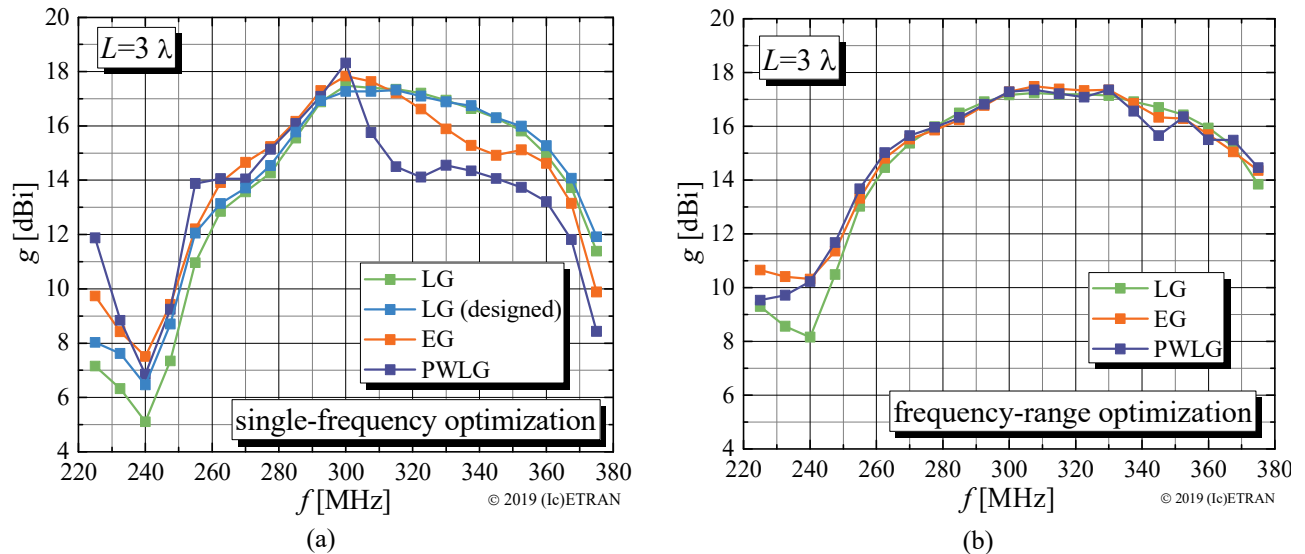
Figure 4.25. Gain of the nonuniform helical antennas: (a) single-frequency optimization (at 300 MHz) [110] and (b) optimization in a frequency range [110].
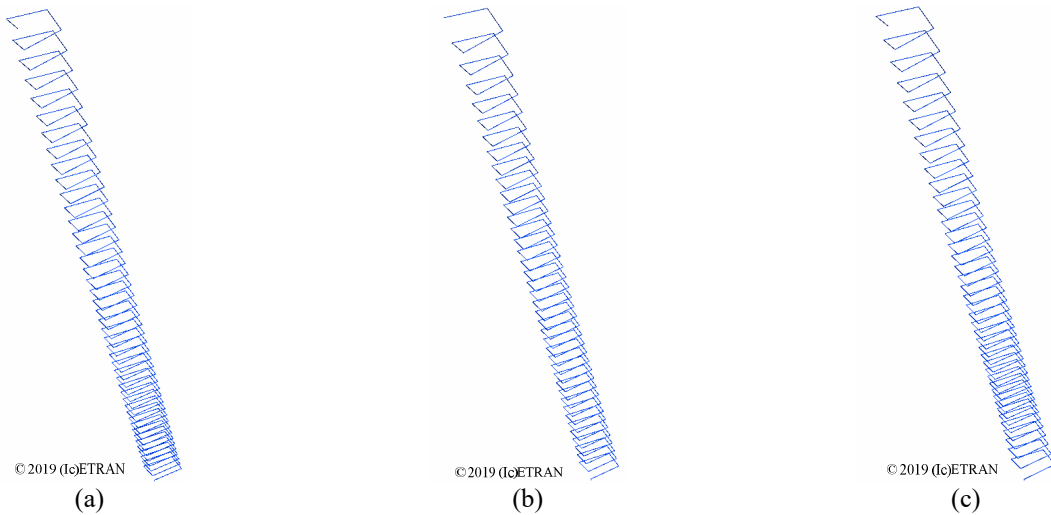
Figure 4.26. WIPL-D models of the optimal (optimization in a frequency range): (a) LG [110], (b) EG [110], and (c) PWLG antennas [110].

Obviously, the optimization in the frequency range leads to the solutions with a wider bandwidth, but this is accompanied with the decrease in the gain at the operating frequency. In the frequency range from 260 MHz to 330 MHz, the antennas of all geometries achieve almost the same gain (the gain differs for less than 0.5 dB within this frequency range). Fig 4.27 compares the gain of the antennas optimized at the single frequency (300 MHz) and in the frequency range. In case of the LG antenna, the optimization in the frequency range results in a small decrease in the gain (for 0.3 dB), but the bandwidth is slightly wider and the required conductor is shorter. The EG antenna optimized in the frequency range achieves around 0.5 dB smaller gain at 300 MHz than the EG antenna optimized in the single frequency. However, the conductor is slightly shorter and the bandwidth is wider. At 300 MHz, the PWLG antenna optimized at the single frequency achieves around 1 dB higher gain than the antenna optimized in the frequency range. Although the PWLG antenna optimized in the frequency range obtains significantly larger bandwidth, the required conductor is for about 20 % longer. Hence, the main advantages of the PWLG antennas optimized at the single frequency (high gain at the operating frequency and short conductor) are not present in case of PWLG antennas optimized in the frequency range.

Therefore, the optimizations for various axial lengths are performed only for LG and EG antennas, since their geometry is simpler. Hence, the optimization requires fewer parameters, which allows us to utilize less iteration.
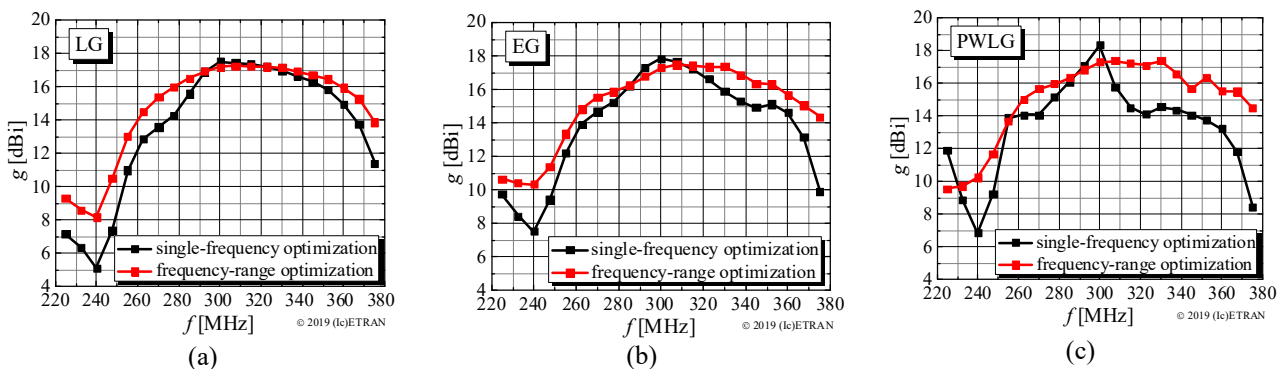
Figure 4.27. Gain of the optimal (a) LG [110], (b) EG [110], and (c) PWLG antenna optimized at a single frequency and in a frequency range [110].

Finally, the optimization of the LG and EG antennas of various axial lengths is performed in the frequency range. The gain of these antennas is compared in Fig. 4.28, whereas the gain at the operating frequency and the required conductor lengths are listed in Table 4.9. The gain of the EG antennas at 300 MHz is slightly higher, especially for longer antennas. Also, for shorter antennas ($L \leq 3\lambda$) the EG antennas require shorter conductors than the LG antennas. However, for longer antennas the situation is reversed.

Finally, it can be concluded that from the practical point of view, EG and LG antennas are very similar with respect to the gain, bandwidth, and even the required conductor length. Hence, EG antennas do not introduce any important advantages over LG antennas.
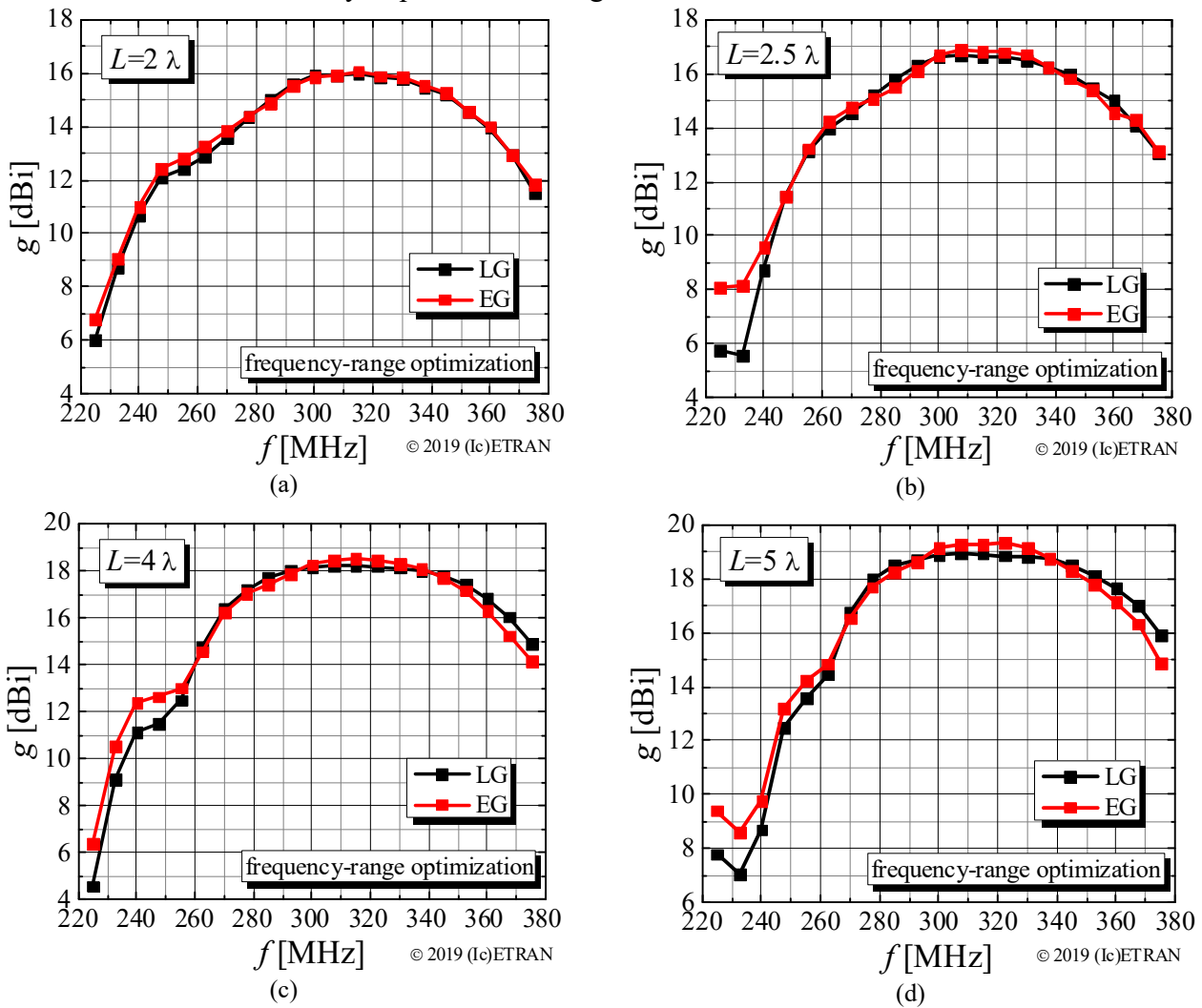
Figure 4.28. Gain of the optimal helical antennas optimized in a frequency range: (a) L=2 λ [110], (b) L=2.5 λ [110], (c) L=4 λ [110], and (d) L=5 λ [110].

Table 4.9.
Conductor lengths and maximal gain of the optimal helical antennas [110].

L	LG antennas		EG antennas	
	conductor length	g [dBi]	conductor length	g [dBi]
2 λ	26.7 λ	16.0	26.7 λ	16.1
2.5 λ	31.8 λ	16.7	31.2 λ	16.9
3 λ	34.9 λ	17.2	31.8 λ	17.5
4 λ	44.0 λ	18.2	45.8 λ	18.5
5 λ	53.2 λ	19.0	54.9 λ	19.3

5. Design procedure and experimental verification

In this chapter we formulate an algorithm (set of the steps) for the design of the optimal nonuniform helical antennas with linearly varying geometrical parameters based on the design equations formulated in Chapter 3. In order to make the design procedure usable for practical purposes, a ground plane of finite dimensions should be chosen following the conclusions from Chapter 4.

We also present a worked-out example, based on which a nonuniform helical antenna was manufactured and tested.

5.1. Design procedure

The targeted antenna gain (at the desired operating frequency) and wire properties (wire radius and conductivity) are assumed to be known. This is justified from the practical point of view, since in most cases a specific material (wire) is available and the targeted gain is defined by the application.

Thereafter the design procedure consists of the steps summarized in Fig. 5.1. The required normalized axial antenna length can be calculated from (3.23). Theoretically, this step requires an inversion of (3.23). Also, according to Subsection 4.2, (3.23) predicts well the gain of antennas whose axial length is an integer multiple of the half-wavelength. Hence, the normalized axial antenna length calculated by the inversion of (3.23) should first be rounded to the nearest greater or equal integer multiple of the half-wavelength and then denormalized by multiplication by λ. Hence, in practical applications, instead of the inversion, the minimal axial antenna length that meets the requested gain can be found by a systematic check of the suggested (discrete) axial antenna lengths, using (3.23). When the required axial antenna length is calculated, (3.8) should be used to check if this design is valid for the available wire conductor and desired axial antenna length. If the normalized conductivity of the wire conductor is higher than $\sigma_{min}\lambda$ (calculated from (3.8)), the design parameters can be calculated from (3.13), (3.14), (3.19), and (3.20), which concludes the design.
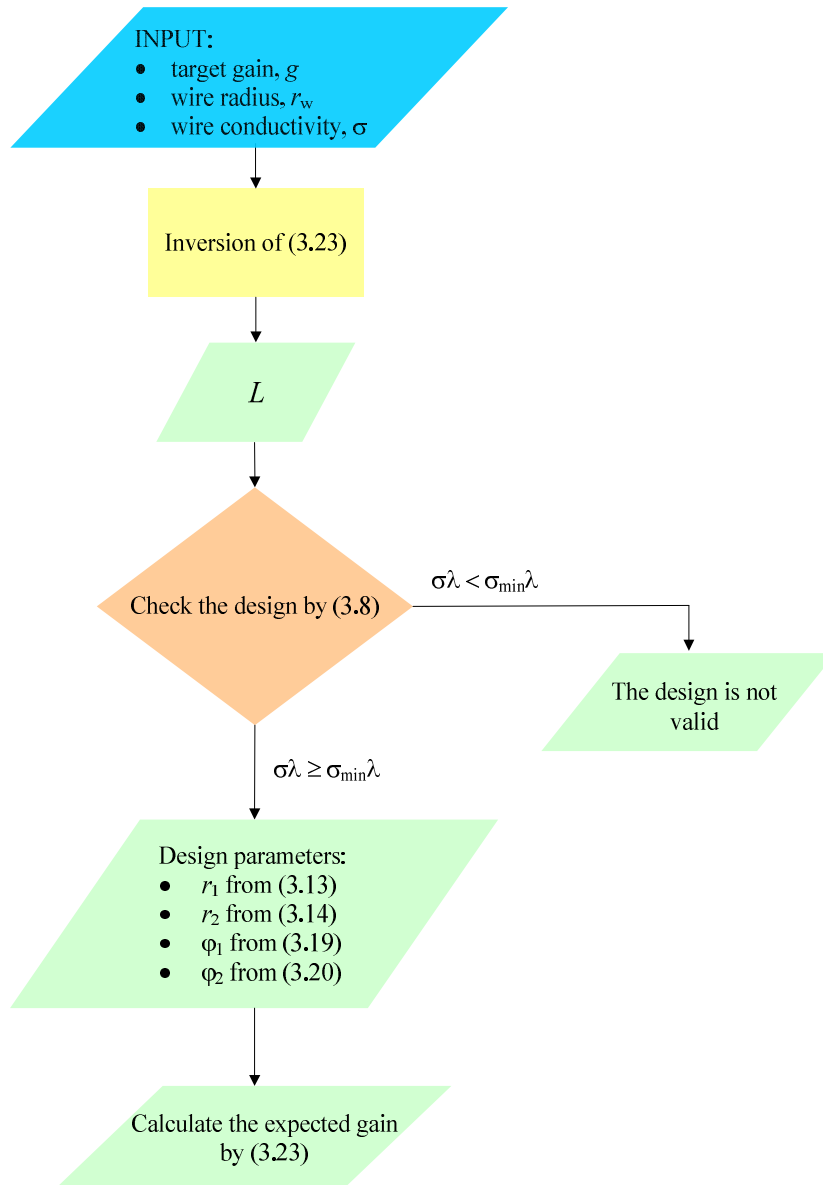
Figure 5.1. Flowchart of the design procedure.

In Table 5.1 the values of σ_{min} for different wire radii and axial antenna lengths at various frequencies are listed and practical feasibility of the design is indicated by the green color and the infeasible designs are denoted in red color. Namely, the green color indicates that, for the observed frequency, wire radius, and axial antenna length, σ_{min} is lower than 100 MS/m (which is indicated as the upper limit for the conductivity defined in Subsection 3.2.2), whereas if the required σ_{min} is greater than 100 MS/m, that cell is colored red. From these results it can be noticed that below around 130 MHz, for all considered axial antenna lengths and wire radii, the corresponding σ_{min} is lower than 100 MS/m. However, above 130 MHz, firstly for the thinnest wires and the longest antennas, the required values of σ_{min} become larger than 100 MS/m. As the operating frequency increases, more cells becomes red (the corresponding σ_{min} is larger than 100 MS/m). Finally, at 6 GHz (which is the highest considered frequency, defined in Subsection 3.2.2), for the wire radius 0.001 λ only the shortest axial antenna length fulfills the limit for σ_{min}.

Further, if it is necessary for a cross-check, the expected gain of the designed antenna can be calculated from (3.23).

It is important to mention that the same design procedure and equations hold for both right-hand and left-hand wound helices.

Also note that if $\sigma_{min}\lambda$ is too high, the geometrical parameters of the optimal antenna calculated from the design equations can be used as a good starting point for further numerical optimization performed by the designer.

Table 5.1.
Values of σ_{min}, in MS/m, at different operating frequencies and for various antenna lengths and wire radii.

		$L = 2\lambda$	$L = 2.5\lambda$	$L = 3\lambda$	$L = 4\lambda$	$L = 5\lambda$	$L = 7\lambda$	$L = 10\lambda$
$f = 30$ MHz	$r_w = 0.0002\lambda$	6.12	8.00	9.87	13.41	16.56	21.27	23.37
	$r_w = 0.0005\lambda$	1.42	1.95	2.49	3.59	4.64	6.38	7.54
	$r_w = 0.001\lambda$	0.47	0.67	0.88	1.33	1.77	2.57	3.21
	$r_w = 0.002\lambda$	0.16	0.23	0.32	0.49	0.68	1.04	1.37
$f = 100$ MHz	$r_w = 0.0002\lambda$	20.39	26.67	32.88	44.68	55.19	70.88	77.88
	$r_w = 0.0005\lambda$	4.73	6.48	8.29	11.95	15.45	21.26	25.13
	$r_w = 0.001\lambda$	1.57	2.22	2.93	4.41	5.90	8.55	10.68
	$r_w = 0.002\lambda$	0.52	0.77	1.03	1.63	2.25	3.44	4.54
$f = 130$ MHz	$r_w = 0.0002\lambda$	26.51	34.67	42.74	58.08	71.74	91.43	101.24
	$r_w = 0.0005\lambda$	6.15	8.42	10.78	15.53	20.08	27.63	32.67
	$r_w = 0.001\lambda$	2.04	2.89	3.80	5.73	7.67	11.11	13.88
	$r_w = 0.002\lambda$	0.68	0.99	1.34	2.11	2.93	4.47	5.90
$f = 300$ MHz	$r_w = 0.0002\lambda$	61.17	80.00	98.62	134.02	165.55	212.63	233.63
	$r_w = 0.0005\lambda$	14.19	19.43	24.86	35.83	46.34	63.76	75.38
	$r_w = 0.001\lambda$	4.70	6.66	8.77	13.21	17.69	25.64	32.04
	$r_w = 0.002\lambda$	1.56	2.29	3.09	4.87	6.75	10.31	13.62
$f = 1$ GHz	$r_w = 0.0002\lambda$	203.90	266.64	328.72	446.72	551.82	708.74	778.75
	$r_w = 0.0005\lambda$	47.29	64.74	82.85	119.44	154.44	212.53	251.25
	$r_w = 0.001\lambda$	15.66	22.19	29.21	44.03	58.94	85.46	106.77
	$r_w = 0.002\lambda$	5.19	7.61	10.30	16.24	22.50	34.36	45.38
$f = 3$ GHz	$r_w = 0.0002\lambda$	611.68	799.92	986.14	1340.16	1655.46	2126.21	2336.23
	$r_w = 0.0005\lambda$	141.87	194.21	248.55	358.30	463.32	637.59	753.74
	$r_w = 0.001\lambda$	46.97	66.56	87.63	132.09	176.82	256.37	320.31
	$r_w = 0.002\lambda$	15.55	22.82	30.90	48.70	67.48	103.08	136.12
$f = 6$ GHz	$r_w = 0.0002\lambda$	1223.36	1599.83	1972.28	2680.32	3310.91	4252.42	4672.46
	$r_w = 0.0005\lambda$	283.73	388.42	497.09	716.60	926.64	1275.18	1507.47
	$r_w = 0.001\lambda$	93.93	133.12	175.25	264.17	353.64	512.73	640.62
	$r_w = 0.002\lambda$	31.10	45.63	61.79	97.39	134.96	206.16	272.24

In order to obtain a complete design algorithm, an infinite ground plane has to be replaced by the ground plane of finite dimensions. Subsection 4.3 (Figs. 4.6, 4.7, and 4.9–4.19) gives results that are relevant for the designer when choosing the appropriate dimensions of the circular or square ground plane. For practical purposes, it is important to stress that the losses in the ground plane do not affect the antenna gain, as it is mentioned in Subsection 4.3.

The other important characteristics (bandwidths, axial ratios, input impedances) of the optimal antennas designed following the presented design algorithm are summarized in Subsection 4.1, whereas the influence of the finite ground plane (square of circular) on these characteristics is discussed in Subsection 4.3.

5.2. Verification of the design procedure

Following the presented algorithm, an antenna that meets concrete specified characteristics is designed. Firstly, the antenna characteristics are checked using the simulations. Thereafter a prototype of the designed antenna is fabricated, and the antenna characteristics are verified by measurements.

We suppose a left-hand wound helical antenna. The target gain is 16 dBi at the operating frequency 1 GHz (the corresponding free-space wavelength is $\lambda \approx 300\,\text{mm}$). The parameters of the wire conductor are $r_w = 0.6\,\text{mm} \approx 0.002\lambda$ and $\sigma = 58\,\text{MS/m}$ (which corresponds to copper). The flowchart of the design procedure performed for the specified input values is shown in Fig. 5.2.

The normalized axial antenna length, required to achieve the targeted gain, is calculated from (3.23), and rounded to the first greater integer multiple of the half wavelength, $L = 2.5\lambda$. The next step is to check if this design algorithm is valid for the desired normalized axial antenna length and conductor properties. From (3.8) σ_{min} is calculated to be 7.6 MS/m ($\sigma > \sigma_{\text{min}}$). Hence, the design equations can be used for calculating geometrical parameters of the optimal antenna. The radii of the first and the last turn, $r_1 = 0.1051\lambda$ and $r_2 = 0.1453\lambda$, are calculated from (3.13) and (3.14), respectively, whereas the pitch angles of the first and the last turn are calculated from (3.19), and (3.20) to be $\varphi_1 = 4.8438°$ and $\varphi_2 = 5.6121°$, respectively. To double-check, the expected gain of the designed antenna (calculated from (3.23)) is 16.40 dBi. Hence, the required specification is fulfilled.
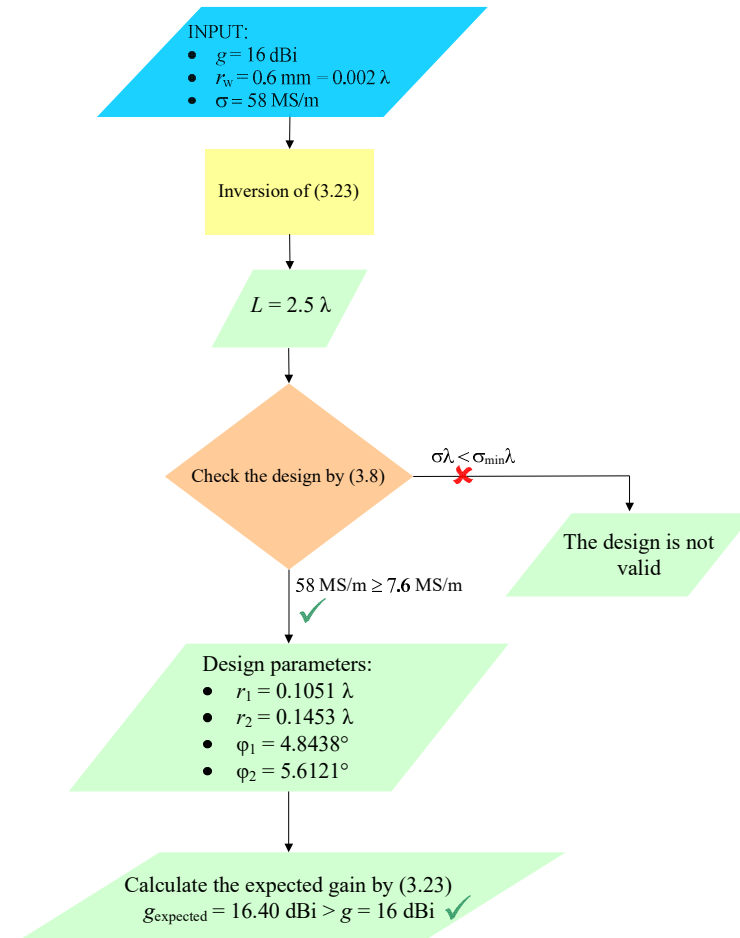
Figure 5.2. Flowchart of the performed design procedure.

66

The models (made in WIPL-D and AWAS) of the designed antenna located above an infinite PEC ground plane are shown in Figs. 5.3a and b. The simulated gain of the designed antenna in a wider frequency range (from 0.75 GHz to 1.25 GHz) is shown in Fig. 5.3c. At the operating frequency (1 GHz) the simulated gain in AWAS is 16.57 dBi, whereas WIPL-D yields 16.62 dBi (this discrepancy is due to the different numerical analyses used by these codes).

(a)   (b)   (c)
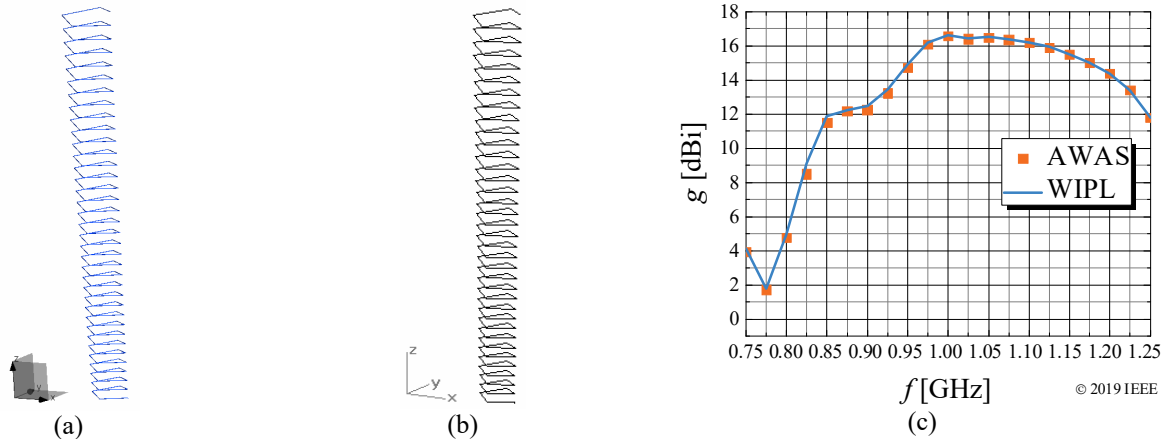
Figure 5.3. (a) WIPL-D and (b) AWAS model of the designed helical antenna located above an infinite PEC ground plane, and (c) simulated antenna gain in the frequency range from 0.75 GHz to 1.25 GHz (antenna operating frequency is 1 GHz) [113].

Although the design parameters are optimized at a single frequency, the antenna designed using the calculated geometrical parameters is reasonably broadband. The relative bandwidths are $BW_1|_{\text{PEC}} = 17.98\%$, $BW_2|_{\text{PEC}} = 24.61\%$, and $BW_3|_{\text{PEC}} = 29.24\%$. These relative bandwidths are in good agreement (the variation is less than 0.2 %) with the results shown in Fig. 4.2d.

The axial ratio of the designed antenna in the direction along the antenna axis and the antenna input impedance in the considered frequency range are shown in Fig. 5.4. At the operating frequency, the axial ratio is 0.49 dB, whereas the input impedance of the antenna at the same frequency is $(121.81 - j23.01)\,\Omega$. The axial ratio and input impedance at the operating frequency are in good agreement with the results shown in Fig. 4.3.

(a)   (b)
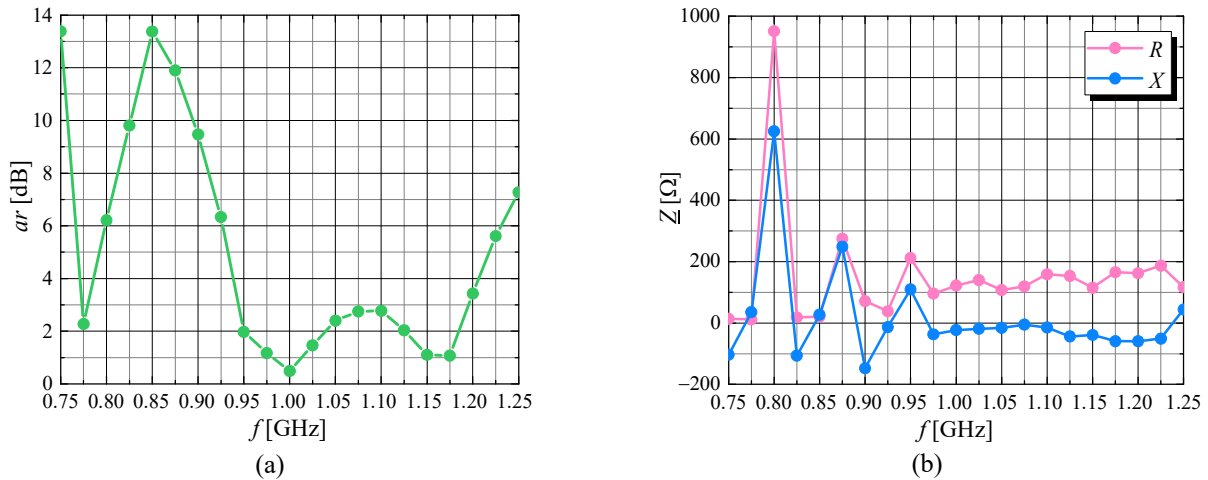
Figure 5.4. (a) Axial ratio in the direction along the antenna axis and (b) input impedance of the designed antenna located above an infinite PEC ground plane in the frequency range from 0.75 GHz to 1.25 GHz (antenna operating frequency is 1 GHz).

In order to take a step towards the design suitable for the fabrication, an infinite ground plane needs to be replaced by a ground plane of finite dimensions. As it is shown in Subsection 4.3, the finite-size ground plane influences the antenna gain, as well as the relative bandwidths, axial ratio, and input impedance. In this work only flat ground planes are considered.

For the present design, a square ground plane is chosen. Considering the results shown in Fig. 4.6d, a square ground plane of the side length of 2.25 λ is sufficient to achieve the same gain as with an infinite ground plane. Furthermore, with the square ground plane of the side 3.33 λ (around

1 m) the antenna gain is more than 0.5 dB higher than the gain calculated from (3.23), as shown in Fig. 4.7d. We chose the ground-plane side to be 3.33λ. From Figs. 4.10d, 4.11d, and 4.12d, the differences of the relative bandwidths (when the antenna is located above a square ground plane and above an infinite ground plane) can be estimated. These differences for the chosen ground plane are $\Delta BW_1 \approx -1\%$, $\Delta BW_2 \approx 0$, and $\Delta BW_3 \approx 2\%$. Further, from Figs. 4.16d and 4.18d the differences of the axial ratio and the input impedance can be estimated to be $\Delta ar \approx -0.13\,\mathrm{dB}$, $\Delta R \approx 10\,\Omega$, and $\Delta X \approx -8\,\Omega$.

The WIPL-D model of the designed antenna located above the square ground plane of the side 3.33λ is shown in Fig. 5.5a. At the operating frequency (1 GHz), the simulated gain is 16.93 dBi, which is for 0.53 dB higher than the gain calculated from (3.23), as it is predicted by the results shown in Fig. 4.7d. At the same frequency, the axial ratio (in the direction along the antenna axis) is 0.37 dB and the input impedance is $(130.27 - j31.59)\,\Omega$, as the results shown in Figs. 4.16d and 4.18d, respectively, estimate.

The antenna gain in a wider frequency range (from 0.75 GHz to 1.25 GHz) is shown in Fig. 5.5b. In the same frequency range the axial ratio and the input impedance are also calculated and shown in Fig. 5.6. The relative bandwidths are $BW_1|_{3.33\lambda} = 16.84\%$, $BW_2|_{3.33\lambda} = 24.53\%$, and $BW_3|_{3.33\lambda} = 31.12\%$. This example confirms that the differences in bandwidths predicted in Figs. 4.10d, 4.11d, and 4.12d, as well as the relative bandwidths for the antennas located above an infinite ground, allow a good estimation of the relative bandwidths for the antennas located above a square ground plane.

(a)

(b)
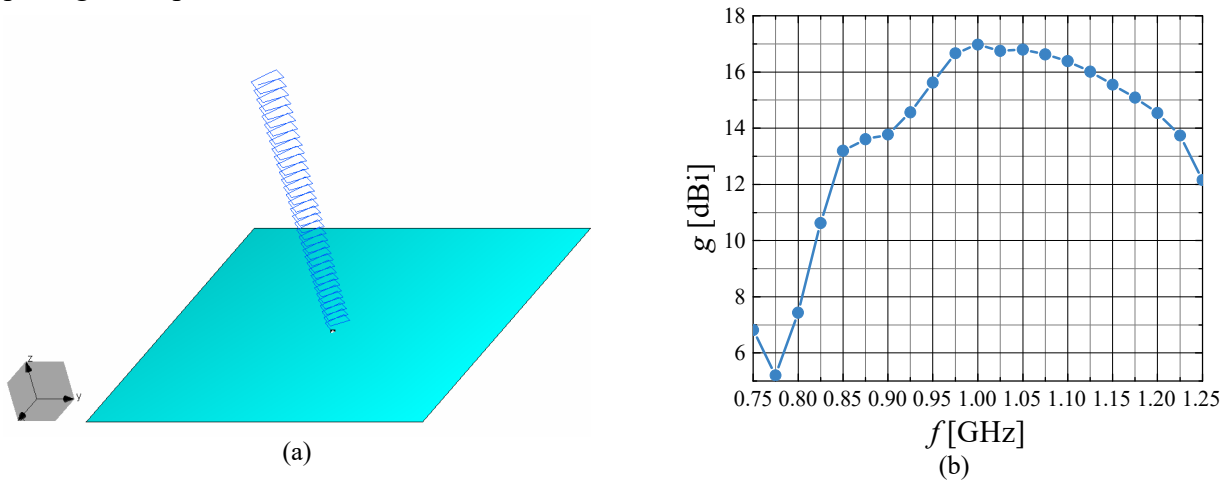
Figure 5.5. (a) WIPL-D model of the designed antenna located above the square ground plane of the side 3.33 λ (around 1 m) and (b) antenna gain in the frequency range from 0.75 GHz to 1.25 GHz (antenna operating frequency is 1 GHz).

(a)

(b)
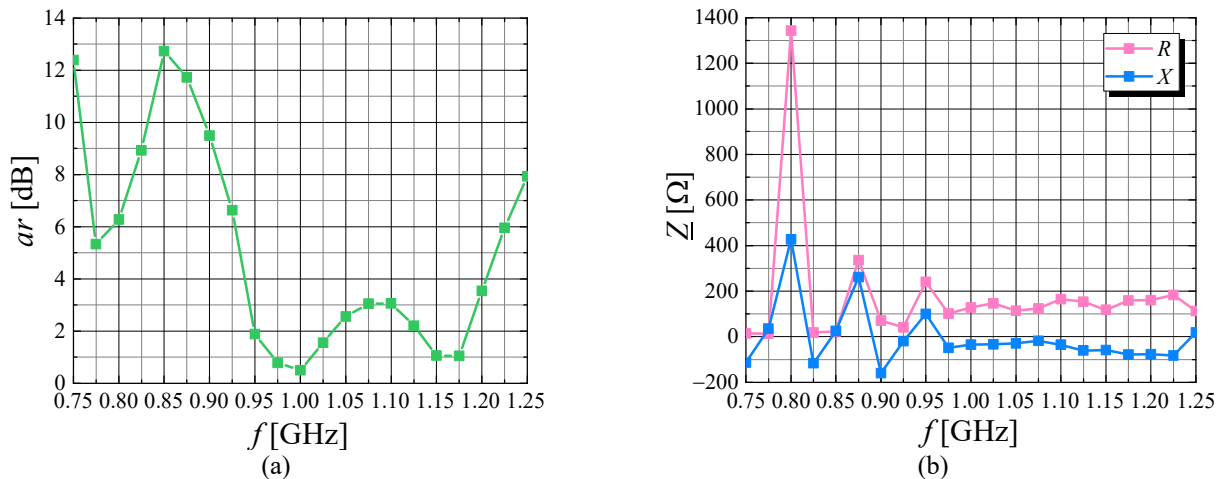
Figure 5.6. (a) Axial ratio in the direction along the antenna axis and (b) input impedance of the designed antenna located above the square ground plane of the side 3.33 λ (around 1 m) in the frequency range from 0.75 GHz to 1.25 GHz (antenna operating frequency is 1 GHz).

Results for the gain, axial ratio, and input impedance at the operating frequency, and relative bandwidths for the designed antenna located above an infinite and a square ground plane are summarized in Table 5.2. Also, Δg, ΔBW_1, ΔBW_2, ΔBW_3, Δar, ΔR, and ΔX from Subsection 4.3 are indicated in Table 5.2.

Table 5.2.
Gains, relative bandwidths, axial ratios, and input impedances for the designed antenna located above an infinite and square ground plane, and differences of these values from Subsection 4.3.

	g		BW_1	BW_2	BW_3	ar	R	X
Infinite ground plane	calculated (3.23) 16.40 dBi	simulated 16.62 dBi	17.98 %	24.61 %	29.24 %	0.49 dB	121.81 Ω	−23.01 Ω
Square ground plane (side 3.33 λ)	16.93 dBi		16.84 %	24.53 %	31.12 %	0.37 dB	130.27 Ω	−31.59 Ω
Type of difference	Δg		ΔBW_1	ΔBW_2	ΔBW_3	Δar	ΔR	ΔX
Achieved	0.53 dB		−1.14 %	−0.08 %	1.88 %	−0.12 dB	8.46 Ω	−8.58 Ω
From Subsection 4.3	0.5 dB		−1 %	0	2 %	−0.13 dB	10 Ω	−8 Ω

5.3. Fabricated prototype

The prototype of the antenna designed in the previous subsection is fabricated and measured.

The antenna prototype consists of a wire, wound in the form of a helix with the specified radius and pitch angle for each turn, and a square ground plane. Theoretically the wire is placed in air (in a vacuum). However, for the required precise positioning of the wire, a supporting structure is necessary. The material of the supporting structure should meet several criteria. Firstly, the influence of the supporting structure needs to be as low as possible. Hence, the material of the supporting structure must have a minimal effect on the field distribution. Secondly, available techniques for cutting the supporting-structure material need to allow precise tailoring. Finally, a good choice of the supporting-structure material implies a material which is not very heavy and very expensive. Taking all these facts into account, acrylic glass is chosen.

The supporting structure is modeled in software Blender [121]. It consists of three acrylic-glass plates (Fig. 5.7a). These plates are precisely tailored so to properly intersect and form a cross-like structure (Fig. 5.7b). Each plate is slotted at the proper location to allow that intersection. The edges of these plates are the corners of the antenna turns (Fig. 5.7c). Hence, the width of the plate corresponds to the realized turn diameter. Along the edge of each plate, small grooves are cut at precisely defined positions. These grooves hold the antenna conductor and provide the required pitch angle. In order to additionally reduce the mass of the supporting structure, big holes are cut in the plates.

The acrylic-glass plates are fabricated and assembled (Fig. 5.8a). At the places of plate intersection, the acrylic-glass plates are glued in order to increase the strength of the supporting structure. At the bottom of the supporting structure, a small footer (also made of acrylic glass) is placed to allow fixing the antenna to the ground plane (Fig. 5.8a). The antenna conductor (copper wire of the circular cross-section of the radius $0.6 \text{mm} \approx 0.002 \lambda$) is wound on the supporting structure (Fig. 5.8b), which is thereafter fixed to an aluminum square plate. The side of the plate is 1 m, which corresponds to 3.33 λ at the operating frequency. The fully assembled antenna prototype is shown in Fig. 5.8c.
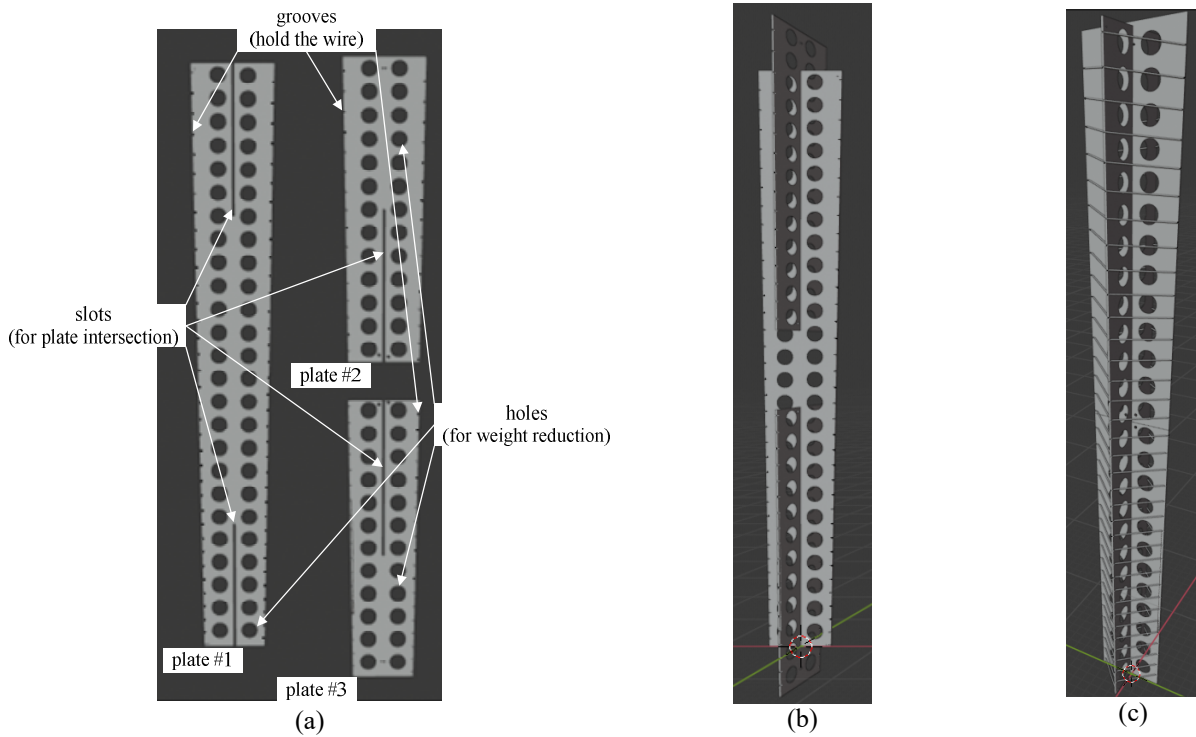
Figure 5.7. Blender models: (a) acrylic-glass plates, (b) the way plates intersect, and (c) full model of the assembled acrylic-glass supporting structure with the antenna conductor.
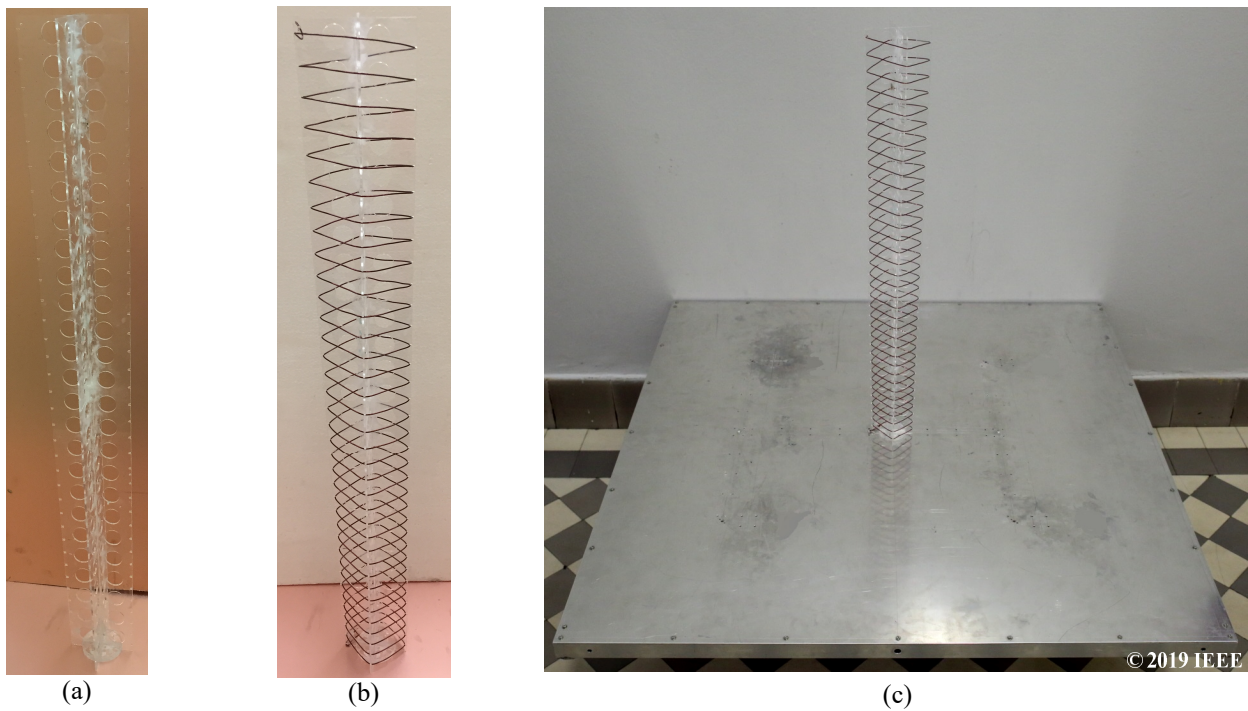
Figure 5.8. (a) Assembled supporting structure, (b) with wound antenna conductor, and (c) assembled antenna prototype [113].

5.4. Measurement procedure and results

Measurements of the designed and fabricated antenna are performed in Idvorsky laboratories [122]. The chamber in Idvorsky laboratories is semianechoic. Hence, additional absorbers are placed on the floor of the chamber in order to reduce the wave reflected from the floor. With these additional absorbers, the semi-anechoic chamber could be considered as a fully anechoic chamber. The measurement setup in the chamber is shown in Fig. 5.9. It consists of the designed nonuniform helical antenna, a well-documented Vivaldi antenna, a vector network analyzer Agilent E5061A, and a laptop for collecting measurement results.
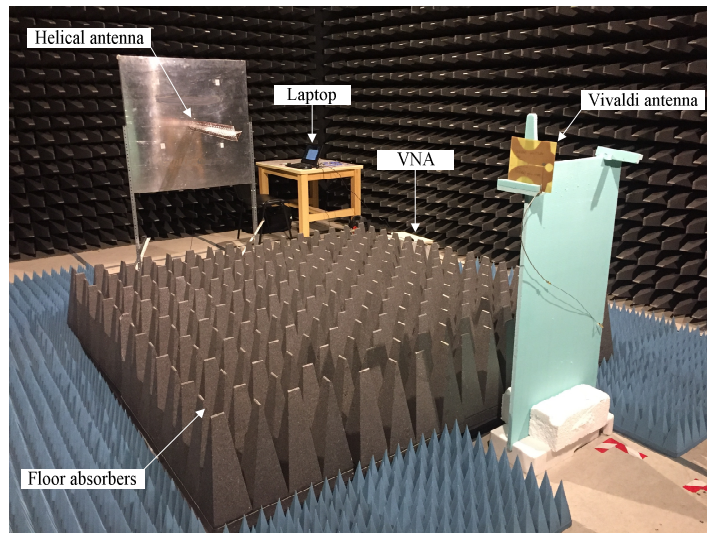
Figure 5.9. Measurement setup in the anechoic chamber in Idvorsky laboratories.

Firstly, the reflection coefficient of the fabricated antenna is measured and compared with the simulated results in the frequency range from 0.75 GHz to 1.25 GHz (Fig. 5.10).

The effect of imperfect wire bendings at the corners of the turns is also taken into account. This is done by scaling the turn radii of the model that is used for the comparison with measured results of the fabricated antenna.

The total wire length of the fabricated antenna is 882.5 cm, whereas the total wire length of the model (without scaling) is 861 cm. Hence, the imperfect bendings at the corners of the turns extends the wire length for around 2.5 %, so that the characteristics of the fabricated antenna are shifted towards lower frequencies in comparison with the computational model. Further, in the model, the conductor is placed in a vacuum, whereas in the case of the fabricated antenna the conductor is wound on the supporting structure made of acrylic glass (a dielectric whose relative permittivity is approximately 3.5). This dielectric also slightly influences the antenna performance, by shifting the antenna characteristics towards lower frequencies.

To take into account the influence of the imperfect bendings and also the influence of the dielectric supporting structure, all simulations (whose results are compared with measurements) are performed for models with 5 % larger turn radii than the turn radii of the fabricated prototype.

The effect of the surface roughness is taken into account by taking the wire conductivity, in the model, to be 29 MS/m, as explained in [43].
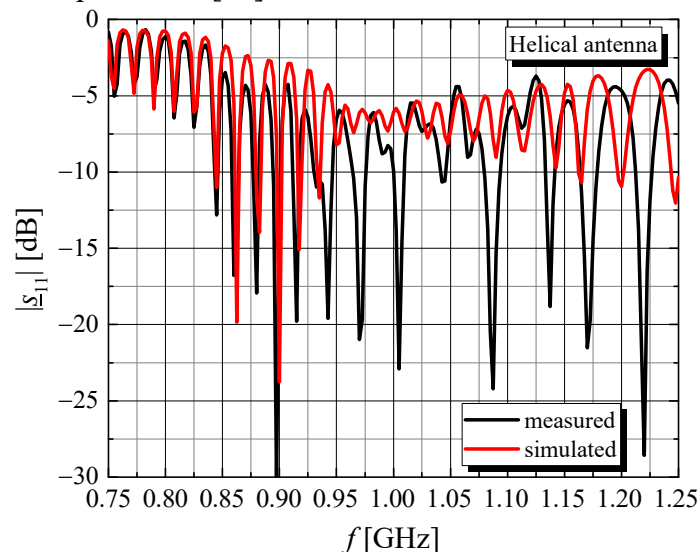
Figure 5.10. Measured and simulated reflection coefficients of the fabricated antenna in the frequency range.

Next, the transmission coefficient between the fabricated helical antenna and the Vivaldi antenna is measured and compared with the simulated results in the frequency range from 0.75 GHz to

1.25 GHz. The simulated results are obtained for the model which emulates real situation, i.e., models of both antennas placed at the actual distance. The tip-to-tip distance between the helical antenna and the Vivaldi antenna is 2460 mm. Since the Vivaldi antenna is linearly polarized, two scenarios are considered, each corresponding to one of the two orthogonal polarizations.

In the first case, the Vivaldi antenna is placed in a vertical position, as in Fig. 5.9. We refer to this scenario as "vertical", and the WIPL-D model for this case is shown in Fig. 5.11a. In the second case, the Vivaldi antenna is rotated for 90°, so it is placed horizontally ("horizontal scenario"), and the WIPL-D model is shown in Fig. 5.11b.

The measured and simulated transmission coefficients for both scenarios are compared in Fig. 5.12. The measured and simulated results are in good agreement.

(a)   (b)

Figure 5.11. WIPL-D models that correspond to the (a) vertical scenario and (b) horizontal scenario.

(a)   (b)
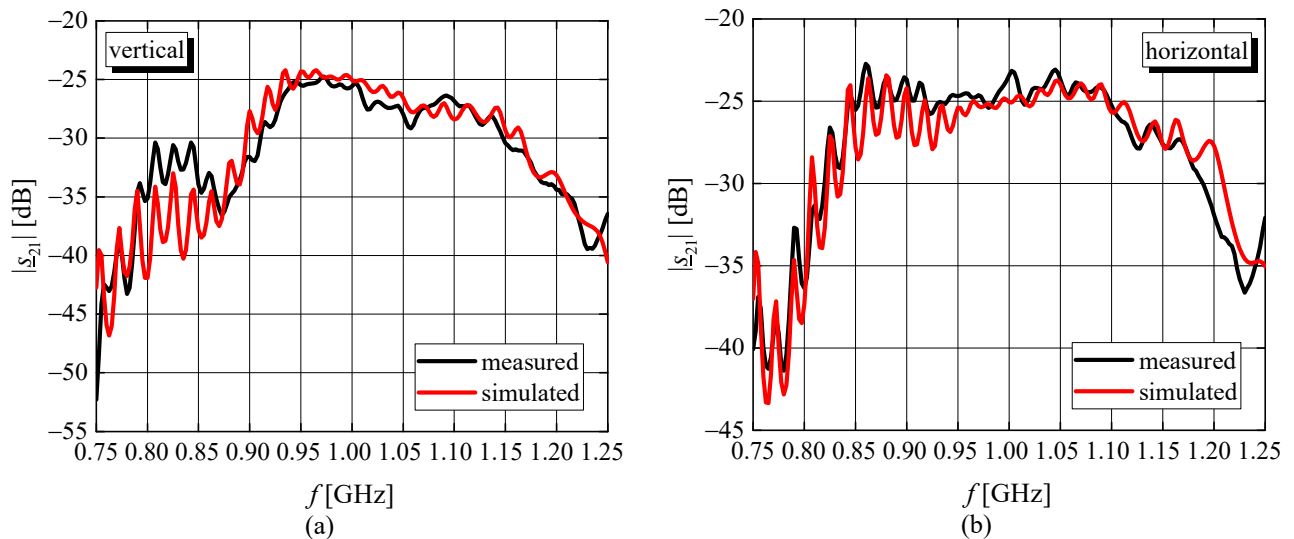
Figure 5.12. Measured and simulated transmission coefficient for (a) vertical and (b) horizontal scenario.

In order to perform measurements in the far field, the three conditions given in Appendix A.3 must be fulfilled. In our case, the critical condition is $r > d_F = 2D^2/\lambda$, where d_F is the Fraunhofer distance, and we take D to be the antenna axial length. For the fabricated antenna $D = 2.5\,\lambda$ and $d_F = 3750\,\text{mm}$. Hence, the measurements are actually performed in the near-field region and, strictly speaking, we cannot extract the antenna gain from the measured data, because the far-field conditions are not fulfilled. Unfortunately, the available chamber is too small to perform far-field measurements.

However, the good agreement between simulated and measured results shown in Fig. 5.12 gives us a strong solid background to believe that the gain of the fabricated antenna is very close to the gain obtained from the simulations.

In order to further increase the confidence in the good gain of the fabricated antenna, the following numerical experiment is performed.

Firstly, two identical Vivaldi antennas are simulated at the distances (d), sweeped from 0.1 m to 5 m (measured from the tip of one antenna to the tip of the other antenna). The frequency for the analysis is 1 GHz. We start from the modified Friis formula

$$\left|\underline{s}_{21}(d)\right|^2 = \left(\frac{\lambda}{4\pi d}\right)^2 G_r G_t \left(1 - \left|\underline{s}_{11}\right|^2\right)\left(1 - \left|\underline{s}_{22}\right|^2\right). \tag{5.1}$$

This formula gives the squared magnitude of the transmission coefficient between the antenna ports. The modification takes into account the mismatch between the antennas and the feeding transmission lines. Note, however, that this formula assumes that the receiving antenna is in the far field of the transmitting antenna. Since the transmitting and the receiving antennas are identical, the antenna gain is $G_r = G_t = G$ and $\left|\underline{s}_{11}\right| = \left|\underline{s}_{22}\right|$. Hence, the transmission coefficient is

$$\left|\underline{s}_{21}(d)\right| = \frac{\lambda}{4\pi d} G \left(1 - \left|\underline{s}_{11}\right|^2\right). \tag{5.2}$$

We use G and $\underline{s}_{11}$ from the simulations in order to calculate $\left|\underline{s}_{21}(d)\right|$ from (5.2). We compare the transmission coefficient from the simulation to the one obtained using the Friis formula. If we use the distance, d, measured between the tips of the antennas, we observe a discrepancy in the transmission coefficients, as shown in Fig. 5.13a. This discrepancy is expected since the Friis formula is valid when the antennas are in the far-field region, but we use it in a region that is not sufficiently far from the antennas, i.e., in a region that is not exactly the far-field region.

In order to mitigate this discrepancy, we need to find the "center" of the Vivaldi antenna, or the correct distance that should be used in the Friis formula. With simple optimization of the distance used in the Friis formula, it is found that the distance between the tips should be increased for approximately 93 mm per antenna, i.e., 186 mm in total. This distance is practically the same as if we measure the distance between the antennas from nearly the mid-point of one antenna to the mid-point of the other antenna. The comparison of the simulated transmission coefficient and calculated transmission coefficient with this distance correction is shown in Fig. 5.13b. From the presented results it can be concluded that if we use the Friis formula for the gain estimation of the fabricated helical antenna, we need to correct the tip-to-tip distance between the helical antenna and the Vivaldi antenna by adding 93 mm. However, we also need a similar correction for the helical antenna.
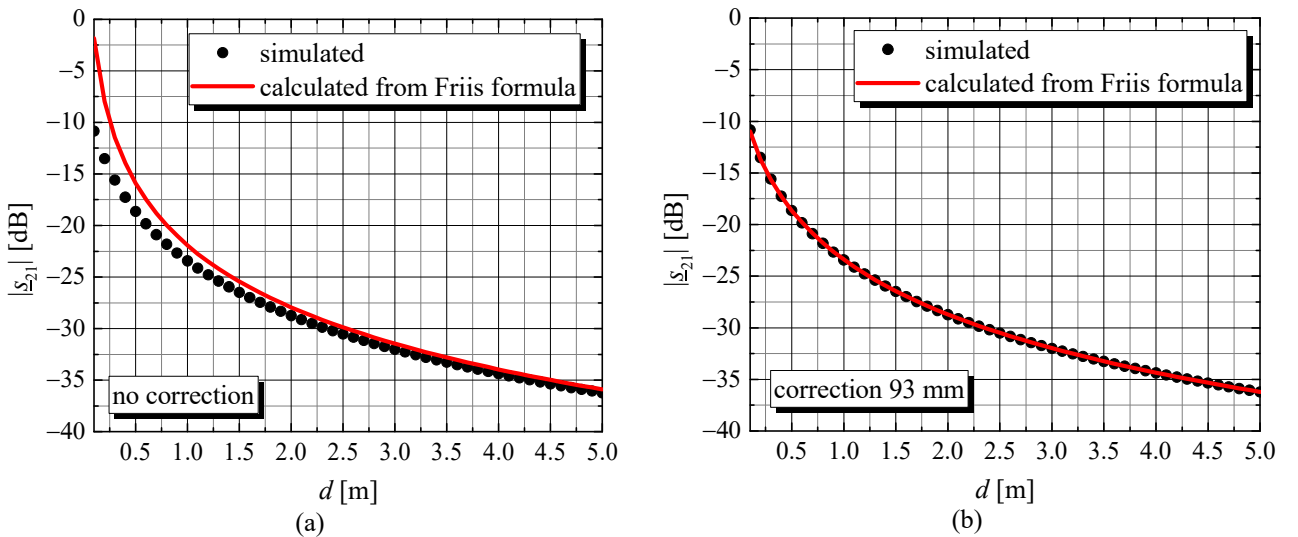
Figure 5.13. Transmission coefficient simulated and calculated from Friis formula (a) without the distance correction and (b) with the distance correction of 93 mm for each Vivaldi antenna.

Further, the same numerical experiment is performed for the designed helical antenna in order to find the distance correction for it. Two identical antennas are analyzed, oriented so to achieve the maximal power transfer. The transmission coefficients obtained without the distance correction and with the distance correction of 680 mm for each helical antenna are shown in Fig. 5.14. Note that for calculating the transmission coefficient using (5.2), the gain and the reflection coefficient are obtained from the simulation of a single helical antenna at the operating frequency. Hence the coupling between helical antennas is not taken into account, unlike in the case of simulated transmission coefficient where this coupling is considered. Therefore the simulated results in Fig. 5.14 show a "zig-zag" behavior.

In the inset of Fig. 5.14b, the position of the antenna "center" with the correction is indicated by a black dot.
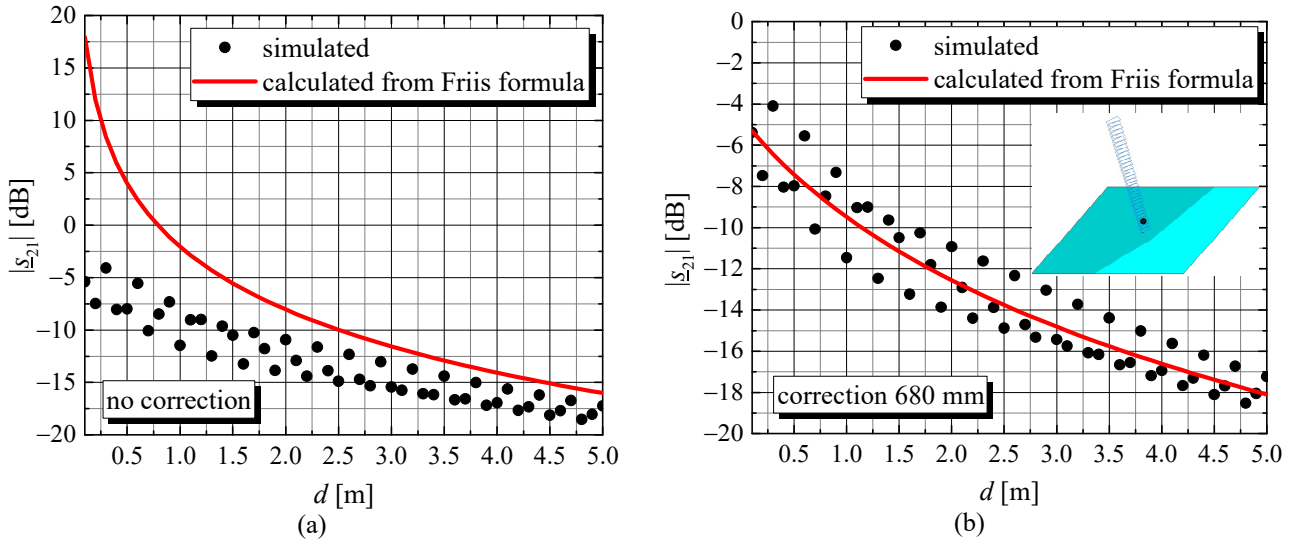
Figure 5.14. Transmission coefficient simulated and calculated from Friis formula (a) without the distance correction and (b) with the distance correction of 680 mm for each helical antenna.

Finally, we use the distance corrections for the Vivaldi antenna and for the designed helical antenna with the measured results for the transmission and reflection coefficients in order to estimate the measured gain. Note that the distance corrections have slight variations with frequency, but we use constant corrections estimated for 1 GHz since the aim of our measurements is primarily to get the gain of the fabricated antenna at 1 GHz.

Since the Vivaldi antenna is linearly polarized and the helical antenna is circularly polarized, the gain obtained from the Friis formula, using the measured results for the transmission and reflection coefficients, corresponds to one of the two orthogonal linear polarizations. The measured gain (in the main radiating direction and in the frequency range from 0.75 GHz to 1.25 GHz) for each polarization is compared with the simulated results in Fig. 5.15. The numerical gain (Appendix A.1) for the circular polarization can be calculated as the sum of the numerical gains for the linear polarizations. Note that if the circular polarization is perfect, the gains of the two orthogonal (linear) polarization components are equal and the logarithmic gain for the circular polarization is 3 dB higher than the logarithmic gain of the linear-polarization components.
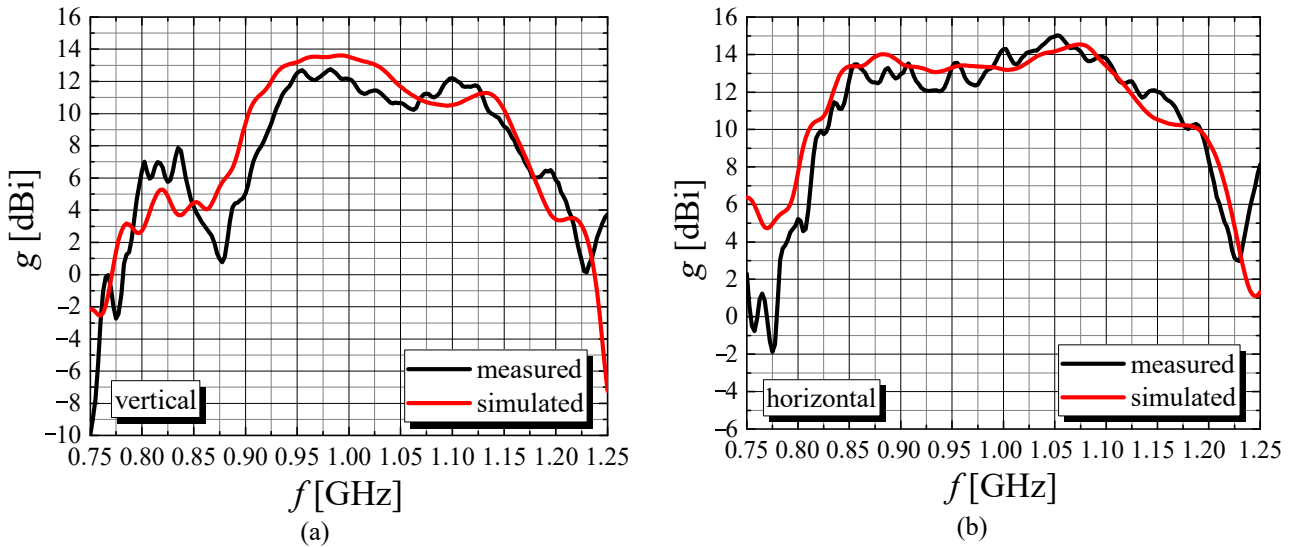
Figure 5.15. Simulated and measured gain for (a) the vertical polarization and (b) the horizontal polarization.

Further, the gain of the fabricated helical antenna prototype in the main radiating direction in the same frequency range is compared with simulated results in Fig. 5.16a. The measured and simulated radiation patterns of the fabricated antenna at 1 GHz in the *xOz* plane (Fig. 5.5a) are compared in Fig. 5.16b. Although the distance corrections are calculated only at the operating frequency (1 GHz), the simulated and measured results shown in Figs. 5.15 and 5.16a are in very good agreement in the full considered frequency range. In particular, the discrepancy at 1 GHz is negligible (less than 0.03 dB).
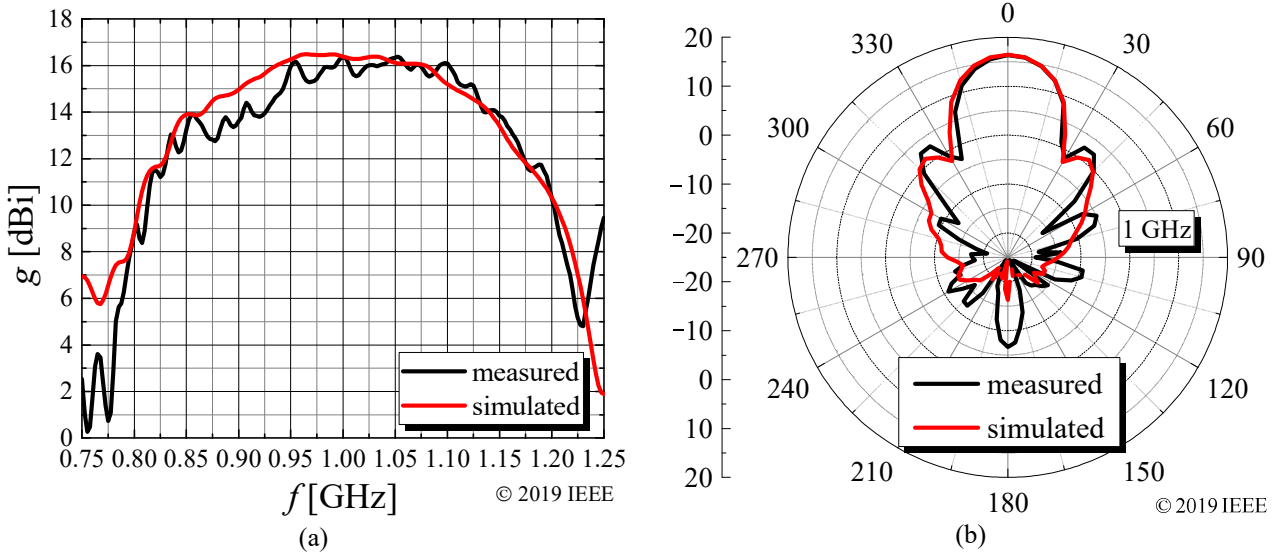
Figure 5.16. Measured and simulated gain of the designed helical antenna (a) in the frequency range from 0.75 GHz to 1.25 GHz [113] and (b) the radiation pattern at the operating frequency of 1 GHz [113].

The radiation patterns in the *xOz* plane (Fig. 5.5a) are also measured at some other frequencies and compared with the simulated results in Fig. 5.17. These results also confirm that the measured gain of the designed antenna is in good agreement with the simulated gain near the main radiating direction (within the main lobe) at all considered frequencies.
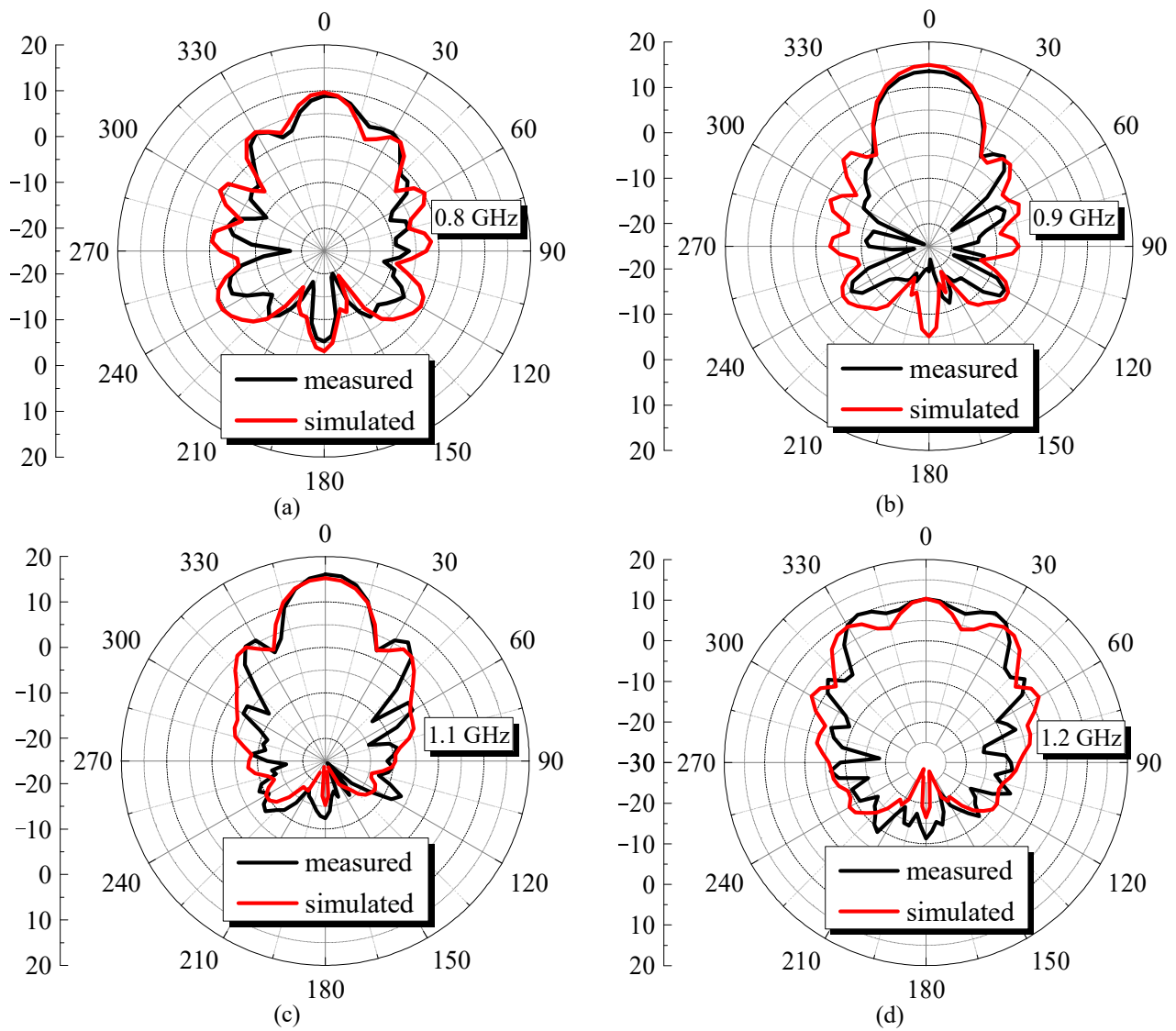
Figure 5.17. Radiation pattern of the designed and fabricated helical antenna at (a) 0.8 GHz, (b) 0.9 GHz, (c) 1.1 GHz, and (d) 1.2 GHz.

Finally, it can be concluded that measurement results demonstrate excellent agreement with the design targets and with the computational models.

6. Design of array of nonuniform helical antennas

In this chapter a complete design of an array of nonuniform helical antennas will be presented in detail. The designed array has to meet predefined design specifications. Hence, this task illustrates a practical engineering problem.

The presented design procedure contains the design of an array of four (2×2) nonuniform helical antennas with linearly varying geometrical parameters, optimization of the antenna positions within the array, and the design of the feeding network that simultaneously is a matching network with respect to $50\,\Omega$. The design procedure is verified through the measurements of the fabricated array.

6.1. Design specifications

The task is to design and verify (through simulations and measurements) an antenna array whose gain is at least 20 dBi within the frequency range from 0.9 GHz to 1.1 GHz, whereas the required gain at the operating frequency 1 GHz is 21 dBi. Hence, BW_1 (defined in Subsection 4.1) is 20 %. The free-space wavelength at the operating frequency is $\lambda \approx 300\,\text{mm}$. It is also required that the antenna is matched with respect to $50\,\Omega$ (the modulus of the reflection coefficient, $\underline{s}_{11}$, is less than $-10\,\text{dB}$) within the same frequency range. The overall antenna dimensions have to be maintained as small as possible, with a tendency to achieve a cuboid shape with the maximal dimension of a side $1\,\text{m} \approx 3.33\lambda$.

6.2. Geometry and model of quad array

To meet the required specifications, we adopt an array of four (2×2) identical nonuniform helical antennas. We refer to this array of antennas as quad array. For this design, we consider nonuniform helical antennas with linearly varying geometrical parameters. The antennas are placed at the vertexes of an imaginary square of a side D (Fig. 6.1a). All antennas have the same orientation. The geometry of the nonuniform helical antennas with linearly varying geometrical parameters is defined by the axial antenna length, L, the radii of the first and the last turn, r_1 and r_2, respectively, and the pitches (or pitch angles) of the first and the last turn, p_1 and p_2 (or φ_1 and φ_2), respectively. The radii and pitch angles of each turn can be calculated using (2.1) and (2.2), where z is the axial coordinate. Alternatively to the pitch angle, the pitch of each turn can be calculated from

$$p = (p_2 - p_1)\frac{z}{L} + p_1. \tag{6.1}$$

The antenna conductor is a wire of a circular cross-section whose radius is r_w. Theoretically, the antenna array can be placed above an infinite perfectly conducting ground plane or above a ground plane of finite dimensions. For this design, we consider a flat, square-shaped ground plane of a side a, Fig. 6.1a.

As it is explained in Subsection 2.2 (where a single helical antenna is considered), a perfectly circular turn can be approximated by a polygonal turn utilizing (2.7). This approximation is also used when making the model of the array, since it speeds up computations and it is necessary to overcome the limitations imposed by the utilized electromagnetic solver, i.e., the solver can analyze only straight-line wire segments. All simulations are run in WIPL-D [111]. The WIPL-D model of the quad array, utilizing the suggested approximation, is shown in Fig. 6.1b.

<div align="center">(a)   (b)</div>
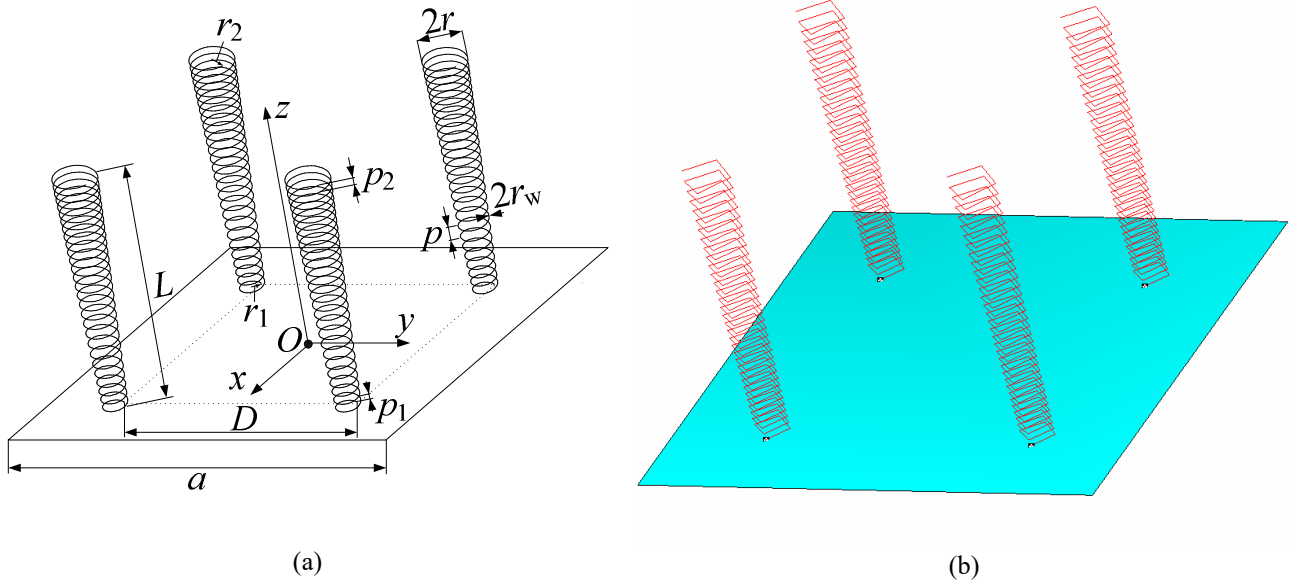
Figure 6.1. Array (2 x 2) of nonuniform helical antennas, quad array: (a) sketch [88] and (b) WIPL-D model [88].

The available conductor is a copper wire of a circular cross-section and radius $r_w = 0.6\,\text{mm} \approx 0.002\,\lambda$. In order to estimate the required axial antenna length, we consider the fact that the array of four antennas can increase the gain by up to 6 dB in comparison with a single helical antenna. Hence, the required gain of a single helical antenna has to be at least 15 dBi at 1 GHz. Utilizing the first step from the flowchart shown in Fig. 5.1 ("Inversion of (3.23)"), the minimal required axial antenna length is estimated to be $2\,\lambda$. However, it is also required that the gain has to be above 20 dBi in the frequency range from 0.9 GHz to 1.1 GHz, i.e., that the required $BW_1 = 20\,\%$. Fig. 4.2d shows that, for the designed antennas, $BW_1 < 20\,\%$. Hence, to be on the safe side, we adopt that the axial length of the antennas in array is $L = 2.5\,\lambda \approx 750\,\text{mm}$. The gain of the nonuniform helical antenna (located above an infinite ground plane) of axial length $2.5\,\lambda$, wire radius $0.002\,\lambda$, and wire conductivity 58 MS/m (which corresponds to the copper) is estimated from (3.23) to be 16.4 dBi. Actually, this is the same antenna as the antenna designed in Subsection 5.2.

Since the maximal dimension of the array is limited to 1 m, we adopt the side of the ground plane $a = 1\,\text{m} \approx 3.33\,\lambda$. In the simulations we consider a lossless ground plane, since the investigation done for a single helical antenna (Subsection 4.3) shows that losses in the ground plane have negligible influence on the antenna characteristics.

In the basic model of the array (shown in Fig. 6.1b), all antennas are fed by voltage delta-gap point generators located on the short vertical wire segment between ground plane and the first antenna turn (as for a single helical antenna). All generators are of the same amplitude and phase. The feeding network will be included in the model later.

6.3. Optimization procedure for basic model

The optimization procedure is similar to the procedure formulated for optimizing nonuniform helical antennas with linearly varying geometrical parameters (Subsection 3.1). The optimization

goal is to maximize the partial gain for the circular polarization in the main radiating direction (Appendix A.1) of the array. The cost function is defined here as the L_2-norm,

$$f_{\text{cost}} = \sqrt{(100 - g)^2} \,, \tag{6.2}$$

where g is the gain of the array. The best possible design corresponds to the global minimum of f_{cost}.

The optimization again contains two steps. For the first step, we utilize the particle swarm optimization (PSO) [116], [117] with a randomly seeded swarm. The second step of the optimization is launched from the best-found solution in the first step. For the second step, local optimization algorithms are utilized, i.e., Nelder-Mead simplex [115] or gradient algorithm.

Different numbers of iterations and algorithm setups are investigated and the following designs (marked as the optimal) are the best-found results.

The optimization of the considered quad array contains 5 optimization variables:

- the radius of the first turn, r_1,
- the radius of the last turn, r_2,
- the pitch of the first turn, p_1,
- the pitch of the last turn, p_2, and
- the distance between the feeding points of the helical antennas, D.

According to the optimal geometrical parameters of the nonuniform helical antennas calculated using (3.13), (3.14), (3.19), and (3.20), the optimization variables are expected to be within the limits:

- $25 \, \text{mm} \leq r_1 \leq 40 \, \text{mm}$,
- $30 \, \text{mm} \leq r_2 \leq 50 \, \text{mm}$,
- $10 \, \text{mm} \leq p_1 \leq 50 \, \text{mm}$, and
- $10 \, \text{mm} \leq p_2 \leq 50 \, \text{mm}$.

The distance between the array elements is investigated in the literature [96], [108]. As it is indicated in Chapter 1, in [108] it is suggested that the array elements should be spaced at least $\sqrt{G_{\text{h}}/(4\pi)}\lambda$, where G_{h} is the (numerical) gain of the single helical antenna. Hence, it can be expected that the optimal spacing between the elements is around $560 \, \text{mm}$. However, we additionally investigated how the distance between array elements affects the gain and the radiation pattern, in order to find a proper range for the optimization variable D.

We consider a quad array of the same axial length, operating frequency, wire radius, and wire conductivity (i.e., $2.5 \, \lambda$, $1 \, \text{GHz}$, $0.002 \, \lambda$, and $58 \, \text{MS/m}$, respectively). The geometrical parameters of the helical antennas are calculated using (3.13), (3.14), (3.19), and (3.20). To simplify the computation, the helices are located above an infinite perfectly conducting ground plane. We vary the distance between the antennas, D, from 200 mm to 700 mm. The radiation patterns (in the $\phi = 0$ cut) are shown in Fig. 6.2, where ϕ and θ are measured from the x axis (in the xOy plane) and the z axis to the considered direction, respectively (Fig. 6.1a). It can be noticed that for D=200 mm, sidelobes are the lowest, but also the gain in the main radiating direction (θ=0) is the lowest. With increasing D, the gain in the main radiating direction increases, but this is accompanied with the increase in the sidelobes. For $D > 600$ mm, no further increase in the gain in the main radiating direction can be noticed; however, the sidelobes increase further. Therefore, we adopt the limits for the optimization variable D to be $400 \, \text{mm} \leq D \leq 600 \, \text{mm}$.
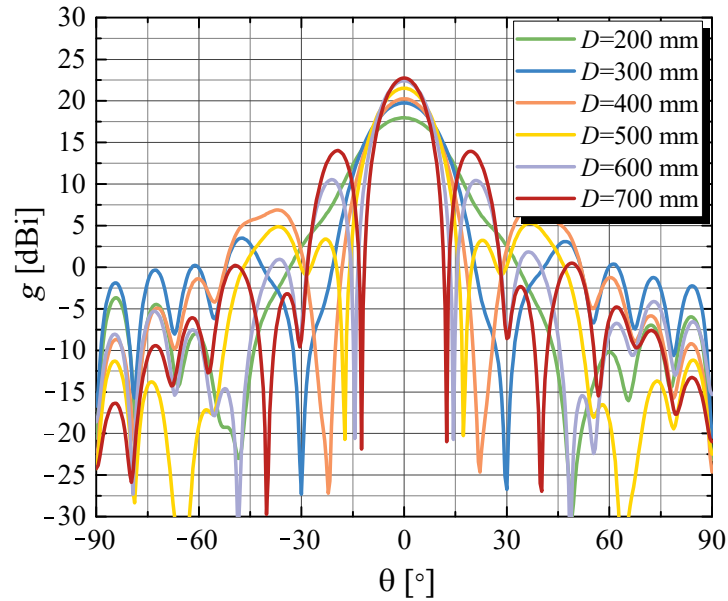
Figure 6.2. Radiation patterns of the array of nonuniform helical antennas for various distances between the elements.

6.4. Optimal basic design

The optimizations are run for the basic model shown in Fig. 6.1a, and the optimal values of the optimization variables are

- $r_1 = 34.9\,\text{mm}$,
- $r_2 = 47.1\,\text{mm}$,
- $p_1 = 17\,\text{mm}$,
- $p_2 = 37.9\,\text{mm}$, and
- $D = 586.9\,\text{mm}$.

We refer to this design as the optimal basic design. The model of this design and the 3-D radiation pattern at 1 GHz are shown in Fig. 6.3. The gain in the main radiating direction is slightly less than 22 dBi, whereas the front-to-back ratio is 21 dB. The ϕ-cut ($\phi = 0$) of the radiation pattern at 1 GHz is shown in Fig. 6.4a. The gain and the axial ratio in the main radiating direction in the frequency range from 0.8 GHz to 1.5 GHz are shown in Fig. 6.4b. The gain is above 20 dBi (as it is required by the design specification) in the frequency range from 0.9 GHz to 1.15 GHz. Within that frequency range, the axial ratio is below 1.4, and the input impedance of each helical antenna is around $(115 - \text{j}20)\,\Omega$.

(a)

(b)
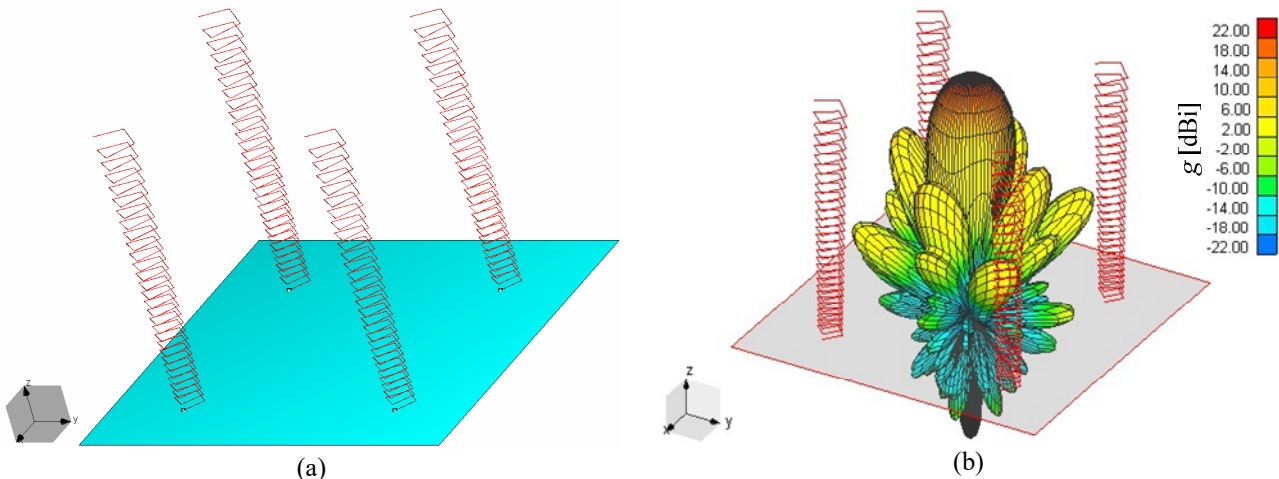
Figure 6.3. Optimal basic design: (a) model [88] and (b) 3-D radiation pattern at 1 GHz [88].
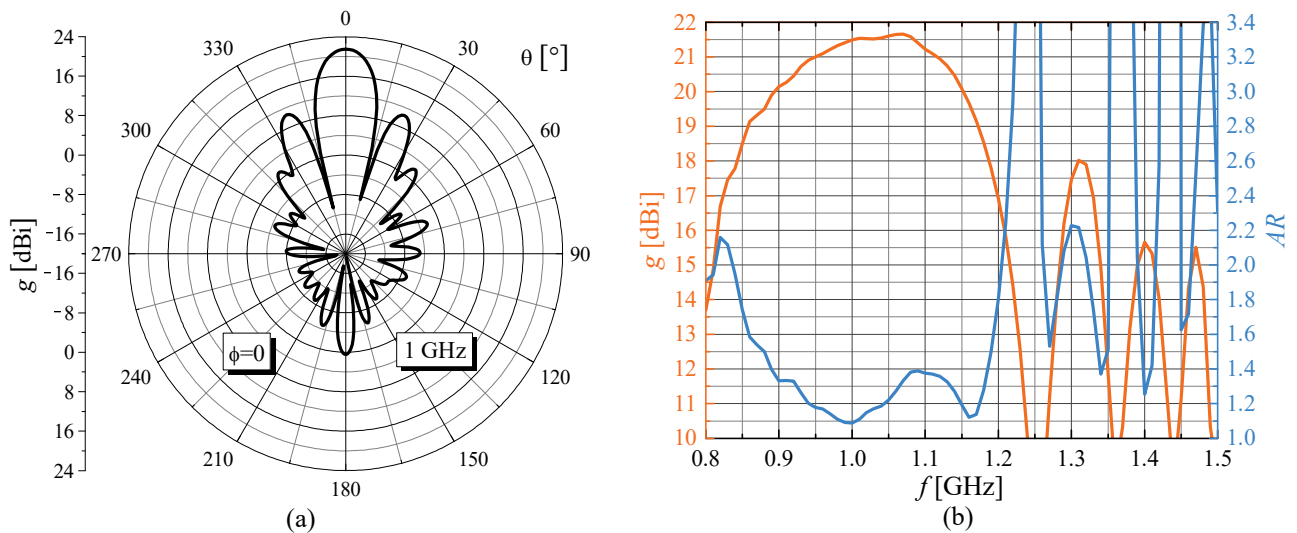
Figure 6.4. Optimal basic design: (a) φ-cut of the radiation pattern at 1 GHz [88] and (b) gain and axial ratio versus frequency [88].

The next step is to introduce the feeding network into the design and to find the best values of the optimization variables in this case.

6.5. Feeding network

The feeding network has two roles. The first role is to feed each helical antenna with the same amplitude and phase. The second role is to match the quad array to 50 Ω.

For these purposes, a H-shaped feeding network is chosen (Fig. 6.5). The network consists of six wire segments. These wire segments are located above a ground plane; hence, they act like transmission lines. Four transmission lines, of a characteristic impedance Z_{c1}, interconnect adjacent helices. These transmission lines transform the impedances of single helical antennas. Pairs of those (transformed) impedances are connected in parallel at points A and B. The impedances at points A and B are further transformed by the transmission lines whose characteristic impedance is Z_{c2}. At the point O, these transformed impedances are again connected in parallel. The point O is the feeding point of the quad array and Z_{c1} and Z_{c2} are chosen so that the impedance at O is as close as possible to 50 Ω, i.e., the quad array is well matched with respect to 50 Ω.
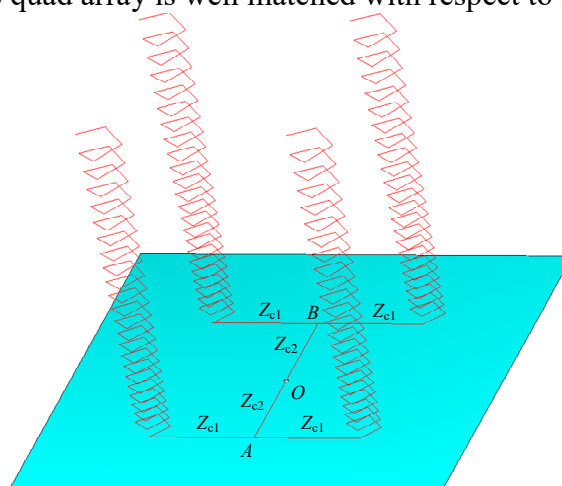
Figure 6.5. Model of the quad array with H-shaped feeding network [88].

The characteristic impedances Z_{c1} and Z_{c2} are determined by the radii of the wire segments and the elevations of the wires above the ground plane. The available wire radii in our lab are 0.3 mm and 0.6 mm. Since it is necessary that $Z_{c1} > Z_{c2}$, the four transmission lines of the characteristic impedance Z_{c1} are realized with the wire of the radius 0.3 mm, whereas the two middle wire

segments are made of the wire of the radius 0.6 mm. The elevation of all wires is 2 mm above the ground plane. For these data, the corresponding characteristic impedances are Z_{c1}=155 Ω and Z_{c2}=112 Ω, calculated using [123].

Further, the geometry of the quad array, with the incorporated feeding network, will be optimized.

6.6. Optimization of quad array with feeding network

The optimization of the quad array with the H-shaped feeding network is challenging since it requires simultaneous maximization of the partial gain for the circular polarization and minimization of the reflection coefficient at the feeding point of the quad array, i.e., matching of the quad array.

Although this is a two-criteria optimization problem, in our case these criteria are weakly coupled. Namely, the gain of the quad array depends only on the geometry of the array (geometry of the helices and the distance between elements). The gain is not affected by the geometry of the feeding network since it practically does not radiate. The geometry of the feeding network has a role in the impedance transformation and affects the reflection coefficient. These conclusions allow us to combine the two criteria into a single cost function, utilizing our engineering experience for estimation of the relative weights of the criteria.

The set of optimization variables and optimization algorithms are the same as for the basic model. In order to broaden the bandwidth, $N = 5$ equidistantly spaced frequencies within the frequency range from 0.95 GHz to 1.15 GHz are considered (~20 % bandwidth). This frequency range is chosen to account for a 5 % frequency shift towards lower frequencies due to the imperfect mounting of wires on the supporting structure and the influence of the dielectric of the supporting structure. Hence, the expected frequency range of the fabricated quad array is from 0.9 GHz to 1.1 GHz,

The cost function is defined as

$$f_{\text{cost}} = \frac{1}{N}\sqrt{\sum_{k=1}^{N}\left(100 - g\right)^2} + \frac{1}{N}\sqrt{\sum_{k=1}^{N}\left(\max\left(\left|s_{11}\right| + 15, 0\right)\right)^2} , \qquad (6.3)$$

where $\left|s_{11}\right|$ is the reflection coefficient in dB at the antenna feeding point.

The optimal values of the optimization variables are
- $r_1 = 34.1\,\text{mm}$,
- $r_2 = 44.6\,\text{mm}$,
- $p_1 = 20.5\,\text{mm}$,
- $p_2 = 49.9\,\text{mm}$, and
- $D = 488.2\,\text{mm}$.

The model of the optimal quad array with the incorporated feeding network, the 3-D radiation pattern and ϕ-cut ($\phi = 0$) of the radiation pattern of this antenna at 1 GHz are shown in Figs. 6.5, 6.6a, and 6.6b, respectively. The results in Figs. 6.3b and 6.4a compared with the results shown in Fig. 6.6 confirm that the feeding network has negligible influence on the radiation properties of the antenna. The optimal radii of the first and the last turn have changed for less than 10 % (in comparison with the basic design, Subsection 6.4). However, the optimal pitches of the first and the last turn are increased due to the incorporated feeding network. From the practical point of view, this change is favorable, since it leads to shortening the antenna wires, i.e., the fabrication requires less material. The distance between the array elements, D, decreases for more than 15 % for the quad array with the incorporated feeding network in comparison with the basic design.

The gain, axial ratio, and reflection coefficient are analyzed within the frequency range from 0.8 GHz to 1.5 GHz (Fig. 6.7). The gain is above 20 dBi from 0.94 GHz to 1.27 GHz, which is an almost 33% bandwidth. The axial ratio within this frequency range is below 1.5 and the reflection coefficient is below −9.3 dB. The wider bandwidth is expected since now the optimization is done

in a frequency range instead at the single frequency. Hence, the designed quad array with the feeding network fulfills the design specifications. The next step is design verification through measurements of a fabricated prototype.

(a)

(b)
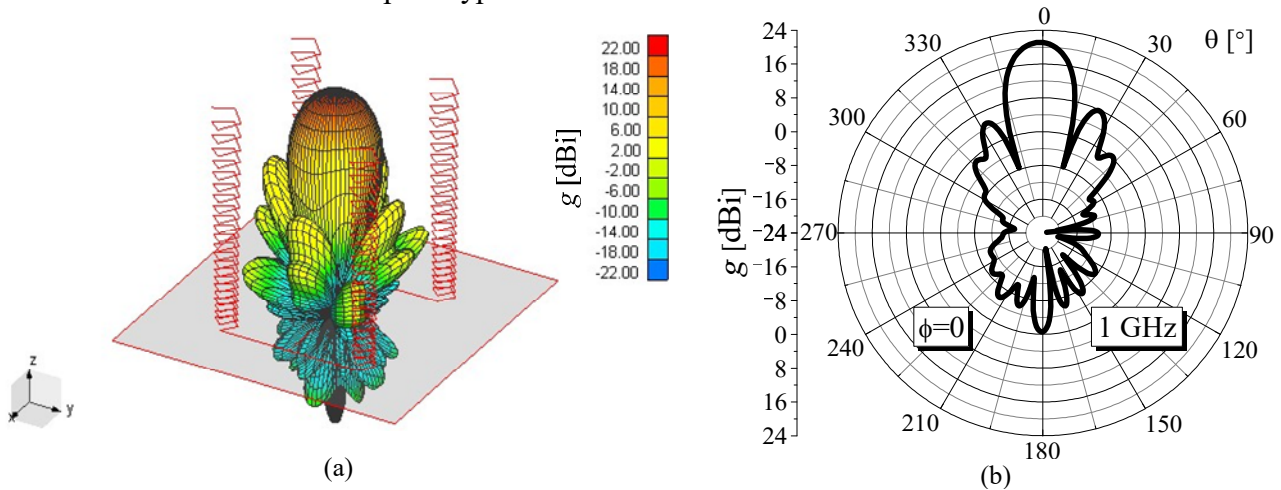
Figure 6.6. Optimal quad array with the feeding network at 1 GHz: (a) 3-D radiation pattern [88] and (b) ϕ-cut of the radiation pattern [88].

(a)

(b)
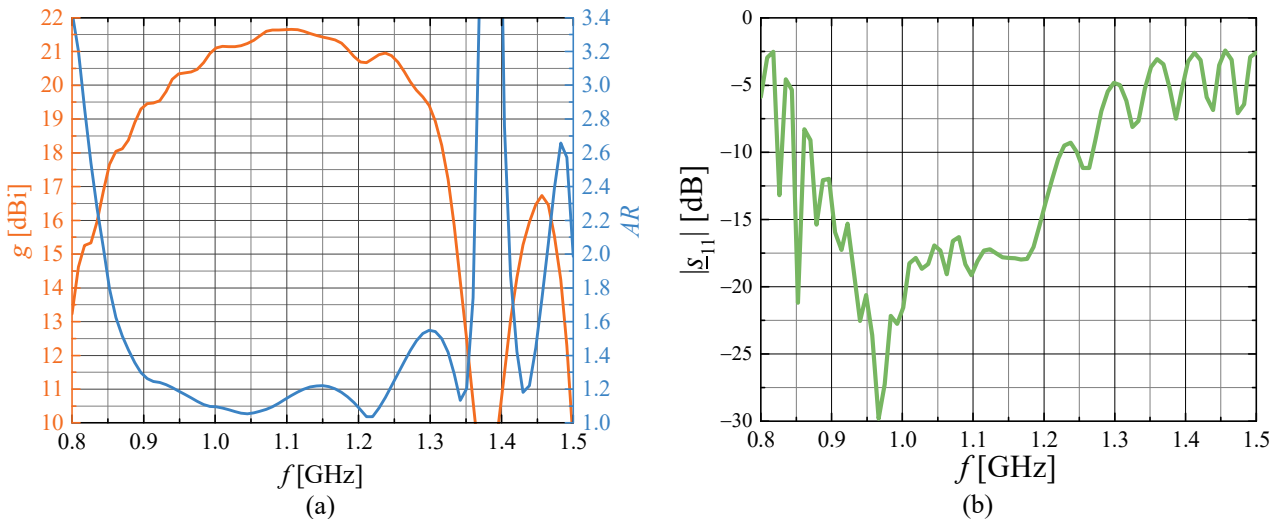
Figure 6.7. Optimal quad array with feeding network: (a) gain and axial ratio [88] and (b) reflection coefficient at the feeding point of the quad array versus frequency [88].

6.7. Prototype of quad array

The fabricated prototype is used for the design verification. The prototype consists of four identical nonuniform helical antennas, the feeding network, and the ground plane. The four helical antennas are designed to be identical. However, due to manual wire winding, small discrepancies are present. Therefore, the feeding network is designed to enable individual testing of each helical antenna, pairs of antennas (connected by the transmission lines of the characteristic impedance Z_{c1}), and the entire quad array. The feeding network keeps the H-shape.

The supporting structure for each single helical antenna is realized following the same procedure and choosing the same technology as described in Subsection 5.3. The wire conductor of radius 0.6 mm is wound on the supporting structure. The assembled single helical antenna is shown in Fig. 6.8a. The reflection coefficients of helical antennas are firstly measured independently in the frequency range from 0.8 GHz to 1.2 GHz. The measured reflection coefficients, with respect to 150 Ω, are shown in Fig. 6.8b. These results confirm that four helical antennas are almost identical despite the small differences due to manual winding. Further, these results are used to additionally optimize the feeding network.

(a)   (b)
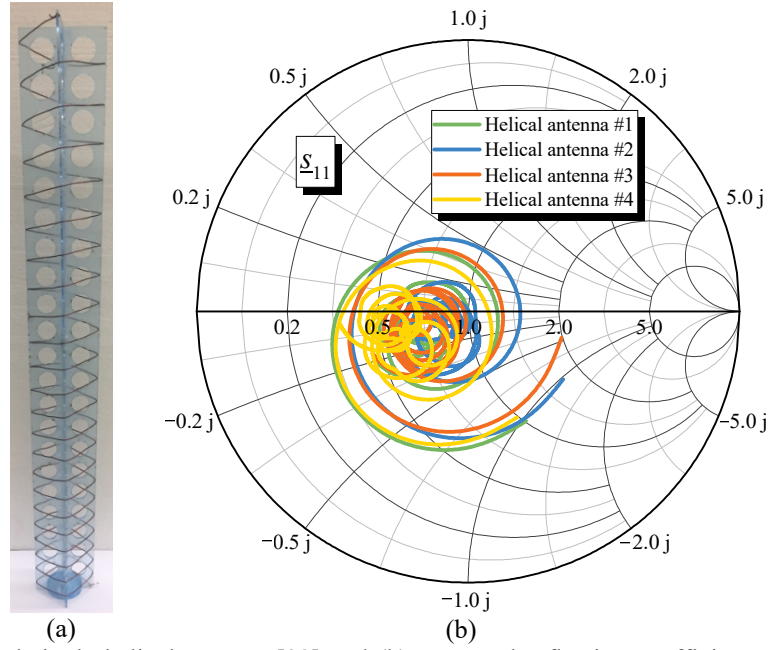
Figure 6.8. (a) Assembled single helical antenna [88] and (b) measured reflection coefficients of helical antennas that make up quad array with respect to $150\ \Omega$ in the frequency range from 0.8 GHz to 1.2 GHz [88].

During the fabrication of the feeding network (shown in Fig. 6.5), we faced difficulties to achieve and maintain the required positions of the wires. Namely, the required height of the wires above the ground plane is almost impossible to maintain precisely along the wires.

To overcome this problem, we changed the technology for the fabrication of the feeding network and realized the feeding network by the printed-circuit technique, on FR-4 substrate. In order to minimize the influence of the substrate (in particular, to reduce losses), the transmission lines are designed as inverted microstrips [124], whose cross-section is shown in Fig. 6.9. The issue of mechanical stability of the feeding network is solved by inserting acrylic-glass spacers between the FR-4 substrate and the ground plane, all along the edges of the lines. The thickness of the substrate and air layer (i.e., the height of the spacers) are $h_\mathrm{s} = 0.5\,\mathrm{mm}$ and $h_\mathrm{a} = 2\,\mathrm{mm}$, respectively, whereas the thickness of the metallization is $t = 36\,\mu\mathrm{m}$.
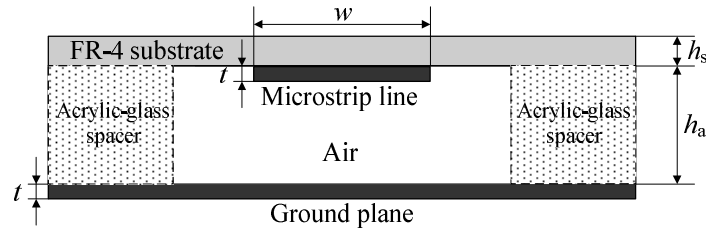
Figure 6.9. Cross-section of inverted microstrip line [88].

The characteristic impedances of the inverted microstrip lines (i.e., the widths of microstip lines) are fine-tuned in Microwave Office (MWO) [125], using the model shown in Fig. 6.10. In this model, the measured reflection coefficients (shown in Fig. 6.8b) are used. The measured reflection coefficients are imported into the model via subcircuits "S11_1", "S11_2", "S11_3", and "S11_4". The transmission lines (of characteristic impedances Z_c1 and Z_c2), that make up H-shaped feeding network, are realized in the model using the subcircuits "Zc1" and "Zc2" shown in Fig. 6.10. Fine-tuning is applied to the microstrip-line widths in these two subcircuits, whereby the reflection coefficient of the quad array is monitored. The resulting line widths are 0.6 mm and 3.4 mm, which correspond to $Z_\mathrm{c1} = 156\,\Omega$ and $Z_\mathrm{c2} = 87\,\Omega$, respectively. The corresponding reflection coefficient of the quad array is shown in Fig. 6.11a. The reflection coefficient is below $-10\,\mathrm{dB}$ in almost the whole frequency range from 0.8 GHz to 1.2 GHz (namely, from 0.815 GHz to 1.2 GHz). The simulated input impedance ($\underline{Z} = R + jX$) of the quad array is shown in Fig. 6.11b. At the operating frequency (1 GHz), $\underline{Z} = (37.53 - j\,7.17)\,\Omega$.
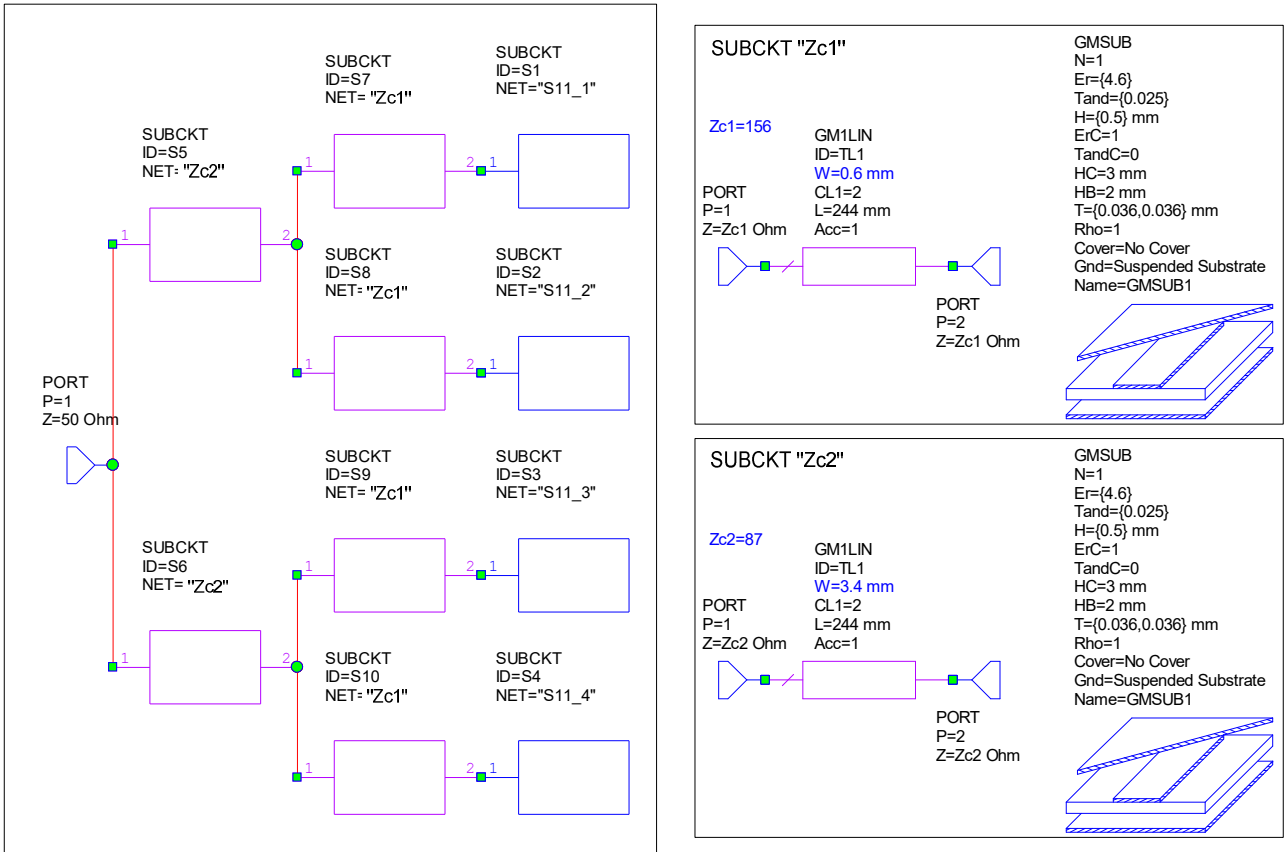
Figure 6.10. MWO model of the feeding network realized in inverted-microstrip technology.
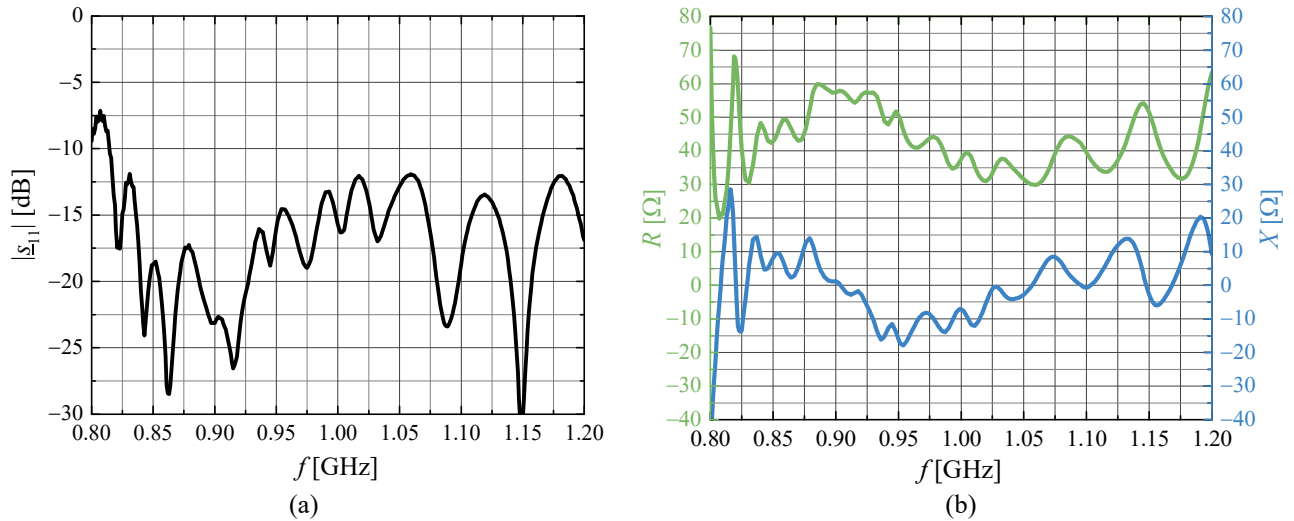
Figure 6.11. Simulated (a) reflection coefficient and (b) input impedance of the quad array.

The ground plane of the quad array is manufactured as a square aluminum plate of a side 1 m and thickness 2 mm. To increase the rigidity of the structure, aluminum tubes are placed along the edges of the plate on the underside (Fig. 6.12a).

The fabricated, fully-assembled quad array with the incorporated H-shaped feeding network is shown in Fig. 6.12b. The inset in Fig. 6.12b shows more details on how the inverted microstrip lines are interconnect and fixed to the ground plane.

(a)   (b)
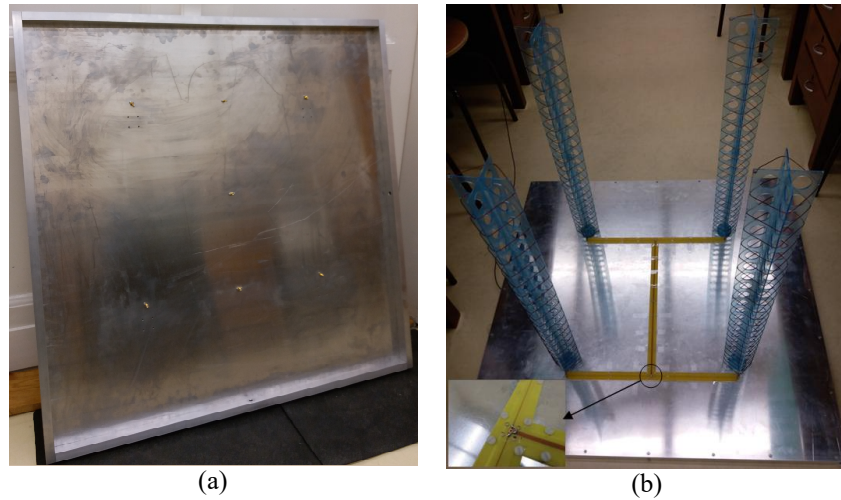
Figure 6.12. (a) Bottom side of aluminum plane used as a ground plane and (b) fully-assembled quad array [88].

6.8. Measurements of quad array

The fabricated prototype of the quad array (shown in Fig. 6.12b) is measured in Idvorsky laboratories [122]. The first measurement setup is the same as for the measurements of the nonuniform helical antenna (explained in Subsection 5.4).

Firstly, the reflection coefficient of the quad array (with respect to $50\,\Omega$) is measured and compared with the simulated reflection coefficient (Fig. 6.11a) in Fig. 6.13. As in the case of the simulated reflection coefficient, the measured reflection coefficient is also below $-10\,\mathrm{dB}$ in almost the entire considered frequency range (namely, from 0.81 GHz to 1.17 GHz).

Further, the measurement setup that consists of the fabricated quad array and a well-documented in-house made Vivaldi antenna is utilized (Fig. 6.14). As it is explained in Subsection 5.4, in order to estimate the gain and the radiation pattern of the quad array (which is circularly polarized), two sets of measurements are necessary. These sets correspond to two linear polarizations; hence, the quad array is placed in two different orientations. When the middle section of the feeding network (the transmission lines of the characteristic impedance Z_{c2}) is positioned horizontally (parallel to the floor of the chamber), we refer to this orientation as "horizontal", whereas when the middle section is vertical (perpendicular to the floor), we refer to this orientation as "vertical". The transmission coefficients between the quad array and the Vivaldi antenna are measured (and simulated) when the distance between the ground plane of the quad array and the tip of the Vivaldi antenna is $D_{\mathrm{Quad\text{-}Vivaldi}} = 1575\,\mathrm{mm}$ (Fig. 6.13b). In the frequency range from 0.9 GHz to 1.1 GHz, the discrepancy between the simulated and measured transmission coefficients is less than 1.5 dB. At 1 GHz, the simulated and measured results agree almost perfectly.

(a)   (b)
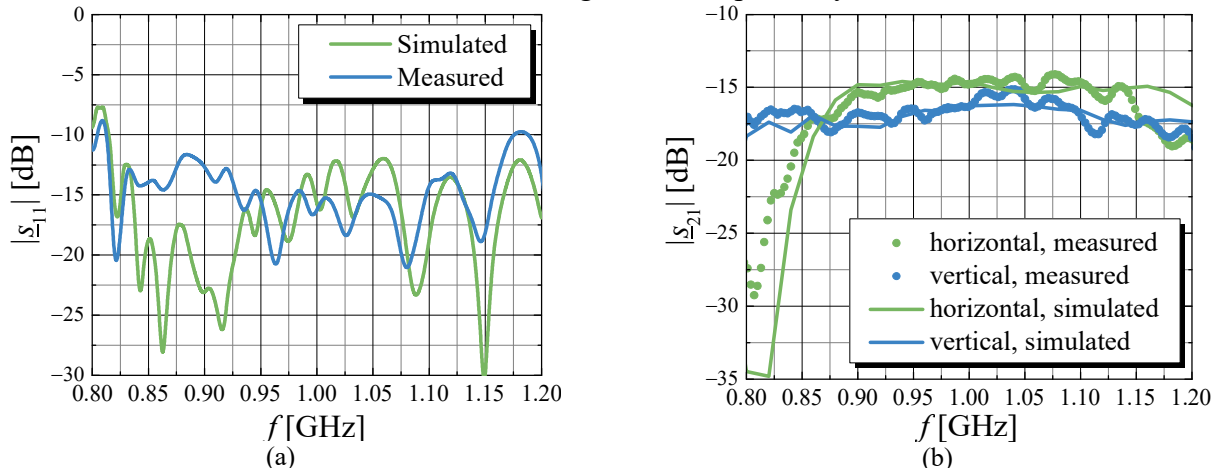
Figure 6.13. Simulated and measured (a) reflection coefficient of the quad array [88] and (b) transmission coefficient between the quad array and Vivaldi antenna [88].
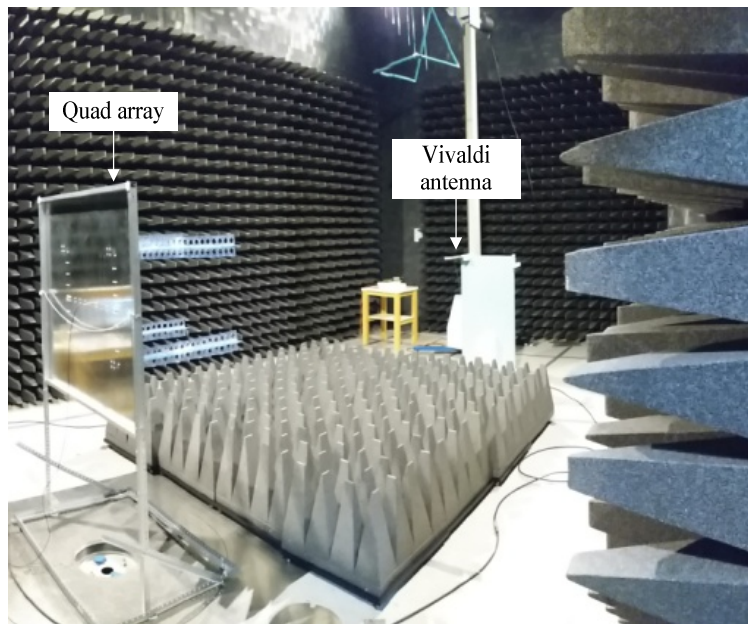
Figure 6.14. Measurement setup consists of quad array and Vivaldi antenna [88].

The radiation patterns of the quad array, in the $\phi = 0$ cut, are measured for both the horizontal and vertical orientations, in the frequency range from 0.95 GHz to 1.1 GHz, and $D_{\text{Quad-Vivaldi}} = 4020\,\text{mm}$. The simulated and measured transmission coefficients, normalized to the maximal level, are compared in Figs. 6.15 and 6.16. The simulated and measured results agree almost perfectly within the main lobe at all considered frequencies and for both orientations.
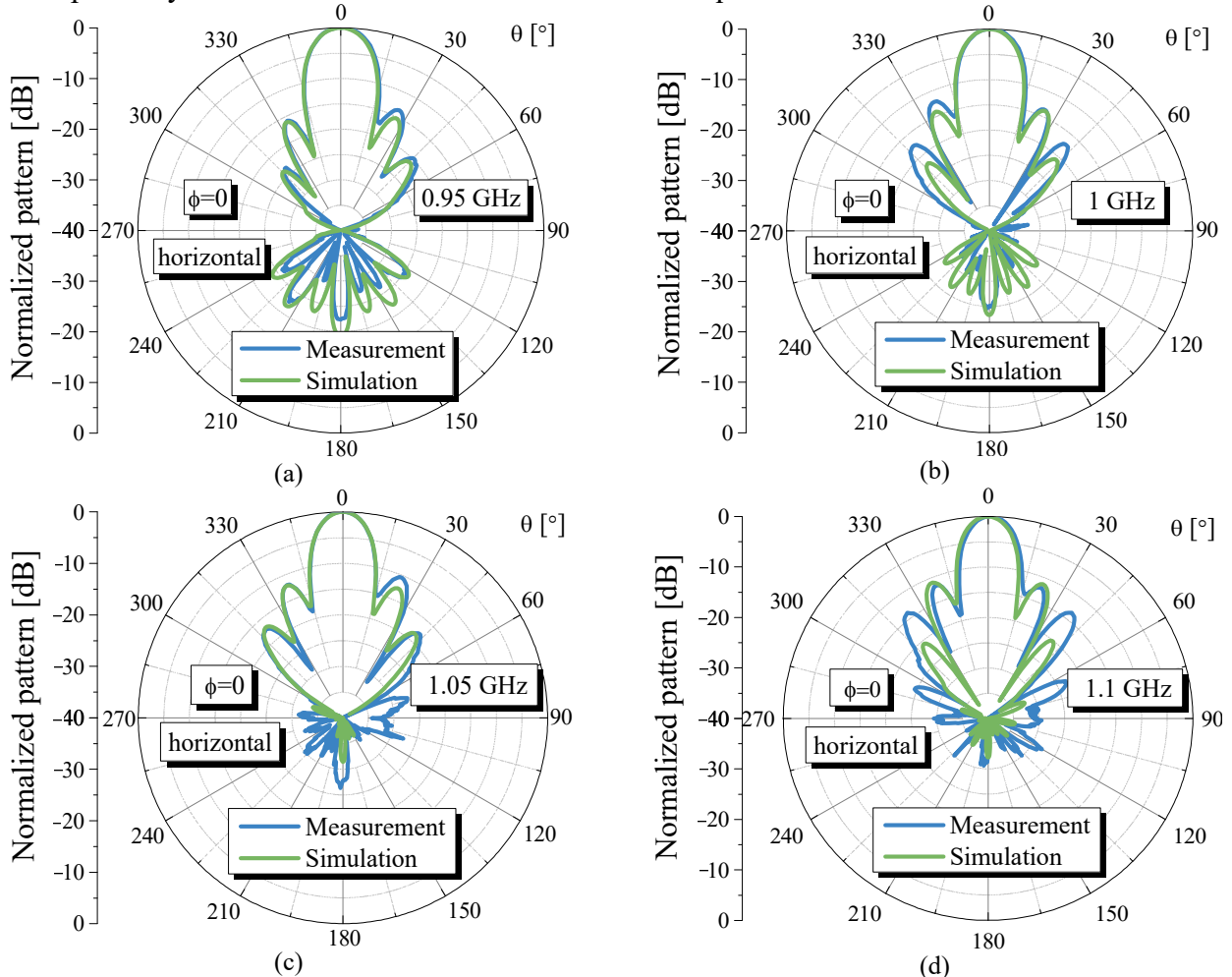
Figure 6.15. Cuts ($\phi = 0$) for the horizontal orientation at: (a) 0.95 GHz [88], (b) 1 GHz [88], (c) 1.05 GHz [88], and (d) 1.1 GHz [88].
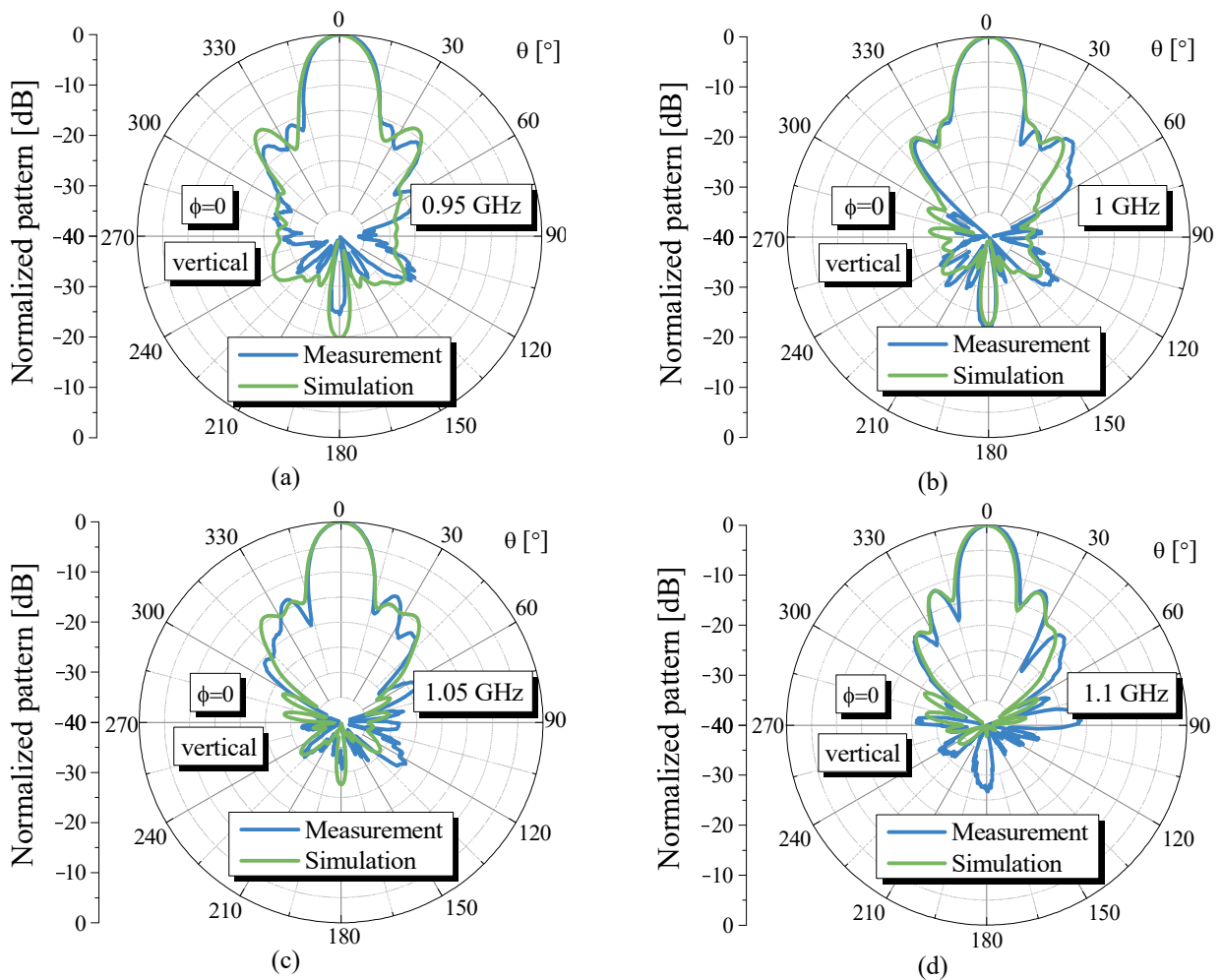
Figure 6.16. Cuts ($\phi = 0$) for the vertical orientation at: (a) 0.95 GHz [88], (b) 1 GHz [88], (c) 1.05 GHz [88], and (d) 1.1 GHz [88].

Finally, another measurement setup (Fig. 6.17) is utilized. In this measurement setup, a signal generator Rohde Schwartz SML03 (whose power level is 0 dBm at 0.99 GHz) is connected to the quad array. A Teseq CLB 6144 BiLog antenna is used as the receiving antenna. Using a Teseq SMR4503 EMI receiver, the electric field is measured at a 3000 mm distance. The simulated and measured normalized radiation patterns (normalized to the maximal level) at 0.99 GHz for both orientations (horizontal and vertical) are compared in Fig. 6.18.
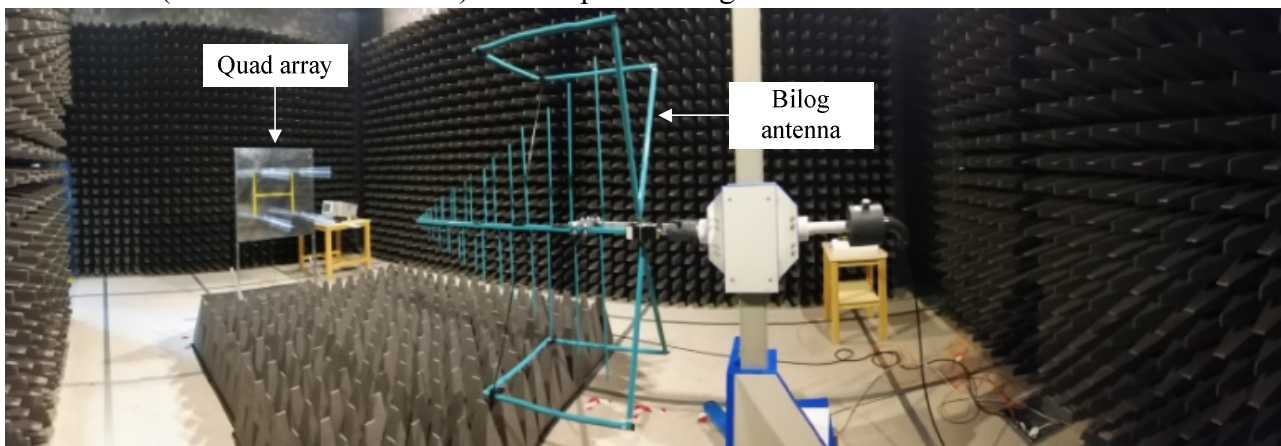
Figure 6.17. Measurement setup consists of quad array and bilog antenna [88].
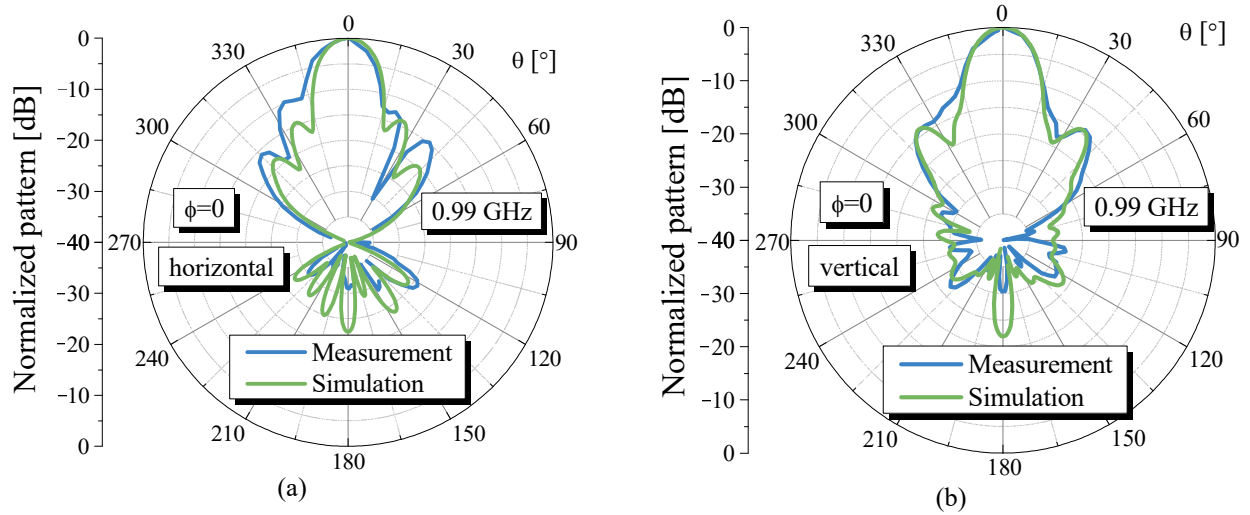
Figure 6.18. Normalized level of electric field for (a) horizontal [88] and (b) vertical orientation at 0.99 GHz [88].

Finally, it can be concluded that the simulated and measured results of the designed and fabricated quad array show good agreement. At the operating frequency 1 GHz the gain is 21 dB, whereas in the frequency range from 0.9 GHz to 1.1 GHz the gain is $(20.5 \pm 1.5)\,\text{dBi}$.

7. Design of optimal quad arrays of nonuniform helical antennas with linearly varying geometrical parameters

In this chapter, design equations for the nonuniform helical antennas with linearly varying geometrical parameters (from Chapter 3) are utilized for the design of quad arrays (2×2 arrays of helical antennas). The design equations from Chapter 3 are used for calculating the optimal geometrical parameters of the nonuniform helical antennas that make up the quad array. Further, optimizations are run in order to find the optimal locations (i.e., distances) of the array elements. These optimizations allow expanding the design equations by an equation for the optimal locations of the array elements. Hence, the complete design procedure for quad arrays is obtained. For the sake of comparison, additional optimizations are performed, where both the geometrical parameters of the helical antennas and their locations are optimized.

Optimizations are made utilizing helical antennas located above an infinite ground plane. Finally, with the purpose to obtain practically realizable designs, the infinite ground plane is replaced by a flat, finite-size square ground plane and the influence of this ground plane on the array gain is investigated.

7.1. Quad array geometry

As it is stated in Subsection 6.2, the quad array consists of four (2×2) identical helical antennas (Fig. 6.1a). The geometry of helical antennas that make up the array is explained in Subsection 2.1.1. The optimal parameters that define the geometry of nonuniform helical antennas with linearly varying geometrical parameters (radii and pitch angles of the first and the last turn) can be calculated from the design equations (3.13), (3.14), (3.19), and (3.20). The radii and pitch angles of other turns can be calculated from (2.1) and (2.2). In the quad array, the helical antennas are located above an infinite ground plane at the vertexes of an imaginary square of a side D. The generators, located between the ground plane and the first turn of the helix, feed each helical antenna. All generators are of the same amplitude and phase. The antenna conductor is a wire of a circular cross-section.

7.2. Optimization procedure

The utilized optimization procedure is similar to the optimization procedure explained in Subsection 3.1 for the optimization of the geometrical parameters of a single helical antenna. Namely, the optimization goal is to maximize the partial gain for the circular polarization in the main radiating direction (see Appendix A.1). Hence, the cost function is again defined by (3.1). In the case of the quad array, the optimization variable is the distance between the adjacent helical antennas, D, whereas the optimal geometrical parameters of helical antennas that make up the quad array are calculated using the design equations from Subsection 3.2.3.

For these optimizations we firstly utilized the systematic search, since there is only one optimization variable. However, we found that the same (or even better) results (i.e., higher gain of the optimal arrays) are achieved utilizing a two-stage optimization with the same total number of

evaluations of the cost function. In the first optimization stage (maximum of) 500 iterations of the particles swarm optimization (PSO) algorithm [116], [117] are utilized (the swarm size is 10), whereas in the second stage (maximum of) 200 iterations of the Nelder-Mead simplex [115] are launched from the best-found solution within the first optimization stage.

The optimizations are performed for different axial lengths (L) of the single helical antennas and radii of the helical conductors (r_w), within the ranges defined in Subsection 3.2.2. Since the design equations are used for calculating the geometrical parameters of the helical antennas, we consider normalized conductivities that are bigger than $\sigma_{min}\lambda$, i.e., the conductivities for which the design equations are valid.

The constraints for the optimization variable D are estimated for each considered axial antenna length (L) following the similar investigations as explained in Subsection 6.3. Namely, we vary the distance D (normalized to the wavelength at the operating frequency) and simulate the radiation pattern of the quad arrays at the operating frequency. As it is explained in Subsection 6.3, when D is small, the sidelobes are low, but the gain in the main radiating direction is also small. When D increases, the gain in the main radiating direction increases, but this is accompanied with the increased sidelobes. In order to utilize the criteria for defining the constrains of the optimization variable D (i.e., $D_{min} \leq D \leq D_{max}$), we perform a set of simulations for various L, assuming the wire radius to be 0.0002λ and the wire conductivity to be σ_{ref}.

Firstly, we simulate the radiation pattern for D within the wide range from 1λ to 5λ, with the step of 0.2λ, and determine the maximal achieved gain (for each L) in the main radiating direction, g_{max}. Finally, we define the following criteria (these criteria are indicated in Fig. 7.1a):

- D_{min} corresponds to the maximal considered distance between the adjacent array elements for which the gain in the main radiating direction is less than 90 % of g_{max},
- D_{max} corresponds to the maximal considered distance between the adjacent array elements for which the level of the first sidelobes is less than 80 % of g_{max}.

The utilized constrains of the optimization variable D are summarized in Table 7.1, whereas the radiation patterns (the $\phi = 0$ cuts) for various axial lengths (L) and corresponding D_{min} and D_{max} are shown in Fig. 7.1. Angles ϕ and θ are measured from the x axis (in the xOy plane) and the z axis to the considered direction, respectively (Fig. 6.1a).

Table 7.1.
Constrains for the optimization variable D.

L	D_{min}	D_{max}
2λ	1.2λ	3λ
3λ	1.4λ	3.4λ
4λ	1.6λ	3.8λ
5λ	1.6λ	4λ
7λ	1.6λ	4.4λ
10λ	1.8λ	5λ
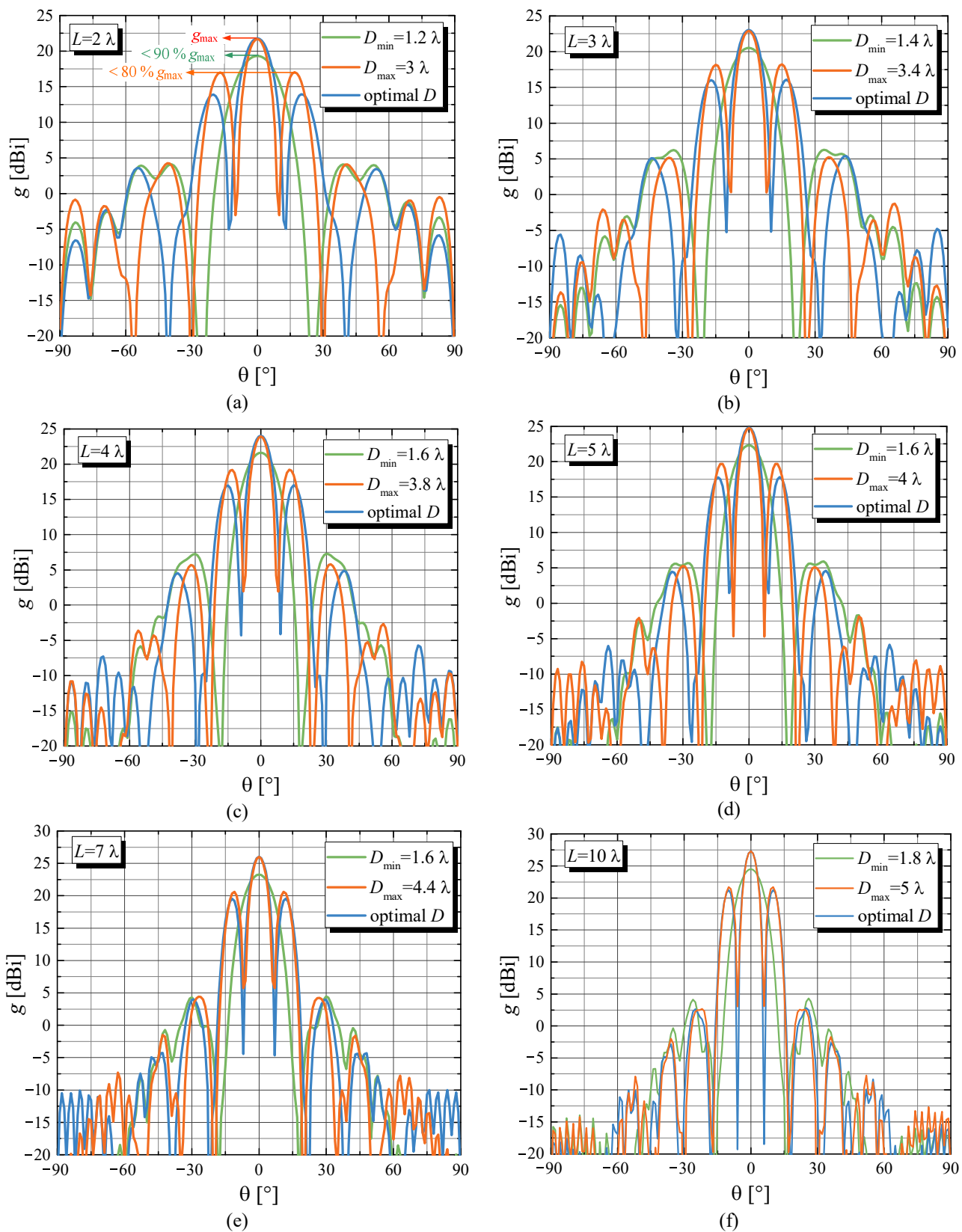
Figure 7.1. Radiation patterns ($\phi = 0$ cuts) of the quad arrays for finding the constrains of the optimization variable D for (a) $L=2\,\lambda$, (b) $L=3\,\lambda$, (c) $L=4\,\lambda$, (d) $L=5\,\lambda$, (e) $L=7\,\lambda$, and (f) $L=10\,\lambda$.

7.3. Optimization results

The optimizations are run for various axial lengths, wire radii, and wire conductivity σ_{ref} calculated from (3.7). The geometrical parameters of the helical antennas are calculated from design equations (3.13), (3.14), (3.19), and (3.20), and the distances between the adjacent array elements are optimized. All optimizations are run at 300 MHz, but all results are normalized to the corresponding wavelength. Hence, they can be scaled to an arbitrary frequency according to the similitude theorem (see Appendix B).

The optimal distances D for different axial lengths and wire radii are shown in Fig. 7.2. These results show that the wire radius negligibly influences the optimal distance. Further, it can be noticed that the optimal distance D shows nearly logarithmic dependence on the axial length. This conclusion is very useful, since it allows fitting the optimal values of D and formulating an equation for calculating these optimal values. This equation has the form $D/\lambda = A_D \log_{10}(L/\lambda) + B_D$. By fine-tuning the constants A_D and B_D, the optimal distance D can be approximated by

$$\frac{D}{\lambda} = 3.41 \log_{10}\left(\frac{L}{\lambda}\right) + 1.15 . \tag{7.1}$$

The optimal distances calculated using (7.1) are indicated by the solid line in Fig. 7.2.
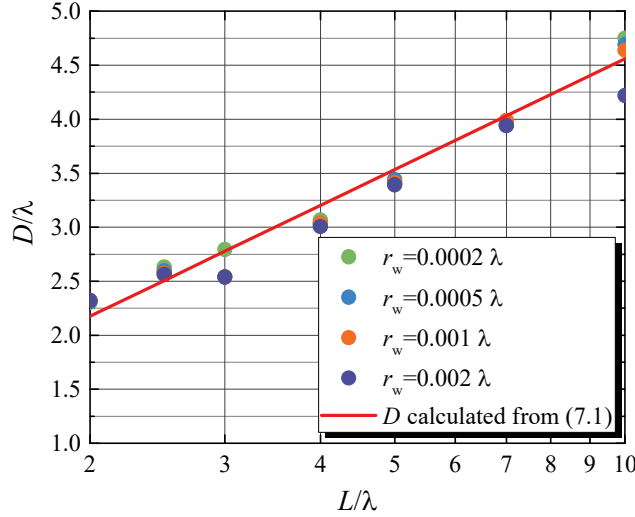
Figure 7.2. Optimal distance D.

The radiation patterns ($\phi = 0$ cuts) for the optimal distances D are shown by blue solid lines in Fig. 7.1 and compared with the radiation patterns of the quad arrays when the distances between adjacent array elements are D_{min} and D_{max}. In the main radiating direction, the gain is almost the same as in the case when the distance is D_{max}, whereas the first sidelobes are lower. This is expected, since the level of the first sidelobes decreases when the distance decreases; hence, for the distance D ($D < D_{max}$) the level of the first sidelobes is lower than when the distance is D_{max}.

For the sake of comparison, we perform additional optimizations where all geometrical parameters of the quad arrays are optimized. Namely, the optimization variables are the radii and the pitch angles of the first and the last turn of the helical antennas, as well as the distance D. For this optimization we utilize the same setup (optimization algorithms, constrains for the optimization variables, cost function) as for the optimization of nonuniform helical antennas (Subsection 3.1) whereas constrains for the optimization variable D are the same as defined in Table 7.1.

Fig. 7.3 compares the gain (at the operating frequency in the main radiating direction) of:
- the quad arrays where only the distance D is optimized and the geometrical parameters of the helical antennas are calculated from design equations (referred to as "optimal"),
- the quad arrays where all geometrical parameters are optimized (referred to as "optimal all"), and

- the quad arrays where the distance D is calculated from (7.1) and the geometrical parameters of the helical antennas are calculated from design equations (referred to as "calculated").

The maximal discrepancy between the gain in the case referred to as "optimal" and the gain in the case when D is calculated from (7.1) is less than 0.04 dB, i.e., this discrepancy is negligible. The discrepancy between the gain in the case referred to as "optimal all" and the gain in the case when D is calculated from (7.1) is less than 0.12 dB, which is also practically negligible.

Since it is expected that the quad array increases the gain for around 6 dB in comparison with a single helical antenna of the same axial length, in Fig. 7.3 the gain calculated from (3.23) increased by 6 dB is also indicated (by solid lines). These results show that the quad array increases the gain by more than 6 dB. The minimal increase is by 6.19 dB.
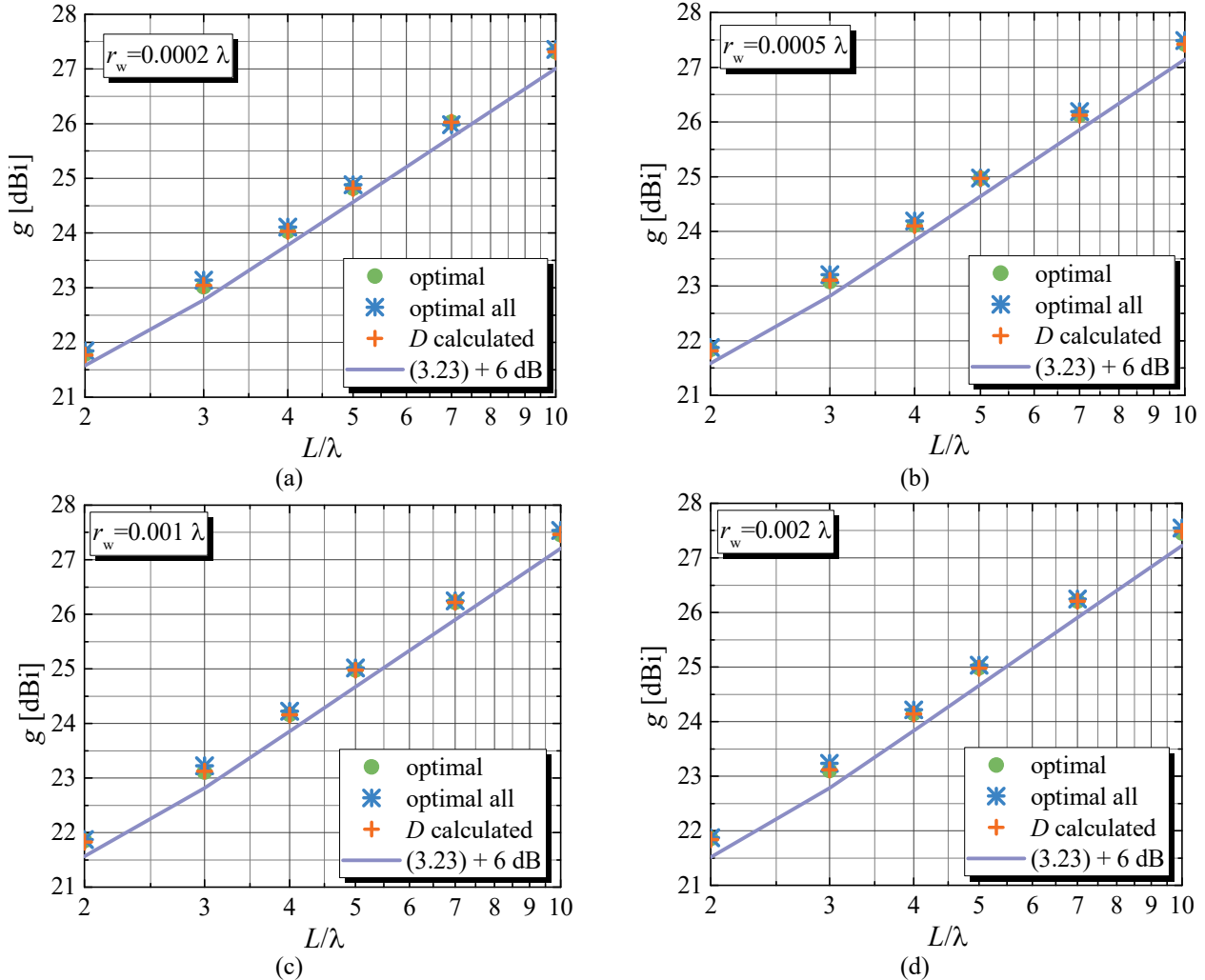
Figure 7.3. Comparison of the gain of the quad arrays where geometrical parameters of helices are calculated from the design equations and the distance D is optimized ("optimal"), where geometrical parameters and the distance D are optimized ("optimal all"), and where geometrical parameters of helices are calculated from the design equations and the distance D is calculated from (7.1) ("calculated") for (a) r_w=0.0002 λ, (b) r_w=0.0005 λ, (c) r_w=0.001 λ, and (d) r_w=0.002 λ.

The optimal distances D obtained from the additional optimization when all geometrical parameters are optimized are compared in Fig. 7.4a with the optimal distances D calculated from (7.1). These results confirm that (7.1) also successfully fits these optimal distances D. In Fig. 7.4b the geometrical parameters of the helices obtained from the optimization of the quad array are compared with the geometrical parameters calculated from the design equations. The optimal geometrical parameters are not perfectly fitted by the design equations formulated for the design of a single nonuniform helical antenna. However, the perfect fitting is not the main evaluation criterion. The gain of the designed antennas is of much greater significance and the fulfillment of that criterion is confirmed by the results shown in Fig. 7.3.
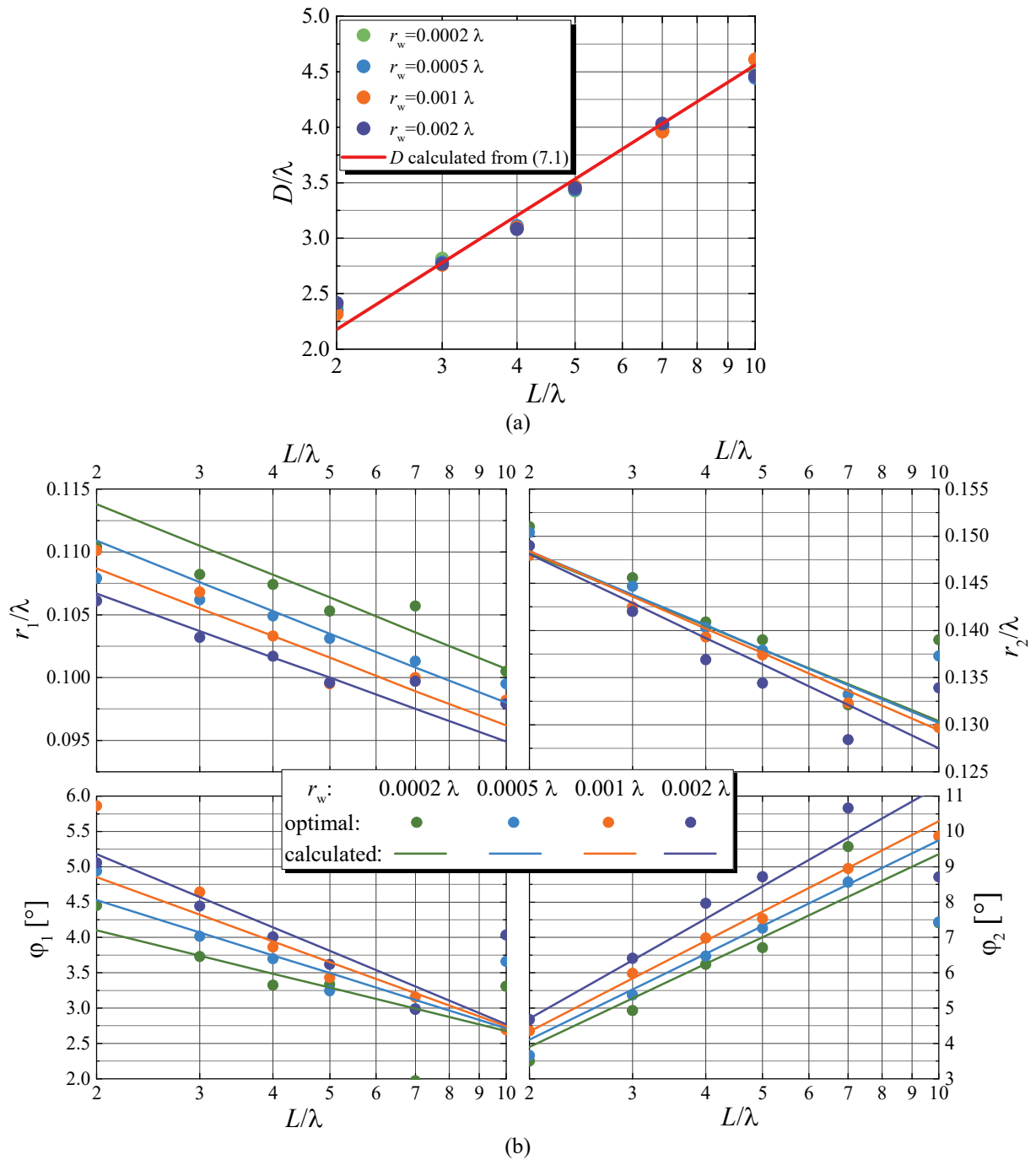
Figure 7.4. Comparison of: (a) the optimal distances D obtained from the optimization when all geometrical parameters are optimized and the optimal distances D calculated from (7.1), and (b) the geometrical parameters obtained from the optimization when all geometrical parameters are optimized and the geometrical parameters calculated from the design equations.

Further, the influence of the wire conductivity on the optimal distance between the adjacent elements is investigated. The optimization variable is again the distance D and the same optimization procedure is utilized. However, in this case we consider two extreme conductivities, σ_{min} and PEC. The optimal distances D obtained from these optimizations are compared with the optimal distances calculated from (7.1) in Fig. 7.5, whereas the gain of these antennas is shown in Fig. 7.6. Additionally, in Fig. 7.6 the gain of the single helical antenna calculated from (3.23) and increased by 6 dB is also indicated.

These results confirm that the optimal distance between the array elements does not depend on the wire conductivity. Hence, (7.1) can be used for calculating the optimal distances D for an arbitrary wire conductivity, as long as the design equations are valid (i.e., for the normalized conductivities $\sigma\lambda \geq \sigma_{min}\lambda$). Further, the design equations can be used for calculating the

geometrical parameters of the helices. These conclusions allow us to formulate the procedure for designing the quad arrays of nonuniform helical antennas with linearly varying geometrical parameters by expanding the previously formulated design procedure for nonuniform helical antennas.
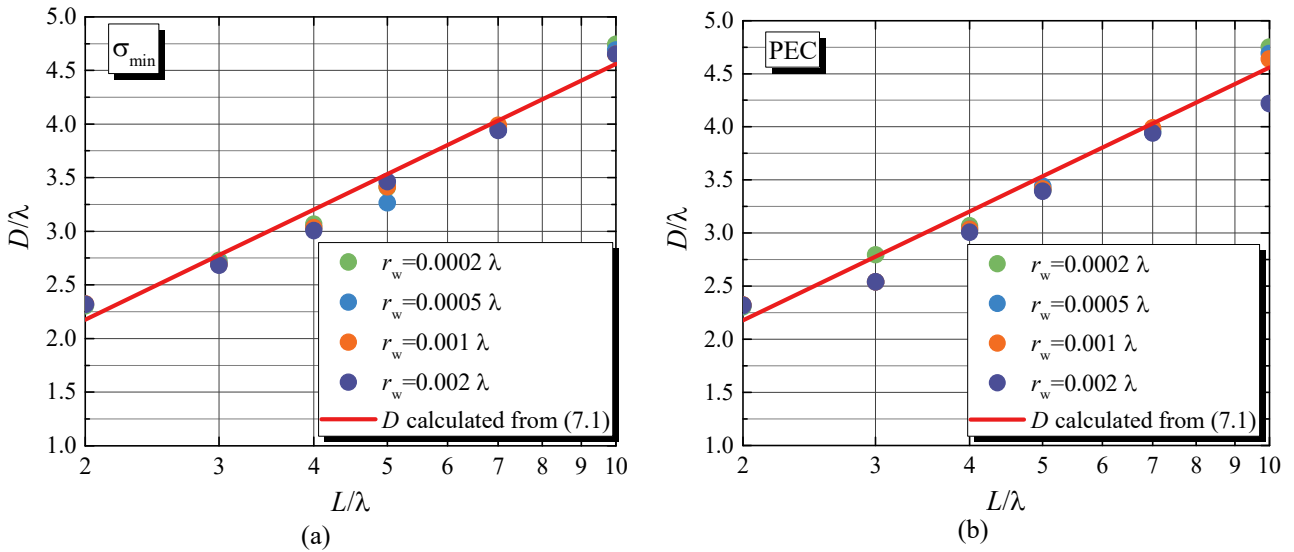
Figure 7.5. The optimal distances D for (a) σ_{min} and (b) PEC.
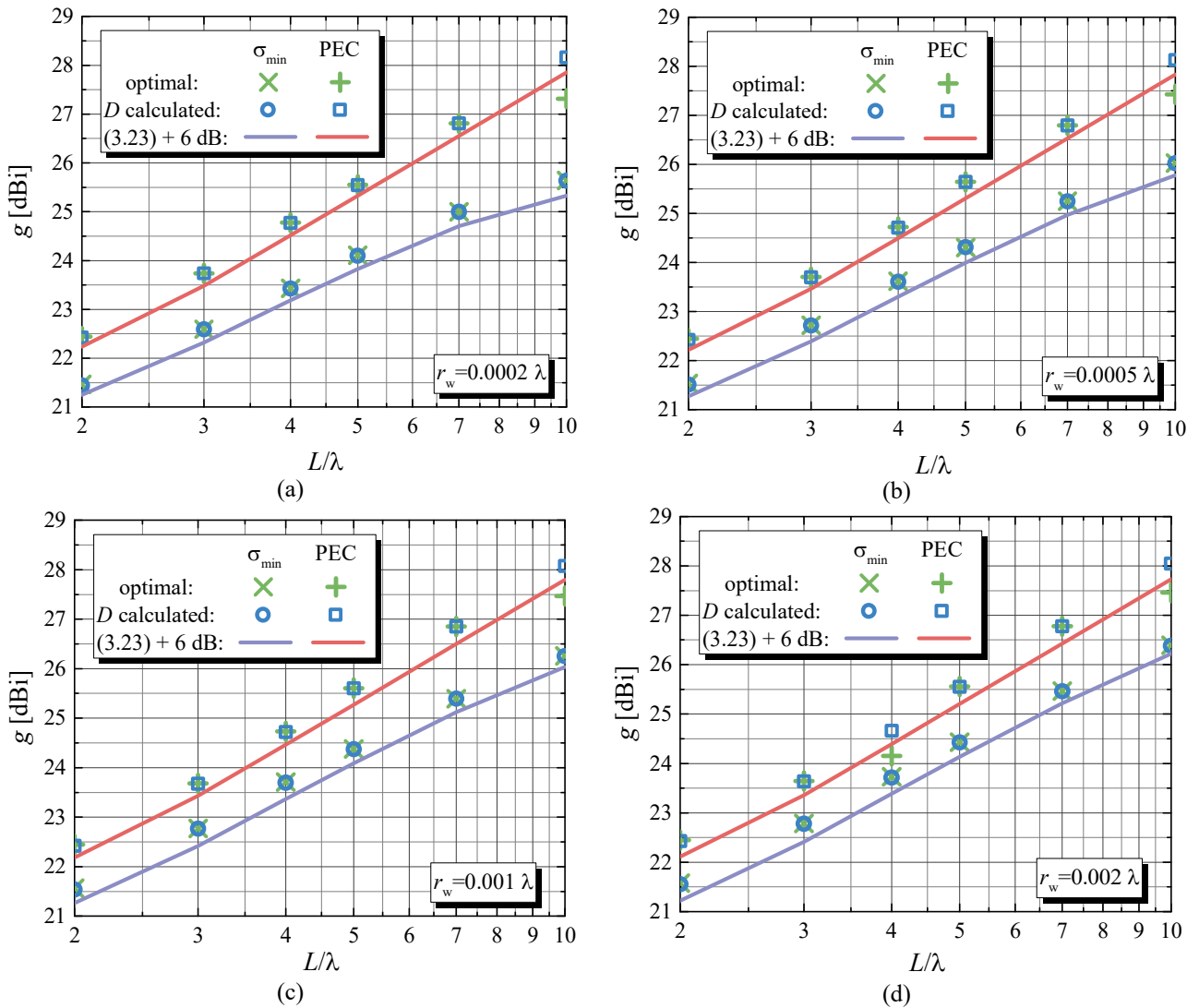
Figure 7.6. The gain of the quad array for the wire conductivity σ_{min} and PEC: (a) r_w=0.0002 λ, (b) r_w=0.0005 λ, (c) r_w=0.001 λ, and (d) r_w=0.002 λ.

Finally, we utilize the design equations (3.13), (3.14), (3.19), and (3.20) for calculating the geometrical parameters of helices and (7.1) for calculating the distance between adjacent elements, and design quad arrays for various axial lengths, wire radii, and a wide range of normalized wire conductivities (from $\sigma_{min}\lambda$ to $10^6\lambda$). Circular markers in Fig. 7.7 show the gain of these arrays. Additionally, we calculate the gain of the single helical antenna (from (3.23)) considering the same axial lengths, wire radii, and wire conductivities as for the quad arrays. The smallest discrepancy between the gain of the designed quad array and the gain calculated from (3.23) is 6.185 dB, whereas the largest discrepancy is 6.369 dB. Therefore, we can formulate an equation that estimates the gain of the designed quad array by adding the constant 6.185 to (3.23):

$$g\,[\text{dBi}] = 8.385\log_{10}\left(\frac{L}{\lambda}\right) + 13.48 - \frac{0.002983\frac{L}{\lambda}}{\left(\frac{r_w}{\lambda}\right)^{0.8411}\sqrt{\lambda\sigma}} + \frac{26.89}{\left(\frac{L}{\lambda}\right)^{6.763}} - 68.71\frac{r_w}{\lambda} + 6.185\,. \quad (7.2)$$

Solid lines in Fig. 7.7 indicate the gain calculated using (7.2). Note that (7.2) underestimates the gain (this property is obtained for the same reason as it is explained for (3.23)). The largest discrepancy between the simulated gain and the gain calculated from (7.2) is less than 0.2 dB.
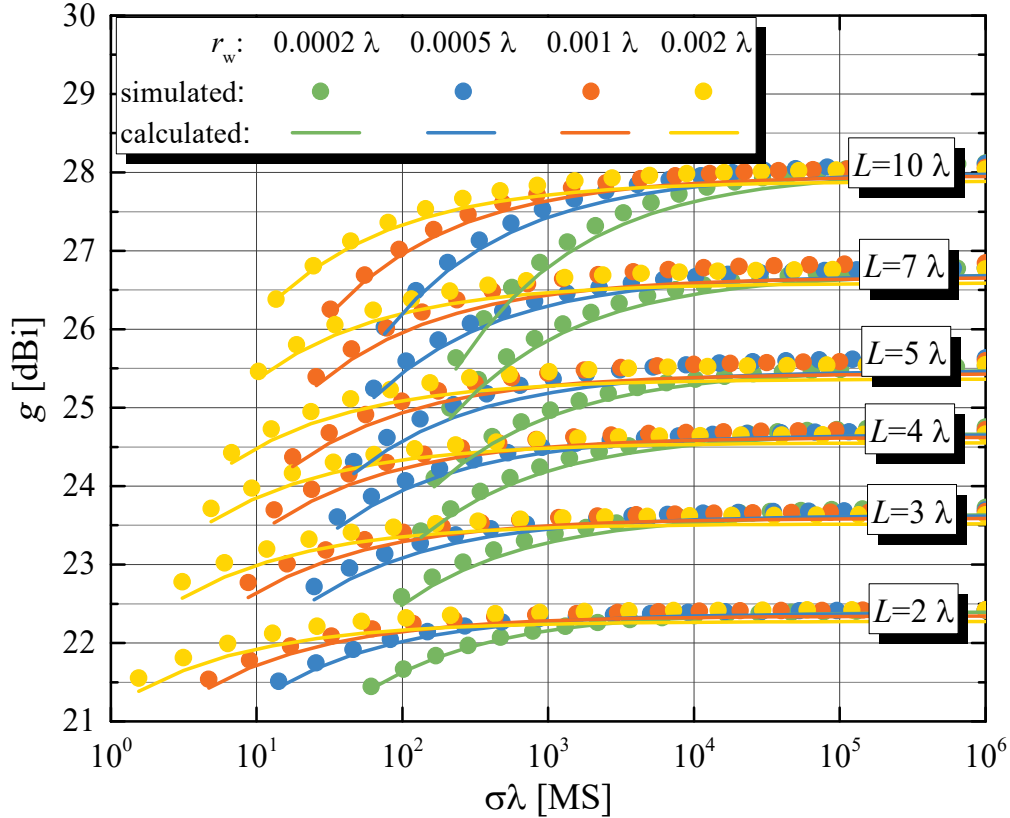
Figure 7.7. Gain of the designed quad arrays in wide range of the normalized conductivities.

7.4. Finite ground plane

The results presented in the previous subsections are obtained considering helices located above an infinite ground plane. This scenario is favorable for simulations (since it reduces the required computation time). However, for the practical purposes, the infinite ground plane has to be replaced by a finite-size ground plane. Therefore, in this subsection we consider helices located above a flat square-shaped ground plane of a side a (Fig. 6.1). The quad arrays are designed utilizing the design equations (3.13), (3.14), (3.19), and (3.20) for calculating the geometrical parameters of the helices, whereas the optimal distances between the adjacent elements are calculated from (7.1). The

influence of the finite-size ground plane is investigated in terms of the gain of the quad arrays at the operating frequency in the main radiating direction, for various axial lengths, wire radii, and wire conductivity σ_{ref}. The difference between the gain of the quad array located above finite ground plane and the gain of the corresponding quad array calculated from (7.2), i.e., the gain of the corresponding quad array located above infinite ground plane, is shown in Fig. 7.8.

These results confirm that the finite-size ground plane can replace the infinite ground plane without sacrificing the gain. Moreover, by appropriate choosing the ground plane dimension, a slightly higher gain can be achieved. However, this increase is lower than in the case of single helical antennas. (The influence of a finite ground plane on the gain of a single helical antenna is investigated in Subsection 4.3.)
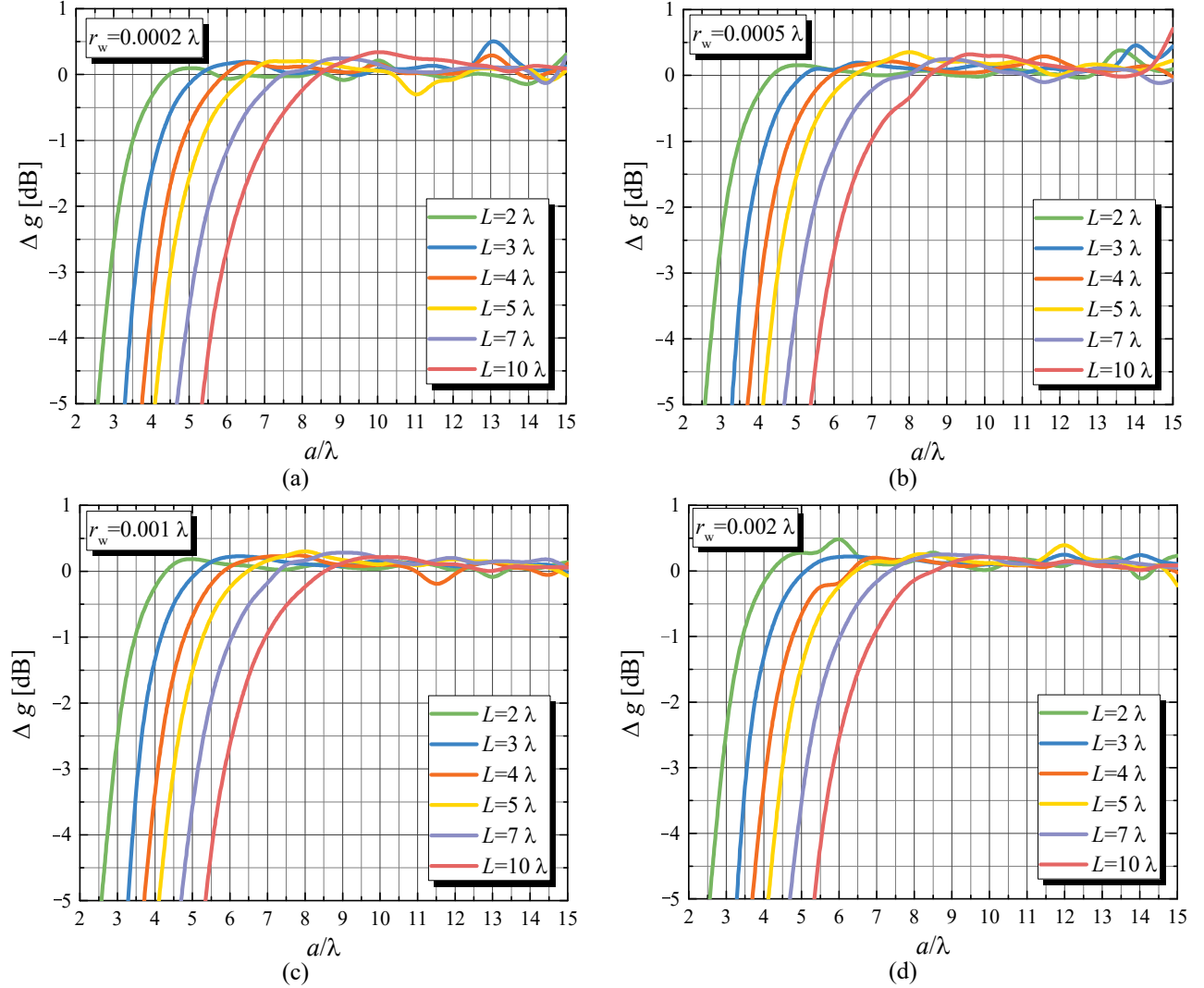
Figure 7.8. Differences between the gain of the designed quad arrays located above the ground plane of a finite dimension and the gain calculated from (7.2) for wire conductivity σ_{ref} and wire radius (a) r_w=0.0002 λ, (b) r_w=0.0005 λ, (c) r_w=0.001 λ, and (d) r_w=0.002 λ.

7.5. Design procedure

The results and conclusions presented within previous subsections allow us to formulate a procedure for designing quad arrays of nonuniform helical antenna with linearly varying geometrical parameters. This procedure is an extension of the design procedure for single helical antennas (formulated in Subsection 5.1), since it utilizes the design equations (3.13), (3.14), (3.19), and (3.20), but also (7.1) is included for calculating the optimal distance between adjacent array elements and the equation for gain estimation is rewritten; hence, the quad gain can be estimated using (7.2).

Finally, the procedure for designing the quad arrays of nonuniform helical antenna with linearly varying geometrical parameters is summarized by the flowchart shown in Fig. 7.9.

For the practical realization of the designed quad array, the infinite ground plane has to be replaced by a finite-size ground plane. For the selection of the appropriate dimension of the square-shaped ground plane and estimation of the gain difference due to the finite dimensions of the ground plane, results shown in Fig. 7.8 can be used.
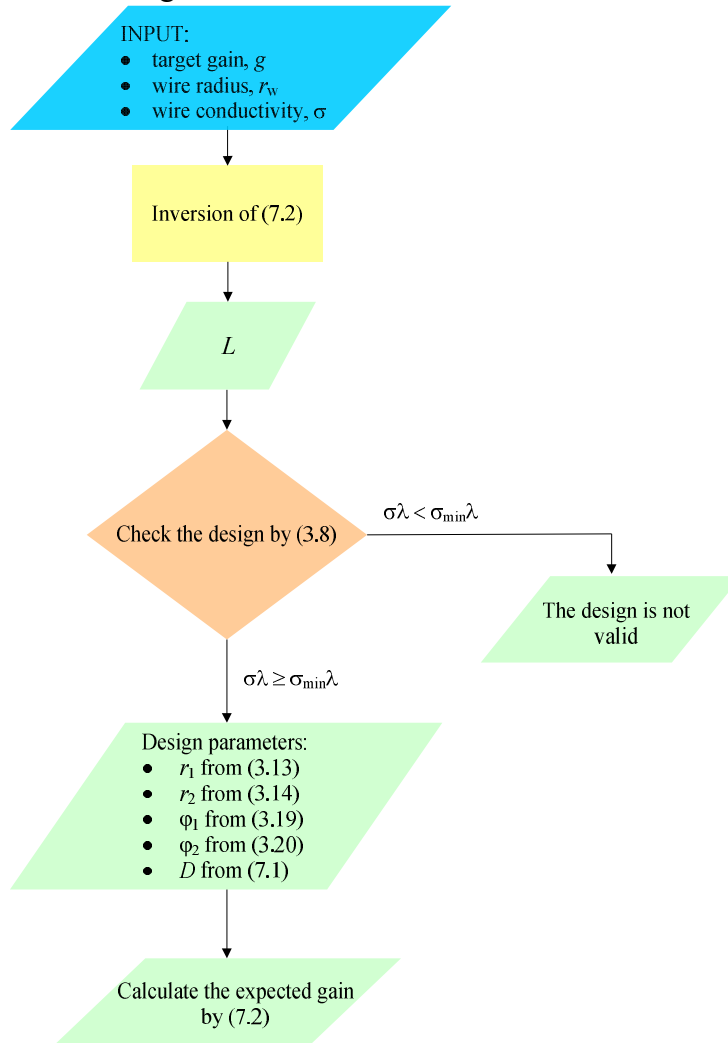
Figure 7.9. Flowchart of the procedure for designing quad arrays.

7.6. Comparison with quad arrays of uniform helical antennas

The quad arrays of nonuniform helical antennas, designed following the design procedure presented in Subsection 7.5, will be compared with the quad arrays of uniform helical antennas, optimized in this subsection.

The geometrical parameters of the uniform helical antennas that make up the quad arrays are calculated from (4.4) and (4.5). The distance between adjacent array elements, D, is optimized. For the optimization we utilize the same setup and procedure as for the quad arrays of nonuniform helical antennas (Subsection 7.3). We consider various axial antenna lengths, wire radii, and wire conductivity σ_{ref}, whereas the operating frequency is 300 MHz and the helices are located above an infinite perfectly conducting ground plane.

The optimal distances D are compared in Fig. 7.10 with D calculated from (7.1), whereas the gain of the optimal quads with uniform and nonuniform helical antennas is compared in Fig. 7.11.

The optimal distances D for the quad arrays with uniform helical antennas are smaller than the optimal distances for the quad arrays with nonuniform helical antennas. Namely, for shorter axial

antenna lengths the discrepancies of these optimal distances are around $0.25\,\lambda$, whereas for longer axial antenna lengths they are around $0.7\,\lambda$.

Further, the discrepancy between the gain of quad arrays of uniform and nonuniform helical antennas is between 1.4 dB (for shorter axial antenna lengths) and 2.2 dB (for longer axial antenna lengths). These discrepancies are similar to the discrepancies between the gain of single uniform and nonuniform helical antennas. Hence, the gain improvement, introduced by the nonuniform helical antennas in comparison with the uniform helical antennas, is maintained when these antennas are employed in quad arrays, as it is expected from the antenna array theory.
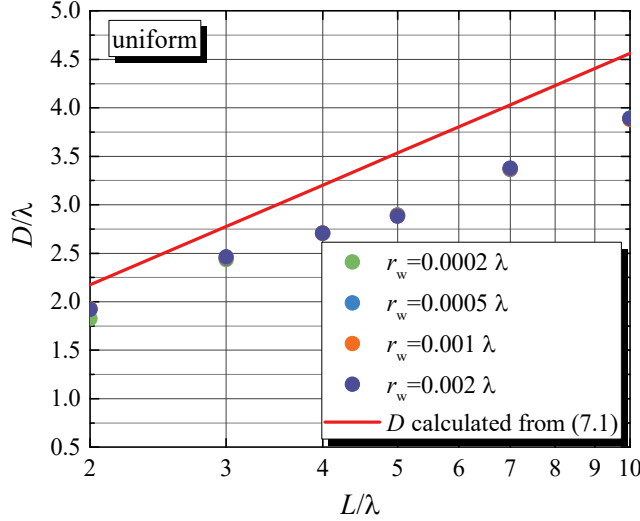
Figure 7.10. Optimal distances D for the quad arrays of uniform helical antennas.
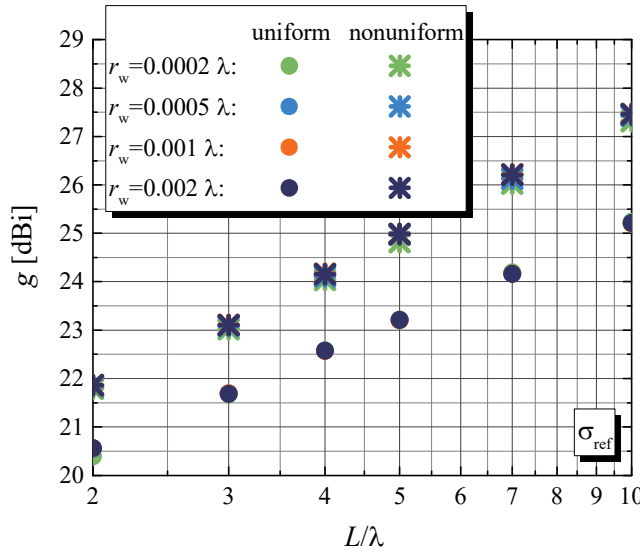
Figure 7.11. Gain of the optimal quad arrays of uniform and nonuniform helical antennas.

7.7. Comparison with a design from literature

In this subsection the quad arrays designed following formulated design procedure are compared with the quad arrays which are designed following the recommendations from [108], where an equation is presented for estimation of the optimal distances between the adjacent elements of the quad arrays

$$\frac{D_{[108]}}{\lambda} = \sqrt{\frac{G_{\mathrm{h}}}{4\pi}}, \tag{7.3}$$

where G_{h} is the (numerical) gain of the single helical antenna. Since the helical antennas that make up the quad array are designed utilizing the design equations (3.13), (3.14), (3.19), and (3.20), we

calculate G_h from (3.23). (The gain g calculated from (3.23) is in dBi, hence it requires a simple conversion $G_h = 10^{g/10}$.) Firstly, the best distances obtained through optimizations (for wire conductivity σ_{ref}), distances calculated from (7.1) and calculated from (7.3) are compared in Fig. 7.12a, whereas the gains of the quad arrays for which distances D are calculated from (7.1) and (7.3) are compared in Fig. 7.12b. The optimal distances D or the distances D calculated from (7.1) are for more than 40 % larger than the distances calculated from (7.3). However, when the distance D is calculated from (7.1), instead of using (7.3), the quad arrays achieve for around 0.5 dB higher gain.
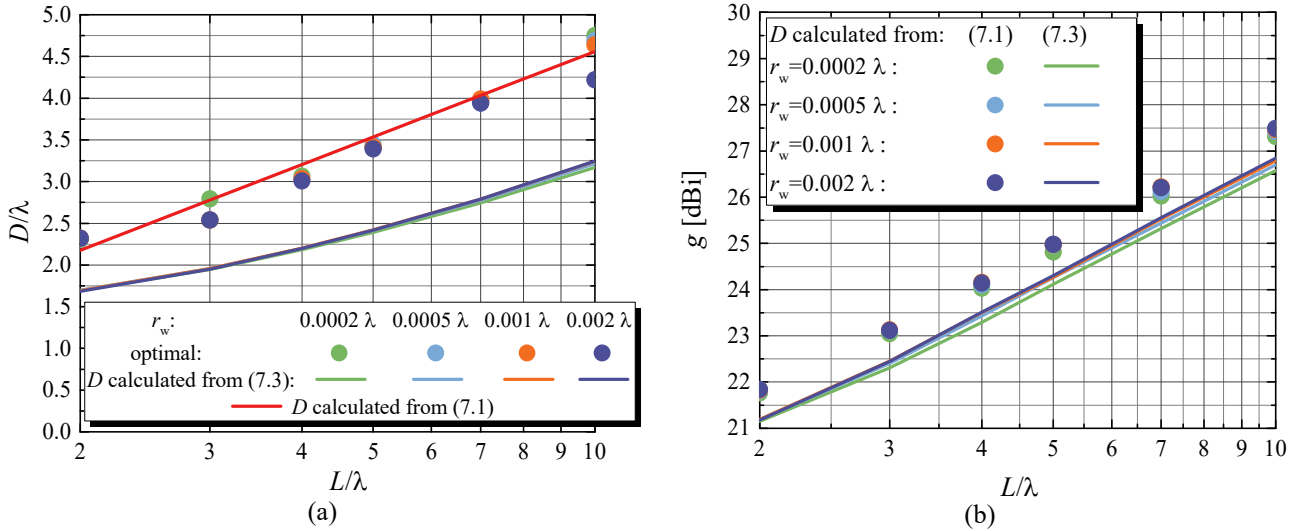
Figure 7.12. Comparison of quad arrays designed using presented design equations and utilizing guidelines from [108] (a) optimal normalized distance D and (b) gain.

The design procedure presented in this chapter allows rapid design of quad arrays of nonuniform helical antennas with linearly varying geometrical parameters. Moreover, comparison made in Fig. 7.12b confirms that, compared to the results presented in the literature, using the presented design procedure guarantees achievement of at least the same (or even higher) gain.

8. Conclusions

The main topic of this thesis is comprehensive investigation of nonuniform helical antennas and quad arrays of such antennas. Using software for numerical simulations of these antennas, optimization procedures were used and a large database of the optimal designs was created. By careful examination of this database, equations were developed that constitute a complete, standalone, and rapid procedure for designing nonuniform helical antennas with linearly varying geometrical parameters, which is the main contribution of the thesis. The proposed design procedure gives all necessary data for the complete design of nonuniform helical antennas, which significantly simplifies the design of these antennas and guarantees achievement of the optimal (or very close to the optimal) characteristics for the chosen conductor and antenna overall dimensions.

This procedure was expanded to the design of quad arrays of nonuniform helical antennas, which is the second major contribution of the thesis.

The validity of the presented design procedures was verified in several ways within this thesis. Firstly, a nonuniform helical antenna was designed following the presented design procedure and it was fabricated and measured. The results of the measurements show excellent agreement with the results of the simulations, which confirms the validity of the proposed design procedures. Secondly, the designed nonuniform helical antennas and arrays were compared with the helical antennas and arrays described in the literature. Our nonuniform helical antennas outperform practically all helical antennas presented in the literature, except in the cases of highly lossy conductor when uniform helical antennas perform better.

Besides nonuniform helical antennas with linearly varying geometrical parameters, other variations of the dimensions were considered (exponential and piecewise linear). It was concluded that all these antennas achieve almost the same gain. However, the geometry of the designed nonuniform helical antennas is simpler and hence preferable for the applications.

Further, it was noticed that nonuniform helical antennas are more sensitive to losses than the uniform helical antennas. Namely, the optimal nonuniform helical antennas achieve up to 2.5 dB higher gain than the optimal uniform helical antennas. However, this discrepancy decreases with the increase of losses. Hence, we also formulated a set of equations for the design of the optimal uniform helical antennas, which are the preferable choice when the losses are high. The clear border is established that suggests which design should be used for the considered axial antenna length, wire radius, and conductivity.

Within this thesis, flat square and circular ground planes were considered. The side of a square ground plane or the radius of a circular ground plane that is required for the achievement of the best performances are around the axial antenna length for shorter antennas, whereas for the longest antennas, they are around one half of the axial antenna length. Although the designed nonuniform helical antennas require a relatively large ground plane, this may not be a problem when such a plane already exists (e.g., certain satellites and vehicles).

Finally, additional contribution of the thesis is the complete, "step-by-step", solution of a real engineering problem, i.e., the design and fabrication of a quad array that meets the pre-defined specifications. This solution contains details about the design and optimization of the geometry of helical antennas and their positions within the array, the design of the feeding and matching network, and details about the fabrication of the prototype. The validity of the solution is verified by measurements.

The investigation and results presented in this thesis open potential topics for the future research. Namely, machine learning algorithms might be use for accelerating the finding of the optimal helical antennas and for considering more criteria or wider search-spaces. For example, the optimization can be directed at simultaneously maximizing the gain and minimizing the length of the helix conductor, which is preferable from the practical point of view. Further, the design of arrays of helical antennas can be generalized to cover an arbitrary number of array elements. Finally, nonuniform helical antennas with a small ground plane may be systematically investigated and their design procedure formulated.

Appendix

A. Gain definitions

In the literature, software, antenna datasheets, and standards the term "antenna gain" is not consistently used, or, at least, it is not used clearly. Problems also exist with the units used for the gain. The objective of this appendix is to clarify the terms and units. We primarily follow [126]. The definitions in this appendix are taken from [126] directly or with minor modifications. However, we have added comments and corrections to these definitions.

We consider an antenna in the transmitting mode. The antenna is fed by a generator that is connected to the antenna by a lossless transmission line, of a given (nominal) characteristic impedance, or a lossless waveguide, of a given wave impedance. The incident wave on the line, viz. waveguide (traveling from the generator towards the antenna) is partly reflected from the antenna due to the antenna mismatch. The reflection coefficient of the antenna is defined with respect to the characteristic impedance of the transmission line, viz. the wave impedance of the waveguide.

A.1. Terms

The **radiation intensity**, in a given direction, is defined as[1] $I = r^2 P$, where r is the distance of the field point from the antenna and P is the intensity of the Poynting vector at the field point[2], $P = |\mathbf{E} \times \mathbf{H}|$ (**E** is the electric-field vector and **H** is the magnetic-field vector).

The **average radiation intensity** is equal to the total power radiated by the antenna divided by the full solid angle[3]. The average radiation intensity of an antenna whose total radiated power is P_{rad} is $I = \dfrac{P_{\text{rad}}}{4\pi}$.

An **isotropic radiator** is a hypothetical, lossless antenna whose radiation intensity is equal in all directions. The radiation intensity of the isotropic radiator whose total radiated power is P_{rad} is $I = \dfrac{P_{\text{rad}}}{4\pi}$ for any direction.

The **radiation efficiency** is the ratio of the total power radiated by the antenna and the net power accepted by the antenna from the connected transmitter.

The **directivity** of the antenna is the ratio of the radiation intensity in a given direction to the radiation intensity averaged over all directions[4]. In the older literature, the term **directive gain** is

---

[1]Although [126] is an engineering text, formulas are avoided, though formulas would provide more compact and clearer statements. Hence, we prefer to at least partly deviate from that style.

[2] The definition in [126] is different: "the radiation intensity, in a given direction, is the power radiated from an antenna per unit solid angle". As in the most texts in English, the construction "per unit..." is used, which is not favored in a rigorous approach. Here, we actually evaluate the power density in the sense of the ratio of the elementary power radiated into an elementary solid angle and that elementary solid angle, i.e., $I = dP / d\Omega$. We do not take the ratio of the power radiated into the unit solid angle and the unit solid angle (which would be 1 steradian).

[3] In [126], it is written "divided by 4π ", where 4π actually means the full solid angle (4π steradians).

[4] "All directions" means here the directions covering the full solid angle (4π steradians). Care should be taken, however, that in some cases only the upper half-space is considered (e.g., in AM broadcasting in the LF, MF, and HF bands).

also used, but this term has been deprecated. The directivity does not take into account the dissipative loss in the antenna or the losses due to the mismatch of the antenna to the feeder and the polarization mismatch.

The **gain** of the antenna in a given direction is the ratio of the radiation intensity in that direction and the radiation intensity that would be obtained if the power accepted by the antenna were radiated isotropically. The term **absolute gain** is also used to stress the distinction from the relative gain. The gain takes into account the dissipative loss in the antenna, but it does not take into account the losses due to the mismatch of the antenna to the feeder and the polarization mismatch. If the antenna is without the dissipative loss, then, for any direction, its gain is equal to its directivity. If the antenna has the dissipative loss, then, for any direction, its numerical gain is equal to its numerical directivity multiplied by the radiation efficiency.

The **realized gain**[5,6] of the antenna in a given direction is the gain of the antenna reduced to take into account the losses due to the mismatch of the antenna to the feeder[7]. The realized gain is the product of the absolute gain and the feeder mismatch factor $1-|\rho|^2$, where ρ is the reflection coefficient of the antenna for the given feeder[8]. The realized gain takes into account the dissipative loss in the antenna and the mismatch of the antenna to the feeder, but it does not take into account the polarization mismatch.

The **relative gain** of the antenna in a given direction is the ratio of the gain of the antenna and the gain of a reference antenna. The maximum gain of the reference antenna is implied[9].

The term the **relative gain** is sometimes used in conjunction with the "relative radiation pattern", meaning the radiation pattern of the antenna normalized to its maximum.

The **partial directivity/gain** (absolute gain, realized gain, or relative gain) of the antenna for a given polarization, in a given direction, is the **directivity/gain** reduced to take into account the losses due to the polarization mismatch. The partial directivity/gain is the product of the total directivity/gain and the polarization mismatch factor $C = I_{\text{copol}}/I_{\text{total}}$, where I_{copol} is the radiation intensity corresponding to the given polarization and I_{total} is the total radiation intensity[10].

For the given direction, the **total directivity/gain** is the sum of the partial directivities/gains for (any) two orthogonal polarizations. The partial directivity cannot be greater than the total directivity. If the direction for the directivity/gain is not specified, the direction of the maximal[11] radiation intensity is implied and the maximal directivity/gain is implied.

In all previous definitions, the directivity and the gain are expressed as ratios of two physical quantities, i.e., the radiation intensities. This ratio is a pure number, i.e., it has no units. We shall

---

[5] An alternative term in English found in the literature is "practical gain"; in Serbian: "pogonsko poja čanje"; in German: "Antennen-Betriebsgewinn".

[6] In [127] the term "absolute gain" is wrongly used to mean the "realized gain: "... we define two gains; one, referred to as gain (G), and the other, referred to as absolute gain (G_{abs}), that also takes into account the reflection/mismatch losses...". The same mistake also appears in [128].

[7] The wording in [126] is "The gain of an antenna reduced by its impedance mismatch factor." By the term "impedance", one should consider the actual impedance for a transmission-line feeder and the wave impedance for a waveguide feeder.

[8] In [126], the feeder mismatch factor is referred to as the impedance mismatch factor, but it is not related to the reflection coefficient.

[9] In [126], it is incorrectly stated that "the maximum gains of the antennas are implied". The problem comes from two different usages of the word "gain". One usage is to denote the gain as the function of the angles of the spherical coordinate system (this defines the "gain pattern"). The other usage is to denote the maximum gain of the antenna. In the first usage, only the maximal gain of the reference antenna is involved. In the second usage, the maximal gain of both antennas is involved.

[10] In [126], the polarization mismatch factor is not defined, but rather the partial directivity/gain are defined from scratch, by considering I_{copol} and the radiation intensity averaged over all directions, viz. the radiation intensity that would be obtained if the power accepted by the antenna were isotropically radiated.

[11] In [126], the word "maximum" is used instead of "maximal". Although linguistically "maximum" is used as an adjective, it is a good practice to distinguish between "maximal" (being an adjective, i.e., "the largest"; in Serbian: "najveći") and "maximum" ("the largest value", as in "the maximum of the sinusoidal function is 1; in Serbian: "najveća vrednost", "maksimum"). A similar disambiguation should be done for "minimum" and "minimal".

refer to this ratio as the **numerical** directivity, viz. gain. We shall use upper-case letters for the numerical directivity (D) and gain (G). We shall use the attribute "numerical" where necessary to distinguish from the logarithmic values.

The directivity and gain are often expressed in decibels by taking $10\log_{10}$ of the numerical directivity, viz. gain. We shall use lower-case letters for the **logarithmic** directivity (d) and gain (g). We shall not stress "logarithmic" unless it is necessary to distinguish it from the numerical gain.

When considering the logarithmic directivity/gain, multiplications/divisions are replaced by additions/subtractions.

The logarithmic gain is the sum of the logarithmic directivity and the logarithmic radiation efficiency.

The realized logarithmic gain is the sum of the logarithmic (absolute) gain and the term $10\log_{10}\left(1-|\rho|^2\right)\text{dB}$.

The relative logarithmic gain is the difference of the logarithmic gain of the antenna and the logarithmic gain of the reference antenna.

The partial logarithmic directivity/gain is the sum of the logarithmic directivity/gain and the term

$$c = 10\log_{10}\frac{I_{\text{copol}}}{I_{\text{total}}}\ \text{dB} .$$

A.2. Units

The averaged radiation intensity amounts to using an isotropic radiator as a reference antenna. Hence, the unit for the logarithmic directivity/gain is **dBi** (decibels with respect to the isotropic radiator).

In the older literature, as a rule, the reference antenna was a half-wave dipole. This reference is nowadays still used in some antenna data sheets and standards (e.g., electromagnetic-compatibility standards). To stress the reference antenna, the unit for the logarithmic directivity/gain in this case is **dBd**.

The antenna directivity/gain in dBi is for 2.15 dB greater than when expressed in dBd.

Circularly-polarized antennas are often used for satellite communications (e.g., for the GPS navigation system). In order to stress that the partial logarithmic directivity/gain for the circular polarization is considered, the unit **dBic** (or **dBiC**) is used.

The attribute "partial" is seldom used, although its usage can be important to avoid ambiguities.

The unit dBi is not used in many cases, but only dB is used instead, leading to possible confusion in books, papers, simulation software, and antenna data sheets.

In software, the unit dB is often used in the meaning "dBi".

When stating the difference between two directivities/gains, which are given in dBi, it is adequate to say that the directivity/gain, is "for n dB higher than...". It is not correct to say that it is "for n dBi higher than...".

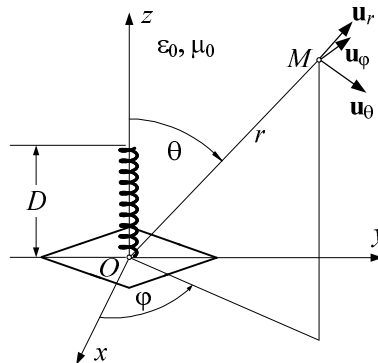## A.3. Derivation of RHCP and LHCP components of the radiated field

Figure A.1. Considered scenario for the derivation of RHCP and LHCP components of the radiated field.

We consider an arbitrary antenna, located near the coordinate origin (Fig. A.1). We observe the far (radiated) field of the antenna, at an arbitrary point M at the distance r from the antenna.

Far-field conditions are (simultaneously):

- $r \gg D$,

- $r > \lambda$,

- $r > \dfrac{2D^2}{\lambda}$ (the Fraunhofer condition),

where D is the maximal linear dimension of the antenna.

In case of helical antennas, $D \approx L > \lambda$ (if the counterbalance is not very large), so that only $r > \dfrac{2D^2}{\lambda}$ matters. (If this condition is fulfilled, then the other two are automatically satisfied.)

In the far-field region, the transversal components of the electric field ($\underline{E}_\theta$ and $\underline{E}_\varphi$ dominate), i.e., $\underline{E}_r \approx 0$ and $\underline{\mathbf{E}} = \underline{E}_\theta \mathbf{u}_\theta + \underline{E}_\varphi \mathbf{u}_\varphi$, where $\mathbf{u}_r$, $\mathbf{u}_\theta$, and $\mathbf{u}_\varphi$ are the unit vectors of the spherical coordinate system. The radiated field is, locally, a TEM wave.

We want to separate $\underline{\mathbf{E}}$ into two circularly-polarized components. The first component is the RHCP component and the second one is the LHCP component (both observed with respect to the direction of wave propagation, i.e., $\mathbf{u}_r$).

Let us first consider the RHCP component, $\underline{\mathbf{E}}_{\text{RHCP}}$. Projections of $\underline{\mathbf{E}}_{\text{RHCP}}$ on $\mathbf{u}_\theta$ and $\mathbf{u}_\varphi$ have the same intensities (the same rms values), they are in phase quadrature (these two conditions are the same for the RHCP and LHCP components), and the phase difference between $\underline{E}_\theta$ and $\underline{E}_\varphi$ is $\pi/2$ ($\underline{E}_\theta$ advances in phase, i.e., $\underline{E}_\varphi$ lags in phase). Hence, we can write $\underline{\mathbf{E}}_{\text{RHCP}} = \underline{E}_{\text{RHCP}\,\theta} \mathbf{u}_\theta + \underline{E}_{\text{RHCP}\,\varphi} \mathbf{u}_\varphi = \underline{E}_{\text{RHCP}\,\theta} \mathbf{u}_\theta - j\,\underline{E}_{\text{RHCP}\,\theta} \mathbf{u}_\varphi$.

Similarly, for the LHCP, $\underline{\mathbf{E}}_{\text{LHCP}} = \underline{E}_{\text{LHCP}\,\theta} \mathbf{u}_\theta + \underline{E}_{\text{LHCP}\,\varphi} \mathbf{u}_\varphi = \underline{E}_{\text{LHCP}\,\theta} \mathbf{u}_\theta + j\,\underline{E}_{\text{LHCP}\,\theta} \mathbf{u}_\varphi$ because now the phase difference between $\underline{E}_\theta$ and $\underline{E}_\varphi$ is $-\pi/2$ ($\underline{E}_\varphi$ advances in phase).

Further, $\underline{\mathbf{E}} = \underline{\mathbf{E}}_{\text{RHCP}} + \underline{\mathbf{E}}_{\text{LHCP}}$, so that $\underline{E}_\theta = \underline{E}_{\text{RHCP}\,\theta} + \underline{E}_{\text{LHCP}\,\theta}$ and $\underline{E}_\varphi = -j\,\underline{E}_{\text{RHCP}\,\theta} + j\,\underline{E}_{\text{LHCP}\,\theta}$. From the last two equations we have $\underline{E}_{\text{RHCP}\,\theta} = \dfrac{\underline{E}_\theta + j\,\underline{E}_\varphi}{2}$ and $\underline{E}_{\text{LHCP}\,\theta} = \dfrac{\underline{E}_\theta - j\,\underline{E}_\varphi}{2}$. We also have $\underline{E}_{\text{RHCP}\,\varphi} = \dfrac{-j\,\underline{E}_\theta + \underline{E}_\varphi}{2}$ and $\underline{E}_{\text{LHCP}\,\varphi} = \dfrac{j\,\underline{E}_\theta + \underline{E}_\varphi}{2}$.

We have completely defined the RHCP and LHCP components. We can also prove that any (arbitrarily) polarized radiated field can be split into these two components. Namely, a time-harmonic field is elliptically polarized in the general case. Hence, it can be expressed in terms of only two orthogonal linearly polarized fields (two fields are sufficient, not three). Each of these two fields can be exressed in terms of two circularly-polarized waves (one RHCP and one LHCP). The resulting RHCP and LHCP waves can be obtained by simple summations.

In the time domain, the vectors $\mathbf{E}_{\text{RHCP}}(t)$ and $\mathbf{E}_{\text{LHCP}}(t)$ rotate in the same plane (the plane defined by $\mathbf{u}_\theta$ and $\mathbf{u}_\varphi$ in our case), in opposite senses, but with the same angular velocity. At certain instances, these two vectors have the same direction (and this situation periodically repeats after an integer multiple of $T/2$, where $T = 1/f$ is the period of the field). At those instances, the intensity of the resulting electric field is maximal, $|\mathbf{E}|_{\max} = E_{\text{RHCP}} + E_{\text{LHCP}}$, where E_{RHCP} is the rms value of $\mathbf{E}_{\text{RHCP}}(t)$, $E_{\text{RHCP}} = \sqrt{2}\,E_{\text{RHCP}\,\theta} = |\mathbf{E}_{\text{RHCP}}(t)| = \sqrt{2}\left|\dfrac{\underline{E}_\theta + j\,\underline{E}_\varphi}{2}\right|$, and E_{LHCP} is the rms value of

107

$\mathbf{E}_{\text{LHCP}}(t)$, $E_{\text{LHCP}} = \sqrt{2}E_{\text{LHCP}\,\theta} = |\mathbf{E}_{\text{LHCP}}(t)| = \sqrt{2}\left|\dfrac{\underline{E}_\theta - \mathrm{j}\,\underline{E}_\varphi}{2}\right|$. A quarter period later, the vectors $\mathbf{E}_{\text{RHCP}}(t)$ and $\mathbf{E}_{\text{LHCP}}(t)$ have opposite directions, when the intensity of the resulting electric field is minimal, $|\mathbf{E}|_{\min} = |E_{\text{RHCP}} - E_{\text{LHCP}}|$. Hence, the numerical axial ratio is

$$AR = \frac{|\mathbf{E}|_{\max}}{|\mathbf{E}|_{\min}} = \frac{E_{\text{RHCP}} + E_{\text{LHCP}}}{|E_{\text{RHCP}} - E_{\text{LHCP}}|} = \frac{|\underline{E}_{\text{RHCP}}| + |\underline{E}_{\text{LHCP}}|}{\left||\underline{E}_{\text{RHCP}}| - |\underline{E}_{\text{LHCP}}|\right|}, \text{ whereas } ar[\mathrm{dB}] = 20\log_{10}\frac{|\underline{E}_{\text{RHCP}}| + |\underline{E}_{\text{LHCP}}|}{\left||\underline{E}_{\text{RHCP}}| - |\underline{E}_{\text{LHCP}}|\right|}.$$

B. Theorem of electromagnetic similitude

The theorem of electromagnetic similitude [118] defines the conditions that have to be satisfied in order to obtain an electromagnetic field similar to the field in a geometrically similar system.

Let us consider two geometrically similar systems (system 1 and system 2), shown in Fig. B.1. The ratio of the linear dimensions of these systems is n, i.e., $\mathbf{r}' = n\mathbf{r}$. (Note that in all equations within this subsection and in Fig. B.1, prime denotes the system 2.) Hence, for $n > 1$ the system 2 is larger than the system 1, and for $n < 1$ the situation is reversed. The electromagnetic similitude theorem is valid when both systems are linear. Hence the permittivity, permeability, and conductivity of the material are

$$\varepsilon'(\mathbf{r}') = e\,\varepsilon(\mathbf{r}), \ \mu'(\mathbf{r}') = m\,\mu(\mathbf{r}), \ \sigma'(\mathbf{r}') = s\,\sigma(\mathbf{r}), \tag{B.1}$$

where e, m, and s are constants. The sources of the electromagnetic field are modeled by impressed currents, which satisfy the relation $\mathbf{J}_i'(\mathbf{r}') = j\,\mathbf{J}_i(\mathbf{r})$, where j is a constant (not the imaginary unit). All phenomena in the system 2 are T times faster than in the system 1, $t' = T t$.

The field vectors in the systems satisfy the relations

$$\mathbf{E}'(\mathbf{r}') = k_E \mathbf{E}(\mathbf{r}), \ \mathbf{H}'(\mathbf{r}') = k_H \mathbf{H}(\mathbf{r}), \tag{B.2}$$

where k_E and k_H are constants. If the same field in the two systems is required, the constants k_E and k_H should be 1.
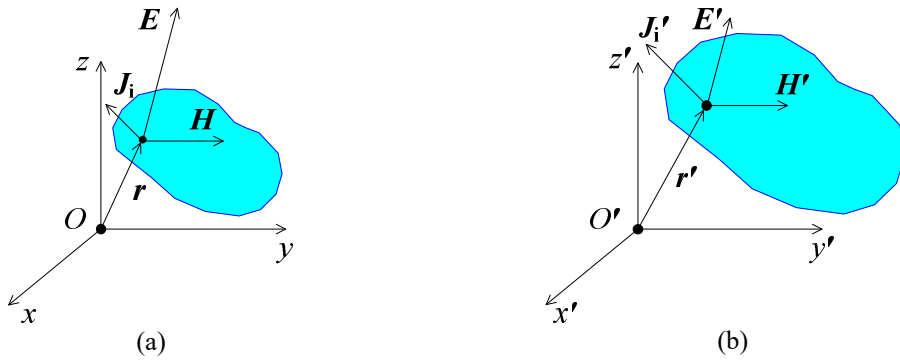
Figure B.1. Sketch of two similar systems: (a) system 1 and (b) system 2.

Maxwell's equations for the systems 1 and 2 are

$$\operatorname{curl}\mathbf{E} = -\mu\frac{\partial\mathbf{H}}{\partial t}, \ \operatorname{curl}\mathbf{H} = \sigma\mathbf{E} + \mathbf{J}_i + \varepsilon\frac{\partial\mathbf{E}}{\partial t}, \tag{B.3}$$

$$\operatorname{curl}'\mathbf{E}' = -\mu'\frac{\partial\mathbf{H}'}{\partial t'}, \ \operatorname{curl}'\mathbf{H}' = \sigma'\mathbf{E}' + \mathbf{J}_i' + \varepsilon'\frac{\partial\mathbf{E}'}{\partial t'}. \tag{B.4}$$

Since the operation curl' refers to a point $\mathbf{r}'$ of the system 2, $\operatorname{curl}' = \operatorname{curl}/n$. After the substitution of the quantities from the system 2 (prime quantities) according to previously defined relations into (B.4), it becomes

$$\operatorname{curl} \boldsymbol{E} = -\left(\frac{nmk_H}{Tk_E}\right)\mu\frac{\partial \boldsymbol{H}}{\partial t}, \ \operatorname{curl} \boldsymbol{H} = \left(\frac{nsk_E}{k_H}\right)\sigma \boldsymbol{E} + \left(\frac{jn}{k_H}\right)\boldsymbol{J}_\mathrm{i} + \left(\frac{nek_E}{Tk_H}\right)\varepsilon\frac{\partial \boldsymbol{E}}{\partial t}. \tag{B.5}$$

In order to obtain the electromagnetic similitude, (B.3) and (B.5) must be identical. Hence, the expressions in parentheses in (B.5) must be equal to unity,

$$\frac{nmk_H}{Tk_E} = 1, \ \frac{nsk_E}{k_H} = 1, \ \frac{jn}{k_H} = 1, \ \frac{nek_E}{Tk_H} = 1. \tag{B.6}$$

Since we are interested in the relative field distribution (for analyzing antenna characteristics), the constants k_E and k_H are 1, which simplifies (B.6) to

$$\frac{nm}{T} = 1, \ ns = 1, \ jn = 1, \ \frac{ne}{T} = 1. \tag{B.7}$$

Practically it is almost impossible to obtain $m \neq 1$, i.e., $\mu' \neq \mu$, and $e \gg 1$ or $1/e \gg 1$. Hence, we can adopt $m = e = 1$ (i.e., we have the same dielectric and magnetic materials in these systems, provided that they are lossless), which additionally simplifies (B.7) to

$$n = T, \ j = \frac{1}{T}, \ s = \frac{1}{T}. \tag{B.8}$$

These conditions lead to the conclusion that if the geometrical parameters are n times larger in the system 2 than in the system 1, the conductivity and the frequency ($1/T$) in the system 2 have to be n times smaller. This allows that the antenna simulations can be run at an arbitrary operating frequency and, by applying the theorem of electromagnetic similitude, the antenna geometry can be scaled so that it corresponds to the desired frequency. The shape (pattern) of the electromagnetic field distribution (hence, the antenna characteristics, such as the impedance and radiation pattern) will be maintained.

References

[1] J. D. Kraus, "Helical beam antennas," *Electronics*, 20, pp. 109-111, April 1947.

[2] J. D. Kraus, "The helical antenna," in *Antennas*, Chapter 7, pp. 265-339, New York, McGraw-Hill, 1988.

[3] G. Zheng and B. Sun, "High-gain normal-mode omnidirectional circularly polarized antenna," *IEEE Antennas and Wireless Propagation Letters*, vol. 17, no. 6, pp. 1104-1108, June 2018, doi: 10.1109/LAWP.2018.2834477.

[4] H. Nakano, N. Ikeda, Yu-Yuan Wu, R. Suzuki, H. Mimaki, and J. Yamauchi, "Realization of dual-frequency and wide-band VSWR performances using normal-model helical and inverted-F antennas," *IEEE Transactions on Antennas and Propagation*, vol. 46, no. 6, pp. 788-793, June 1998, doi: 10.1109/8.686763.

[5] S. Zhu et al., "Miniaturized tunable conical helix antenna," *Proceedings of 2014 IEEE Radio and Wireless Symposium (RWS)*, Newport Beach, CA, 2014, pp. 100-102, doi: 10.1109/RWS.2014.6830109.

[6] J. T. Rowley, R. B. Waterhouse, and K. H. Joyner, "Modeling of normal-mode helical antennas at 900 MHz and 1.8 GHz for mobile communications handsets using the FDTD technique," *IEEE Transactions on Antennas and Propagation*, vol. 50, no. 6, pp. 812-820, June 2002, doi: 10.1109/TAP.2002.1017661.

[7] G. Lazzi and O. P. Gandhi, "On modeling and personal dosimetry of cellular telephone helical antennas with the FDTD code," *IEEE Transactions on Antennas and Propagation*, vol. 6, no. 4, pp. 525-530, April 1998, doi: 10.1109/8.664116.

[8] I. Egorov and Z. Ying, "A non-uniform helical antenna for dual-band cellular phones," *Proceedings of IEEE Antennas and Propagation Society International Symposium. Transmitting Waves of Progress to the Next Millennium. 2000 Digest. Held in conjunction with: USNC/URSI National Radio Science Meeting*, Salt Lake City, UT, 2000, pp. 652-655 vol. 2, doi: 10.1109/APS.2000.875272.

[9] G. Zhou, "A non-uniform pitch dual band helix antenna," *Proceedings of IEEE Antennas and Propagation Society International Symposium. Transmitting Waves of Progress to the Next Millennium. 2000 Digest. Held in conjunction with: USNC/URSI National Radio Science Meeting*, Salt Lake City, UT, 2000, pp. 274-277, vol. 1, doi: 10.1109/APS.2000.873761.

[10] S. M. Farghaly Sayed and O. Y. K. Alani, "A dual-mode helical antenna design for on-and off-body communication in body sensor networks," *Proceedings of 2016 3rd International Conference on Soft Computing & Machine Intelligence (ISCMI)*, Dubai, 2016, pp. 239-243, doi: 10.1109/ISCMI.2016.18.

[11] N. T. Tuan et al., "Deterministic equation of self-resonant structures for normal-mode helical antennas implanted in a human body," *IEEE Antennas and Wireless Propagation Letters*, vol. 17, no. 8, pp. 1377-1381, Aug. 2018, doi: 10.1109/LAWP.2018.2846600.

[12] O. H. Murphy, C. N. McLeod, M. Navaratnarajah, M. Yacoub, and C. Toumazou, "A pseudo-normal-mode helical antenna for use with deeply implanted wireless sensors," *IEEE Transactions on Antennas and Propagation*, vol. 60, no. 2, pp. 1135-1139, Feb. 2012, doi: 10.1109/TAP.2011.2173106.

[13] S. Koulouridis and K. S. Nikita, "Study of the coupling between human head and cellular phone helical antennas," *IEEE Transactions on Electromagnetic Compatibility*, vol. 46, no. 1, pp. 62-70, Feb. 2004, doi: 10.1109/TEMC.2004.823612.

[14] G. S. Stamatakos, K. S. Nikita, and N. K. Uzunoglu, "Analysis of the interaction between a layered spherical human head model and a helical dipole antenna," *Proceedings of the 22nd Annual International Conference of the IEEE Engineering in Medicine and Biology Society (Cat. No.00CH37143)*, Chicago, IL, 2000, pp. 1007-1010, vol. 2, doi: 10.1109/IEMBS.2000.897895.

[15] C. Donn, "A new helical antenna design for better on- and off-boresight axial ratio performance," *IEEE Transactions on Antennas and Propagation*, vol. 28, no. 2, pp. 264-267, March 1980, doi: 10.1109/TAP.1980.1142323.

[16] T. Sproewitz, S. Reershemius, L. C. Hauer, S. Fexer, M. Schütze, and B. Suhr, "Development, testing and in-orbit verification of a large CFRP helical antenna on the AISat mission," *Proceedings of 2020 IEEE Aerospace Conference*, Big Sky, MT, USA, 2020, pp. 1-9, doi: 10.1109/AERO47225.2020.9172803.

[17] J. Costantine, K. Y. Kabalan, A. E. Hajj, Y. Tawk, and C. G. Christodoulou, "A reconfigurable/deployable helical antenna for small satellites," *Proceedings of 2013 IEEE Antennas and Propagation Society International Symposium (APSURSI)*, Orlando, FL, 2013, pp. 390-391, doi: 10.1109/APS.2013.6710856.

[18] J. Costantine, Y. Tawk, and C. G. Christodoulou, "Reconfigurable deployable antennas for space communications," *Proceedings of 2014 International Workshop on Antenna Technology: Small Antennas, Novel EM Structures and Materials, and Applications (iWAT)*, Sydney, NSW, Australia, 2014, pp. 151-154, doi: 10.1109/IWAT.2014.6958623.

[19] Z. Blazevic and M. Skiljo, "Helical antennas in satellite radio channel," *Advances in Satellite Communications*, doi: 10.5772/21833.

[20] S. Fu, Q. Kong, S.-J. Fang, and Z. Wang, "Optimized design of helical antenna with parasitic patch for L-band satellite communications," *Progress In Electromagnetics Research Letters*, vol. 44, pp. 9-13, 2014, doi: 10.2528/PIERL13093002.

[21] S. A. Hasan, "Simulation and measurement analysis for innovative lightweight, circularly polarized, ultra wideband, wide coverage, single turn axial mode monofilar helical antenna for space applications," *Proceedings of 2011 IEEE International Conference on Microwave Technology & Computational Electromagnetics*, Beijing, 2011, pp. 88-91, doi: 10.1109/ICMTCE.2011.5915170.

[22] J. Wettergren, P. Dimming, J. F. Johansson, and M. Öhgren, "A high gain X-band isoflux helix antenna," *Proceedings of 2016 10th European Conference on Antennas and Propagation (EuCAP)*, Davos, 2016, pp. 1-4, doi: 10.1109/EuCAP.2016.7481874.

[23] A. Khaleghi, I. Balasingham, and A. Vosoogh, "A compact ultra-wideband spiral helix antenna for in-body communications," *Proceedings of 8th European Conference on Antennas and Propagation (EuCAP 2014)*, The Hague, 2014, pp. 3093-3096, doi: 10.1109/EuCAP.2014.6902482.

[24] C. Liu, Y. Guo, and S. Xiao, "Circularly polarized helical antenna for ISM-band ingestible capsule endoscope systems," *IEEE Transactions on Antennas and Propagation*, vol. 62, no. 12, pp. 6027-6039, Dec. 2014, doi: 10.1109/TAP.2014.2364074.

[25] A. Boothby, R. Hwang, V. Das, J. Lopez, and D. Y. C. Lie, "Design of axial-mode helical antennas for Doppler-based continuous non-contact vital signs monitoring sensors," *Proceedings of 2012 IEEE Radio and Wireless Symposium*, Santa Clara, CA, 2012, pp. 87-90, doi: 10.1109/RWS.2012.6175377.

[26] H. Luyen, S. C. Hagness, and N. Behdad, "A balun-free helical antenna for minimally invasive microwave ablation," *IEEE Transactions on Antennas and Propagation*, vol. 63, no. 3, pp. 959-965, March 2015, doi: 10.1109/TAP.2015.2389223.

[27] Li-Ruei Kuo and Hsi-Tseng Chou, "A printed helix-type antenna array for wireless communications at high frequencies," *Proceedings of 2007 IEEE Antennas and*

Propagation Society International Symposium, Honolulu, HI, 2007, pp. 4429-4432, doi: 10.1109/APS.2007.4396525.

[28] T. Sharma and H. Vasu, "Designing and comparative study of parameters affecting helix performance at 1420 MHz," *Proceedings of 2013 International Mutli-Conference on Automation, Computing, Communication, Control and Compressed Sensing (iMac4s)*, Kottayam, 2013, pp. 318-325, doi: 10.1109/iMac4s.2013.6526430.

[29] T. Sharma, "Simulation and optimal design of a monofliar helix antenna for 1420 MHz," *Proceedings of 2012 Second International Conference on Advanced Computing & Communication Technologies*, Rohtak, Haryana, 2012, pp. 245-250, doi: 10.1109/ACCT.2012.103.

[30] F. Ghayem and F. Rassaei, "Helical antenna to measure radiated power density around a BTS: Design and implementation," *Proceedings of 2014 3rd Asia-Pacific Conference on Antennas and Propagation*, Harbin, 2014, pp. 185-188, doi: 10.1109/APCAP.2014.6992448.

[31] A. N. Jaafar et al., "Analysis of helical antenna for wireless application at 2.4 GHz," *Proceedings of 2019 IEEE Asia-Pacific Conference on Applied Electromagnetics (APACE)*, Melacca, Malaysia, 2019, pp. 1-5, doi: 10.1109/APACE47377.2019.9020810.

[32] S. A. Nauroze and M. M. Tentzeris, "A novel printed stub-loaded square helical antenna," *Proceedings of 2015 IEEE International Symposium on Antennas and Propagation & USNC/URSI National Radio Science Meeting*, Vancouver, BC, 2015, pp. 774-775, doi: 10.1109/APS.2015.7304774.

[33] Z. Song, Y. Li, H. Zheng, Y. LI, M. Wang, and E. Li, "Design of an axial mode wideband helical dielectric resonator antenna for 5G applications," *Proceedings of 2019 12th International Workshop on the Electromagnetic Compatibility of Integrated Circuits (EMC Compo)*, Hangzhou, China, 2019, pp. 117-120, doi: 10.1109/EMCCompo.2019.8919745.

[34] N. Destria et al., "Design of 2.4 GHz helix antenna for increasing wifi signal strength using Mmanagal and wirelesmon application," *Proceedings of 2017 International Conference on Computing, Engineering, and Design (ICCED)*, Kuala Lumpur, 2017, pp. 1-5, doi: 10.1109/CED.2017.8308117.

[35] L. Liu, Y. Li, Z. Zhang, and Z. Feng, "Circularly polarized patch-helix hybrid antenna with small ground," *IEEE Antennas and Wireless Propagation Letters*, vol. 13, pp. 361-364, 2014, doi: 10.1109/LAWP.2014.2306494.

[36] N. Neveu et al., "Miniature hexaferrite axial-mode helical antenna for unmanned aerial vehicle applications," *IEEE Transactions on Magnetics*, vol. 49, no. 7, pp. 4265-4268, July 2013, doi: 10.1109/TMAG.2013.2242870.

[37] S. Ozman, A. H. Shah, S. Ali, S. K. Selvaperumal, and V. Thangasamy, "Gain enhancement of axial mode helical antenna for UAV applications," *Proceedings of 2015 6th International Conference on Intelligent Systems, Modelling and Simulation*, Kuala Lumpur, 2015, pp. 237-241, doi: 10.1109/ISMS.2015.51.

[38] N. Rimbault, A. Sharaiha, and S. Collardey, "High gain design of small axial mode helical antenna over a cylindrical cavity for RFID applications," *Proceedings of 2012 IEEE International Conference on RFID-Technologies and Applications (RFID-TA)*, Nice, 2012, pp. 433-436, doi: 10.1109/RFID-TA.2012.6404562.

[39] N. Rimbault, A. Sharaiha, and S. Collardey, "Low profile high gain helix antenna over a conical ground plane for UHF RFID applications," *Proceedings of 2012 15 International Symposium on Antenna Technology and Applied Electromagnetics*, Toulouse, 2012, pp. 1-3, doi: 10.1109/ANTEM.2012.6262424.

[40] J. Choo, H. Choo, L. Park, and Y. Oh, "Design of multi-layered polygonal helix antennas for RFID readers in UHF band," *Proceedings of 2005 IEEE Antennas and Propagation Society International Symposium*, Washington, DC, 2005, pp. 283-286 vol. 2B, doi: 10.1109/APS.2005.1551996.

[41] H. M. Aumann and N. W. Emanetoglu, "Effect of axial rotation on mutual coupling between helical antennas in a doppler radar," *Proceedings of 2017 IEEE International Symposium on Antennas and Propagation & USNC/URSI National Radio Science Meeting*, San Diego, CA, 2017, pp. 2275-2276, doi: 10.1109/APUSNCURSINRSM.2017.8073180.

[42] M. Secmen, S. Demir, A. Hizal, and O. A. Civi, "An elliptically polarized axial-mode helical antenna with a conformal polarizer," *Proceedings of The Second European Conference on Antennas and Propagation, EuCAP 2007*, Edinburgh, 2007, pp. 1-4, doi: 10.1049/ic.2007.1503.

[43] S. Adibelli, R. Golubović, A. Djordjević, D. Olćan, and A. Zajić, "Design and fabrication of nonuniform helical antennas for detection of side-channel attacks in computer systems," *Proceedings of 12th European Conference on Antennas and Propagation (EuCAP 2018)*, London, 2018, pp. 1-5, doi: 10.1049/cp.2018.0564.

[44] M. Marton, L. Ovsenik, J. Turan, M. Spes, and J. Vasarhelyi, "Possibility of increasing availability of FSO/RF hybrid system with implementation of helix antenna for 5.2 GHz," *Proceedings of International Carpathian Control Conference (ICCC)*, Szilvasvarad, 2018, pp. 498-501, doi: 10.1109/CarpathianCC.2018.8399681.

[45] H. King and J. Wong, "Characteristics of 1 to 8 wavelength uniform helical antennas," *IEEE Transactions on Antennas and Propagation*, vol. 28, no. 2, pp. 291-296, March 1980, doi: 10.1109/TAP.1980.1142322.

[46] J. Wong and H. King, "Empirical helix antenna design, "*Proceedings of 1982 Antennas and Propagation Society International Symposium*, Albuquerque, NM, USA, 1982, pp. 366-369, doi: 10.1109/APS.1982.1148836.

[47] G. A. Thiele and W. L. Stutzman, "Helical antennas" in *Antenna theory and design*, Subchapter 7.3, pp. 225-233, New York: J. Wiley, 2012.

[48] D. T. Emerson, "The gain of the axial-mode helix antenna," *Antenna Compendium*, 4, pp. 64-68, 1995.

[49] A. R. Djordfevic, A. G. Zajic, M. M. Ilic, and G. L. Stuber, "Optimization of helical antennas [Antenna Designer's Notebook], " *IEEE Antennas and Propagation Magazine*, vol. 48, no. 6, pp. 107-115, Dec. 2006, doi: 10.1109/MAP.2006.323359.

[50] Poynting, "Helical Antenna Design Curves", www.poynting.co.za/tech_training/helical.shtml.

[51] A. R. Djordjevic, A. G. Zajic, and M. M. Ilic, "Enhancing the gain of helical antennas by shaping the ground conductor," *IEEE Antennas and Wireless Propagation Letters*, vol. 5, pp. 138-140, 2006, doi: 10.1109/LAWP.2006.873946.

[52] T. E. Tice and J. D. Kraus, "The influence of conductor size on the properties of helical beam antennas," *Proceedings of IRE*, vol. 27, pp. 1296–1296, Nov. 1949.

[53] D. I. Olcan, A. R. Zajic, M. M. Ilic, and A. R. Djordjevic, "On the optimal dimensions of helical antenna with truncated-cone reflector," *Proceedings of 2006 First European Conference on Antennas and Propagation*, Nice, 2006, pp. 1-6, doi: 10.1109/EUCAP.2006.4584946.

[54] A. R. Djordjevic, M. M. Ilic, A. G. Zajic, D. I. Olcan, and M. M. Nikolic, "Why does reflector enhance the gain of helical antennas?," *Proceedings of The Second European Conference on Antennas and Propagation, EuCAP 2007*, Edinburgh, 2007, pp. 1-8, doi: 10.1049/ic.2007.0966.

[55] K. R. Carver, "The helicone–a circularly polarized antenna with low sidelobe level", *Proceedings of IEEE*, vol. 55, no. 4, pp. 559-559, April 1967, doi: 10.1109/PROC.1967.5584.

[56] H. Nakano, K. Hitosugi, N. Tatsuzawa, D. Togashi, H. Mimaki, and J. Yamauchi, "Effects on the radiation characteristics of using a corrugated reflector with a helical antenna and an electromagnetic band-gap reflector with a spiral antenna," *IEEE Transactions on Antennas and Propagation*, vol. 53, no. 1, pp. 191-199, Jan. 2005, doi: 10.1109/TAP.2004.840755.

[57] X. Tang, Y. He, and B. Feng, "Design of a wideband circularly polarized strip-helical antenna with a parasitic patch," *IEEE Access*, vol. 4, pp. 7728-7735, 2016, doi: 10.1109/ACCESS.2016.2628044.

[58] R. Cai *et al.*, "Design and experiment of a high gain axial-mode helical antenna," *Proceedings of 2010 IEEE 12th International Conference on Communication Technology*, Nanjing, 2010, pp. 522-525, doi: 10.1109/ICCT.2010.5688887.

[59] P. Xu, Z. Yan, G. Yuan, and T. Zhang, "Design of a high gain axial-mode helical antenna with a loaded plate," *Proceedings of 2013 International Workshop on Microwave and Millimeter Wave Circuits and System Technology*, Chengdu, 2013, pp. 113-115, doi: 10.1109/MMWCST.2013.6814581.

[60] Y. Wu and J. L. Li, "Gain enhancement of axial-mode helical antenna with a cylindrical ring," *Proceedings of ISAPE2012*, Xian, 2012, pp. 128-132, doi: 10.1109/ISAPE.2012.6408725.

[61] J. Kim, S. H. Cha, Y. Yoon, J. Ryu, and J. S. Choi, "Axial mode helical antenna with circular prasitic rings for gain enhancement," *Proceedings of 2017 International Symposium on Antennas and Propagation (ISAP)*, Phuket, 2017, pp. 1-2, doi: 10.1109/ISANP.2017.8228819.

[62] R. M. Barts and W. L. Stutzman, "A reduced size helical antenna," *Proceedings of IEEE Antennas and Propagation Society International Symposium 1997. Digest*, Montreal, Quebec, Canada, 1997, pp. 1588-1591 vol. 3, doi: 10.1109/APS.1997.631477.

[63] W. Lee *et al.*, "Lossy ferrite core-dielectric shell structure for miniature GHz axial-mode helical antenna," *IEEE Antennas and Wireless Propagation Letters*, vol. 18, no. 5, pp. 951-955, May 2019, doi: 10.1109/LAWP.2019.2906505.

[64] J. Lj. Dinkić, M. S. Tasić, and A. R. Đorđević, "Influence of conductor shape and size on properties of helical antennas," *Proceedings of 5th International Conference on Electrical, Electronic and Computing Engineering iETRAN 2018*, Palić, Serbia, June 2018.

[65] S. Yao and S. V. Georgakopoulos, "Origami segmented helical antenna with switchable sense of polarization," *IEEE Access*, vol. 6, pp. 4528-4536, 2018, doi: 10.1109/ACCESS.2017.2787724.

[66] X. Liu, S. Member, C. L. Zekios, and S. V Georgakopoulos, "Analysis of a packable and tunable origami multi-radii helical antenna," *IEEE Access*, vol. 7, pp. 13003–13014, 2019, doi: 10.1109/ACCESS.2019.2892711.

[67] X. Liu, S. Yao, S. V. Georgakopoulos, B. S. Cook, and M. M. Tentzeris, "Reconfigurable helical antenna based on an origami structure for wireless communication system," *Proceedings of 2014 IEEE MTT-S International Microwave Symposium (IMS2014)*, Tampa, FL, 2014, pp. 1-4, doi: 10.1109/MWSYM.2014.6848553.

[68] S. I. Hussain Shah, S. Ghosh, and S. Lim, "A novel DNA inspired mode and frequency reconfigurable origami helical antenna," *Proceedings of 2018 IEEE International Symposium on Antennas and Propagation & USNC/URSI National Radio Science Meeting*, Boston, MA, 2018, pp. 187-188, doi: 10.1109/APUSNCURSINRSM.2018.8608572.

[69] Z. Ren, S. Qi, Z. Hu, Z. Shen, and W. Wu, "Wideband water helical antenna of circular polarization," *IEEE Transactions on Antennas and Propagation*, vol. 67, no. 11, pp. 6770-6777, November 2019, doi: 10.1109/TAP.2019.2922846.

[70] Y. Zhou, S. Fang, H. Liu, and S. Fu, "A liquid metal conical helical antenna for circular polarization-reconfigurable antenna", *International Journal of Antennas and Propagation*, vol. 2016, Article ID 3782373, 7 pages, 2016. https://doi.org/10.1155/2016/3782373

[71] S. Jalali Mazlouman, A. Mahanfar, C. Menon, and R. G. Vaughan, "Reconfigurable axial-mode helix antennas using shape memory alloys," *IEEE Transactions on Antennas and Propagation*, vol. 59, no. 4, pp. 1070-1077, April 2011, doi: 10.1109/TAP.2011.2109686.

[72] J. Kraus, "A 50-ohm input impedance for helical beam antennas, " *IEEE Transactions on Antennas and Propagation,* vol. 25, no. 6, pp. 913-913, November 1977, doi: 10.1109/TAP.1977.1141687.

[73] J. Che and C. Chen, "Wideband axial-mode helical antenna with 3D printed proliferated radome," *Proceedings of 2017 IEEE International Symposium on Antennas and Propagation & USNC/URSI National Radio Science Meeting*, San Diego, CA, 2017, pp. 695-696, doi: 10.1109/APUSNCURSINRSM.2017.8072390.

[74] S. V. Savić, M. M. Ilić, and A. R. Djordjević, "Design of internal wire-based impedance matching of helical antennas using an equivalent thin-wire model," *International Journal of Antennas and Propagation*, vol. 2017, Article ID 7365793, 5 pages, 2017. https://doi.org/10.1155/2017/7365793

[75] S. V. Savić, M. M. Ilić, and A. R. Djordjević, "Influence of wire-based impedance-matching on helical antenna radiation," *Proceedings of 2018 26th Telecommunications Forum (TELFOR)*, Belgrade, 2018, pp. 1-4, doi: 10.1109/TELFOR.2018.8611904.

[76] D. W. Liao, X. Y. Wang, B. Zhou, and F. Wei, "A novel impedance matching method of helix antenna, " *Proceedings of 2016 IEEE International Conference on Microwave and Millimeter Wave Technology (ICMMT)*, Beijing, 2016, pp. 771-773, doi: 10.1109/ICMMT.2016.7762437.

[77] D. J. Angelakos and D. Kajfez, "Modifications on the axial-mode helical antenna," *Proceedings of the IEEE*, vol. 55, no. 4, pp. 558-559, April 1967, doi: 10.1109/PROC.1967.5583.

[78] J. Wong and H. King, "Broadband quasi-taper helical antennas," *IEEE Transactions on Antennas and Propagation*, vol. 27, no. 1, pp. 72-78, January 1979, doi: 10.1109/TAP.1979.1142033.

[79] W. E. Jennings and A. R. Clark, "An investigation into the properties and limits of quasi-taper helical antennas," *Proceedings of IEEE Antennas and Propagation Society Symposium*, Monterey, CA, USA, 2004, pp. 2903-2906, vol. 3, doi: 10.1109/APS.2004.1331985.

[80] H. M. Elkamchouchi and A. I. Salem, "Helical antennas with nonuniform helix diameter," *Proceedings of the Eighteenth National Radio Science Conference. NRSC'2001 (IEEE Cat. No.01EX462)*, Mansoura, Egypt, 2001, pp. 143-152 vol. 1, doi: 10.1109/NRSC.2001.929187.

[81] H. M. Elkamchouchi and A. I. A. Salem, "Effects of geometrical parameters, loading, and feeding on nonuniform helical antennas," *Proceedings of the Nineteenth National Radio Science Conference*, Alexandria, Egypt, 2002, pp. 90-100, doi: 10.1109/NRSC.2002.1022610.

[82] R. Golubovic, A. Djordjevic, D. Olcan, and J. Mosig, "Nonuniformly-wound helical antennas," *Proceedings of 2009 3rd European Conference on Antennas and Propagation*, Berlin, Germany, pp. 3077-3080, March 2009.

[83] A. M. Menon and S. S. Kumar, "Optimum design of axial mode helical antenna with nonlinear pitch profile modeled using Catmull-Rom spline and Particle Swarm Optimization," *Proceedings of 2011 International Conference on Communications and Signal Processing*, Calicut, 2011, pp. 146-150, doi: 10.1109/ICCSP.2011.5739288.

[84] K. Jimisha and S. Kumar, "Optimum design of exponentially varying helical antenna with non uniform pitch profile," *Procedia Technology*, vol. 6, pp. 792-798, 2012, https://doi.org/10.1016/j.protcy.2012.10.096.

[85] C. H. Chen, E. K. N. Yung, B. J. Hu, and S. L. Xie, "Axial mode helix antenna with exponential spacing," *Microwave and Optical Technology Letters*, vol. 49, no. 7, pp. 1525-1530, July 2007, doi: 10.1002/mop.22485.

[86] J. D. Kraus, "Helical beam antennas for wide-band applications," *Proceedings of the IRE*, vol. 36, no. 10, pp. 1236-1242, October 1948, doi: 10.1109/JRPROC.1948.231603

[87] M. B. Dragović, "Antenna systems," in *Antennas and propagation* (in serbian), Chapter 7, pp. 65-88, Belgrade, Academic mind, 2003.

[88] J. Lj. Dinkić, D. I. Olćan, A. R. Djordjević, and A. G. Zajić, "High-gain quad array of nonuniform helical antennas," *International Journal of Antennas and Propagation, Hindawi*, vol. 2019, 12 pages, 2019, doi: 10.1155/2019/8421809.

[89] Y. A. Ho, H. T. Hui, and E. K. N. Yung, "A 1x2 dielectric-loaded helical antenna array," *Proceedings of IEEE Antennas and Propagation Society International Symposium. 1996 Digest*, Baltimore, MD, USA, 1996, pp. 1962-1965, vol. 3, doi: 10.1109/APS.1996.549990.

[90] P. Kumar Mishra, D. R. Jahagirdar, and G. Kumar, "Broadband circularly polarized helical array antenna design for ground to air data link," *Proceedings of 2019 IEEE Indian Conference on Antennas and Propogation (InCAP)*, Ahmedabad, India, 2019, pp. 1-5, doi: 10.1109/InCAP47789.2019.9134567.

[91] H. Nakano, N. Asaka, and J. Yamauchi, "Short helical antenna array fed from a waveguide," *IEEE Transactions on Antennas and Propagation*, vol. 32, no. 8, pp. 836-840, August 1984, doi: 10.1109/TAP.1984.1143417.

[92] A. Sudhakar and J. Ravindranadh, "Realization of desired shaped beam array of helical antennas," *Proceedings of 2017 Progress In Electromagnetics Research Symposium - Spring (PIERS)*, Saint Petersburg, Russia, 2017, pp. 3326-3329, doi: 10.1109/PIERS.2017.8262331.

[93] Y. Andreev, V. Koshelev, and S. Smirnov, "Characteristics of an ultrawideband 8x8 array of cylindrical helical antennas," *Proceedings of 2018 20th International Symposium on High-Current Electronics (ISHCE)*, Tomsk, 2018, pp. 66-69, doi: 10.1109/ISHCE.2018.8521217.

[94] Y. Andreev *et al.*, "Radiation of high-power ultrawideband pulses with elliptical polarization by four-element array of cylindrical helical antennas," *Laser and Particle Beams*, vol. 33, pp. 633-640, December 2015, doi: 10.1017/S0263034615000725.

[95] H. Ho, "A helical antenna array design for mobile satellite communication system," *Proceedings of 1997 Asia-Pacific Microwave Conference*, Hong Kong, China, 1997, pp. 657-659, vol. 2, doi: 10.1109/APMC.1997.654627.

[96] H. King and J. Wong, "Directivity of a uniformly excited NxN array of directive elements," *IEEE Transactions on Antennas and Propagation*, vol. 23, no. 3, pp. 401-404, May 1975, doi: 10.1109/TAP.1975.1141064.

[97] H. T. Hui, E. K. N. Yung, C. L. Law, Y. S. Koh, and W. L. Koh, "Design of a small and low-profile 2x2 hemispherical helical antenna array for mobile satellite communications," *IEEE Transactions on Antennas and Propagation*, vol. 52, no. 1, pp. 346-348, Januar 2004, doi: 10.1109/TAP.2003.822410.

[98] S. I. S. Hassan, M. F. Ain, and A. R. Arief, "Four beams helical antenna array for mobile satellite application," *Proceedings of 2004 RF and Microwave Conference (IEEE Cat. No.04EX924)*, Selangor, Malaysia, 2004, pp. 53-55, doi: 10.1109/RFM.2004.1411073.

[99] C. Liu, Y. Guo, X. Bao, and S. Xiao, "60-GHz LTCC integrated circularly polarized helical antenna array," *IEEE Transactions on Antennas and Propagation*, vol. 60, no. 3, pp. 1329-1335, March 2012, doi: 10.1109/TAP.2011.2180351.

[100] Á. Palomares-Caballero, A. Alex-Amor, J. F. Valenzuela-Valdés, and P. Padilla, "Helix antenna array based on higher symmetries for antenna miniaturization and mutual coupling reduction," *Proceedings of 2019 IEEE-APS Topical Conference on Antennas and Propagation in Wireless Communications (APWC)*, Granada, Spain, 2019, pp. 272-275, doi: 10.1109/APWC.2019.8870497.

[101] X. Li, Q. Liu, J. Zhang, and L. Zhao, "16-element single-layer rectangular radial line helical array antenna for high-power applications," *IEEE Antennas and Wireless Propagation Letters*, vol. 9, pp. 708-711, 2010, doi: 10.1109/LAWP.2010.2059371.

[102] J. Zemanovic, P. Hajach, and P. Podhoransky, "Verification of four elements helical antennas array design procedure," *Proceedings of 2008 14th Conference on Microwave Techniques*, Prague, Czech Republic, 2008, pp. 1-4, doi: 10.1109/COMITE.2008.4569937.

[103] C. Phongcharoenpanich, T. Lertwiriyaprapa, S. Lamultree, P. Wounchoum, S. Kosulvit, and M. Krairiksh, "Characteristics of a helical array antenna radiating circularly polarized conical beam," *Proceedings of IEEE Antennas and Propagation Society International Symposium. 2001 Digest. Held in conjunction with: USNC/URSI National Radio Science Meeting (Cat. No.01CH37229)*, Boston, MA, USA, 2001, pp. 557-560 vol. 4, doi: 10.1109/APS.2001.959524.

[104] X. Li, Q. Liu, X. Wu, L. Zhao, J. Zhang, and Z. Zhang, "A GW level high-power radial line helical array antenna," *IEEE Transactions on Antennas and Propagation*, vol. 56, no. 9, pp. 2943-2948, September 2008, doi: 10.1109/TAP.2008.928781.

[105] H. Nakano, H. Takeda, T. Honma, H. Mimaki, and J. Yamauchi, "An extremely low-profile helical array antenna," *Proceedings of International Symposium on Antennas and Propagation Society, Merging Technologies for the 90's*, Dallas, TX, USA, 1990, pp. 702-705 vol. 2, doi: 10.1109/APS.1990.115206.

[106] H. Nakano, H. Takeda, Y. Kitamura, H. Mimaki, and J. Yamauchi, "Low-profile helical array antenna fed from a radial waveguide," *IEEE Transactions on Antennas and Propagation*, vol. 40, no. 3, pp. 279-284, March 1992, doi: 10.1109/8.135470.

[107] T. Noro and Y. Kazama, "Helical array antennas with high efficiency, wide frequency bandwidth and simple structure," *Proceedings of IEEE Antennas and Propagation Society Symposium, 2004.*, Monterey, CA, USA, 2004, pp. 1050-1053, vol. 1, doi: 10.1109/APS.2004.1329854.

[108] H. King, J. Wong, and E. Newman, "Helical antennas," in *Antenna Engineering Handbook* (Volakis, J.L., Ed.), Chapter 12, New York, McGraw-Hill Companies, 2007.

[109] S. Fu, Q. Kong, and C. Li, "New design of helical antenna array for L-band land mobile satellite communications," *Proceedings of 2014 3rd Asia-Pacific Conference on Antennas and Propagation*, Harbin, China, 2014, pp. 37-39, doi: 10.1109/APCAP.2014.6992404.

[110] J. Dinkić, D. Olćan, and A. Đorđević, "Comparison of various geometries of nonuniform helical antennas", *Proceedings of 6th International Conference on Electrical, Electronic and Computing Engineering icETRAN 2019*, Srebrno jezero, Serbia, June 3-6, 2019.

[111] WIPL-D, Belgrade, Serbia. (2017). WIPL-D Pro v11.0—3D EM Solver. [Online]. Available: www.wipl-d.com.

[112] A. R. Djordjević, M. B. Baždar, V. V. Petrović, D. I. Olćan, T. K. Sarkar, and R. F. Harrington, AWAS for Windows: Analysis of Wire Antennas and Scatterers, Software and User's Manual, Boston: Artech House, 2002.

[113] J. Dinkić, D. Olćan, A. Djordjević, and A. Zajić, "Design and optimization of nonuniform helical antennas with linearly varying geometrical parameters," *IEEE Access*, vol. 7, pp. 136855-136866, 2019, doi: 10.1109/ACCESS.2019.2942363.

[114] J. Dinkić, D. Olćan, A. Djordjević, and A. Zajić, "Comparison of optimization approaches for designing nonuniform helical antennas," *Proceedings of 2018 IEEE International Symposium on Antennas and Propagation & USNC/URSI National Radio Science Meeting*, Boston, MA, 2018, pp. 1581-1582, doi: 10.1109/APUSNCURSINRSM.2018.8608928.

[115] J. A. Nelder and R. Mead, "A simplex method for function minimization," *The Computer Journal* 7, pp. 308–313, 1965.

[116] J. Kennedy and R. Eberhart, "The particle swarm," in *Swarm Intelligence*, Chapter 7, pp. 287–326, 1st ed., Morgan Kaufmann, 2001.

[117] J. Robinson and Y. Rahmat-Samii, "Particle swarm optimization in electromagnetics," *IEEE Trans. on Antennas and Propagation*, vol. 52, pp. 397–407, 2004.

[118] B. D. Popovic, "Electromagnetic field theorems," *Proceedings of IEE*, vol. 128, no. 1, pp. 47-63, January 1981.

[119] J. D. Kraus, "Arrays of point sources," in *Antennas*, Chapter 4, pp. 118-199, New York, McGraw-Hill, 1988.

[120] J. Dinkić, D. Olćan, A. Djordjević, and A. Zajić, "Comparison of the optimal uniform and nonuniform lossy helical antennas," *Proceedings of 2020 IEEE International Symposium on*

Antennas and Propagation and North American Radio Science Meeting, Montreal, QC, Canada, 2020, pp. 423-424, doi: 10.1109/IEEECONF35879.2020.9330063.

[121] Blender – a 3D modeling and rendering package, Blender Foundation, 2017.

[122] http://www.idvorsky.com/en/

[123] A. R. Djordjević, M. B. Baždar, R. F. Harrington, and T. K. Sarkar, LINPAR for Windows: Matrix Parameters for Multiconductor Transmission Lines, Boston, MA, Artech House, 1999.

[124] B. E. Spielman, "Dissipation loss effects in isolated and coupled transmission lines," *IEEE Transactions on Microwave Theory and Techniques*, vol. 25, no. 8, pp. 648-656, Aug. 1977, doi: 10.1109/TMTT.1977.1129180.

[125] www.awrcorp.com

[126] *IEEE Standard for Definitions of Terms for Antennas*, IEEE Antennas and Propagation Society, IEEE Std 145TM-2013, The Institute of Electrical and Electronic Engineer, New Yor, NY, USA. 2014.

[127] C. A. Balanis, "Gain," in *Antenna Theory, Analysis and Design*, Subchapter 2.9, pp. 65-69, Wiley-Interscience, John Wiley & Sons, Hoboken, NJ, USA, 2005.

[128] C. A. Balanis, "Gain," in *Modern Antenna Handbook*, Subchapter 1.9, pp. 23-26, John Wiley & Sons, Hoboken, NJ, USA, 2008.

Biography

Jelena Dinkić was born in Negotin, Serbia, on December 3, 1991. She graduated from the Mathematical Grammar School, a school with the High National Distinction status, with a number of top awards in physics and math competitions in the Republic of Serbia.

Jelena Dinkić received the B.Sc. degree in 2014 with the average grade 9.83 (out of 10.00), and M.Sc. degree in 2015 with the average grade 10.00 (out of 10.00), both from the School of Electrical Engineering, University of Belgrade, Department of Electronics. She was a recipient of the scholarships awarded by the City of Belgrade in 2010, 2012, and 2013, and by Studenica Foundation in 2012/2013 and 2013/2014.

From August 2014 to November 2014 Jelena Dinkić worked as a student intern at the University of California, San Diego, in Photonics Systems Group.

She is enrolled in Ph.D. studies in 2015 in the Department of Microwave Engineering at the School of Electrical Engineering, University of Belgrade. Her average grade during Ph.D. studies is 10.00 (out of 10.00). During Ph.D. studies Jelena Dinkić participated in three courses organized by European School of Antennas: Antenna Imaging Techniques (Delft, July 2015), Microwave Imaging and Diagnostics (Taormina, October 2016), and Diagnostic and Therapeutic Applications of Electromagnetics (Naples, September 2019).

She is co-author of 14 papers (2 papers in the international journals, 2 papers in the national journals, 7 papers at the international conferences, and 3 papers at the national conferences), 2 textbooks, and she has participated in 3 projects.

In 2014, she joined the School of Electrical Engineering, University of Belgrade, as a Teaching Assistant at the Department of General Electrical Engineering.

Изјава о ауторству

Име и презиме аутора ___Јелена Динкић_____

Број индекса ___2015/5026_____

Изјављујем

да је докторска дисертација под насловом

Неуниформне хеликоидалне антене

(Nonuniform helical antennas)

- резултат сопственог истраживачког рада;
- да дисертација у целини ни у деловима није била предложена за стицање друге дипломе према студијским програмима других високошколских установа;
- да су резултати коректно наведени и
- да нисам кршио/ла ауторска права и користио/ла интелектуалну својину других лица.

Потпис аутора

У Београду, __26.04.2021.__ године

Изјава о истоветности штампане и електронске верзије докторског рада

Име и презиме аутора ___Јелена Динкић___

Број индекса ___2015/5026___

Студијски програм ___Електротехника и рачунарство, Микроталасна техника___

Наслов рада ___Неуниформне хеликоидалне антене (Nonuniform helical antennas)___

Ментор ___проф. др Антоније Ђорђевић и в. проф. др Драган Олћан___

Изјављујем да је штампана верзија мог докторског рада истоветна електронској верзији коју сам предао/ла ради похрањивања у **Дигиталном репозиторијуму Универзитета у Београду.**

Дозвољавам да се објаве моји лични подаци везани за добијање академског назива доктора наука, као што су име и презиме, година и место рођења и датум одбране рада.

Ови лични подаци могу се објавити на мрежним страницама дигиталне библиотеке, у електронском каталогу и у публикацијама Универзитета у Београду.

Потпис аутора

У Београду, ___26.04.2021.___ године

Изјава о коришћењу

Овлашћујем Универзитетску библиотеку „Светозар Марковић" да у Дигитални репозиторијум Универзитета у Београду унесе моју докторску дисертацију под насловом:

Неуниформне хеликоидалне антене
(Nonuniform helical antennas)

која је моје ауторско дело.

Дисертацију са свим прилозима предао/ла сам у електронском формату погодном за трајно архивирање.

Моју докторску дисертацију похрањену у Дигиталном репозиторијуму Универзитета у Београду и доступну у отвореном приступу могу да користе сви који поштују одредбе садржане у одабраном типу лиценце Креативне заједнице (Creative Commons) за коју сам се одлучио/ла.

1. Ауторство (CC BY)

2. Ауторство – некомерцијално (CC BY-NC)

3. Ауторство – некомерцијално – без прерада (CC BY-NC-ND)

4. Ауторство – некомерцијално – делити под истим условима (CC BY-NC-SA)
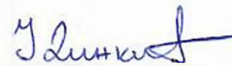
5. Ауторство – без прерада (CC BY-ND)

6. Ауторство – делити под истим условима (CC BY-SA)

(Молимо да заокружите само једну од шест понуђених лиценци.
Кратак опис лиценци је саставни део ове изјаве).

Потпис аутора

У Београду, 26.04.2021. године

1. **Ауторство**. Дозвољавате умножавање, дистрибуцију и јавно саопштавање дела, и прераде, ако се наведе име аутора на начин одређен од стране аутора или даваоца лиценце, чак и у комерцијалне сврхе. Ово је најслободнија од свих лиценци.

2. **Ауторство – некомерцијално**. Дозвољавате умножавање, дистрибуцију и јавно саопштавање дела, и прераде, ако се наведе име аутора на начин одређен од стране аутора или даваоца лиценце. Ова лиценца не дозвољава комерцијалну употребу дела.

3. **Ауторство – некомерцијално – без прерада**. Дозвољавате умножавање, дистрибуцију и јавно саопштавање дела, без промена, преобликовања или употребе дела у свом делу, ако се наведе име аутора на начин одређен од стране аутора или даваоца лиценце. Ова лиценца не дозвољава комерцијалну употребу дела. У односу на све остале лиценце, овом лиценцом се ограничава највећи обим права коришћења дела.

4. **Ауторство – некомерцијално – делити под истим условима**. Дозвољавате умножавање, дистрибуцију и јавно саопштавање дела, и прераде, ако се наведе име аутора на начин одређен од стране аутора или даваоца лиценце и ако се прерада дистрибуира под истом или сличном лиценцом. Ова лиценца не дозвољава комерцијалну употребу дела и прерада.

5. **Ауторство – без прерада**. Дозвољавате умножавање, дистрибуцију и јавно саопштавање дела, без промена, преобликовања или употребе дела у свом делу, ако се наведе име аутора на начин одређен од стране аутора или даваоца лиценце. Ова лиценца дозвољава комерцијалну употребу дела.

6. **Ауторство – делити под истим условима**. Дозвољавате умножавање, дистрибуцију и јавно саопштавање дела, и прераде, ако се наведе име аутора на начин одређен од стране аутора или даваоца лиценце и ако се прерада дистрибуира под истом или сличном лиценцом. Ова лиценца дозвољава комерцијалну употребу дела и прерада. Слична је софтверским лиценцама, односно лиценцама отвореног кода.